Development of Enabling Technologies for Ultra-high Dose Rate and Spatially Fractionated Radiation Therapy

by

Nolan M. Esplen
B.Sc., University of Victoria, 2014

A Dissertation Submitted in Partial Fulfillment of the
Requirements for the Degree of

DOCTOR OF PHILOSOPHY

in the Department of Physics and Astronomy

Development of Enabling Technologies for Ultra-high Dose Rate and Spatially Fractionated Radiation Therapy

by

Nolan M. Esplen
B.Sc., University of Victoria, 2014

Supervisory Committee

Dr. Magdalena Bazalova-Carter, Main Supervisor
(Department of Physics and Astronomy)

Dr. Derek Wells, Departmental Member
(Department of Physics and Astronomy)

Dr. Julian Lum, Outside Member
(Biochemistry and Microbiology)

ABSTRACT

Despite the important advances that have been made in radiation therapy (RT) over recent decades, there remains an ongoing demand for treatments which are capable of widening the therapeutic window. This might be achieved, for example, by reducing the normal-tissue toxicity observed following RT with curative intent. Ultra-high dose rate (UHDR) FLASH-RT and spatially-fractionated RT (SFRT) techniques are both promising examples of emerging therapies primed to address this unmet need. Unfortunately, the technological requirements for delivering these new modalities have proven to be exceptionally demanding and a limiter to their adoption in a broader context. Therefore, innovative new strategies are required to bring these techniques into a larger number of research centers around the world and to facilitate greater mechanistic understanding ahead, and in support, of future clinical translation.

In this body of work, new technologies have been developed which facilitate the delivery, and improved accessibility, of FLASH-RT and SFRT for radiobiological research. Firstly, a multi-slit collimator design and proof-of-concept demonstrated a cost-effective means of enabling micro-beam SFRT on a commercial small-animal irradiator. Thereafter, the design and validation of an anatomically realistic, 3D-printed mouse phantom for small-animal radiobiology research was conducted. The rodent-morphic phantom provides a useful tool for simulation and dosimetric verification of complex experimental configurations in the absence of treatment planning capabilities and supports improved reliability and accuracy of pre-clinical outcomes data. Lastly, in an effort to facilitate x-ray FLASH radiobiology experiments, two different sources were functionalized for UHDR photon beam production: first, using a commercial 160 kVp X-ray tube and, secondly, through the development of a megavoltage (MV) electron-to-photon converter for a high-powered electron linear accelerator. The MV source represented a world-first 10 MeV UHDR-compatible x-ray irradiation platform which was subsequently characterized for use in a first radiobiological experiment investigating FLASH effects in normal tissue for healthy mice at the clinically-relevant treatment energy of 10 MV.

Contents

List of Tables

List of Figures

Acknowledgements

The work presented herein would not have been possible without the contributions and support of numerous individuals and organizations. I would like to foremost thank my supervisor Dr. Magdalena Bazalova-Carter for her peerless mentorship, encouragement and patience. Thank you for making the PhD experience such an amazing and positive one, for the inspired research projects, rewarding opportunities, tireless support, and not to mention for building an amazing lab full of such amazing and talented people. This journey has given me countless opportunities for academic growth and successes that I have been able to take immense pride in. I would also like to deeply thank my supervisory committee members, Dr. Julian Lum and Dr. Derek Wells, for their thoughtful insights and guidance throughout the evolutionary course of this turbulent but exciting PhD, and to the academic advisors and chair for their support of my defense. A heartfelt thanks goes out to all members of the XCITE lab (past and present), who have not only provided thoughtful ideas, scientific feedback, and creative inspiration, but powerful camaraderie and lasting friendship. Special thanks to Chris Johnstone, Clay Lindsay, Samantha van Nest and Chelsea Dunning for long days of fruitful discussion and brainstorming. To Luca Egoriti, friend and colleague without whom the ARIEL collaboration would not have been possible, and to all my collaborators at TRIUMF, especially Alex Gottberg, Cornelia Hoehr, Thomas Planche, Stephanie Radel, and the members of the ARIEL e-linac development and operations teams for their tireless experimental support and hospitality during the FLASH campaign and throughout my time as a visitor. I would also like to thank the Natural Sciences and Engineering Research Council of Canada for providing generous CGS-D funding in support of my PhD studies. The department and FGS for their award nominations and for having created a friendly and supportive academic environment that enabled me to thrive in my time at the university. And lastly, to my friends and family - your support helped me to persist through challenging times and motivate me to succeed in my academic pursuits.

Dedication

For my parents

whose support and encouragement have lifted me up and carried me forward. In light of the challenges you helped me through, I am more thankful than these words can say.

"Little by little, one travels far." - J.R.R. Tolkien

This work embodies a years-long journey complete with the inspirations, trials and celebrations, meetings and partings, and sense of discovery that any good adventure might have. I am beyond thankful to have shared this pivotal chapter with wonderful mentors, colleagues and friends who have motivated me to dare, inspired me to think and challenged me to achieve. For these formative years, I am immensely thankful to have been provided so many opportunities for personal, academic and professional growth. From life-long friendships and fond memories, to irreplaceable experiences and newfound confidence, I owe much to my time at the University of Victoria and as a proud member of the XCITE lab. I know, without a doubt, that I will look back fondly as I move excitedly towards the next chapter.

Chapter 1

Introduction

1.1 Introduction

In the context of public health today, cancer remains among the leading causes of death worldwide. As of 2020, the World Health Organization reported approximately 19.3M new cases worldwide and 9.9M cancer-related deaths. In North America alone, there were 2.5M new cases and 0.7M cancer-related deaths. By current estimates for North America, the cumulative risk of being diagnosed with cancer by age 75 is 33.9% and it is predicted that cancer incidence will continue to rise [1]. Consequently, increasingly efficacious and economical cancer treatment are needed to meet the increasing and accelerated demand for cancer care.

Among today's leading modalities for cancer care, radiation therapy (RT) remains an essential and prevalent option for both curative and palliative treatments. In fact, it is estimated that up to 50% of all diagnosed patients will receive RT in the course of their disease development [2, 3]. Moreover, while RT accounts for only a small percentage of overall cancer care costs it accounts for up to 40% of treatments resuting in cancer cure [4].

Today, the form of radiation most often employed in RT are electromagnetic rays (i.e. x-rays or gamma rays), typically identified using their particle-equivalent nomenclature - photons - and delivered using medical linear accelerators (linacs). Following their discovery in 1895 by William Roentgen [4], the potential use of x-rays as agents for cancer diagnosis and curative therapy was quickly recognized. Throughout the 20th century, steady advancements have been made in the domains of physics and medicine for external beam radiation therapy using both electromagnetic and particle radiation.

Regardless of its nature, radiation is inherently toxic to living cells through its capacity to deposit enough energy (dose) in matter to create direct or indirect chemical damage to important bio-macromolecules - such as nuclear deoxyribonucleic acid (DNA) - and within the various cellular compartments. The ensuing biochemical damage cascades may lead to loss of proliferation potential and ultimately cell death if the damage cannot be effectively repaired [5]. Thus, the basic principle behind radiotherapy cancer treatment is simple: to preferentially kill cancer cells through radiation

exposure while maximally sparing healthy tissue. Progress towards this goal has driven numerous technological and methodological advancements in the fields of radiation oncology and physics.

The first, and perhaps most obvious, means to elicit the desired differential effect in RT is through maximal avoidance of healthy tissue while sufficiently exposing the tumor. Typically, RT treatments achieve this by utilizing advanced image guidance (i.e. computed tompgraphy, magnetic resosnance imaging) and intensity modulation to precisely irradiate the treatment volume. Precision therapies, such as stereotactic body RT (SBRT) and radiosurgery, which leverage high-dose fractions (hypo-fractionation) and small field sizes, may further reduce the amount of normal tissue that is exposed to the external beam as it passes through the patient. Alternatively, improved tumor targeting and conformity is theoretically achievable by leveraging the favourable ballistic (i.e. electronic stopping) properties of particle radiations (i.e. electrons, protons, heavy ions). By using modern imaging technologies and advanced delivery techniques, improved tissue tolerance has afforded a wider therapeutic window. Furthermore, with the advent of more advanced techniques so too has there evolved the subject of small-animal radiotherapy in order to simulate and optimize new therapies in a scaled down context. In this way, researchers have been able to more systematically study the radiobiology underlying RT dose-response relationships which ultimately drive clinical decision making.

Unfortunately, despite advances in image-guidance and intensity-modulated techniques, along with the introduction of charged particle therapies to the clinic, RT is unable to completely spare healthy tissue surrounding the treatment volume. Thus, normal-tissue toxicity remains a key limiter to the curative potential of RT; this is especially true for pediatric treatments or those cases involving dose-limiting organs-at-risk (OARs) and radioresistant tumors. In a bid to combat these extant limitations, emergent modalities capable of reducing radiation-induced toxicity without compromising overall treatment effectiveness are attracting substantial interest within the medical physics and oncological communities. Spatially-fractionated RT (SFRT) and ultra-high dose rate (UHDR) FLASH-RT stand as notable examples, each having demonstrated an extraordinary capacity for normal tissue sparing and selective tumoricidal effects [6–11]. Nevertheless, there remains a need to elucidate the biological mechanisms which drive these observed benefits in order to allow their safe exploitation in clinical contexts.

To pursue a clinical translation of FLASH and SFRT, advanced radiation sources and novel delivery schemes must be made available to support these unconventional treatments. However, due to the relative inaccessibility of SFRT and FLASH-capable sources at the time of writing [12, 13], research in these domains tends to be restricted to the few institutions with access to the requisite technologies. For this reason, there exists an immediate demand for improved access to UHDR-compatible irradiation platforms suitable for critical SFRT and FLASH preclinical experiments.

It is precisely this unmet need which motivates the work exposited in this dissertation, namely, the development of enabling technologies to facilitate the delivery of novel radiation modalities which are capable of improving the RT therapeutic index. By expanding capabilities or providing a proof-

of-concept in the domains of FLASH, SFRT, and the small-animal RT dosimetry which bridges the two, this doctoral thesis comprises a novel and, as will be argued, significant contribution within these subject areas.

In the following introductory sections, the basic principles and defining features of each therapy is introduced while a relevant review of literature is covered in chapters pertaining to each subject matter. Thereafter, significance claims and an outline of the document structure are presented.

1.1.1 Spatially Fractionated Radiotherapy (SFRT)

In the context of conventional RT, the term fractionation typically refers to the segmentation of beam delivery in time. Spatial fractionation, by contrast, refers to a spatial segmentation of beam within a single delivery, effected by using appropriate beam collimation, scanning, or combination thereof (Figure 1.1). Among the existing SFRT modalities, micro-beam (MRT) and mini-beam radiotherapy (MBRT) have become well known for their capacity to reduce normal-tissue toxicity at very high dose, thus offering significant utility in cases where OAR would otherwise limit the efficacy of conventional treatment [6–9, 14]. These modalities are typically characterized by the use of microplanar x-ray beams to deliver ablative doses within a single treatment fraction. The resultant dose distributions comprise alternating high-dose (peak) and non-irradiated (valley) regions. For such highly inhomogeneous dose distributions, the therapeutic efficacy critically depends on the ability to ablate neoplastic tissue without compromising the desired normal tissue sparing effect. Therefore, for the optimization of any spatially-fractionated modality, it is imperative that the peak-to-valley dose ratio (PVDR) be maximized so as to minimize valley tissue dose, which is believed to govern the dose limiting toxicity [14–20].

To date, a majority of preclinical MRT research has employed arrays of parallel, microplanar x-ray beams, generally $<$100 µm wide and spaced 50–400 µm on-center [6–8, 14, 15, 21, 22]. More recently, however, groups have opted to study the effects of using larger aperture sizes, typically larger than 200 µm, designated as minibeam radiotherapy (MBRT) [16, 18, 23–25] as well as the feasibility of micro-aperture GRID treatment [26,27]. The requisite arrays of millimetric beamlets are traditionally generated using high-intensity synchrotron sources with mean energies between 50 and 125 keV [9,23, 28,29]. Employing UHDR sources for SFRT is motivated by the need to limit organ movement within the delivery timeframe so as to preserve the fractionated dose distribution, and thus PVDR, over time; meanwhile, a lower beam energy affords sharp beam profiles and lower valley doses. Unfortunately, the limited accessibility and high-cost associated with the use of synchrotron facilities remains a major obstacle to widespread implementation and advancement of MRT and MBRT research. As such, the use of commercial small animal irradiators, such as the image-guided small animal radiation research platform (SARRP) [30], to deliver SFRT treatments is proving attractive for some research groups [16, 31]. Additional work is needed to establish the relative benefits and limitations of MRT/MBRT and for 2D SFRT analogues (i.e. GRID), including the use of larger beam sizes, possibly coupled with

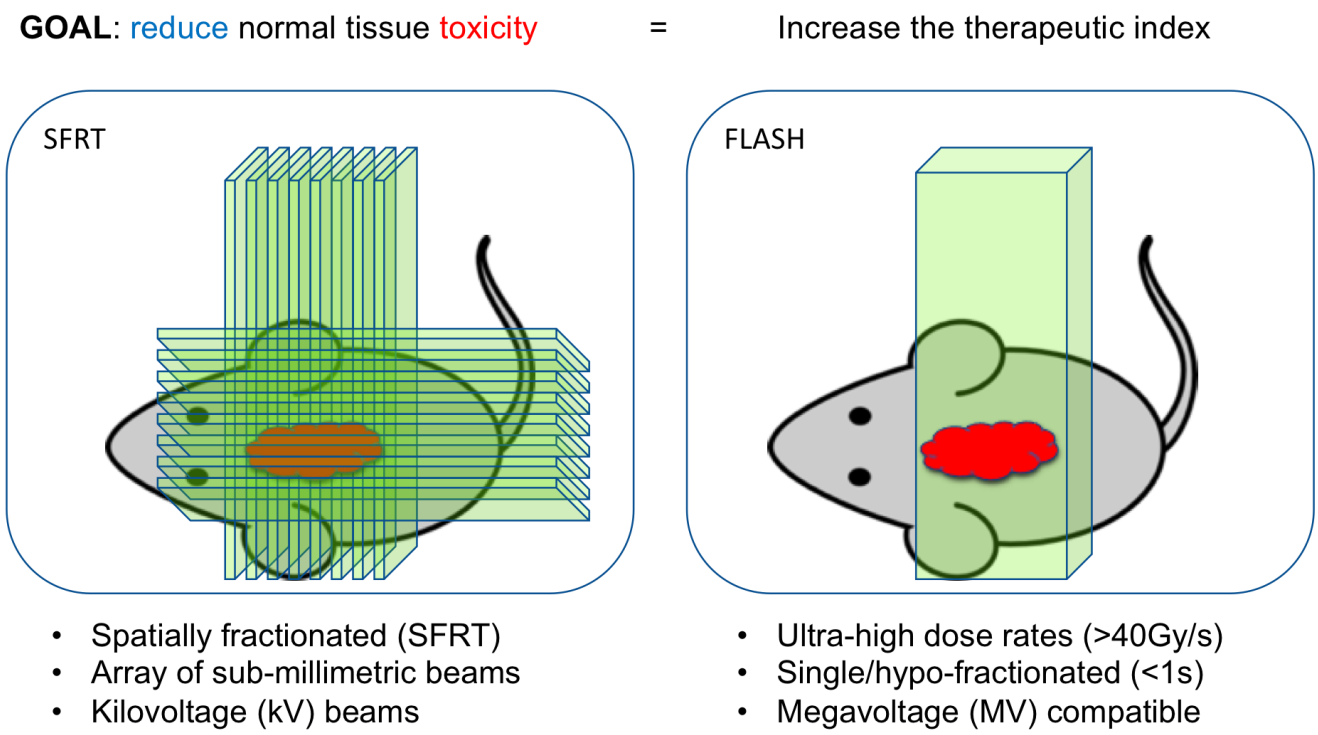

Figure 1.1: Illustrative depiction of the two novel RT modalities studied: SFRT and FLASH-RT.

higher beam energies in various preclinical subjects. While small-animal irradiators may enable such explorations, it comes at the expense of UHDR capatilibies unless the system is functionalized for UHDR delivery [32, 33]; alternatively, novel MV x-ray sources [27, 34] or high-intensity, high-energy particle (i.e. proton, very high-energy electron) modalities [35–37] may provide viable alternatives to synchrotron-generated x-rays.

1.1.2 Ultra-fast and ultra-high dose-rate radiotherapy (FLASH)

FLASH RT is a novel modality, employing dose-rates >1000-times those used in the clinic, and has recently gained considerable attention for being a radical solution towards minimizing side effects following curative RT. Interest in UHDR therapy, while not altogether new, has been rekindled following a series of publications which demonstrated a substantial reduction in normal-tissue toxicity in various small-animals models and across multiple tissue types [10, 11, 38, 39]. Furthermore, it appears that FLASH RT elicits this normal tissue protective effect – since termed the FLASH effect - while maintaining the same degree of tumor control as for conventional dose-rate RT [11, 38, 40–43]. This capacity to foster a differential response between normal and tumor tissue presents a point of commonality between FLASH and SFRT and an important advancement over conventional therapies [44].

To date, FLASH-RT has been nominally characterized by irradiation at ultra-high dose rates <40 Gy/s in order to effect single sub-second treatment fractions [10, 11, 38] (see also Figure 1.1).

However, because the physical beam parameters required to drive the normal tissue sparing remain to be elucidated, this dose-rate definition is currently in flux. In particular, inter-dependent parameters such as the dose per pulse, the number of pulses, intra-pulse dose-rate, pulse repetition frequency (PRF), average dose rate and the total irradiation time may each be of particular importance [12, 45–47]. The role of each must be further explored to determine the delivery conditions required for the safe exploitation of FLASH-RT and optimization of any therapeutic benefit.

At present, there remains an immediate need to identify the beam requirements for FLASH-RT. While there is a growing number of systems available which are capable of reaching the requisite dose rates they remain largely limited to a few well-endowed facilities and research groups world-wide [13]. In an attempt to rapidly address the outstanding questions associated with FLASH-RT, existing accelerators technologies are being adapted [44, 48–50], and new technologies developed [51–53] in order to improve the accessibility of sources capable of FLASH delivery. Additionally, there is interest in extending the applicability of FLASH to modalities which may be better suited to the treatment of deep-seated tumors, namely very high energy electrons (VHEE), megavoltage (MV) x-rays and protons, combined with intensity-modulated treatment [49, 52, 54–58].

1.1.3 Small animal radiotherapy

As novel RT treatment methodologies and technologies emerge it is imperative that the efficacy of the new approach be evaluated, verified and reproduced in controlled settings ahead of clinical translation. To this end, pre-clinical research is often employed using various small-animal models, most commonly mice. Through small-animal radiotherapy research, new techniques and technologies may be studied in a scaled down context bearing greater biological similarity to humans when compared with *in-vitro* studies. This is especially valuable for those therapies which exhibit outcomes that are sensitive to the biological context and which may benefit considerably from research *in-vivo*. FLASH and UHDR-SFRT therapies are relevant examples which appear particularly sensitive to physiological parameters such as oxygenation and vascularity, respectively, and which may rely on the action of cellular redox and immunologic components of damage response to elicit their respective tissue sparing effects.

Small-animal RT is often delivered with the assistance of irradiators that are designed to accommodate the animals while enabling diagnostic and therapeutic intervention. For example, systems such as the small-animal radiation research platform (SARRP) enables both micro-CT image-guidance, integrated treatment planning, and x-ray irradiation at energies up to 225 kVp [30, 59, 60]. However, small-animal RT is complicated by the need for accurate small-field dosimetry and presents an active area of research interest [61]. Medical physics and radiobiology researchers are ultimately concerned with being able to provide reliable dose measurements with which to associate pre-clinical treatment outcomes, given that these underpin the evaluation of therapeutic efficacy. Unfortunately, reproducibility of dose measurements in radiobiology experiments suffers from significant cross-institutional variability which has persisted in spite of advancements in the capabilities of modern small-animal

irradiators [62–65]. This may be a consequence of numerous factors, but obvious among them is a lack of standardization compared to what is found in the clinic. Clearly, there remains a need for new dosimetry methods and protocols to help reduce dose uncertainties such that reliable and reproducible outcomes data might be acquired to support a safer and more efficient clinical translation.

Small animal RT represents an underlying theme of the aforementioned FLASH and SFRT modalities developed in this dissertation, each being at a preclinical stage of development where there exists a need to better understand the dose-response relationships and identify optimal delivery parameters based on the associated outcomes. Such advancement in understanding will inevitably be driven by an improved understanding of the radiobiological mechanisms underlying the perceived therapeutic benefit. To answer important biologic questions ahead of clinical translation, small-animal radiotherapy will play an indispensable role. Methods for improving accuracy in small-animal dosimetry therefore serve to assist in optimization of SFRT and FLASH RT and avoid complicating the already challenging dosimetry required for UHDR irradiations.

1.1.4 Primary Contributions and Significance of the work

The dissertation scope may be summarized as the design and simulation, fabrication and validation of technologies which support the delivery of novel forms of radiation therapy (RT).

In brief, the body of work explores phantom development for small-animal RT as well as the technical implementation of SFRT and FLASH modalities using conventional (i.e. x-ray tubes, small-animal irradiators) and UHDR-compatible sources. The core contributions are summarized below.

Contributions

1 **SFRT**
- Design of a divergent microbeam collimator for use on the commercial SARRP

2 **Small-animal Radiotherapy**
- Fabrication and dosimetric validation of a rodent-morphic 3D-printed mouse phantom

3 **FLASH-RT**
- Delivery of UHDR x-rays for FLASH research using conventional kV and novel MV radiation sources
  - i *160 kVp X-ray tube*
  - ii *10 MeV electron-to-photon converter for a superconducting research e-linac*

Throughout this document, the primary aim is to support the claim that a significant contribution has been made in these three key domains towards provision of accessible tools or knowledge with the aim of improving adoption of each preclinical technique and thereby support accelerated clinical translation. The following section presents an outline of the primary contributions, their significance, and how they help to address the unmet needs in the domain of radiotherapy research, as identified in the previous sections.

1.1.5 Structure of the Thesis

Chapter 3: SFRT on the small-animal radiation research platform (SARRP)

Hypothesis: A commercial small-animal irradiator and divergent keV x-ray beam can be effectively collimated for SFRT research.

Significance: This initial body of work contributes to an active and growing body of research relating to the development and implementation of SFRT collimation schemes that would enable microbeam radiotherapy to be delivered using small animal irradiators in place of synchrotron accelerators. As a result of this optimization work, the relative importance and sensitivity of various design parameters could be established within a set of realistic constraints. Such insights may help researchers to find reasonable compromises in the design process and motivate the use of more cost-effective manufacturing technologies, in contrast with the current norm. Recommendations were made on the basis of improving the affordability and accessibility of MRT so as to support the acceleration of modality development. This work resulted in a 2018 publication in *Physics in Medicine and Biology* [31].

Chapter 4: Pre-clinical Mouse Phantoms for Improved Dosimetry in Radiobiology

Hypothesis: 3D printed rodent-morphic phantoms can aid in accurate preclinical dose measurement and treatment verification using water-equivalent, small-field dosimeters.

Significance: In the second core contribution, a methodology is presented for fabricating a 3D-printed mouse phantom for use in radiobiology experiments along with a dosimetric validation across three different treatment plans. The phantom was modelled using micro-CT data to provide a faithful recreation of realistic target geometries, and was modified to accommodate both radiochromic film and plastic scintillating dosimeters. Use of such a phantom design could enable more accurate and reproducible dose verification procedures in radiobiological experiments by reducing cross-institutional and intra-experimenter variability. It is hoped that the methodology presented might help to lay the foundation for more consistent dosimetry by providing a common, cost-effective means of production and a design that may be easily printed and modified, where necessary, by other institutions. To our knowledge this work presents the first fully 3D-printed, heterogeneous mouse phantom for use in pre-clinical radiation dosimetry. This work resulted in two *Medical Physics* publications in 2019 [66, 67].

Chapters 5-6: Development of UHDR x-ray sources for FLASH-RT Research

Hypothesis: UHDR dose rates may be achieved using x-rays generated by a commercial keV x-ray

tube and specialized MeV transmission targets.

Significance: The third contribution concerns the functionalization of two different sources to deliver UHDR photon beams for FLASH radiobiological experiments: firstly, using a commercial 160 kVp x-ray tube and, secondly, through the development of a megavoltage (MV) electron-to-photon converter on a 10 MeV electron linear accelerator (e-linac).

In a first of its kind study, it was demonstrated that a conventional 3 kW x-ray tube may be used to deliver >40 Gy/s, under the constraint of short SSD. Simulated results were found to agree well with experimental measurements using dose-rate independent film dosimetry. While the low energy and thus limited penetration of the beam precludes FLASH experiments at distances more than a few millimetres from the beam exit window, such a system remains an accessible and affordable alternative for systematic and easily controlled *in-vitro* or animal experiments using miniaturized models, such as *drosophila* (fruit flies). The results of this work promise to improve the accessibility of FLASH *in-vitro* and small-scale *in-vivo* UHDR experiments given the ubiquitous nature of suitable x-ray tubes in laboratories around the world.

To enable delivery of clinically-relevant MV photon beams at dose rates which are theoretically compatible with FLASH radiotherapy, a Bremsstrahlung target and supporting preclinical treatment platform was developed for the TRIUMF Advanced Rare Isotope Laboratory (ARIEL) e-linac. The ARIEL FLASH irradiation platform represents the world's first experimental platform for UHDR photon irradiations using a 10MV beam. The Bremsstrahlung source leverages a unique thin-target 'window' design comprising a cost-effective (<100 $/yr) high-Z (tantalum) conversion layer explosion bonded to a low-Z, water-cooled conductive substrate (aluminum). The target assembly facilitates megavoltage x-ray irradiations at dose-rates between $10^{-2} - 10^{2}$ Gy/s and thereby allows for conventional (low dose-rate) and "FLASH" irradiations to be delivered on a common irradiation platform for FLASH radiobiological experiments *in-vitro* or *in-vivo*. Film dosimetry and real-time beam current monitoring were together used to offer high spatial and temporal resolution in order to demonstrate the system's compatibility with achieving dose rates >40 Gy/s. This work concerns the first recorded demonstration of an ultra-high dose rate, sub-second irradiation using 10MV x-rays which may be leveraged for FLASH radiobiological experiments. Henceforth, with a functional FLASH converter in place, it is now possible to deliver UHDR treatments at beam energies ranging between 8–10 MeV with a wide range of beam parameters (i.e. current, pulse width, pulse frequency). The ability to study the relative therapeutic benefits across this large parameter space is an important and unique capability of the new system. The development of FLASH-capable irradiation platforms for translational research is essential and the ARIEL electron beamline at TRIUMF is well positioned to address this need. This work has culminated in a *Medical Physics* [50] letter and a paper in *Physics in Medicine and Biology* comprising the multi-year ARIEL collaboration [53]. The dosimetry presented in this dissertation and preclinical follow-up experiments are expected to yield future publications.

Chapter 2

Overview of Fundamental Concepts and Methodology

In the scope of the work compiled for this dissertation, a common theme lies in improving accessibility of novel preclinical therapies including design and fabrication of collimators, dosimetry phantoms and radiation sources along with demonstrated applications of each. In this chapter, theoretical fundamentals and general methods which underpin the procedures of each core contribution are reviewed, beginning with the physical basis for radiation dose delivery in matter.

2.1 Radiation Therapy Physics

The delivery of radiation for therapeutic patient benefit and, optimally, the eradication of malignant disease is predicated on the ability for medical physicists to understand and estimate the delivery of absorbed dose (energy/mass) within the human body. The ability to deliver accurate and precise conformal therapies, employ intensity modulation as well as develop particle RT modalities is founded on principles of how radiation interacts with matter and, in oncological contexts, biological tissue. In the forthcoming section, the presiding radiation interactions of relevance to photon-based radiotherapeutic techniques, and of the production of the beams themselves, will be discussed.

2.1.1 Review of photon interactions in matter

Higher energy electromagnetic radiation is typically emitted through nuclear (radioactive) decay (gamma rays) or via Bremsstrahlung production (x-rays). The resulting electromagnetic quanta, or photons, are neutral (uncharged) particles and therefore do not strongly interact with target nuclei. Instead, photon primaries transfer their energy in relatively sparse scattering or absorption events which may result in the production of secondary charged particles or nuclear transformation.

Photons are considered a form of indirectly ionizing radiation since the majority of ionization in an absorber derive from interactions of emitted secondary radiation, predominantly electrons with lower-energy (E) compared with the interacting photon (i.e. $E_e < E_\gamma$) electrons. These secondary electrons collectively deposit much of the energy transferred from the incident (primary) photon, less a radiative fraction, within a finite distance away from the interaction site that depends on

their energy. This two-step process forms the physical basis for how photons deposit their energy throughout a volume of material and thus deliver radiation dose (D; units: Gy=J/kg)).

The concept of (indirect) dose deposition via secondary electrons facilitates understanding the surface-dose build-up observed in the characteristic percentage depth-dose (PDD) curve of MV photon beams (see Figure 2.1). Up to the depth of maximum dose (d_{max}), the secondary charged particle fluence increases until transient charged particle equilibrium (TCPE) is established. At this point the energy absorbed (dose) locally is maximum and equal to the energy transferred to the medium through photon interactions (i.e. the collision Kerma [68]). Subsequently, photon scattering and attenuation are responsible for the gradual dose fall-off after d_{max} due to the reduction in beam intensity (I). For example, in the case of a monoenergetic photon beam ($E = h\nu$) with initial intensity (I_o; units: N/cm^2), the attenuation may be described by a simple exponential: $I = I_o\, exp(-(\mu/\rho)\rho t)$, where the final intensity after penetrating a material with density ρ and thickness t depends on the linear attenuation coefficient (μ). The mass attenuation coefficient (μ/ρ) is proportional to the total interaction cross-section and is a function of energy; for polyenergetic beams, spectrum-averaged quantities must be used. The product of μ/ρ and the mean fractional energy transferred is known as the mass-energy absorption coefficient and is proportional to absorbed dose under conditions of TCPE [68–70].

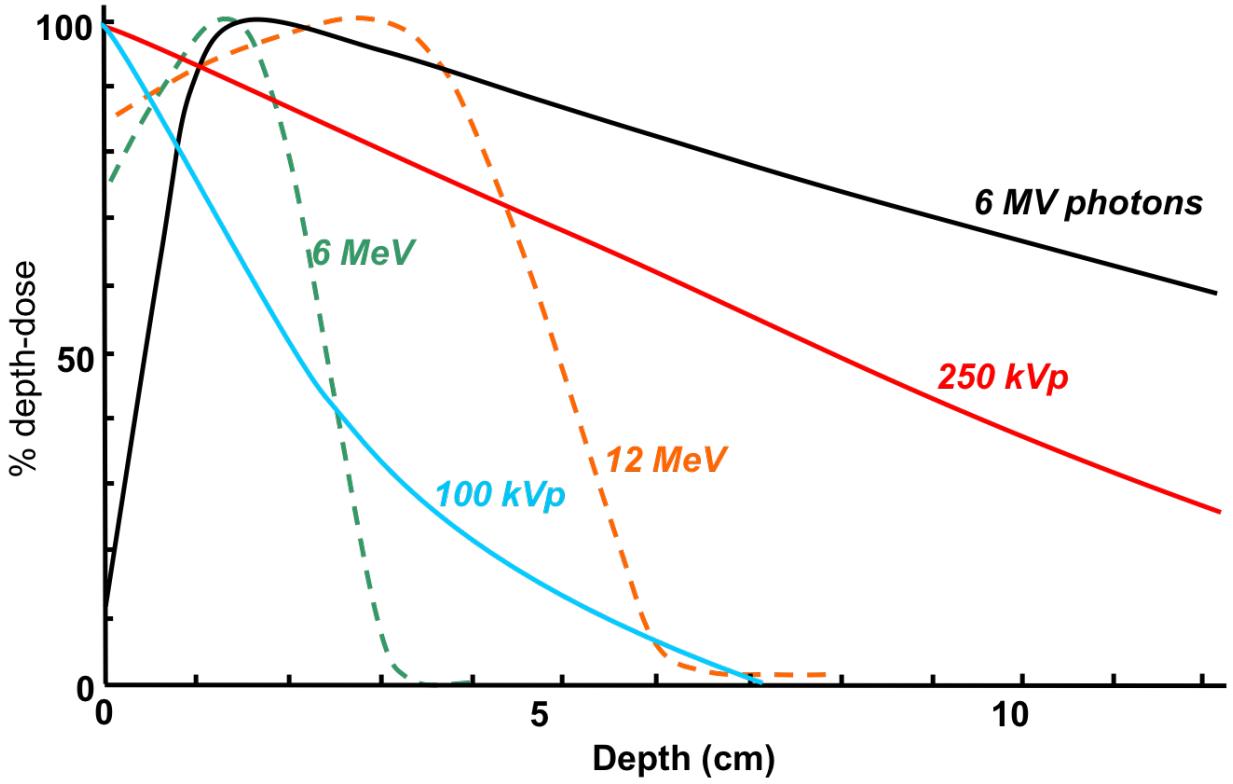

Figure 2.1: Illustrative percentage depth-dose (PDD) curves for photon beams of various energies (100 kVp to 6 MV). For comparison, electron beam depth dose curves are included (6 to 12 MeV).

Photon attenuation, resulting from the transfer of energy to aforementioned secondaries as well as scattering of primaries out of the beam, is due to a number of fundamental interactions between photons and atoms in the attenuating material. The cross-sections (σ) for each of the aforementioned interactions, and corresponding mass attenuation coefficients ($\sigma \propto \mu$), measure the probability that those interactions will occur. A brief description of these primary modes of photon interaction in matter are included below [68, 71].

Rayleigh (coherent) scattering: At low energy, photons may interact with the entire atom, causing the incident energy to be re-radiated. This phenomenon is effectively an elastic scattering event in which the photon energy remains the same; moreover, the scattered radiation is emitted essentially isotropically about the interaction point. The Rayleigh cross-section is proportional to $(Z/E)^2$ and becomes important mainly in high-Z materials and low energy. Given that no energy is lost in the process, Rayleigh scattering contributes to beam attenuation, but not to absorbed dose.

Photoelectric (PE) Effect: At low photon energies the photon may be absorbed completely and result in excitation of the target atom and consequent emission of an orbital electron and an energy equal to the difference between the photon energy and the electron binding energy. When the photon energy equals the binding energy for one of the atomic shells the interaction probability (i.e. cross-section) increases greatly resulting in 'absorption edges' in the differential cross-section and corresponding spectral peaks at that energy. The PE cross-section is proportional to Z^4/E^3. These dependencies notably explain the relative importance of this interaction in high-Z material, such as shielding and collimating components in accelerators, and for low energy (i.e. diagnostic x-rar) beams as compared to clinical MV beams for which other processes dominate (see below).

Compton (incoherent) scattering: Compton scattering result when an incident photon inelastically scatters from an orbital electron. The photon is scattered at an oblique angle (θ) which depends on the initial energy and results in the release of a recoil electron with energy E_{e-} at angle ϕ. The relation in the energy of the scattered photon (E_γ) and electron is:

$$E_\gamma = h\nu' = \frac{h\nu}{1 + \alpha(1 - cos\theta)} \tag{2.1}$$

where $\alpha = h\nu/m_e c^2$, $E_{e-} = h\nu - h\nu'$, and $\cot\phi = (1+\alpha)\tan\theta/2$. h is Planck's constant, ν and ν' are the initial and final photon frequency, and m_e is the mass of the electron. From these relations it becomes evident that maximum energy transfer occurs for photon backscattering ($\phi \approx 0$). The scattering direction for the Compton process, and therefore electron energy, follow a distribution known as the Klein-Nishina formula. The differential form of this relation with respect to the photon scattering angle θ is as follows:

$$\frac{d\sigma}{d\theta} = (2\pi \sin\theta)\{\frac{e^4}{m_o^2 c^2}(\frac{h\nu'}{h\nu})^2(\frac{h\nu}{h\nu'} + \frac{h\nu'}{h\nu}) - \sin^2\theta\} \tag{2.2}$$

The Compton (recoil) electron deposits its energy in the surrounding medium and may be energetic enough to create further ionization, especially at higher photon energies - these secondaries are sometimes referred to as delta-rays. This interaction is dependent on the electron density, and therefore Z, of the material; the interaction cross-section decreases with increasing beam energy.

Pair and triplet production: Above a threshold energy of $2m_ec^2 = 1.02\,\text{MeV}$ a photon may interact with the Coulomb field of the target nucleus and result in absorption of the photon and creation of an electron-positron pair. The creation of the particle mass from a mass-less photon accounts for the combined rest-mass energy threshold for this interaction to occur. Triplet production instead occurs in the field of an orbital electrons with a threshold energy twice that of pair production and results also in the emission of an orbital electron. The interaction probabilities increase with increasing photon energy and atomic number (Z) of the absorber. Pair and triplet production generates positrons which eventually annihilate through interaction with a free electron (i.e. low binding E), producing two 0.511 MeV photons (higher if the positron kinetic energy is non-zero) emitted in opposite directions to conserve both momentum and energy.

Inner atomic shell vacancies produced from the ejection of an orbital electron following PE, Compton scattering or triplet production result in relaxation events. Namely, the inner shell vacancy can be filled by an outer shell electron resulting in the emission of characteristic x-rays, whose energy equals transition energy difference, or Auger electrons due to internal energy transfer to another orbital electron.

Photonuclear reaction and transmutation: At sufficiently high energy above the threshold for photonuclear reactions, typically ≥10MeV [72], photons (γ) may be absorbed by the target nuclei and result in the production of neutrons (n), protons (p) or alpha particles (α), mostly through (γ, n) and (γ,2n), (γ, p) or (γ, α) reactions, and consequent nuclear transformation which results in more or less neutron-rich products. This process may leave the nuclei in an excited state which must decay, often by MeV γ emission; moreover, the energetic photo-neutrons may induce further material transmutation.This interaction type contributes little to the overall beam attenuation and energy deposition for poly-energetic beams and may thus be reasonably ignored in practical RT contexts, except where radio-activation of the target material or resultant neutron flux (i.e. for patient safety) is concerned. The cross-sections are generally highly peaked around an isotope-specific giant dipole resonance energy with a relatively narrow energy-bandwidth [72, 73].

A graphical depiction of the relative predominance of these effects and the total attenuation coefficient in water as a function of energy is presented in Figure 2.2. In general, PE and Rayleigh interactions predominate at low energy while Compton interactions are most important for a range of medically-relevant beam energies in RT. Pair and triplet production and photonuclear reactions become more important at high beam energy above their respective threshold energies; the latter represents only a minor contribution to overall photon attenuation and is dependant on the target nuclide and the beam spectrum.

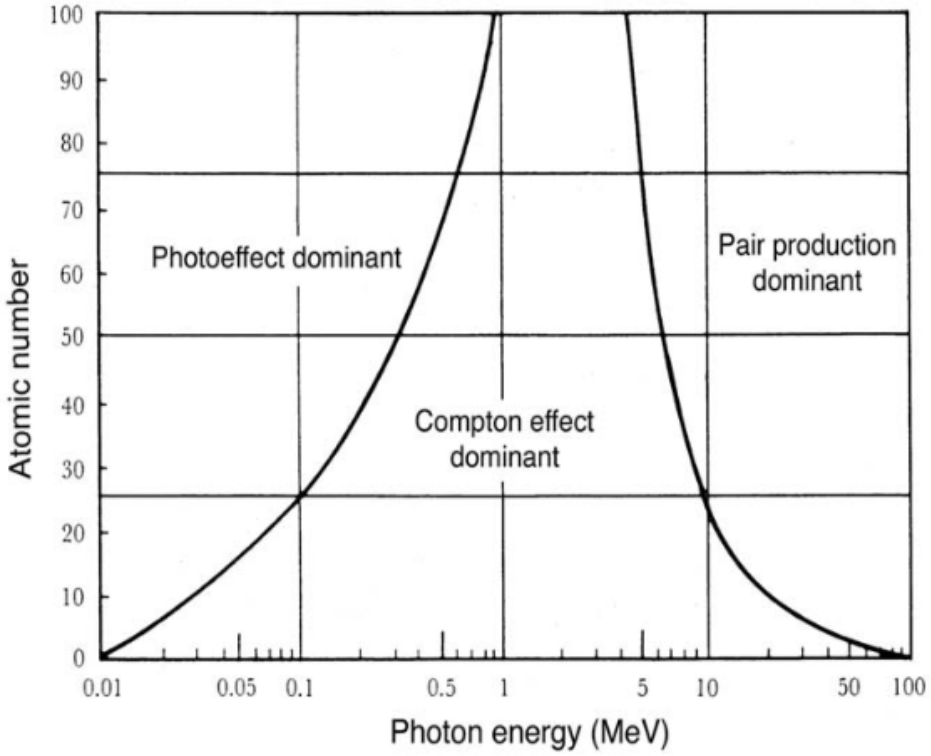

Figure 2.2: Regions of predominance for the main photon interactions based on absorber atomic number (Z) and incident photon energy. The two curves indicate the points where the atomic attenuation coefficients of the interactions in the bounding regions are equal. Photonuclear interactions represent only a small contribution of overall beam attenuation at high energy and are omitted. Adapted from Podgorsak (2005) [68]

2.1.2 Review of electron interactions in matter

As noted above, the directly ionizing, secondary (i.e. delta) electrons are responsible for much of the dose deposition due to photon interactions in matter and thus their interactions and overall transport within tissue are critical to understanding photon energy transport in matter. Moreover, their interaction in high-Z materials forms the basis for the production of x-rays via Bremsstrahlung conversion. As these principles are relevant to the understanding of photon beam dose distributions and to beam production, the basic interactions are outlined here.

Electrons deposit their energy predominantly by Coulombic interaction with other charged particles, namely bound atomic electrons within the absorber material. Typically, only small fractions of the incident electron's energy is transferred in each interaction. The rate of energy loss per unit length (dE/dx) is defined as the stopping power (S) and is comprised of collisional and radiative components. The collision (electronic) stopping power derives from collisions which result in excitation and ionization of atoms and contributes primarily to the continuous energy loss, and therefore dose deposition, of the primary particles within the target media [68,74,75]. The governing equation

for the mass collision stopping power (S_{col}/ρ) based on the Bethe theory is:

$$\frac{S_{col}}{\rho} = \frac{4\pi N_A Z}{A}\frac{r_e^2 m_e c^2}{\beta^2} z^2 \left[\ln\frac{2m_e v^2}{I} - ln1 - \beta^2 - \beta^2 - \frac{C}{Z}\right] \tag{2.3}$$

where $\beta = v/c$ is the usual ratio of the particle velocity to the speed of light ($c = 2.998 \times 10^8$ m/s), r_e is the classical electron radius (2.818×10^{-15} m), N_A is Avogadro's number (6.022×10^{23}), Z is the atomic number (number of protons in the nucleus), A is the atomic mass number (number of nucleons), z is the projectile charge, I is the mean excitation potential ($I \propto Z$) and the ratio C/Z is the shell correction factor [68]. Notably, the collision stopping power is independent of the particle mass and instead only depends on the charge and velocity of the particle and properties of the absorbing medium. The Z/A linearity bears an interesting corollary for hydrogen given that is has at least twice as many atomic electrons per unit mass as any other element, and the highest Z/A ratio at about 0.99 [76]. The the use of materials with greater hydrogen content therefore leads to higher superficial doses, sharper dose fall-off and, consequently, reduced electron ranges. This is relevant, for example, in the construction of water-equivalent phantom materials using hydrogenous plastics (organic polymers), such as polymethyl methacrylate (PMMA) or polyethylene. While unimportant for the relatively low mass electron, larger charged ions may also undergo elastic collisions with the entire atom resulting in a nuclear stopping power term.

Radiative stopping power concerns the electron energy loss by production of "Bremsstrahlung" (breaking radiation) photons. Generally, this radiated energy leaves the interaction site and may proceed to deposit dose at a distance, elsewhere in the same media or outside of it. The Bethe-Heitler theory yields the following equation defining the mass radiative stopping power (S_{rad}/ρ):

$$\frac{S_{rad}}{\rho} = \sigma_o \frac{N_A Z^2}{A}(E_k + m_e c^2)\bar{B}_r \tag{2.4}$$

where σ_o is a constant ($5.80 \times 10^{-28}\,\mathrm{cm}^2$/atom), $\bar{B}_r$ is a function of Z and E_k, the electron kinetic energy [68]. The proportionality of S_{rad} to an electron's kinetic energy is responsible for the relative importance of Bremsstrahlung production at higher electron beam energies while the Z^2 term explains the predominance of the radiative interaction in higher Z materials.

Below is the collision and radiative stopping power for water and tungsten derived from the NIST ESTAR database illustrating these dependencies on Z and electron energy (Figure 2.3). For very high energy electrons (VHEEs), the radiative contribution to stopping power is increasingly significant but the average energy loss due to collisions asymptotes; as a consequence, VHEE beams deposit a similar amount of energy within the attenuating media but do not see drastic increases in range due to an increase in total stopping power thanks to the radiation losses (see Equation 2.4 above).

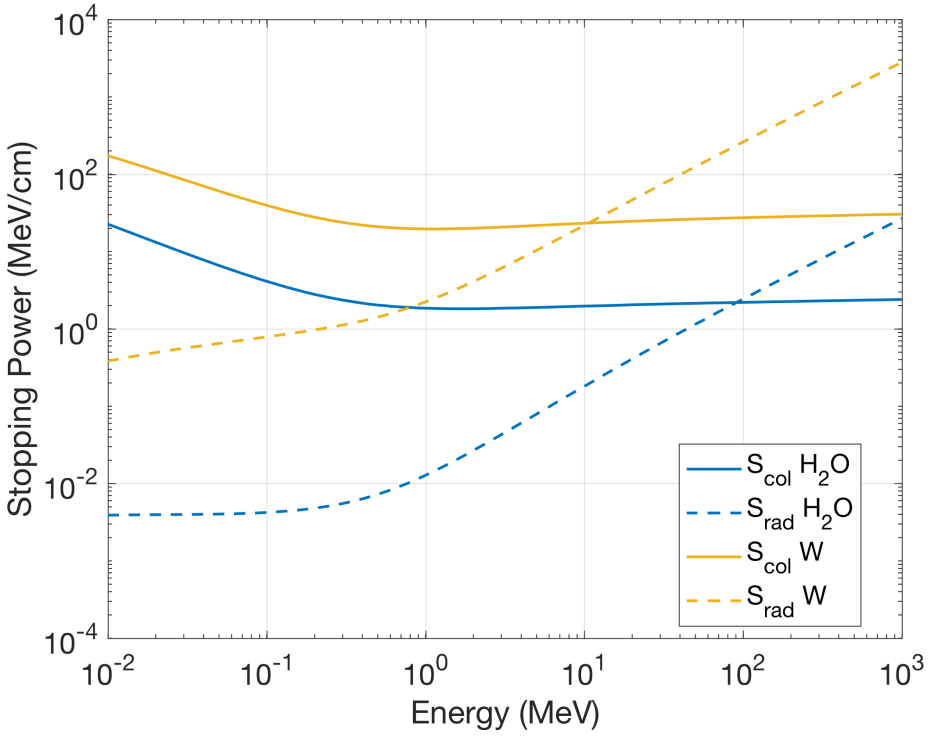

Figure 2.3: Collision and radiative (mass) stopping powers for water and tungsten, which are relevant materials for electron interaction and energy conversion in biological media (water) and x-ray conversion targets, respectively.

In the course of coming to rest, electrons undergo multiple scattering with atomic nuclei resulting in deflections from their initial direction resulting in complex transport trajectories as compared to photons or high energy heavy-ions. This behaviour explains why the actual range (along the incident particle direction) is less than that estimated in the continuous slowing down approximation (CSDA), which would represent the mean path length based on integrating the reciprocal total stopping power (dx/dE) for $E \in [0, E_o]$. Electron scattering is of critical importance to understanding field size effects, isodose curves and beam penumbra for both clinical electron and photon beams. In particular, as electron energy increases, the scattering frequency decreases as does the probability of large angle scatter (i.e. $>0.1°$) such that most electrons are scattered in the forward-direction. Below ~ 1 MeV, however, the small-angle (forward-directed) scatter and large-angle scatter contributes near equally [75]. This behaviour is important due to the ubiquitous nature of such low energy electrons which are encountered, for example, in clinical electron beams at depths in water, due to continuous slowing down of >1 MeV primaries, or in photon beams due to the low energy of ejected delta-rays (see 2.1.1). In clinical practice, the lateral electron scatter accounts for broadening of dose distributions and rapid build-up regions in low-energy electron beams as well as broader penumbra and reduced central-axis (CAX) depth-doses due to lateral electronic disequilibrium in small-field photon beams. In addition to their role in electron stopping and dose deposition, the electron interactions introduced

here are pertinent to x-ray conversion targets, discussed in Section 2.2.4. Briefly, Coulomb collisions (S_{col}) results in energy deposition which in solid-state materials (i.e. metals) goes into the formation of material defects (deformation) and heat generation; meanwhile, radiative interactions provide the means by which incident electron beams are ultimately converted to x-rays in accelerators with an efficiency represented by the ratio of the radiative and total stopping power (S_{rad}/S_{tot}), the radiative yield.

2.2 Electron linear accelerators and x-ray sources

External beam RT is primarily delivered using medical linear accelerators, a practice which can be dated back to the early 1950s [77]. These critical treatment devices comprise an electron linear accelerator and associated peripherals to enable conformal, intensity-modulated and dynamic therapies, supported by advanced computer and treatment planning systems [78]. While particle-beam RT utilization has grown in recent decades [79], MV x-rays remain the dominant radiation modality for the majority of indications for RT in the treatment of cancer. Consequently, electron linacs continue to represent the majority of clinically relevant accelerators when compared with cyclotrons, synchro-cyclotrons or synchrotrons which might be used in the delivery of particle therapies with protons or heavier ions.

Advances in accelerator physics and engineering have led to the development of ever more capable high-gradient radiofrequency (RF) accelerators, although the fundamentals of their operation have remained largely the same. Typically, for medical linacs the accelerating structure comprises a number of key features which are schematically identified in Figure 2.4.

Most notable are the electron source (the gun), resonantly coupled accelerating wave guide, vacuum systems and RF power components. The accelerating wave-guide consists of many small resonant cavities energized by a common RF amplifier, such as a klystron, and may include either on-axis or side-coupling cavities depending on whether the linac operates in traveling or standing-wave mode, respectively. Medical linacs, for example, often include side-coupled standing-wave accelerating structures given that this helps to reduce the length of the structure by up to 50% [68].

The principles of beam delivery for any RF electron linac include the release of electrons from the gun, often via thermionic emission from a heated cathode, and injection into an RF driven accelerating cavity which progressively accelerates the electron to highly relativistic kinetic energies. In standing-wave guides, forward and reflected RF (microwave) power gives rise to stable accelerating electric fields with 180°phase shifts between adjacent cavities; this contrasts with phase velocity matching of the RF and electrons in traveling-wave systems [80].

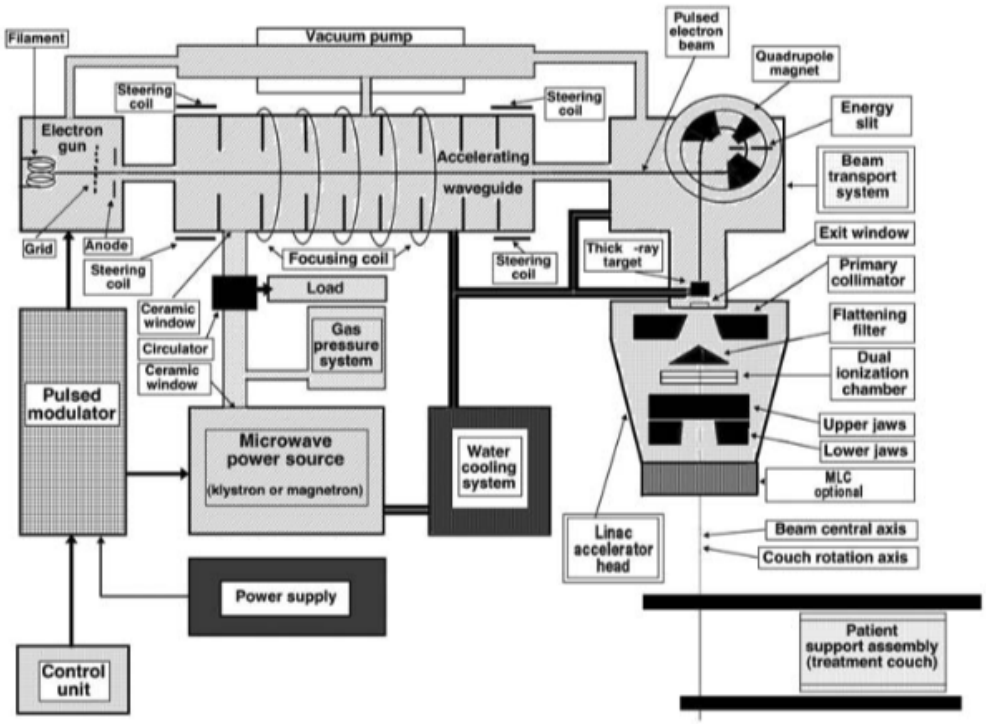

Figure 2.4: Schematic illustration of c-gantry mounted medical linear accelerator. The major components and sub-systems are identified. Adapted from Podgorsak (2005) [68]

Electrons gain energy as they traverse each cavity up to a maximum dictated by the power efficiency of the entire structure. In general, the cavities have tight manufacturing and performance tolerances to ensure they all resonate at the same frequency; cryogenic cooling may be used to ensure stable cavity temperatures and ensure the resonant frequencies remain matched to that of the klystron power source. To allow for accelerating gradients on the order of 10 MeV/m, the peak RF power must be on the order of megawatts.

Following beam injection, magnetic transport systems center and guide the beam to the beamline exit, which may be either a vacuum window - for direct electron delivery - or an x-ray conversion target. The high heat capacity, high-Z target and beam shaping devices, including collimators, are located downstream of a bending (quadrupole) magnet which doubles as an electron energy selector. The principles of x-ray production via electron beam interaction in these targets will be covered in the Section (2.2.4). Typical dose rates for clinical liancs are on the order of

For medical accelerators, applicators and other collimation accessories are routinely attached to customize treatment while computer-controller beam shaping devices such as multi-slit collimators (MLCs) provide real-time re-configuration of the field allowing for robust intensity-modulation to conform dose to the planning treatment volume (PTV). In addition, flattening filters may be used to flatten the beam, at the expense of dose-rate, in order to improve dose coverage and uniformity across the PTV. Various imaging technologies are also included on-board, such as for cone-beam kV and MV

computed tomography (CT) and digital radiography or, more recently, magnetic resonance imaging (MRI) [81]. The accelerating and imaging components are typically mounted on a gantry, which may be rotated to affect dynamic-arc and co-planar multi-beam treatments for modern volumetric-modulated arc therapy (VMAT) and intensity-modulated radiotherapy (IMRT) techniques, respectively. With modern VMAT, computer-based treatment planning and the fact that treatment volumes are not uniform (i.e. curved and inhomogeneous), there is less demand for beam flattening and thus flattening filter free (FFF) irradiation has been adopted [82]. Importantly, FFF photon beams allow a higher dose-per-pulse (DPP), and thus dose-rate, to be achieved relative to conventional (flattened) clinical photon beams. For example, flattened and FFF dose-rates are of the order $\approx 10^{-1}$–10^{0} ($DPP \approx 10^{-3}$–10^{-2} Gy/pulse) and $\approx 10^{0}$–10^{1} Gy/min ($DPP \approx 10^{-2}$–10^{-1} Gy/pulse), respectively [13, 82].

Because of the c-arm gantry on which the accelerating structures are commonly mounted, there is a practical limit to the length of accelerating structure, and thus beam energy. S-band linacs are traditionally favored due to the high accelerating gradient which may achieved over short distances and reduced sensitivity to manufacturing and processing tolerances [83]. S-band systems can nominally provide electron energies up to 10 MeV with average beam powers of up to 25 kW [80]. New C-band and X-band linacs have more recently been developed with an eye towards increasing the accelerating gradient within a more compact form factor [77, 83]. By reducing the size and load requirements, new delivery platforms may benefit by combining additional imaging peripherals and o-ring gantries, bearing relevance to the VERO system [84] and MRI-linacs [81]. Furthermore, high-gradient linacs may be of relevance to future x-ray and VHEE UHDR sources [52, 77, 85].

On medical and compact industrial accelerators, electron beams are pulsed at some fundamental frequency with an overlying macro-pulse structure. A low duty factor is often used in medical and industrial linacs in order to reduce the average power loss and therefore mitigate demands on power input and temperature control, which have consequences for stable and precise beam transport. While research linacs lack the patient treatment peripherals they often offer a much greater range of beam control and provide the user access to a range of temporal beam parameters which may be of interest. For example, these sources may be able to deliver continuous-wave (CW) beams or leverage higher accelerating voltages and beam power, thanks in part to relaxed length requirement and larger power supplies; this flexibility, in turn, facilitate a wider range of dose-rates and beam configurations [80, 86–88]. These systems are especially useful for research concerned with detectors or biological systems that may be sensitive to the beam temporal parameters, which is particularly relevant to the FLASH and SFRT modalities examined herein. Generally speaking, improvements in flexible energy selection, stability at high beam-current and fine control over temporal beam structure may allow for a greater range of applications and more effective use in pre-existing contexts, not the least of which includes FLASH-RT.

2.2.1 Accelerators for UHDR applications

Of relevance to the work presented in this dissertation, linacs represent the predominant means of FLASH delivery [12, 13] as well as a viable source for 2D SFRT (GRID) therapies [37, 89, 90]. Specifically, FLASH irradiations are reliant upon accelerators which are capable of delivering a beam with sufficiently high current and energy to be applicable to the treatment of preclinical, and eventually clinical, subjects. In fact, the normal tissue sparing potential of UHDR irradiation was first demonstrated using electron linacs in a number of radiobiological studies which began in the 1970s [91, 92]. Today, the low- and medium-energy (<10 MeV) e-linacs are among the most recognizable FLASH irradiators in the current literature, having been used for successful *in-vivo* treatments of small-animal models and veterinary cases. Modern clinical linacs are typically limited to ~ 24 Gy/min while using FFF photon modes (i.e. Varian TrueBeam 10X-FFF) [93], but may be modified to accommodate UHDR irradiations using electrons [48, 49]. Furthermore, sophisticated new accelerators have been developed which are capable of delivering pulsed beams with a wide variety of temporal configurations at UHDR, including prototype [94, 95] and commercial intra-operative radiotherapy (IORT) devices [96]. Research accelerators, such as superconducting e-linacs, are also capable of delivering high-power, UHDR-compatible beams. Such sources share the same fundamentals as those found in clinical accelerators, namely use of a thermionic source, RF power input and standing-wave accelerating cavities [78, 94, 97], but offer access to much larger parameter space for evaluation of temporal beam parameters and dose-rate effects involving continuous and pulsed mode deliveries.

Electron linacs boasting UHDR capabilities can also find use outside of cancer treatment; for example, in food irradiation, material sterilization and inspection, space materials engineering (i.e. damage studies), as well as nuclear and particle physics. Among these applications, the domain of food irradiation and sterilization benefits greatly from the use of high-powered (i.e. 10^2–10^3 kW), low-energy (<10 MeV) electron accelerators capable of delivering UHDR in order to improve mass throughput and thus the time/cost efficiency of this commercial processing technique. Advancements in the domain of industrial and medical accelerator development may therefore be mutually beneficial to improving availability of compact UHDR accelerators for electron and photon irradiation [83, 98]. In fact, methods of design optimization and insights gleaned from the literature on industrial accelerators and related target infrastructure informed some of the methodology used in the ARIEL target design (Chapter 5).

2.2.2 X-ray tubes: basic principles of operation

X-ray tubes find ubiquitous use in preclinical RT experiments owing to the practicality of using the kV photon beams they generate, suitable for both imaging and therapy applications in small-animal subjects. Here a brief overveiw of the operational principle for the x-ray tube is presented; their use in small-animal irradiators is discussed in Section 2.2.3.

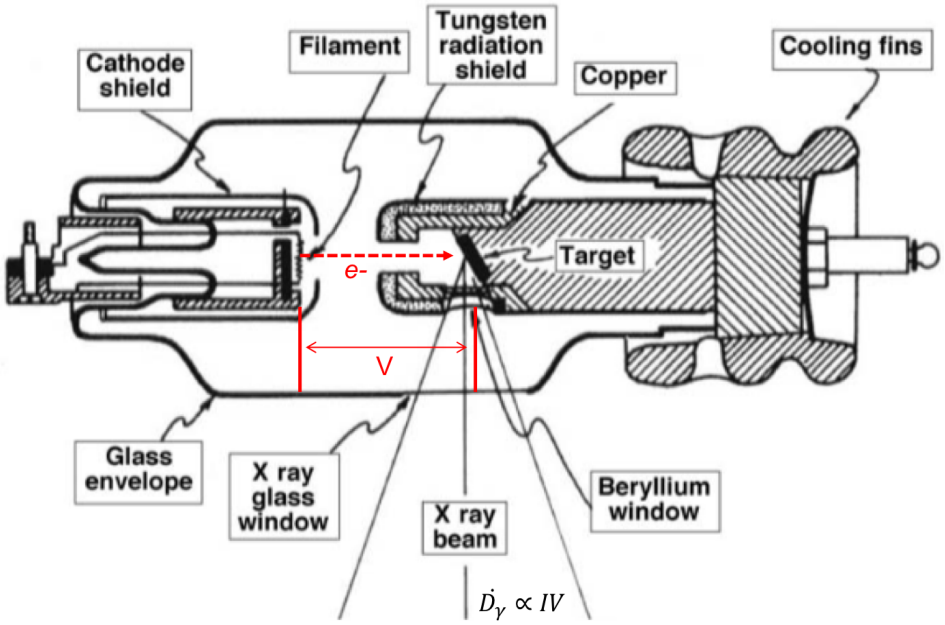

Figure 2.5: Schematic illustration of an x-ray tube with key features and acceleration region identified. Adapted from Johns and Cunningham (1983) [100].

Fundamentally, the x-ray tube can be considered a compact electrostatic linear accelerator predicated on the use of an electron source (cathode) and bremsstrahlug conversion target (anode). Analogous to linear accelerators (section 2.2), electrons are provided by means of thermionic emission from a heated filament (the gun). Unlike an e-linac, however, acceleration is driven solely by electrostatic attraction of the electrons which gain energy (in MeV) equal to the potential difference (tube voltage) between the cathode and anode [68]. The electrons are simultaneously focused and accelerated through the vacuum tube towards the target anode, which acts also as the conversion target and is generally comprised of a high heat capacity and high-Z metallic (often refractory) elements such as tungsten or molybdenum [99]. Owing to the low accelerating voltage V, the photon field is emitted near isotropically (Section 2.1.2). As a result, the x-ray beam can be captured in directions orthogonal to the direction of the incident electrons and so-called reflection targets are used in order to avoid self-attenuation (Figure 2.5). The anode is set at an angle (the anode angle) to similarly reduce attenuation from photons emitted further from the tube exit window.

An additional benefit to the reflection target design is that the anode can be made thicker to allow for improved heat management. Furthermore, depending on beam power requirements, targets may be static, with active water cooling and high thermal conductivity heat sink (i.e. copper; Figure 2.5), or rotating which allows the heat to be distributed over a larger surface area and reduces the cooling demands, in turn allowing higher tube current setting I and higher dose-rates to be achieved ($\dot{D} \propto P = IV^2$).

2.2.3 Small-animal irradiators

Small animal irradiators generally encompass a range of kilovoltage x-ray tube cabinet (i.e. self-shielded) irradiators with the capacity to accommodate small-animal RT treatments. Key features to support this application include on-board CT image-guidance (i.e. cone-beam CT) and some form of treatment-planning capacity. Moreover, sophisticated systems include the ability to simulate dynamic arc therapies by mounting the x-ray source on a gantry and table rotation, such as might be found on the small-animal radiation research platform (SARRP, Xstrahl Ltd., Walsall, UK) utilized in this body of work. Consequently, these compact radiotherapy platforms allow for a scaled down simulations of more complex and clinically-relevant treatments at low energies which are suitable for radiobiology research in rodent models and which may be accommodated in smaller lab spaces without the need for dedicated rooms/shielding. Figure 2.6 shows the SARRP cabinet, including an internal view with some of these key features identified. Typically, the x-ray source for small-animal irradiators like the SARRP leverage orthovoltage (100 kVp to 500 kVp) x-ray, which are discussed in Section 2.2.2.

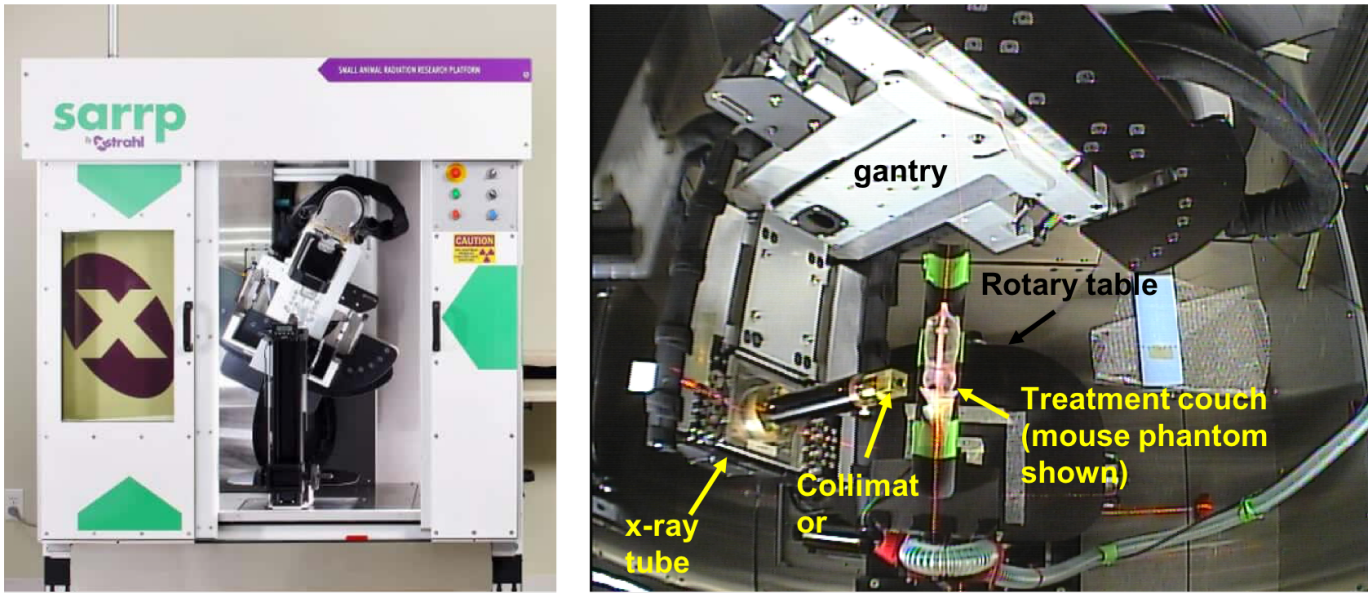

Figure 2.6: Image of the commercial SARRP system (left; https://xstrahl.com) which was employed in this work. An internal view of the irradiator during an arc treatment (right) is shown using a 3D-printed mouse phantom after CT image-guided localization of the film plane (see Section 4). The x-ray tube, collimator assembly (with the MRT collimator inserted; Sec. 3) are also labelled. The imager panel is located out of frame to the left.

The SARRP system was employed in a number of experiments included within this dissertation and additional specifics may be found in Chapters 3 and 4.

2.2.4 X-ray production targets for electron accelerators

Electron linacs may be used to generate x-ray beams by means of an electron-to-photon conversion target. Typically such targets are made from a high-Z refractory metal such as tungsten, tantalum

or molybdenum depending on the use case and beam properties. When the electrons impinge on the metal target they deposit energy by means of the collision processes described in Section 2.1.2. Notably, as a result of the progressive slowing down of electrons due to radiative interactions with target atoms, bremsstrahlung photons are emitted with a total power (P) governed by the Larmor formula: $P \propto (e^2/c)\,|\dot{v}|^2$ [101], where e is the fundamental charge of the electron and $|\dot{v}|^2$ the magnitude of the acceleration. The energy loss is described by S_{rad} (2.4) while the angular dependence $(\frac{dP}{d\Omega})$ of the photon emission is proportional to $sin^2\theta/(1-(v/c)\cos\theta)^5$, where θ is the angle between the observation point and the direction of acceleration due to (classical) Coulomb interaction with the target nucleus. The velocity (v) term accounts for the energy dependence of the photon emission angle with incident electron kinetic energy.

Given the linear (Z/A) and inverse $\ln(I)$ dependence of S_{col} (Eq. 2.3), as well as the predominance of radiative interactions of electrons at high Z and high energy (Figure 2.3), there are multiple benefits to using high-Z targets in medium-to-high energy electron beams for x-ray production. Firstly, the obvious increase in radiative yield mediated by the Z dependence in S_{rad} allows for reduced power requirements to reach a desired fluence output. Furthermore, less energy is deposited per unit length (i.e. S_{col} decreases) thus there is a lower heat (power) density within the material. Assuming that two hypothetical materials feature comparable heat capacities, a reduction in S_{col} would amount to a decrease in the temperature increase for a given electron flux and energy spectra. This opens up interesting questions about the suitability of materials boasting both sufficiently high radiative yield and melting points, but feature different power density distributions, under identical loads, and therefore different temperature responses. The power density at any given point in the material should ultimately be weighed against the material's ability to manage the heat load based on thermal conduction and expansion effects, which are often analyzed using thermomechanical simulations (see Figure 2.10). These principles are discussed at greater length in subsection 2.2.4.1.

In addition to the radiative yield, the selection of an appropriate target material is predicated on whether its thermomechanical properties are suitable to withstand high instantaneous thermal power loads imparted by the driving electron beam. For example, a high heat capacity (units: J/K) and high melting point are required to ensure that a larger amount of energy (i.e. dose) can be deposited before effecting a unit temperature increase and that the requisite amount of beam power can be accepted without compromising the target integrity. The use of metals with sufficient thermal conductivity ensures that heat can be more effectively removed from the interaction site while a high heat capacity is important for limiting the operating temperature and heating rate, with implications to stresses that develop within the target (see also Section 2.2.4.1)

The target design itself partially governs the production efficiency for photons. For example, increasing target thickness has an effect on beam output by way of increasing self-attenuation. Moreover, for a given thickness, a lower-Z target and sufficiently high beam energy might allow for similar beam outputs, albeit with lower mean energy, due to reduced attenuation within the target. This

represents an additional point of optimization given how the target thickness can be selected based on the combination of primary electron ranges within the material, its thermomechanical stability, as well as the desired output energy fluence or spectral filtration of the photon beam.

In low energy accelerating structures, such as a conventional x-ray tube, the reduced bremsstrahlung conversion efficiency (i.e. radiation yield) means that an increase in beam power is required to reach a desired dose-rate; moreover the broader angular distribution of the emitted photon field reduces the CAX energy fluence, further constraining output. Consequently, the use of high-Z, high melting point materials is critical for kV x-ray machines given that the majority of incident electron energy will be converted into heat which must be tolerated.

Bremsstrahlung spectra resulting from electron conversion in high-Z targets are inherently heterogenous and, rather than being a continuum, become filtered due to attenuation in the target and any downstream beam modifying components. Filtration may be deliberately added to harden or soften the beam – i.e. increasing or decreasing mean energy ($\bar{E}$), respectively – as might be required in kV imaging applications, and on small-animal irradiators discussed in the preceding section 2.2.3. At lower electron beam energies the characteristic x-rays resulting from internal electronic transitions in excited target atoms constitute a large percentage of the fluence, while for MV accelerators this contribution to the spectrum is negligible. For MV linacs, transmission targets are used since converted photons are preferentially emitted in the forward direction; this contrasts with kV units which rely on reflection targets due to the photons being emitted perpendicular to the electron beam direction.

2.2.4.1 Energy Conversion and thermomechanical effects

As a result of the collisional energy losses characterized by S_{col} (Eq. 2.3), a number of downstream physical processes take place in the target. Specifically, the electron kinetic energy which is not lost as Bremsstrahlung largely ends up as heat energy within the target, represented by the thermal motion of the constituent atoms and a consequent increase in temperature (T). Due to this increase in T, there is an associated expansion of the material, increasing the energy stored in the material (strain energy) and potentially producing permanent changes in the material structure. Permanent (inelastic or plastic) strain (ε_p) results when enough work has been done to rearrange atoms through the breaking of inter-atomic bonds, resulting in the creation and movement of dislocations (lattice defects); this contrasts with recoverable elastic strain (ε_e) observed at lower stresses (σ).

In general, as materials reach their elastic limit, defined by a stress known as the yield strength (σ_Y), the material will begin to undergo plastic deformation. If a material is strained beyond the yield point then it does not assume its original shape upon unloading and will contain residual strain. As metals plastically deform, they see a reduction in the rate at which strain increase with increasing stress. More specifically, through the accumulation of plastic strain, and thus dislocation density, the material acquires a resistance to further deformation; this manifests as an increase in the material

yield strength (strain hardening), albeit at the expense of ductility.

The phenomenological Ramberg-Osgood equation models the true stress-strain relationship, including hardening, in metals using both elastic and plastic contributions and takes the following form:

$$\varepsilon = \frac{\sigma}{Y} + K\left(\frac{\sigma}{E_Y}\right)^n \tag{2.5}$$

where $E_Y = \sigma/\varepsilon$ is the usual Young's modulus (i.e. tensile modulus of elasticity) sub-scripted for clarity, K is the strength coefficient and n is the strain hardening coefficient, which are material specific parameters [102]. The first term represents the linear elastic response while the second accounts for the power-law stress-strain dependence due to strain hardening effects. Note that the true stress (σ_T) and strain (ε_T), which accounts for the instantaneous sample area and length, is related to the often reported engineering stress and strain, normalized to the initial area and length, as $\sigma_T = \sigma(1+\varepsilon)$ and $\varepsilon_T = \ln(1+\varepsilon)$.

Depending on whether a material is ductile or brittle, it may be characterized by different failure modes. In the case of brittle failure, for example, fracture tends to occur when the material rapidly expends its capacity for plastic deformation as the stress exceeds a well-defined yield strength, with fracture occurring shortly thereafter at the ultimate tensile strength (σ_T) – in this case very little plastic deformation (strain energy) is accommodated. Ductile materials, by contrast, are defined by their capacity to withstand plastic deformation, but often at the expense of a lower σ_T. Thus, ductile failure may be characterized instead by gradual elongation until a point of necking (cross-sectional area reduction) and eventual fracture, defined at the % elongation-at-break (ε_{max}), which occurs gradually once the stress reaches σ_T. Consequently, ductile metal targets benefit from tolerance to catastrophic failure at loads which exceed the yield strength of the material, depending on strain rate, duration and loading conditions. A visual representation of these behaviours and associated quantities are included in the representative stress-strain curve shown in Figure 2.7. The functional form of real stress-strain curves deviates from the simple model described Equation 2.5 above due to complex micro- and macro-scopic interactions within the material structure.

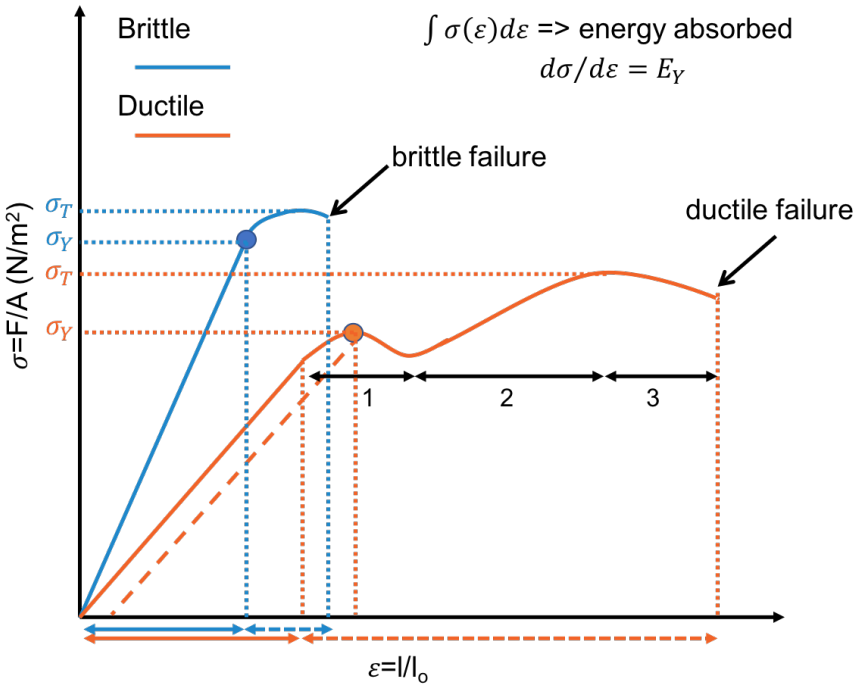

Figure 2.7: Engineering stress-strain curves for uniaxial tensile elongation of a uniform specimen of initial length L under load due to a force (F) over cross-sectional area (A). Representative curves with key mechanical quantities in a brittle (blue) and ductile (orange) material are shown. Filled circles denote the yield points, with corresponding yield strength (σ_Y) and is well-defined for the brittle material curve. The dotted orange line represents the offset yield point, generally corresponding to 0.2% plastic strain, and defines the yield strength on the ductile stress-strain curve. The highest point on both curves corresponds to the ultimate tensile strength (σ_T). The linear elastic (solid arrows) and non-linear plastic (dashed arrows) response regions for each material are shown below the strain axis; in the former the stress and strain are proportional with a slope equal to the Young's modulus (E_Y). The domains of plastic deformation (and strain softening; 1), strain hardening (2) and necking instability (area reduction; 3) are identified below the ductile curve.

Note that strain and strain and (second-rank) tensor quantities (i.e. fields). Strain represents the relative elongation (unitless) while stress is the force per unit area (Na/m^2=Pa). Given that the yield and tensile strengths of materials are uniaxial quantities, comparison against the tensor stress can be conveniently done using the von Mises stress (σ_{vm}) criterion, whereby if the calculated $\sigma_{vm} > \sigma_Y$, then the material is said to have yielded [103]. The von Mises stress is defined from the components of the stress tensor (σ_{ij}) as follows

$$\sigma_{vm} = \sqrt{0.5\left[(\sigma_{11}-\sigma_{22})^2 + (\sigma_{22}-\sigma_{33})^2 + (\sigma_{33}-\sigma_{11})^2 + 6(\sigma_{12}^2+\sigma_{23}^2+\sigma_{31}^2)\right]} \tag{2.6}$$

In the case of electron beam heating, the induction of thermal loads and resulting strain is cyclic in nature. In addition to reversible (elastic) or irreversible (plastic) deformation within the target, there are long-term effects due to creep, the time-dependant deformation at constant stress, and fatigue

which can lead to failure even without tensile fracture (i.e. thermal shock) [104]. For cyclic loads with high stress-amplitudes ($\sigma_a = 0.5(\sigma_{max} - \sigma_{min})$) producing corresponding plastics strains, low-cycle fatigue data is used to estimate the number of stress/strain cycles, namely from beam-induced heating (and expansion), until target (fatigue) failure. Due to irreversible plastic (residual) strain, particularly for high-T applications, the stress-strain response forms a hysteresis loop, which may change over time (cyclic strain hardening or softening) or remain stable; a representation of initial loading followed by a single fully-reversed stress cycle is shown in Figure 2.8. A useful strain-life correlation for modeling fatigue life (N, the number of cycles) due to both low-cycle (inelastic) and high-cycle (elastic) loading is:

$$\frac{\Delta\epsilon}{2} = \frac{\sigma_f{}'}{E}(2N)^b + \varepsilon_f{}'(2N)^c \tag{2.7}$$

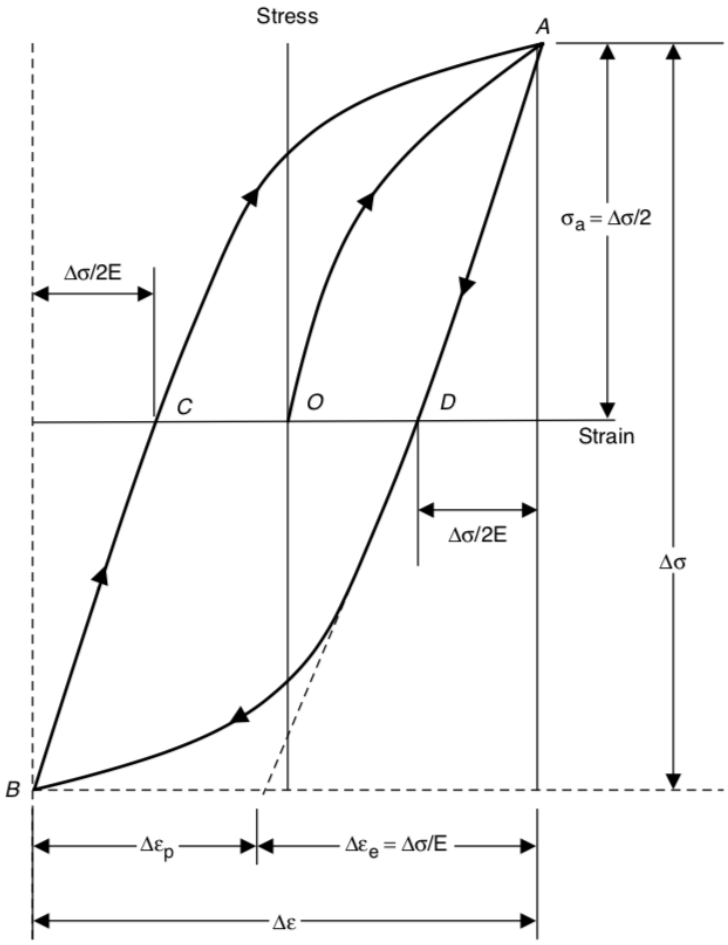

Figure 2.8: Stable cyclic stress-strain (hysteresis) curve for fully-reversed loading illustrating the relevant stress (σ) and both elastic and plastic strain (ε_e or ε_p resp.) quantities. The initial loading (OA), unloading (AD), reversed loading (DB) and unloading (BC) before re-loading (CA), results in a component of elastic strain and recovery along with a permanent (plastic) deformation component denoted by $\varepsilon_p = \varepsilon - \Delta\sigma/E$. Not shown is the evolution of the cyclic curve over many cycles due to strain hardening or softening behaviour which depends on the material conditioning/history and inherent ductility. Figure adapted from [104]

where ε_f' is the fatigue ductility coefficient, c is the fatigue ductility exponent, $\Delta\varepsilon/2$ is the strain amplitude (elastic or plastic), σ_f' is the fatigue strength coefficient and b is the fatigue strength exponent. In this relation, the first term accounts for low-cycle, high-strain fatigue (i.e. with plastic component) while the second term describes high-cycle, low-strain (elastic) fatigue and are known as the Basquin and Coffin-Manson equations, respectively. Correspondingly, the behaviour of strain-life curves tends towards the plastic and elastic relations at low and high strain amplitudes. This model was used in the estimation of fatigue life for the tantalum target layer which is the subject of Chapter 5.6.

It is interesting to note that for fatigue in ductile materials, an applied cyclic load may exceed σ_Y without risk of fracture due to cyclic (strain) hardening. High-strength but brittle metals, on the other hand, are liable to soften and are less tolerant to plastic strains, depending on the temperature, in which case it is important that the design stress be kept below σ_Y to minimize plastic strain altogether. In either case, strain cycling over many cycles will eventually lead to fatigue failure for most metals under high-temperature operation. Resistance to fatigue is characterized by the material fatigue strength (or endurance limit), which denotes the σ_a below which the material will not fracture (or only after some pre-defined N, i.e. 10^8).

Considering the high-temperature operation and large thermal cycles experienced by conversion targets, the implications of thermomechanical stresses and consequent strains should be considered beyond the linear elastic regime and, ideally, over many cycles (i.e. fatigue analysis). This contrasts with designs based on brittle-type failure, whereby applied stress might simply be compared against the material's temperature-dependent σ_Y and σ_T; in this case, however, ductile behaviour is neglected in target material for operating temperatures beyond their ductile-brittle transition temperature (DBTT). Therefore, where data is available, it is prudent to incorporate temperature-dependent stress-strain data into the analysis.

Among those materials suited to photon converter designs, the DBTT for tantalum and TZM are below room temperature which means that under e-beam irradiation these materials behave inelastically over the temperature cycling range observed during beam-on cycles. Tungsten alloys, on the other hand, can suffer from low ductility at low-temperature (high DBTT), thereby limiting fatigue life under plastic strain conditions, as well as high-temperature (recrystallization) embrittlement featuring a reduced resistance to crack initiation [105]. Nevertheless, the high tensile strength of tungsten makes it well-suited to high-cycle, elastic deformation where there is little, if any, plastic yielding of the material, as might be the case for thicker targets with more thermal mass. Thin targets, by contrast, are likely to benefit from more ductile materials that can accommodate yielding under high-temperature conditions and cyclic strain hardening, which can improve fatigue strength.

At sufficiently high operational temperatures, above the recrystallization temperature, and depending on the environmental conditions, annealing of the target material can also result in changes in the material properties. In effect, diffusion of lattice atoms and alloying elements in solid solution

leads to the redistribution and removal of dislocations (lattice defects) and the internal stresses they create. This stress-relief leads to improved ductility, at the expense of reduced hardness (softening) and thus the uniaxial yield strength. Moreover, recrystallization can increase the DBTT and is of particular detriment to high-strength body-centered-cube refractory metals and alloys such as tungsten [106–108]. In general, high-temperature operation reduces the yield and tensile strengths, and thus fatigue strength, of the material; these factors must be considered together with the ductile failure modes that are relevant to the material's fatigue life under high-T cyclic loading. Finally, in the case of extreme heat loads, superficial heating can create temperatures in excess of the material melting point and result in localized melting and changes in surface morphology.

Other effects of electron irradiation include the production of irradiation damage, primarily through Frenkel pair (vacancy-interstitial) point defects [109, 110]. More generally, radiation damage in materials can lead to embrittlement over time due to defect production within the lattice structure that depends upon the target treatment history, irradiation temperature, and interstitial impurities and ambient O_2 and H_2 concentrations [111, 112]. The effects of electron irradiation damage and estimates for changes in target ductility over operational lifetimes were not evaluated in this work, but were expected to represent a low risk for our applications and expected beam uptime.

A few notable thermomechanical properties which govern the suitability of a material to tolerate and transport heat effectively include the (specific) heat capacity (c_p; units: $\mathrm{J/kg\,K}$), thermal expansion coefficient (α; units: $\mathrm{K^{-1}}$) and thermal conductivity (k; units: $\mathrm{W/m\,K}$). Respectively, these quantities define a materials ability to absorb heat (energy) before increasing in temperature, withstand the consequent expansion (strain), and to transport heat away from the source and consequently reduce the local temperature.

The basic formula governing linear expansion, or strain, due to an increase in temperature (ΔT) is $\varepsilon = \alpha * \Delta T$, where alpha is the linear coefficient of thermal expansion. For a given thermally-induced strain, the corresponding thermal stress (σ) is related by the usual proportionality between stress and strain, namely $\sigma \propto \varepsilon$. The constant of proportionality is known as the (Young's) modulus of elasticity (E_Y) and therefore the simplest relation for thermal stress and strain is:

$$\sigma = \alpha E_Y \Delta T \tag{2.8}$$

The temperature increase, assuming negligible radiochemical action, can be estimated as $\Delta T = D/c_p$, where D is the absorbed dose (J/kg). In order to transfer heat away from the interaction site, the conductivity of the material should be as high as possible (see Equation 2.10 below).

Given the importance of managing the target temperature to preserve structural integrity and prolong its life, effective cooling strategies are important for radiation targetry. Most common are water-cooled interfaces which rely on rapid flow and a large temperature gradient to manage the heat loads by way of convective heat transfer. The basic equation for convective heat transfer rate is

readily derived from Newton's law of cooling:

$$h = \frac{d\dot{Q}}{dA\Delta T} \tag{2.9}$$

where h is the heat transfer coefficient ($\mathrm{W/m^2\,K}$) and $\frac{d\dot{Q}}{dA}$ is the heat flux ($\mathrm{W/m^2}$) [113].

Ideally, the cooling medium will not be in direct contact with the target metal in order to reduce the risk of corrosion and erosion effects; for example water radiolysis can produce hydrogen peroxide (H_2O_2) species which can compromise the target condition through corrosive action or and H_2 and O_2 gas buildup in the downstream cooling loop. Transferring the target's heat to a conductive substrate which is resistant to erosion-corrosion by the cooling medium is a commonly employed strategy. The heat conduction from the hot target to the conducting interface depends on the nature of the interface (i.e. pressure, roughness),the geometry, as well as heat distribution. The physical properties which govern the transfer include the conductivity (k) and the conductance across the interface. By Fourier's law of heat conduction, the basic relation between a temperature gradient (in 1D: $\nabla T = dT/dx_i$) and heat flow (q) is:

$$q = -k\nabla T \tag{2.10}$$

Multiplying by the contact area gives total heat flow, however in reality a temperature discontinuity exists at the interface due to the imperfect contact. In such cases, conduction across the interface is characterized by the thermal contact conductance ($\mathrm{W/m^2\,K}$), for which correlations must be determined experimentally [114]. Cooling by natural convection under various scenarios was considered in the design of the electron collimator and for offline thermal tests of the ARIEL converter, which are covered in Appendix A.3 and A.5. In order to maximize the thermal contact conductance for the design of the ARIEL target assembly (Chapter 5.6), a novel means of assembly involving a shrink (interference) fit was used to maximize the thermal contact conductance.

Besides the thermomechanical properties discussed above, the chemical inertness of the target and ambient conditions must also be considered. For example, in the presence of certain atmospheric gases, such as hydrogen and oxygen, embrittlement due to reactions with the lattice atoms may also occur [115, 116]. The most common effect includes oxidation and formation of an oxide scale which, even when stable, acts to corrode the target surface and thereby reduce its effective conversion thickness and mechanical strength properties, particularly at the scale-metal interface. By placing the conversion targets in high and ultra-high vacuum (UHV) environments, the risk of oxidation can be mitigated as long as the oxygen partial pressure is below the threshold required for spontaneous oxidation reactions to occur. Appendix A.4 includes details of a simplified oxidation model for the high-temperature tantalum target studied in Chapter 5.6 under UHV conditions.

As an example of applying the aforementioned thermomechanical and material-property considerations, the ARIEL target design incorporated a tantalum (Ta) conversion layer instead of competing high-Z candidates (i.e. tungsten, molybdenum). Like other refractory metals, Ta is characterized by

a high atomic number and mass density, both desirable for photon conversion, and the high melting point necessary to tolerate very high power deposition. While the thermal conductivity of Ta is lower than tungsten (W), it increases substantially with temperature and the metal benefits from up to a $\approx 14\%$ higher specific heat capacity. More importantly, Ta is highly ductile and does not become brittle at room temperature (i.e. low DBTT) and therefore the risk of brittle fracture and fatigue failure over many cycles is expected to be lower than a W target of comparable thickness. The improved ductility is particularly relevant for high-temperature operation on a thin (i.e. 1 mm), highly strained target and presents a favorable thermophysical characteristic when compared with W, which is more commonly used in x-ray producing linear accelerators. Had the target been thicker, and the plastic strain reduced, W might have been a preferred material candidate, in particular due to the high tensile and yield strengths at high operating temperature (see also Chapter 5.6).

2.3 Radiochromic film dosimetry

The use of radiation, whether in the clinic or the laboratory, relies upon the ability to accurately determine the absorbed dose delivered to the medium of interest; most often, this includes water or water-equivalent materials, given their physical similarity to normal tissue. For example, this is critical in order for outcomes of radiobiological research to be understood and interpreted accurately, especially in consideration of the uncertainties inherent to biological and pre-clinical research.

Absolute dosimetry is often made possible through cross-calibration of relative dosimeters with a primary reference dosimeter, such as ionization chambers, whose dose-response can be traced to a primary standards laboratory. Moreover, measurement of dose-to-water is required under a wide variety of conditions, and selection of suitable dosimetry methods should take into consideration the dependencies of the detector in question as well as the properties of the radiation source [117]. In the context of small-animal radiotherapy and UHDR research, this subject becomes non-trivial with detector selection being an important aspect of experimental design.

Among commonly used dosimeters, radiochromic films have proven suitable to a wide array or experimental conditions. These films are comprised of radiation-sensitive, self-developing active layer and bounded by a protective polyester layer. After exposure to radiation, the dose-dependent change in film optical density (OD) can be measured by way of digital readout, whether by an optical densitometer (single-channel) or through a flat-bed scanner capable of digitizing the film image and presenting three-color (RGB) channels of response which can be correlated to an absorbed dose. This dose interpolation step is accomplished by following established procedures for film calibration against a reference dosimeter under reference conditions whose calibration can be traced to an accredited metrology/standards laboratory.

In the work summarized in this document and associated publications, relative dosimetry using the common EBT3 Gafchromic® film variety was primarily employed for absolute dose measurements. Favorable properties of EBT Gafchromic films include dose-rate independence, sub-millimeter resolu-

tion, minimal energy response (especially >1 MeV) and a low-dose sensitivity (down to 10 cGy) [118]. These aspects establish EBT3 as being well-suited to extract information from the microscopic features and high dose-gradients that demand high dose and spatial resolution and which might be encountered, for example, in SFRT dose profiles or small-animal (small-field) RT contexts; moreover, the established dose-rate independence has cemented it as a measurement standard for UHDR applications.

A detailed description of the EBT film characteristics in the context of UHDR and small-field (i.e. SFRT) therapies is discussed in the following section. Part of this brief review of literature was included in the scope of a comprehensive FLASH review paper published in *Physics in Medicine and Biology* [13].

2.3.1 Key Properties of EBT3 film for SFRT and UHDR therapies

Radiochromic films are self-developing radiation dosimeters whose detection principle relies on radiation induced polymerization of an active (diacetylene) layer resulting in coloration and a measurable increase in OD [119, 120]. The most common radiochromic films, Gafchromic films, are inherently 2-dimensional and have been consistently demonstrated as having low dose-rate and energy dependencies, as discussed herein. These features are standout as being desirable in UHDR dosimetry in order to provide absolute dose, dose-rate and dose distribution data for the highly variable, non-standard beams utilized in the current FLASH-RT landscape. To date, Gafchromic films of various generations have been successfully utilized as convenient systems for dose measurement for both routine and non-standard fields including UHDR VHEE irradiation [58, 121, 122] and spatially micro-fractionated synchrotron therapies, most notably MRT/MBRT [123–125]. The high resolution provided is also relevant for radiobiological small-animal irradiations, which are of immediate relevance to the research aimed toward clinical translation of FLASH-RT.

EBT-3 and EBT-XD models consist of a 28-µm and 25-µm thick active layers, respectively, and two symmetric 125-µm thick polyester layers. Recent UHDR experiments have reaffirmed the dose-rate independence of these films for various modalities and energies [126, 127]. For example, EBT films have been validated for use in MRT synchrotron studies, where kGy/s (i.e. $\sim 10^4$ Gy/s) dose-rates are encountered [44, 123, 125, 128], in VHEE irradiations [58, 121], and recently in ultrahigh dose-rate proton irradiations [51, 129, 130]. As pertains to the x-ray FLASH source development in this work, the application of EBT films to UHDR x-ray irradiation at MV beam energies has recently been demonstrated by Gao *et al.* [131] and in the 10MV FLASH-RT experiments which are summarized later in this dissertation (Chapter 6). Considering the cross-modality relevance of FLASH-RT and its applicability to a range of particle energies, both energy and particle-type independence of EBT films are highly desirable traits amongst candidate dosimeters at UHDR. At megavoltage energies, modern EBT films also feature reduced energy dependence compared to their predecessors [132, 133]. While an even lower energy-dependence was observed for EBT-XD films compared to EBT-3, the overall

response remained comparable (to within 3.5%) for energies >100 keV and doses up to 15 Gy [134]. This is relevant to UHDR MV photon beams which employ broad spectra and large single-fraction doses in FLASH-RT.

Given that EBT-3 films were utilized at UHDR and in mixed particle MeV beams for the work conducted at ARIEL (see Chapter 6), it is also important to understand any change in film response with electron energy. Fortunately, between 6 and 16 MeV the response was found to be <0.5%, at least for a single low-dose level of 2 Gy [135]. More recently, this energy independence was further established for electron energies of 4–12 MeV and doses between 0.25 Gy and 30 Gy [127].

FLASH-RT is currently characterized by the delivery of high-dose single fractions and therefore the limited sensitivity ranges of EBT films become a noteworthy consideration. In particular, the new EBT-XD film has been utilized for (electron) FLASH-RT [126,136], and found to have improved sensitivity over EBT-3 for doses >5 Gy [134]. Nevertheless, while the dynamic dose range for ETB-3 is 0.1–20 Gy, suitability up to 40 Gy has also been suggested [137,138]. This expansion of the usable dose range for EBT-3 films was exploited during the dosimetric characterization of the ARIEL x-ray beam and is the subject of Chapter 6.2.2.

2.3.2 Ionization chamber cross-calibration

Before films can be employed for relative dosimetry, batch calibration of the Gafchromic® EBT3 film is required. This was accomplished by cross-calibrating against a PTW TN3001 (Farmer type) cylindrical ion chamber. Absolute dose measurements with the ion chamber were taken according to the procedure set out by AAPM's TG-51 or TG-61 protocol, as is appropriate for MV and kV energy photon beams, respectively [139,140]. In general, doses under reference conditions appropriate to the chamber type and beam energy are measured while films are exposed under (near) identical conditions. Film responses are then correlated with the associated doses and a calibration curve can be constructed. The appropriate fitting function according to the literature is either a rational or polynomial function with sufficient degrees of freedom; throughout this dissertation the fitting function used is of the following form [118]:

$$OD(D) = \frac{a+b}{D-c} \tag{2.11}$$

For film calibrations conducted on the SARRP, the dose rate was measured at iso-center in order to enable estimation of the irradiation times necessary to reach each target dose. In the case of a clinical linac, however, the dose per monitor-unit (MU), which corresponds to the dose-to-water at a reference depth (nominally 1 MU/cGy at 10 cm depth or d_{max}), is instead used. Unless otherwise specified, ion chamber measurements were completed for each film calibration point under as close to identical conditions as possible.

In order to accommodate high-resolution scans required for MRT and small-field measurements,

it was prudent to create a custom set of calibration and analysis scripts in MATLAB. Throughout this dissertation calibration fits and interpolated results for single-channel dosimetry were checked against the triple-channel dosimetry method employed by the commercial FilmQA Pro^{TM} software (Ashland Advanced Materials, Bridgewater, NJ, US). Red-channel dosimetry is everywhere employed, unless otherwise specified, and the results are generally found to be in excellent agreement out to the highest doses (see Figure 2.9), even for kV beam energies which exhibit a greater sensitivity to the film composition and non-uniformities [141]. Calibration and measurement film scanning is conducted 24 hrs post-irradiation and a resolution >72 dpi is employed with the exact value depending on the application (see each chapter's methods section for details).

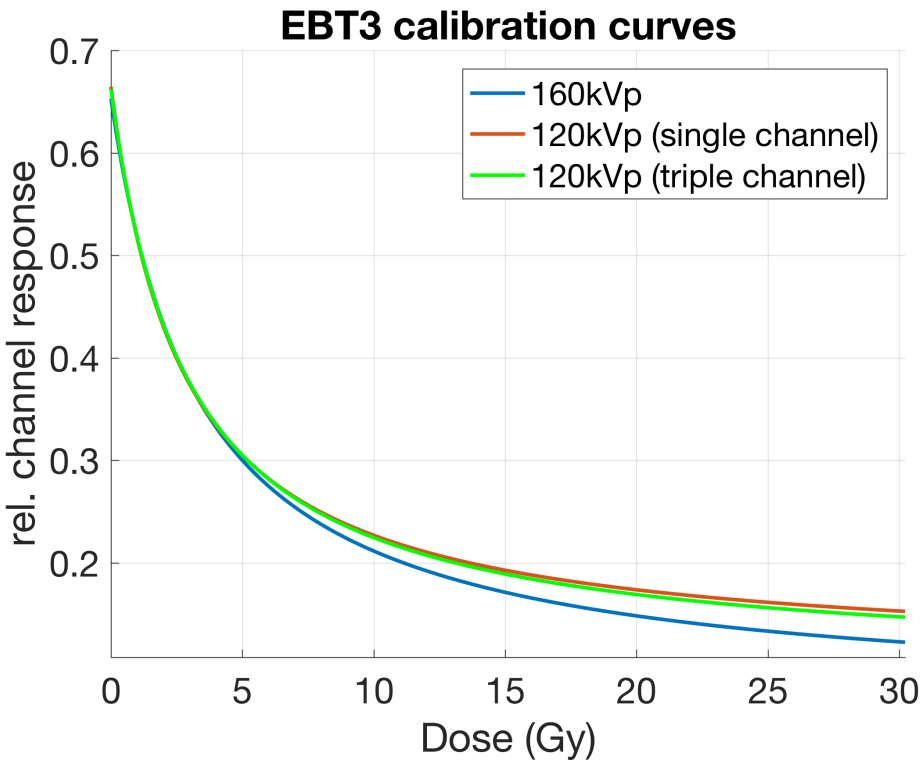

Figure 2.9: Example of EBT3 film calibration curve fits for a Comet MXR-160/22 x-ray tube. The sensitivity of the film to beam energy, especially at higher dose, and the relative insensitivity to using the (single) red channel calibration as compared to the triple-channel correction in FilmQA Pro^{TM}

2.4 Simulation Software

2.4.1 Monte Carlo

Monte Carlo (MC) simulations provide a means of modeling complex physical phenomenon by using random numbers drawn from the probability distributions which govern the various interactions described previously (Section 2.1.1). In medical physics, the MC method is often employed to simulate particle transport whereby a large number (N) of initial particles (histories) are tracked through a

series of discrete (stochastic) physical interactions in matter which are sampled based on the relative probabilities for the interactions to occur. In simplified terms, particle transport and physical processes can be modeled by using repeated random number sampling in order to yield an approximation of the expected (integral) response; in effect, the response of the system given a set of initial conditions will converge to the expected solution as N, the number of independent samples, tends to infinity. While modern MC codes employ efficient and sophisticated algorithms for statistical accumulation and robust theoretical models, the underlying principle remains largely the same whereby random numbers are drawn from the probability distribution which governs the interaction of interest at any given point.

2.4.1.0.1 Simulated Compton Scattering Example As a rudimentary example of the process, consider below a monoenergetic photon beam in an attenuating medium and the Compton effect: Firstly, modeling photon attenuation per the usual exponential probability distribution $p(x) = \mu e^{-\mu x}$, such that the cumulative probability may be calculated as:

$$P(x) = \int_0^x p(x)dx = \int_0^x \mu e^{-\mu x} dx = 1 - e^{-\mu x} \tag{2.12}$$

Then, the transformation method may be applied, whereby r_i, a uniformly distributed random number generated between 0 and 1 is set equal to this distribution (i.e. $r_i = P(x)$). Re-arranging, the distance to the next point of interaction becomes simply: $x_i = -\lambda ln(r_i)$, where $\lambda = 1/\mu$, and μ is the *total* linear attenuation coefficient.

The choice of interaction follows by sampling a uniformly distributed random number (r_i) and selecting the appropriate interaction with a probability equal to the ratio of the interaction cross-section (or equivalently linear attenuation coefficient) over the total cross-section (i.e. the relative interaction probability).

The Compton interaction can be simulated using the acceptance-rejection MC method to sample the Klein-Nishina formula (Equation 2.2) while the resultant photon and electron energies may be found using the kinematic equation 2.1.

The distribution may be sampled as follows: i) Take θ to be a random number sampled uniformly in [0,π], ii) sample a second uniform random number (R) such that $R \in [0, max(d\sigma/d\theta)]$, iii) IF $d\sigma/d\theta(\theta) > R$ then the sampled angle is accepted, if not then a new angle is 'drawn' from the distribution. Note that this angle is only the polar angle with respect to the direction of the initial photon momentum vector, on which the scattering angle depends. For the independent azimuthal angle ϕ, the angle can be drawn uniformly ($\phi = 2\pi r_e$) for the random number $r_e \in [0, 1]$ and the electron would then take the complementary angle to ensure momentum conservation. Together these angles define the direction cosines in spherical coordinates at the point of interaction.

2.4.1.1 Radiation Transport Codes

A variety of dosimetric quantities of importance to medical physics may be calculated in MC codes, including the absorbed dose, fluence, spectral distribution, mean energy and the associated statistical errors (i.e. standard deviation) and are frequently employed in the body of the presented work.

The MC codes used in this dissertation include TOPAS, EGSnrc and Molflow of which the first two are used in radiation transport and dose calculation while the latter is for simulation of gas transport and pressure evolution in vacuum systems. Each is applied according to different use cases and will be briefly introduced here along with examples of application suitability.

EGSnrc, which began as the Electron Gamma Shower (EGS) code, is an efficient and well characterized MC code well-suited to the simulation of photons and electrons using relatively simple geometries [142]. The code features a graphical user interface (GUI) and various configurable geometry templates (component modules). The code accommodates a two-stage workflow for end-to-end simulation of photon production and transport; namely, the BEAMnrc accelerator simulation code and DOSXYZnrc, which facilitates phantom dose simulations. While BEAM can facilitate simple depth-dose scoring in a water phantom and phase space scoring, DOSXYZ has the benefit of allowing for customizable voxelized phantom import, including those derived from CT images (i.e. *.ctphant* files). The EGS code is efficient and readily parallelized making it effective for large scale simulations; this is beneficial in simulations where good statistics are important in the evaluation of dosimetric quantities with modest computational demands.

The **Tool for Particle Simulation (TOPAS)** is a wrapper and extension of GEANT4 [143] well-suited to the simulation of a wide variety of particles and features a flexible text-based interface. Given that it leverages a GEANT4 backend, the user has access to a wide variety of physics libraries and can therefore simulate neutrons and hadrons in addition the electrons, positrons and photons, something which is not possible in EGSnrc. Moreover, the user has access to a wide range flexible geometries which can be layered in arbitrary ways using the code's 'layered mass geometry' functionality. TOPAS has also added the functionality to enable import of CAD (i.e. .stl) files in order to faithfully recreate the simulated volumes representing real components, for example realistic phantoms and custom beam shaping devices which are of interest in this dissertation. CT volumes can also be imported to enable comparison or treatment planning system and MC dose distributions. In contrast to EGSnrc, TOPAS simulations were typically more resource demanding and therefore run in parallelized sets on research computing servers such as those provided by Compute Canada.

2.4.1.2 Vacuum Simulation - Molflow+

Separate from the radiation transport MC codes described previously, Molflow+ is a MC program which simulates gaseous particle transport in predominantly ultra-low density (vacuum) environments [144–146]. Particles (histories) are tracked in their course of desorbing, diffusing, reflecting and

adsorbing onto vacuum structures, such as beamlines. The desorption (release) of gases and vapours (i.e. H_2, O_2 and H_2O) from vacuum components held at constant temperature can be simulated along with the effects of pumping or vacuum leaks. The code is fast and undemanding of system hardware and can enable efficient simulation of transient and steady-state conditions in vacuum in real-time. Quantities of interest include the pressure gradients (instantaneous and steady-state) as well as the velocities and densities of the various gaseous species. Inputs to the code include geometries, which can be modeled internally or imported as CAD files, pumping speeds ($\mathrm{L\,s^{-1}}$), environmental conditions (i.e. temperatures, pressure) and outgassing rates ($\mathrm{Pa\ m^3\,s^{-1}}$). Properties may be assigned on a per facet (surface element) basis and can vary in time by using custom functions to describe the temporal evolution of the physical quantity.

2.4.2 Finite Element Analysis

Finite Element Analysis (FEA) involves the simulation of physical phenomenon using the numerical technique for solving differential equations known as the finite element method (FEM). Many physical processes of relevant to thermal (Figure 2.10), fluid transport (i.e. diffusion equations) and structural mechanics (i.e. elastostatics) are described using partial differential equations (PDEs) which must be solved to estimate, for example, the stress-strain response of a system under various loads and are also used in coupled fluid- or thermo-mechanical problems.

In brief, the method of calculation involves the discretization of a larger (continuous) system into small, simple 'finite elements', which is accomplished through meshing of the system geometry. The PDE is then solved locally considering the physical and material parameters, as well as initial and boundary conditions appropriate to the problem. The mesh geometry consists of many small elements, essentially calculation sub-domains, that together form the shape of the simulated structure(s). For every element, sets of element equations are found which locally approximate the unknown solution for the governing boundary-value problems. The resultant systems of equations are comprised of linear algebraic solutions (steady-state) or ordinary differential equations (transient) which govern the evolution of a quantity at discretely sampled points, typically at the boundary of the element, known as nodal points. The simple equations found for these finite elements are then combined into a global system of equations, via transformation of coordinates, within the global coordinate system which models the entire problem. The FEM approximates the global solution by minimizing an associated error function (i.e. the residual of a trial solution). An iterative solution process, sometimes including adaptive meshing, proceeds until the (trial) solution converges to the real solution with an acceptable error (residual) [147].

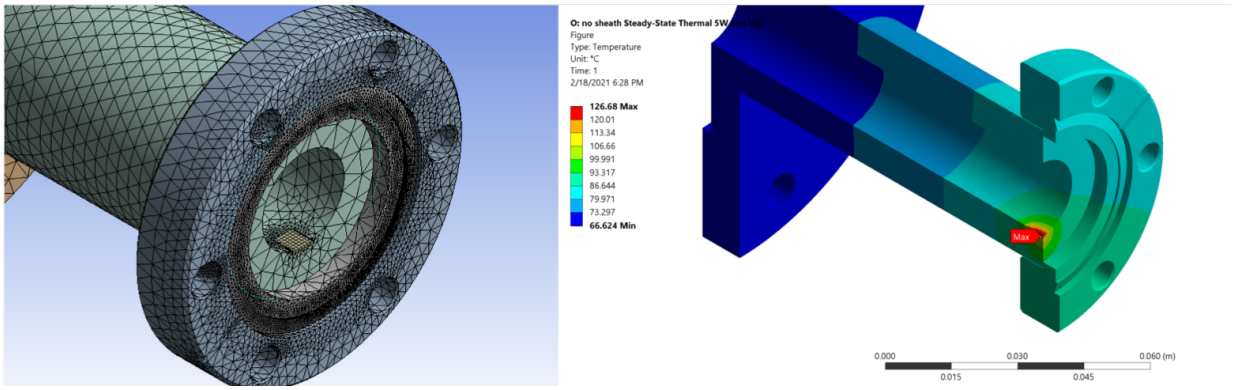

Figure 2.10: Example of an FEA simulation using the meshed CAD geometry (left). Shown is the electron collimator designed to ensure target and machine safety for the ARIEL FLASH irradiation platform (see Appendix A.5) and the steady-state thermal simulation (right) for accidental exposure to the 10 MeV accelerated electron beam at the 5 W (i.e. 0.5 µA) trip limit.

Once the solution for a given quantity is known at discrete calculation nodes, the distribution between nodes is found by interpolation. Consequently, it is important to use a sufficiently fine mesh (i.e. small elements size) for regions with high field gradients, in cases where sharp boundaries or discontinuities may exist, or where a finer resolution of the desired quantities is needed for meaningful analysis. Depending on the nature of the calculation and the boundaries, a curved surface will require a greater number of elements (i.e. mesh refinement) to adequately model the boundary effects. By changing the element sizes, and therefore the number of degrees of freedom, it is important to verify that changes in element size do not significantly affect the result. To this end, a mesh convergence study is usually undertaken to find the largest mesh size for which mesh refinement does not appreciably change the quantities of interest.

The discretization of a continuous system is a key feature of the FEA method whereby comparatively simple (element) equations are used to locally approximate the original, and more complex, physical problem. The numerical methods of FEA leverage error minimization to approximate solutions of the mathematical expressions that would otherwise be difficult to treat analytically due to complex loading history or coupled interactions, non-linear material properties, as well as non-simple geometries and boundary conditions (i.e. contacts).

2.5 Additive Manufacturing: 3D printing

Additive manufacturing, including 3D photopolymer and metal printing, has significantly improved in recent years as the technology has enabled the fabrication of increasingly complex geometries with stricter tolerances. As opposed to the laborious machining practices which require tight tolerances and specialized tooling, 3D printing helps to mitigate financial risk by providing a comparatively affordable and reproducible fabrication modality.

Throughout this dissertation different forms of 3D material printing have been utilized for precise

fabrication of CAD-modeled geometries. Most notable are the anatomically realistic mouse phantom (Chapter 4) using multi-material jetting, and laser-sintered metal printing for the collimator and field inserts for the ARIEL FLASH irradiation station. SFRT collimator fabrication, which traditionally required laborious and costly micro-machining [16, 128] or modular design strategies [31], represents another example of where demanding fabrication requirements might be alleviated through 3D printing.

For medical physicists, a notable benefit to using 3D-printed phantoms, collimators or other beam shaping components is that they can be fabricated from common sterolithography (.stl) CAD file format. This supports more convenient sharing and iteration between groups which may use different, or altogether lack, CAD software. Furthermore, modern MC codes such as TOPAS (see Section 2.4.1.1 above) provide support for importing .stl files making it possible to precisely reproduce the conditions of the physical experiment by simulating particle transport through geometries which faithfully reproduces the real-world specifications.

The various 3D printing modalities may employ different materials such as thermoplastics (fused deposition modeling (FDM)), photo-curable resins (sterolithography (SLA), digital light processing (DLP), low force stereolithography (LFS) and material jetting), or metals (selective laser sintering (SLS)). Oftentimes, selection of a suitable printing modality is primarily motivated by the resolution of the underlying technology, which is often reported in terms of the xy (horizontal) resolution - typically the greatest determinant of print quality - and the z (vertical) resolution (i.e. layer thickness). In terms of resolution, resin-based printing is often preferable given that the superior z and xy-resolutions, on the order of 10^1µm, enables fabrication of precise and smooth parts able to accurately reproduce sharp model contours and small feature sizes [148]. Moreover, the print accuracy is oftentimes greater than the limiting resolution due to the flexibility of mechanical control. On the other hand, resin modalities offer trade-offs in print resolution along different axes depending on the nature of the printer's operation. For example, the xy resolution of SLA (or LFS) and SLS depend largely on the laser spot-size, used to cure the resin at any xy position, and the motion stage's smallest movement increment (step-size). Material jetting, meanwhile, operates analogously to conventional printers by depositing photocurable polymer droplets which are subsequently UV-cured; in this case, resolution is limited predominantly by the particle size, nozzle diameter. Lastly, DLP uses a number of micro-mirrors to project the 2D image for the current print layer onto the base of the resin bath (build area) and is thus is limited in resolution by the light-transferring "pixel" size. Practically speaking, DLP tends to be faster than SLA and jetting in most cases, but it generally produces less accurate surface features where curved boundaries are encountered due to the fixed pixel (image) matrix. In contrast to the resin-printing option above, the thermoplastic based FDM modality represents a far more cost effective and accessible modality, at the expense of a reduced resolution (Z:$\sim$ 100 µm; xy: $>$102 µm), and the potential induction of surface defects (i.e. layer striations), limited not only by extruder nozzle size but also complex plastic flow dynamics of the

melted filament material. In every case, the mechanical motion accuracy and step-size limit the overall print accuracy.

Candidate materials may also have bearing on the selection of a suitable 3D-printing modality. For example, polycarbonate (PC) and acrylonitrile butadiene styrene (ABS) mimetic materials for 3D printers are commonly sought after; in medical physics contexts, these boast many characteristics comparable to those of PMMA, but the widest selection of structural plastics are available through FDM. SLS technology is predominantly used with Nylon and thermoplastic polyurethane, although the principle of SLS also underlies SL melting (SLM) used to produce 3D-printed metal parts. In contrast, material jetting is uniquely suited to multi-material fabrication within a single print job, necessitating only a change in the desired photo-polymer (i.e. type or color). While some 3D printing plastics are very rigid and resistant to heat and chemical deformation, few have been stress-tested and none of these plastics have been systematically tested for radiation hardness and inferences can only be made by comparing against data on similarly structured thermoplastics formed through conventional means [149].

From an imaging and radiological perspective, further advancement in the development of 3D-printable material is warranted to accommodate tissue simulation for multiple imaging modalities simultaneously [148, 150]. Therapeutically, water-simulating thermoplastic and photo-curable resins available with the above-stated print modalities may be sufficiently well-suited to accurate dose estimation *in vivo*, as will be demonstrated in Chapter 4.

Foreword on research The proceeding physics principles, tools (software and instrumentation), methods and their underlying fundamentals have been applied in the course of developing the core contributions of this dissertation (Section 1.1.4). Much of the work which follows (Chapters 3-5) has been published in peer-reviewed scientific journals along with a description of methods, motivations and results/discussion; therefore, methods that employ the basics covered here are expanded upon, as required, in the context of the Methods and Materials sections within each chapter. Nevertheless, I hope that this section may provide a useful, contextual overview regarding the general knowledge, theory and practical considerations behind the technologies which have been either applied or studied in the forthcoming chapters.

Chapter 3

Spatially-fractionated radiotherapy on a commercial small-animal irradiator

Monte Carlo optimization of a microbeam collimator design for use on the small animal radiation research platform (SARRP)[1]

3.1 Introduction

The ongoing effort to reduce radiation-induced side effects during radiation therapy (RT), and thereby improve the therapeutic ratio, continues to drive the development of sophisticated conformal techniques and new charged particle therapies. While these advanced modalities are capable of producing highly accurate, conformal dose distributions, even the most carefully executed therapies are unable to completely spare healthy tissues surrounding the treatment volume. As such, research directed at minimizing normal tissue toxicity, without compromising treatment effectiveness, remains a critical priority within the oncological and physics community. One novel technique has emerged in the form of microbeam radiation therapy (MRT). As a preclinical modality, MRT has gained considerable attention for its demonstrable capacity to spare normal tissues and preferentially damage tumors [6,7,21,23,24,151–153]. Notable areas of application include cases concerned with dose-limiting organs-at-risk, particularly those within the central nervous system (CNS), and those dealing with radioresistant tumor varieties.

Physically, MRT is characterized by its use of intense microbeam arrays to deliver very high doses (several hundred Gy) within a single fraction. The resultant dose distributions are comprised of alternating high-dose (peak) and non-irradiated (valley) regions, a common feature amongst spatially fractionated techniques. In such a context, the therapeutic efficacy critically depends on the ability to ablate neoplastic tissue without compromising the desired normal tissue sparing effect. Therefore, for the optimization of any spatially fractionated modality, it is imperative that the peak-to-valley dose ratio (PVDR) be maximized. Typical surface PVDR values found in the literature vary based on technique, but have often ranged between 15 and 30 [14–20].

[1] This work was published in *Physics in Medicine and Biology* [31]

To date, the majority of preclinical MRT research has employed arrays of parallel, microplanar x-ray beams, generally <100 µm wide and spaced 50–400 µm on-center, generated using synchrotron sources with mean energies in the range between 50 and 125 keV [6–8, 14, 20–22, 153, 154]. More recently, however, groups have opted to study the effects of using larger aperture sizes, typically larger than 200 µm, designated as minibeam radiotherapy (MBRT) [16, 18, 23–25]. Application of larger apertures has helped to circumvent some of the experimental and design-related limitations associated with the use of smaller beams. However, there is evidence to suggest that an upper limit (between 700–1000 µm) could be placed on the effective MRT/MBRT beam size, beyond which long-term tissue toxicity may be observed due to reduced tolerances of healthy microvasculature [20, 155]. In the case of rodent brain irradiations, beam widths larger than 680 µm have been associated with a marked decrease in tolerated peak dose, although the exact response is inevitably dose-dependent [23, 25]. Additional work is needed to establish the relative benefits and limitations of MRT and MBRT and, in general, the use of larger apertures, possibly coupled with a higher mean spectral energy in larger preclinical subjects.

An active body of research continues to reaffirm the existence of unique tissue-sparing and tumoricidal effects in MRT, however the mechanisms behind the surprising dose-effect relationship remain poorly understood. While the dose-volume effect [156] is believed to play a role, other mechanisms are expected to participate so as to explain the observed outcomes. Prevailing theories surmise that damaged (ablated) tissues experience rapid biological repair courtesy of the minimally irradiated cells contiguous to the irradiated slices and possibly promoted by a bystander effect [7, 8, 157]. In addition, normal micro-vasculature intersected by the thin microbeams is believed to possess significant regenerative capacity while a preferential tumoricidal effect derives from the lack of recovery in tumor vasculature by comparison [6, 15, 21, 25, 152, 158, 159]. In the context of preclinical research, a reduction in normal cell death has been consistently demonstrated following high dose MRT treatments when compared with lower dose conventional RT producing the same degree of tumor cell kill. Similarly, a reduction in the severity of normal tissue side-effects has been observed across a number of biological endpoints [6–9, 17, 21, 24, 158, 160, 161].

Presently, a major obstacle for the widespread implementation of preclinical work in MRT is the limited accessibility of synchrotron facilities used to generate the requisite microbeams. Traditionally, synchrotron sources have been preferred for their minimal divergence and high dose rates (hundreds of Gy/s), but new research on the use of conventional (i.e. x-ray tube) sources has shed light on the possibility of MRT implementation on a smaller scale [16, 18, 19, 162, 163]. Small animal irradiators, such as the image-guided small animal radiation research platform (SARRP) [30], are proving to be attractive systems for ongoing research in this context. Moreover, employing small-scale, gantry mounted sources could aid researchers in implementing multi-beam, interleaved MRT treatment plans by which improved tumor coverage and a reduction in healthy tissue exposure might be achieved [23, 162].

While the improved accessibility and reduced cost of small animal irradiation platforms make them attractive for preclinical work, there are a few notable points that require elucidation before widespread adoption becomes feasible. For one, the consequences of employing a broad-spectrum, divergent source in MRT, relative to conventional RT or synchrotron-based MRT, are not fully known. Furthermore, the use of a conventional source necessitates a substantial increase in the treatment time required to deliver ablative doses that are otherwise achieved nigh instantaneously with synchrotron beamlines. In this regard, while anesthetic guidelines for animal research present an overarching constraint, long treatments can also result in blurring of the microbeam dose distribution due to vascular pulsations and cardio-synchronous movement in target tissues [23,164,165]. Combating this potential loss of beam spatial resolution is of critical importance in MRT, as the treatment efficacy depends strongly upon the preservation of the fractionated dose distribution within healthy tissue [6,7,21,151]. Cardiac gating has been proposed as one possible solution that may help in transitioning to effectively deliver MRT on SARRP-like systems [162]. However, even without compensation for physiological motion there exist cases that are particularly well-suited to microbeam therapies, namely those less sensitive to respiratory, cardiac and vascular movement. Targets within the CNS stand as notable examples. Radioresistant glioma models are especially interesting candidates for the reason that additional benefit can be gleaned from the improved therapeutic index afforded by MRT.

At present, the implementation of microbeam collimation with conventional kilovoltage x-ray sources has presented numerous challenges. Concerns over beam divergence and smearing due to physiological motion are widely recognized as complicating factors; furthermore, variation across lateral microbeam profiles, which may result from geometric irregularities, ultimately complicate the validation procedure [128]. In order to resolve these issues, the current paradigm has required highly precise, but laborious and costly machining practices. To date, only a few divergent collimators have been produced in light of these restrictions [16, 19]. Prezado *et al.* (2017) adapted a commercial SARRP system for in vivo MBRT and were capable of delivering sufficiently high dose (>50 Gy) within the time-limits for small animal anesthesia. Their robust solution provided a solid proof of concept, but the collimation system required significant modification of the system. While a simpler mode of proximal collimation has shown some promise [18], such a solution would not facilitate a flexible framework for multi-beam single fraction treatments, due to the need for subject/target re-orientation. Consequently, the ability to produce and validate an inexpensive, yet portable, divergent multi-slit collimator (MSC) design suitable for application with the SARRP offers a competitive advantage in terms of facilitating adoption of MRT/MBRT in the broader research community.

In this work, the design of a theoretical MSC, capable of fitting within the stock $10 \times 10\,\mathrm{mm}^2$ treatment nozzle of the SARRP, was optimized. The central goal was to inform the MSC design process using Monte Carlo simulations and a realistic set of geometric and source constraints. The relative sensitivities of key performance metrics, including the PVDR and dose rate to changes in

MSC design and x-ray beam parameters were studied. The framework presented is being used to help our group conditionally maximize performance while maintaining a reasonably cost-effective MSC construction for the SARRP.

3.2 Methods and Materials

3.2.1 Source description: The Small Animal Radiation Research Platform (SARRP)

The SARRP (Xstrahl Ltd., Walsall, UK) system uses a water-cooled, dual focal spot (0.4 m or 3.0 m in IEC366 convention), constant voltage x-ray tube mounted on a rotating gantry. It boasts a tungsten anode with a target angle of 20°and 0.8 mm inherent Be filtration. The source-to-isocenter distance (SID) is 35 cm and multi-stage collimation is used to restrict the field size before reaching the final adjustable aperture, whose base is situated 5 cm above isocenter. The largest collimated field size afforded by the SARRP is constrained by its tertiary collimator, $\simeq$12.7 m in diameter, which is located just above the treatment nozzle. Johnstone *et al.* (2018) describe the SARRP model which was defined using careful measurement of various components and manufacturer specifications where available [166].

The SARRP's therapy beam operates with a tube potential of 220 kVp (mean energy 78.4 keV), a maximum tube current of either 2.9 mA (small focal spot, SFS) or 13 mA (large focal spot, LFS) and 0.15 m of added Cu filtration. The 80 and 40 kVp imaging beams (mean energies 41.2 and 27.1 keV), which were similarly investigated for MRT, accommodate maximum tube currents of 8 and 16 mA, respectively, and 1.0 m of added Al filtration. In contrast to the 220 kVp therapy beam, only the small focal spot was investigated when using the selected imaging beam energies.

3.2.2 Modeling of MRT dose distributions

3.2.2.1 Monte Carlo simulation

In the present work, Monte Carlo (MC) simulations have been employed to inform the optimal design of a theoretical multi-slit collimator (MSC). The TOPAS (v3.1.1) [143] MC code was used to simulate various beam and MSC configurations. TOPAS is an extension and wrapper of the Geant4 (v 10.3.p01) [167] particle transport code, made suitable for both clinical x-ray and charged particle therapy simulations over a broad range of energies. Input phase-space files were generated using a BEAMnrc [142] model of the SARRP that was validated to directly calculate delivered dose from MC dose expressed in Gy/particle based on beam current and irradiation time [166]. The phase-space files were recorded for each beam energy of interest (220,80,40 kVp) and both focal spot sizes. The source plane was located just above the variable MSC geometry, 26.55 cm from the source, within the SARRP's $10 \times 10\,\text{mm}^2$ treatment nozzle (Figure 3.1a). By decoupling the SARRP (BEAMnrc) and MSC (TOPAS) simulations in this manner it was possible to significantly reduce the

computation time required per MRT simulation. Results for the TOPAS simulations were validated against the abovementioned BEAMnrc model by comparing the absolute dose at a depth of 2 cm in a water phantom for an SSD of 33 cm using the $10 \times 10\,\mathrm{mm}^2$ field size and maximal output technique (220 kVp, 13 mA, large focal spot). The absolute dose difference between the two MC codes was found to be less than 1%.

A robust physics list suitable for low energy applications (G4EmStandardPhysics_option4) was selected and applied globally across all simulations. This list leverages the low-energy Livermore and Penelope models for particle transport, ICRU73 ion stopping power data and an improved low energy Compton scattering model, which includes simulation of Doppler broadening and atomic de-excitation. Fluorescence and Rayleigh scattering were enabled by default and particle-induced x-ray emission (PIXE) was optionally enabled. The global energy/range cut for all particles was set to 1 µm and no bremsstrahlung splitting or other variance reduction techniques were employed. Over 10^9 primary histories were simulated for each MSC model configuration, with the exact number selected so as to achieve an approximate 2% uncertainty or less in the peak dose regions.

For each TOPAS MRT simulation, a fractionated beam, created by transport through the variable MSC geometry, impinged on a $1 \times 1 \times 3\,\mathrm{cm}^3$ water phantom (Figure 3.1a) in order to approximate the effects of particle transport through a biologically relevant target (i.e. tumor, mouse head). Dose was scored in $0.005 \times 1 \times 0.3\,\mathrm{cm}^3$ voxels suitable for resolving features of the lateral dose profile with sufficient acuity and without compromising the scoring statistics. Lateral dose profiles and depth dose data were calculated for various collimator-to-surface distances (CSD) and different collimator designs as described below.

3.2.2.2 Collimator geometry and optimization parameters

As the primary aim of this work was to inform the design of a divergent tungsten (ρ=19.3 g cm^{-3}) MSC suitable for use with the SARRP system, a number of source and MSC-specific parameters were varied so as to find an optimal configuration with respect to key performance metrics. These metrics included the peak-to-valley dose ratio (PVDR), microbeam full-width at half-maximum (FWHM) and the surface dose rate. In practice, each of these quantities were derived from the simulated dose distribution data by taking an average across all microbeams in their respective arrays. The microbeam 80-20% penumbra was defined as the lateral distance between points lying on the profile where the dose reaches 80% and 20% of the maximum (peak) dose. Since maximizing the PVDR is considered vital to the therapeutic efficacy of the modality it was used as the primary optimization endpoint.

The process of selecting a subset of MSC and beam parameters was motivated by the results presented in the literature as well as the dimensional and operational constraints of the SARRP system. These parameters included the CSD, slit width, collimator thickness, choice of slit material, and the focal spot size (Figure 3.1b). Moreover, three different treatment energies were independently

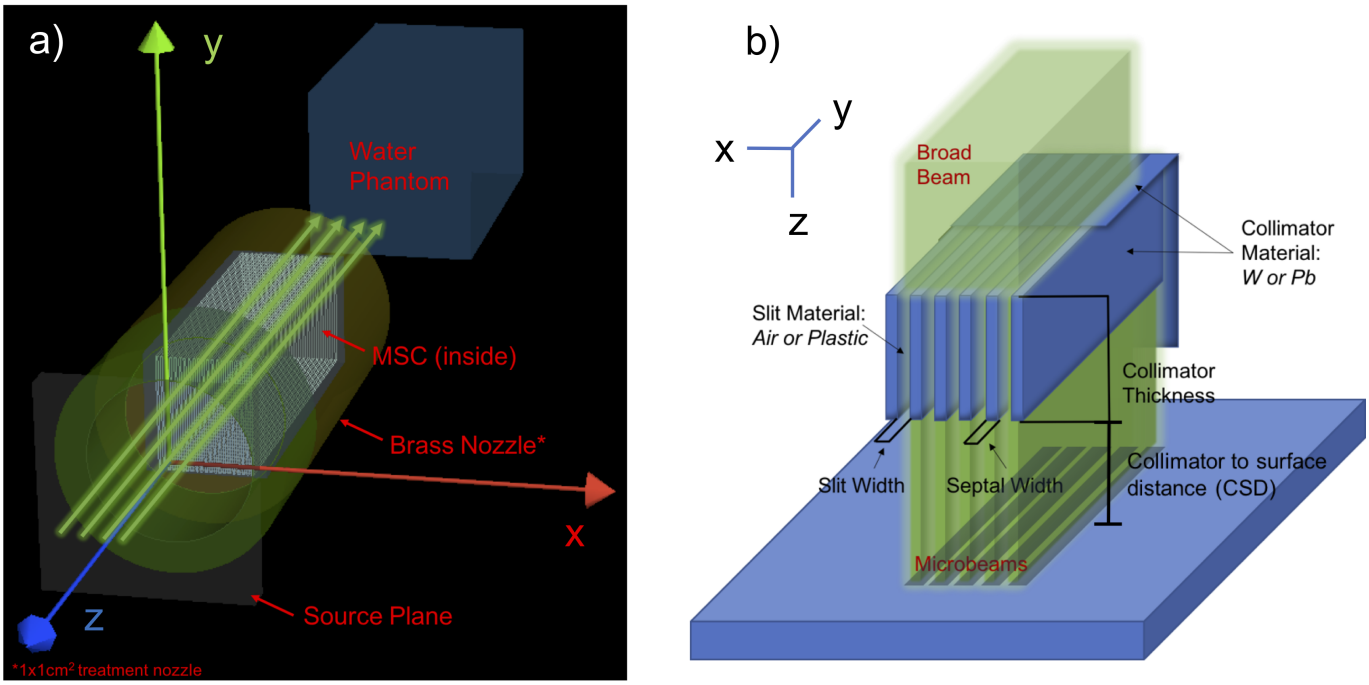

Figure 3.1: Visualization of the TOPAS Monte Carlo simulation setup (a) and diagrammatic representation of a general MSC configuration (b). The various MSC design parameters of interest are labeled in panel b), whereas a) illustrates MRT functionalization of the SARRP's $10 \times 10\,\mathrm{mm}^2$ brass treatment nozzle and the irradiation of a water phantom at a specified CSD.

considered (220, 80 and 40 kVp). Unless otherwise stated, a 2.5 cm collimator thickness was used in the results presented herein. For all configurations, the MSC geometry was simulated within, and did not extend beyond, the SARRP's $10 \times 10\,\mathrm{mm}^2$ treatment nozzle, which terminates 30 cm from the source. The relative output factor (ROF), defined as:

$$ROF = \frac{\dot{D}_{msc}}{\dot{D}_{open}} \tag{3.1}$$

where $\dot{D}_{msc}$ and $\dot{D}_{open}$ are the surface dose rates for the collimated and open ($10 \times 10\,\mathrm{mm}^2$) fields, respectively, was used to compare the output efficiency of MSC collimation across each candidate energy. In this context, only the 3-cm CSD was used in what was considered a worst-case configuration, assuming realistic setup constraints. $\dot{D}_{msc}$ and $\dot{D}_{open}$ were calculated as the average dose rate taken across all microbeam profiles within the surface dose distribution.

In the process of evaluating the effects of changing the slit size, a 2-dimensional visualization scheme was employed that leveraged 2D data interpolation. For this purpose, a dynamic-window, smoothing spline interpolant was applied which was non-destructive to well-behaved data, particularly in the high gradient regions. This enabled the simultaneous evaluation of PVDR trends for each sampled slit width at every depth. So as to isolate the effect of changing the slit or septal width from the center-to-center (c.t.c) spacing that is commonly reported in MRT studies, results were considered for a constant septal width of 200 µm. This approach was justified on the basis that an affordable MSC construction would not support adjustable septal widths.

As a means to enable the affordable construction of a modular MSC with reproducible slit dimensions, the application of low-density plastic spacers was also investigated. The proposed design involves having a tungsten frame fitted within the SARRP nozzle and allow for a modular MSC by sandwiching the spacers between tungsten sheets (septa). To inform the design process, a carefully selected pair of slit (i.e. spacer) materials were considered. One of polyethylene terephthalate (PET, ρ=1.38 g cm^{-3}) or polypropylene (PP, ρ=0.946 g cm^{-3}) were used in identical slit configurations. The changes in PVDR and dose rate were used to evaluate the performance when compared with the optimal case where no spacer material is used (i.e. air slits).

For each MSC and source configuration, single-beam simulations of a water phantom, described above, were employed to investigate changes in the dose distribution that result from variation of each parameter in turn. More specifically, the dose distribution data was analyzed to calculate the metrics of interest and to underscore the various dependencies of those quantities across a larger parameter space. Table 3.1 summarizes the parameters considered in the scope of this study.

3.2.3 Prototype collimator experiment and MC simulations

Preliminary MRT experiments were completed using a simple parallel slit collimator, able to fit within the SARRP $10 \times 10\,\mathrm{mm}^2$ treatment nozzle. Our first-generation parallel multi-slit collima-

Table 3.1: Studied MSC and MRT parameters.

Parameter	Values
Collimator material	tungsten
Slit material	air, PET, PP
Collimator-to-surface distance	1, 2, and 3 cm
Slit width	100, 125, 150, 175, 200 µm
Focal spot size	0.4 and 3.0 m
Beam energy	220, 80, and 40 kVp

tor was comprised of 12.7 m long, 0.36 m thick steel septa separated, as regularly as possible, using 135 µm thick double-sided tape (Figure 3.2). This configuration resulted in the production of slits approximately 0.135–0.175 mm wide. Radiochromic films were sandwiched between 0.3 cm slabs of solid water at depths between 0 and 2.1 cm. Dose profiles were obtained at six depths within the phantom, from which a percentage depth-dose (PDD) curve could be constructed. A combined uncertainty of 3% was used for all film measurements; this includes the uncertainty from the calibration procedure and the film's intrinsic error, informed through the manufacturer specifications [118]. A single irradiation was completed using the 220 kVp therapy beam, operating with the small focal spot at 2.9 mA. The CSD was set to 3 cm and a three-minute exposure was applied. The additional thickness of the film was accounted for in the measured depth-dose data. The film analysis procedure is described in Section 3.2.4.

MC simulations of the collimator were used for comparison with the experimental data. The simulated collimator was comprised of 135 µm air slits and 360 µm steel septa, chosen so as to best approximate the construction of the parallel MSC, despite the exact dimensions being unknown. Similar to the optimization study outlined above, the MRT dose distribution was scored in a $1 \times 1 \times 3\,\text{cm}^3$ water phantom using $0.005 \times 1 \times 0.3\,\text{cm}^3$ voxels.

An open field 2D dose distribution was used to evaluate the level of agreement between the MC model of the SARRP and experimental film data. The experimental data was acquired in the same solid water phantom, at a depth of 5.5 m, using the $10 \times 10\,\text{mm}^2$ nozzle and an SSD of 31.2 cm. The 220 kV beam operated at 13 mA with the LFS and the phantom was irradiated for 90 s. The MC open field dose calculation mimicked the experimental setup and used a voxel size of $0.02 \times 0.02 \times 0.3\text{cm}^3$. MC and film open field lateral (x-axis) profiles extracted from an area consistent with MRT dose profiles were compared.

3.2.4 Film dosimetry

Gafchromic® EBT3 dosimetric film (Ashland Advanced Materials, Bridgewater, NJ) provides sub-millimeter resolution (<25 µm), minimal energy response and sensitivity to low dose (down to 10 cGy) [118] making it well-suited to the extraction of information across the microscopic, high-

gradient features encountered in MRT research. A batch of EBT3 films, handled according to supplier guidelines, was cross-calibrated using a PTW Farmer® TN30013 type ion chamber according to the procedure set out by AAPM's TG-61 protocol [140]. Twelve films were individually irradiated to doses ranging from 0 to 8 Gy using 220, 80, and 40 kVp beams while preserving the setup of the corresponding ion chamber measurements. An 18-cm diameter open field was used to irradiate the chamber and film at a depth of 2 cm in solid water at isocenter. The ion chamber calibration, made suitable for use with orthovoltage irradiators, is traceable to the standard laboratories of the National Research Council of Canada (NRC).

For the experimental measurements described above, irradiated films were scanned, at least 24h after exposure, using an EPSON® 10000XL flatbed scanner (Epson America, Long Beach, CA) at a resolution of 1200 dpi in order to resolve features on the order of 20 µm. A Matlab® (Mathworks, Nattick, MA) script was used to process the scanned films using a single color (red) channel. The results were checked against FilmQA pro® (Ashland Advanced Materials, Bridgewater, NJ), which employs triple-channel dosimetry, and a negligible difference was found for the case presented here. A 0 Gy reference film was included in all scans to provide a baseline.

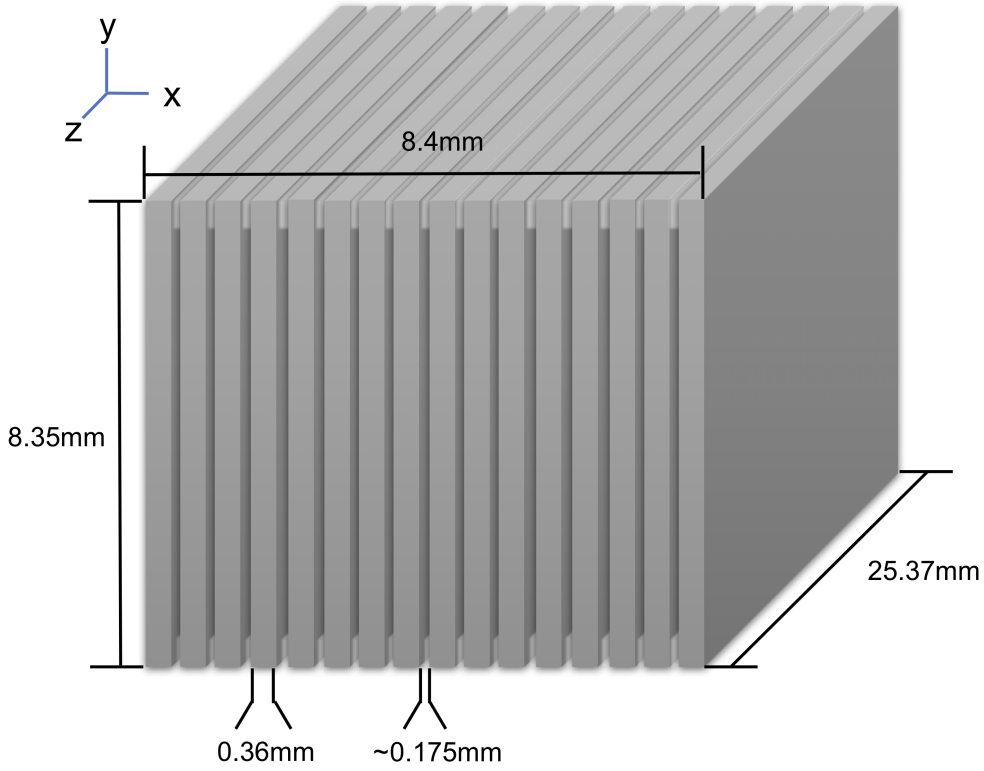

Figure 3.2: Schematic representation of the prototype parallel-slit MSC consisting of steel septa held together with a double-sided tape. The slit widths are a best estimate on the basis of the available means of measurement. The double-sided tape is approximately represented in the figure, by way of the spacers situated towards the top and the bottom, which run the entire length of the steel septa. The beam direction is along the z-axis.

3.3 Results

3.3.1 MSC optimization study

3.3.1.1 Focal spot size

Figure 3.3 depicts the effect that changing the focal spot size has on a representative MRT dose profile. The MSC was comprised of 27, 100-µm divergent air slits separated by 200 µm tungsten septa and dose profiles for the 220 kVp beam at CSDs of 1 cm and 3 cm are presented. The most notable results include the significant difference in dose rate, which is significantly lower for the SFS, and the effects of beam divergence on the microbeam array. In addition, there are noticeable changes to the individual microbeam profiles between the two cases. Specifically, the beams generated using the LFS are visibly broader, which accounts for the obvious increase in penumbra overlap when compared with the SFS distribution, particularly at larger CSD (Figure 3.3c, d). At 1-cm CSD the mean FWHM for the SFS and LFS are 98 ± 3 µm and 104 ± 2 µm, respectively, but the difference increases significantly at 3-cm CSD to 105 ± 3 µm and 135 ± 6 µm correspondingly.

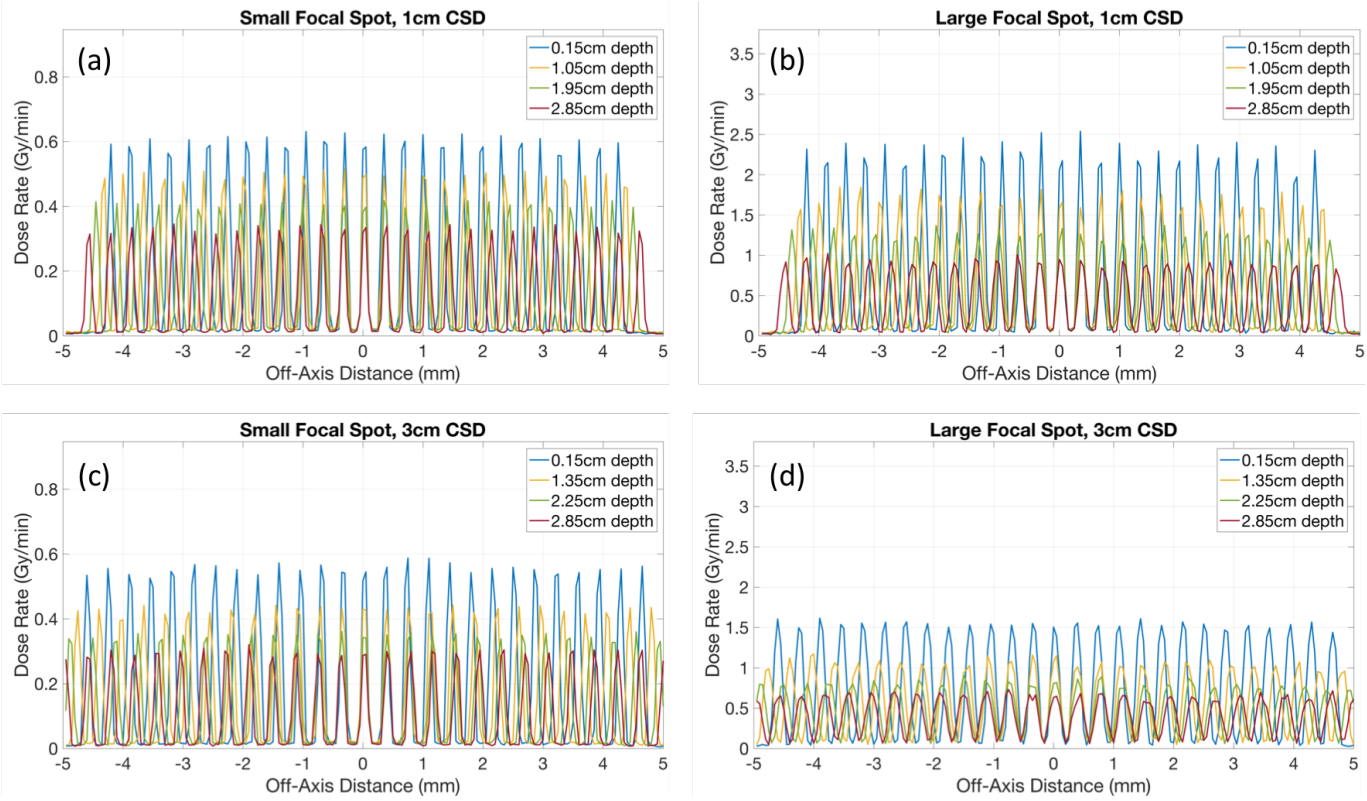

Figure 3.3: MC dose profiles in water for 220 kVp microbeams for an MSC consisting of 27 100-µm wide divergent air slits, separated by 200 µm tungsten septa. The lateral dose distributions for the SFS (a, c) and LFS (b, d) and 1-cm CSD (a, b) and 3-cm CSD (c, d) are shown.

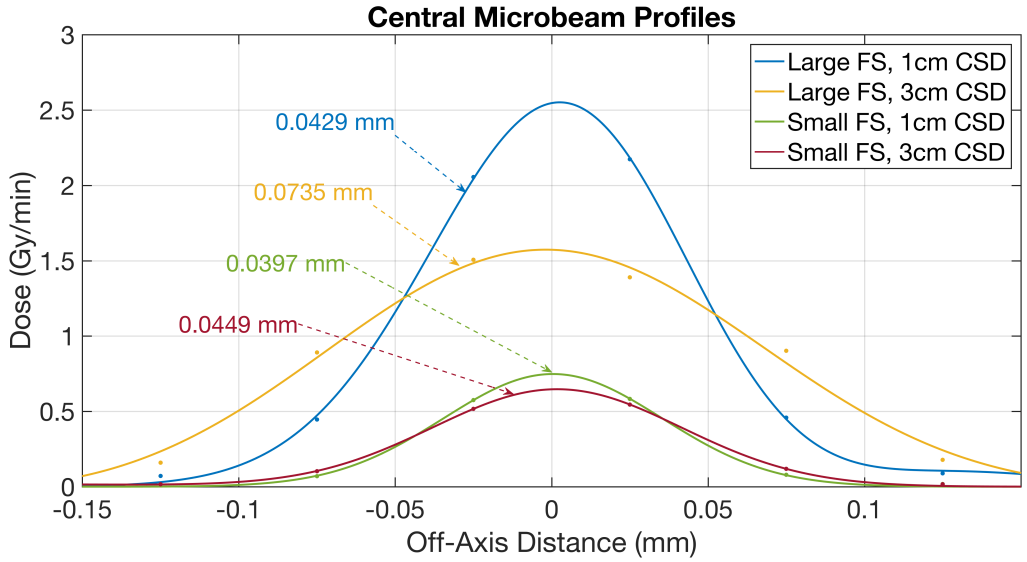

Figure 3.4: Central microbeam profiles and 80-20% penumbra for the data sets presented in Figure 3.3.

Figure 3.4 highlights the corresponding effect on the central microbeam 80-20% penumbra for both focal spot sizes. By increasing the CSD from 1 to 3 cm, the beam penumbra increased by 13.1% and 71.3% for the SFS and LFS, respectively. While the LFS profile features are considered sub-

optimal from an optimization standpoint, the significant increase in dose rate afforded is important for ensuring compatibility with small animal irradiations in future radiobiological work.

The relative effect of using the different focal spots on the PVDR is illustrated in Figure 3.5. The MSC configuration was identical to that used in Figure 3.3, but the following trends prevailed for various other MSC configurations. In addition to the obvious differences in PVDR, an important result manifests in the relative sensitivity to changes in CSD. Evidently, use of the SFS not only improves the PVDR, relative to the LFS case, but also significantly reduces sensitivity to changes in CSD (from 1 to 3 cm). It is interesting to note that the difference in PVDR increases with depth, most notably at the shorter 1-cm CSD.

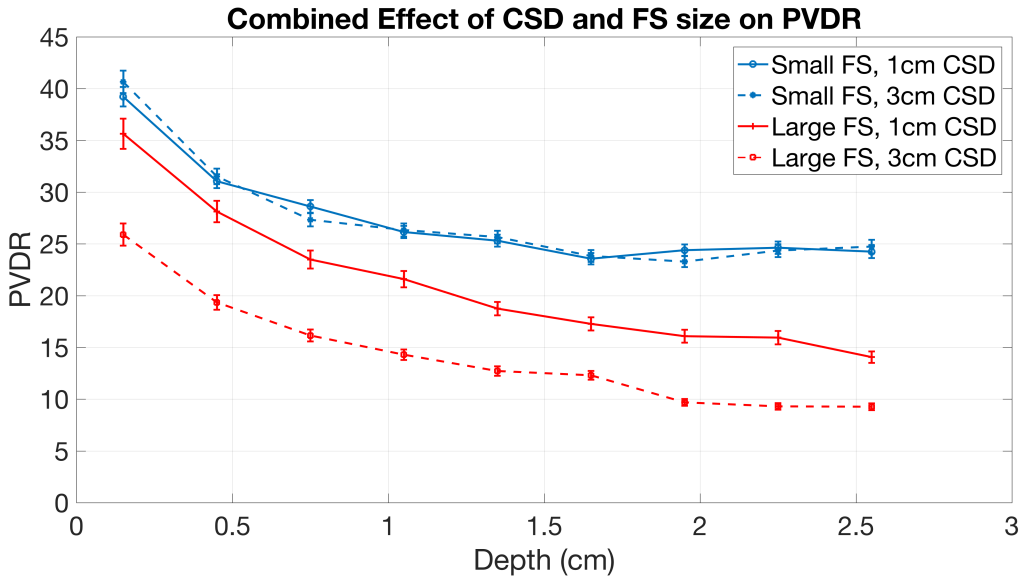

Figure 3.5: Comparison of PVDR at different CSDs for both FS sizes. The relative sensitivity to changes in between 1-cm and 3-cm SCD for a given MSC configuration is demonstrated.

3.3.1.2 Beam energy

The effect that beam energy has on the PVDR is shown in Figure 3.6a. Clearly, the 220 kVp beam provides an increase in PVDR when compared with the 80 and 40 kVp beams, which are themselves negligibly different down to a depth of roughly 1.50 cm. Beyond this point, however, the 80 kVp beam is found to perform slightly better than the 40 kVp beam. The corresponding effect of energy selection on the depth dose, for both the collimated and $10 \times 10\,\text{mm}^2$ open fields, is presented in Figure 3.6b. For the 40 and 80 kVp beams, inclusion of the MSC is found to increase the rate of dose fall off with depth. By contrast, the 220 kVp PDD experiences only a negligible decrease at shallow depths and the two data sets remain consistent within the bounds of the associated uncertainties beyond 1.50 cm.

Table 3.2 summarizes the effect of focal spot size on dose rate for the 220 kVp beam as well as the

effect of MRT collimation on output across all candidate beam energies. It is readily apparent that use of the LFS with the 220 kVp beam affords a much higher dose rate when compared with the SFS, as noted previously (Figure 3.3), due to the increased upper limit in tube current. Interestingly, the effect that microbeam collimation has on the output is much more pronounced with the LFS configuration, as demonstrated by the reduced ROF, and suggests it provides a less efficient collimation scheme. Nevertheless, use of the LFS increases the dose rate by a factor of approximately 2.8, which could reduce treatment times by up to 64% when compared with the SFS.

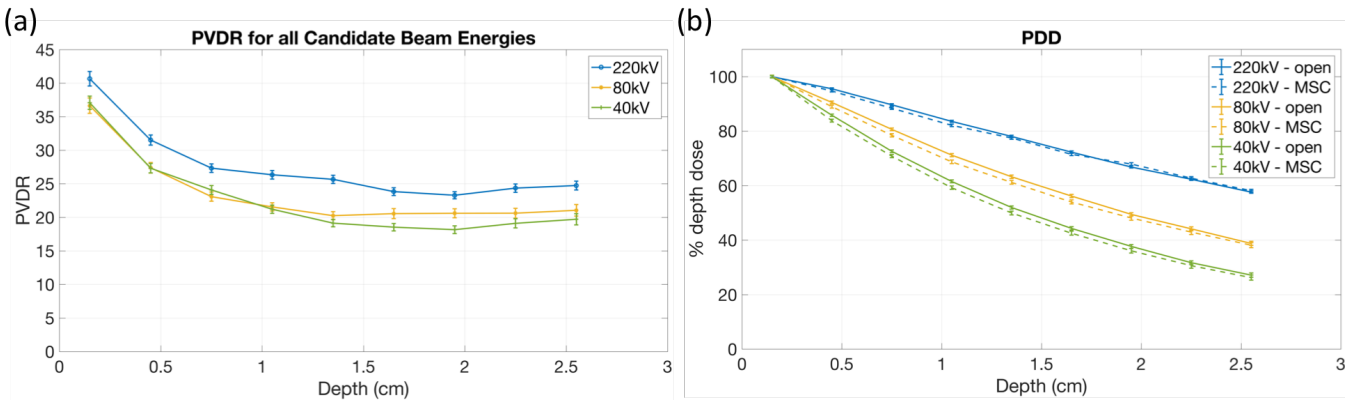

Figure 3.6: Effect of beam energy on the PVDR (a) and PDD (b). The PDD for both the open ($10 \times 10\,\text{mm}^2$) and collimated fields are included. In all configurations, 100 µm slits and a CSD of 3 cm is utilized. Only the small focal spot is used in order to facilitate cross-comparison across all beam energies.

Table 3.2: Summary of simulated SARRP surface Dose Rates and MSC Relative Output Factors (ROF) for each beam energy operating at maximum tube current and using the $10 \times 10\,\text{mm}^2$ treatment nozzle at 3 cm CSD.

Energy (kVp)	Configuration	Dose Rate (cGy/min)	ROF
220 (Large FS)	Open	310.2	**0.493**
	MSC	153.0	
220 (Small FS)	Open	64.2	**0.859**
	MSC	55.2	
80	Open	48.6	**0.865**
	MSC	42.0	
40	Open	26.2	**0.874**
	MSC	22.9	

Since the 220 kVp beam is found to increase both the PVDR and dose rate when compared with the lower energy (80 and 40 kVp) imaging beams, it is considered optimal for the purposes of this work. Consequently, the results that follow only consider optimization with respect to the 220 kVp therapy beam at maximum output.

3.3.1.3 Slit size and collimator-to-surface distance

In order to ascertain the effect that changing aperture size has on system performance and on the sensitivity to CSD, a 2-dimensional visualization scheme is employed in Figure 7. All PVDR data is calculated for depths in water between 0.15 cm to 2.55 cm for each of the sampled slit widths (100, 125, 150, 175 and 200 µm). While the left-hand side of Figure 3.7 provides explicit information for the dependence of the PVDR data on aperture size (slit width), the contour plots (Figure 3.7b, d, f, h) are valuable for interpreting the relative impact that varying slit width has across each configuration.

The most important result derives from the observation that the LFS configurations are much less sensitive to changes in slit width. This is evidenced through the verticality of the contour lines, which represents how, as slit width is varied across the sample space, only a subtle change in the PVDR is effected at all depths. The small focal spot, by contrast, shows significant sensitivity to slit width, especially as the width is increased just above 100 µm; this is demonstrated by the strong deviation of the contour lines away from the vertical axis (i.e. large gradients at constant depth). Interestingly, for the LFS case at 3-cm CSD (Figure 3.7c, d) the effect of varying slit width is reduced, which would imply that minimization of the CSD should be a first priority in contexts where the LFS must be utilized. As an added consequence of this trend, there is decreased sensitivity to changes in CSD for the LFS PVDR data at larger slit sizes. The SFS contour data (Figure 3.7f, h), on the other hand, remain very similar, which serves as a visual manifestation of the minimal degradation in PVDR that occurs with increased CSD. Note that this trend was previously observed using the 100 µm slit configuration in a singular comparison of the two focal spot sizes at 1 and 3-cm CSD (Figure 3.5), but is demonstrated here for the range of slit widths under consideration.

Another important observation relates to how LFS configurations experience a monotonic decrease in PVDR with depth, down to 2.55 cm, whereas for SFS configurations the PVDR plateaus, thus preserving the tissue sparing effect at depth (see also Figure 3.5). This is a highly favorable trait unique to the SFS; however, for larger slit widths the plateau appears at a lower PVDR, as might be expected, due to the abovementioned sensitivity to aperture size.

Examination of the PVDR gradient at constant depth for the SFS data (Figure 3.7e-h) reveals what appears to be a relatively simple, non-linear trend between the PVDR and slit width, albeit with a strong functional dependence on depth. For example, as the slit width increases, the constant-PVDR lines (contours) push up towards shallower depths; however, this change becomes much less pronounced as slit width increases. Additional data, especially at shallower depths, would be required before a functional form for this multi-variate relationship could be established.

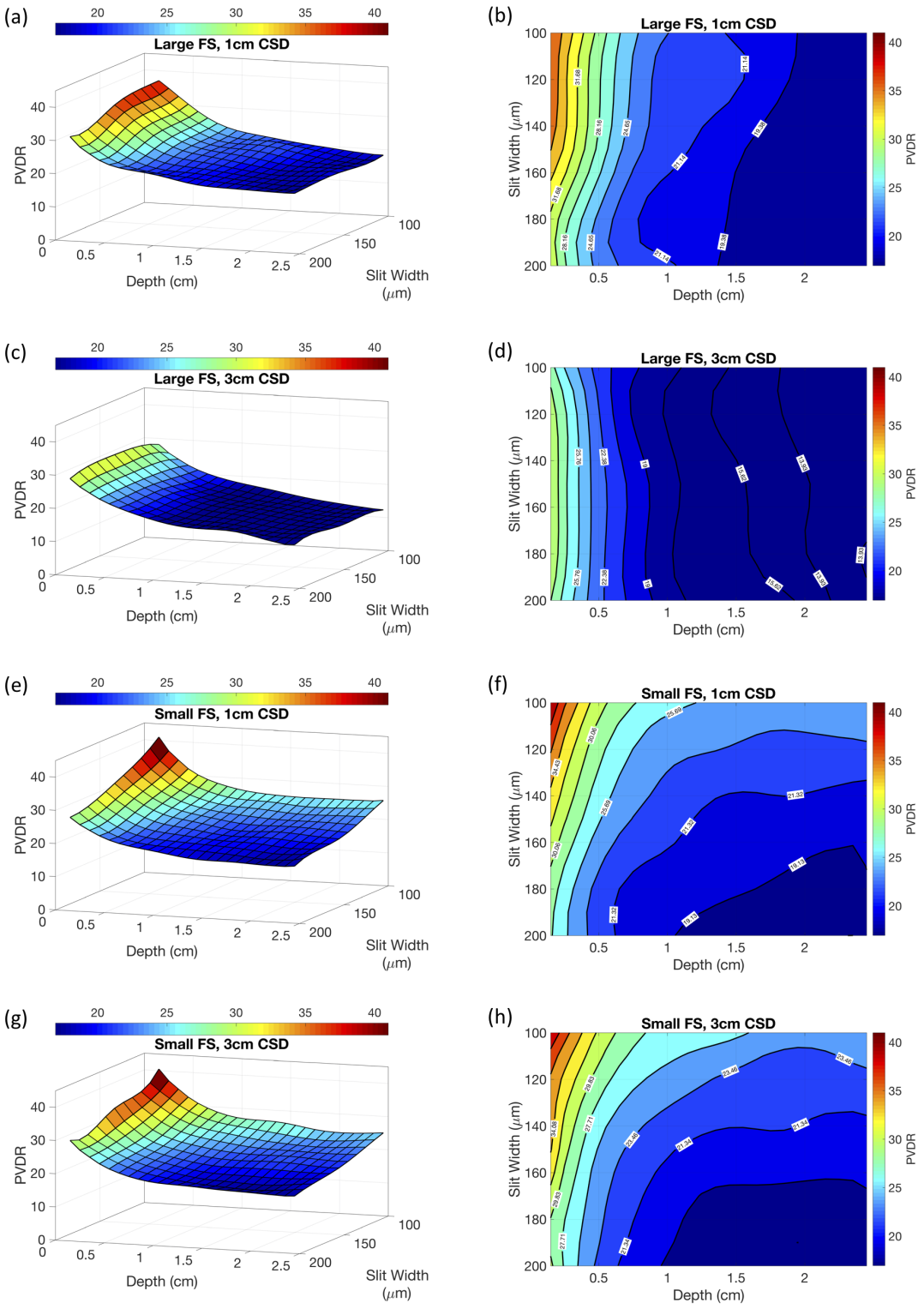

Figure 3.7: Effect of slit width on the 220 kVp beam PVDR for the large focal spot (a-d) and small focal spot (e-h) at both 1-cm (a, b, e, f) and 3-cm (c, d, g, h) CSD. Surface plots are presented in the left-hand column with the corresponding contour plots on the right.

It should be noted that the results presented above pertain to a 3-cm thick collimator. Using a thicker collimator was found to produce a slight ($< 8\%$) increase in PVDR at the surface and for 1-cm CSD. As such, the thicker collimator was used to maximally improve the PVDR while using the SFS. Each LFS simulation uses the same configuration in order to allow a direct comparison with the SFS data. Interestingly, the LFS configurations actually appeared to benefit from using a shorter collimator, with up to 9% improvement in PVDR when using the 1.5-cm MSC. This highlights a subtle yet interesting inverse relation between the choice of focal spot size and the effect of collimator thickness on the PVDR.

3.3.1.4 Slit material

Figure 3.8 demonstrates the effects of using different slit (spacer) materials on the dose rate and PVDR. Clearly, there is a substantial decrease in output that results from the use of the plastic spacer materials when compared to air, although polypropylene, being the lower density candidate, performed slightly better than polyethylene. The PVDR values at all depths were comparable for all plastic spacer materials. However, there is a $\approx 4\%$ overall improvement in PVDR for cases where the plastic spacers are used in place of air. The average output relative to air for polypropylene (PP) and polyethylene terephthalate (PET) were 0.63 and 0.53, respectively.

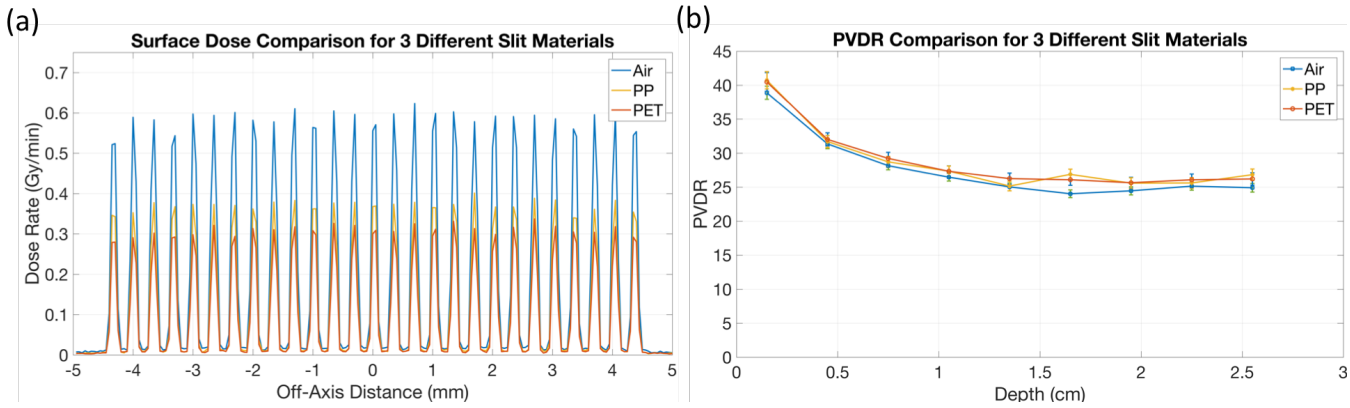

Figure 3.8: Effects of using selected slit materials on beam output (a) and PVDR (b) for the 220 kVp beam and SFS. A tungsten collimator with 100 µm slits, described in Section 3.1.1, was used with a 1-cm CSD.

3.3.2 Parallel-slit collimator experiment

Figure 3.9 summarizes the results for the parallel-slit MRT phantom experiment and MC simulations for the 220 kVp beam at 3-cm CSD. For the lateral dose profile, there is poor agreement due to misalignment and intra-fraction deformation of the MSC as well as asymmetry present in the experimental dose distribution that had not been accounted for in the simulated source. The latter is exemplified in Figure 3.10 wherein differences manifest for the $10 \times 10\,\text{mm}^2$ open field dose profile.

Nevertheless, the absolute dose for the maximum intensity peak (150 ± 5 cGy) in the film data was found to agree reasonably well with MC data for the corresponding peak (156 ± 4 cGy). The mean valley doses, on the other hand, were 8.0 ± 0.2 cGy and 3.0 ± 0.6 cGy for the film and MC results, respectively, which represents a significant relative deviation. The PDD curves were found to agree within the range of their associated errors at each depth.

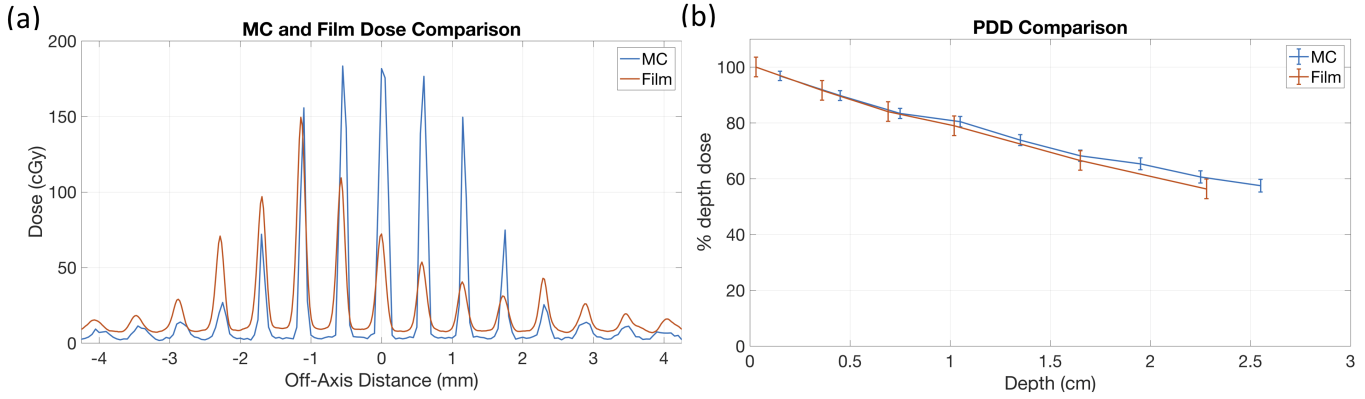

Figure 3.9: Dosimetric results of the parallel-slit MSC experiments. Surface MRT dose profiles (a) generated by the physical collimator and an overlay of the MC-calculated doses are presented along with the corresponding PDDs (b) for the experimental and MC derived dose distributions.

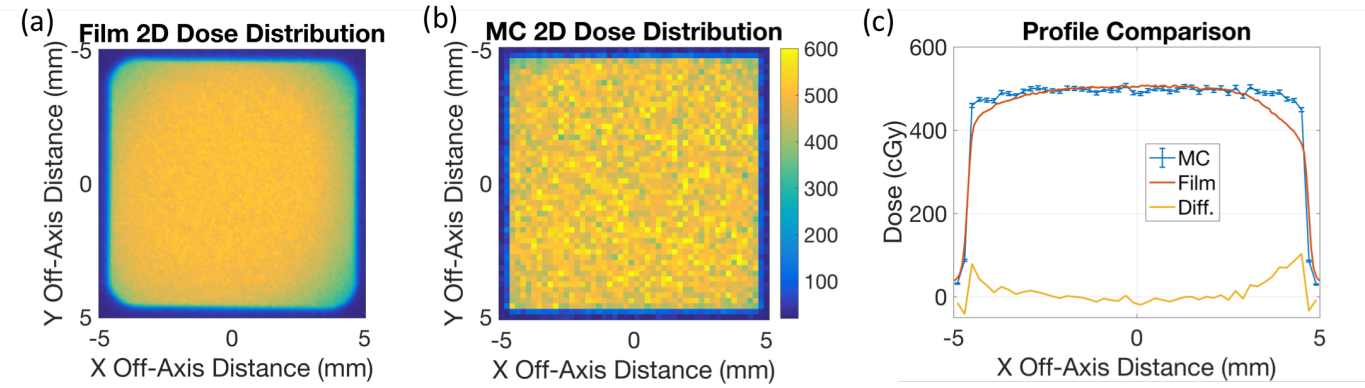

Figure 3.10: Commissioning film (a) and TOPAS MC (b) 2D dose distributions. A comparison of the lateral beam profiles (c) is shown for an ROI consistent with that used in creating the experimental MRT dose profile.

3.4 Discussion

Owing to the limited accessibility of high-flux MRT-capable synchrotron sites, translational research aiming to implement MRT/MBRT on conventional x-ray sources has gathered substantial interest. Recently, pre-clinical MBRT studies using small animal irradiators, such as the SARRP, have demonstrated a reduction in radiation toxicity similar to that observed in synchrotron MRT/MBRT [16,18]. However, further work is necessary in order to develop increasingly cost-effective, portable microbeam

collimators suitable for widespread application with these sources. Such an accomplishment would assist in facilitating increased adoption of MRT research outside of highly specialized facilities and is a primary motivator for this work. In the present study, a systematic Monte Carlo investigation allowed the determination of the relative importance of various beam (SARRP) and collimator (MSC) parameters.

3.4.1 Focal spot

In the context of applying conventional sources to MRT research, it is particularly interesting to examine the impact that changing the focal spot size has on system performance. For the simulated cases, the SFS offered a noticeable improvement in the PVDR, albeit at the cost of reducing the dose rate (Figures 3.3 and 3.4). The LFS microbeam profiles featured larger geometric penumbra when compared with those of the SFS due to the greater discrepancy in focal spot and aperture size. A consequent increase in profile overlap (Figure 3.3) directly affected the valley dose and served as a major factor effecting the observed decrease in PVDR (Figure 3.5).

The obvious variation in dose rate resulted from the differences in permissible tube current, which is limited to 2.9 mA for the SFS at 220 kVp, due to the reduced heat loading of the anode, and 13 mA for the LFS. For work done in vivo, the benefit of improving the PVDR with the SFS must therefore be weighed against the reduction in peak dose that could reasonably be delivered within anesthetic guidelines. Potential detriment to cell cultures held outside of incubation in vitro may also be a point of concern in radiobiological contexts. Naturally, these concerns are case dependent - certain CNS targets, for example, may be insensitive to longer treatments when the targets are effectively localized - and the dose requirements for ablation may change based on various other delivery parameters and their corresponding impact on the PVDR. In this respect, the selection of source focal spot size should be motivated in part by the maximum achievable PVDR, the peak dose requirement and limitations to treatment duration.

Interestingly, use of the SFS was found to reduce the system's sensitivity to changes in CSD. Furthermore, the difference between LFS and SFS PVDR values increased with depth in water. These observations might be explained by the fact that LFS microbeam overlap increases substantially with distance from the source, whereas the SFS microbeams remain sufficiently separated, even at larger CSD. Such a reduction in sensitivity offers an important advantage for the SFS and also provides justification for its use when larger CSDs are required or inter-fraction setup error is of particular concern.

These observations highlight the importance of the inter-(micro)beam spacing, or, more generally, the relative size of slits and their adjacent septa. Ideally, such parameters would be optimized with respect to the beam energy, focal spot size and treatment SSD, as required by the therapeutic application.

For all SFS configurations, the PVDR appeared to plateau for depths between 1.50 and 2.55 cm.

This contrasts with LFS irradiations where the PVDR was found to decrease monotonically to a depth of ∼2.0 cm before beginning to plateau, in alignment with the results of Bazyar *et al.* (2017) [18]. At 1-cm CSD, the PVDR difference between the LFS and SFS data sets increases from 10% at the surface to over 72% at depths below 2.5 cm. The PVDR differential increased noticeably at 3-cm CSD. This trend was corroborated for a range of slit widths (Figure 3.7), discussed below, and cross-verified for cases using various collimator thicknesses and CSDs.

3.4.2 Beam energy

Another source-specific parameter of interest was the energy of the primary beam and its associated spectrum. It is imperative that the chosen peak energy provides sufficient penetrating power without compromising the overall dose distribution. For the kilovoltage sources in question, Compton interactions predominate in water and soft tissue; as such, the valley doses mainly derive from Compton scattered photons. This assumes, of course, that the primary spectrum is of sufficiently low energy to ensure that the secondary (Compton) electrons are unable to deposit substantial dose outside of the microbeam path. For the lowest-energy primaries, however, photoelectric absorption becomes increasingly important and the ejected photoelectrons, which boast higher energies when compared to their Compton counterparts, begin to contribute significantly to the dose to media. As such, optimization of the beam energy for small animal irradiators is an interesting subject, especially as the energy spectra are broad in comparison with many of the synchrotron beams used traditionally.

In order to determine how beam energy would affect the PVDR, three candidate tube voltages were simulated. The 220 kVp therapy beam was directly compared with the 80 and 40 kVp imaging beams using the small focal spot (Figure 3.6) and nominal 100 µm air slits. While the imaging beams have a larger, albeit non-dominant, photoelectric component, the majority of secondary electrons still do not contribute significantly to the valley dose. For the 220 kVp beam, on the other hand, the CSDA range in water for electrons at or above the mean energy (78.4 keV) begins to approach the approximate beam width of approximately 100 µm [76]. Nevertheless, use of the 220 kVp beam yielded an increase in PVDR when compared with the lower beam energies. This might be explained by the reduced photoelectric contribution and lower average energy of Compton-derived electrons, which results in a much lower mean energy for the secondary electron spectrum. In a worst case, even with the most energetic 220 keV photons, only 20% of the incident photon energy (44 keV), on average, would be given to the Compton electron and this fraction decreases for lower photon energies [68]. Thus, for a photon with the 78.4 keV mean energy of the 220 kVp beam, even should 20% of its energy (i.e. 15.7 keV) be provided to the electron, the CSDA range would remain on the order of micrometers. This contrasts with the photoelectrons generated at mean energies for the 40 and 80 kVp beams (41.2 and 27.1 keV), which boast CSDA ranges (≈15 and 31 µm, respectively) large enough to carry them across a non-negligible percentage of the total profile width for the slit sizes under consideration [76].

The 220 kVp therapy beam was found to maximize beam output while using the SFS (Table 3.1), which is unsurprising owing to the improved bremsstrahlung efficiency at higher photon energy. On the other hand, the 40 and 80 kVp beams offered greater output efficiency when collimated (a higher ROF). Interestingly, inclusion of the MSC with the lower energy beams increased the depth dose drop-off (Figure 3.6b); this may be a result of a reduced scatter contribution from valley regions contiguous to each microbeam. As an example of the dose rate implications, the maximum achievable doses at 3-cm CSD, assuming a 1 hour limit for gaseous anesthesia, would be 13.7, 25.2, 33.1 and 91.8 Gy for the 40, 80, 220 kVp (SFS) and 220 kVp (LFS) beams, respectively.

Owing to its superior PVDR and dose rate, the 220 kVp beam was used as the primary source candidate in the optimization of various other source and MSC parameters. The result that a higher beam energy, at least compared to what is typically employed (i.e. ∼100 keV), might prove optimal in MRT is consistent with the results of previous energy optimization studies that observed an optimal spectral energy of 375 keV; although that result was established using an MBRT-enabled synchrotron source with a different beam quality [168].

3.4.3 Slit width, CSD and collimator thickness

In order to visually ascertain the effects that changing slit width has on system performance, surface and contour PVDR plots were employed (Figure 3.7). Such figures helped in defining regions where changes to slit width are critical and where compromises might otherwise be made to determine reasonable manufacturing tolerances within which the PVDR could be conditionally maximized.

The results demonstrated that the LFS was largely insensitive to changes in slit width and so the CSD became a much more important optimization target. By contrast, the SFS configurations displayed a strong dependence on both slit width and the depth (in water) at which the data was probed. It is interesting to note, however, that using the SFS together with a larger slit size (i.e. 150–200 µm) resulted in increased contour verticality (Figure 3.7f, h). This would suggest that there is lesser detriment to the PVDR in that domain.

While the SFS was largely independent of CSD, in agreement with results derived previously (Figure 3.5), the LFS PVDR was lower and appeared to degrade more quickly at 3-cm CSD than it did at 1 cm. This would seem to imply that, for large CSD, LFS treatments might suffer from a more pronounced reduction in normal tissue sparing at depth, which would be relevant for non-superficial tumors sites.

The stated results bare some useful implications for MSC design considerations. Most notably, they indicate that there may be some flexibility with manufacturing tolerances in select domains, but when applying the SFS, at least, minimization of the slit width remains an important optimization goal. In the case of the LFS, minimizing the slit width yields a less substantial performance gain, which appeared negligible at larger (3 cm) CSD (Figure 3.7c, d). Finally, in situations demanding the use of larger slit sizes, the PVDR gains afforded by using the SFS are reduced and use of the

LFS becomes more attractive to leverage the substantial increase in dose rate.

Collimator thickness was considered simultaneously with the abovementioned slit width simulation study using the 220 kVp beam and both focal spot sizes. For each of the 1.5-,2.5- and 3.0-cm thick collimators, the PVDR varied subtly at the phantom surface and the results otherwise overlapped within the range of the estimated uncertainties. At larger CSD the influence of collimator thickness became even less evident. For the SFS, a weak trend existed to suggest that a thicker collimator could allow a slight improvement in surface PVDR (<8%). In the case of the LFS a comparable improvement in PVDR (<9%) was found when utilizing the shortest collimator. This inverse trend between the two focal spot sizes was somewhat unexpected and the significance remains uncertain in light of the magnitude of the absolute PVDR difference being on the order of the aggregate uncertainty.

From an optimization standpoint, at least, modification of the collimator thickness is not critical when compared with other, more sensitive parameters. However, when using the LFS, an increase in dose rate did manifest when using the shorter (1.5, 2.5 cm) collimators; this difference was particularly obvious at shorter CSD. As this improvement in dose rate is paired with a slight increase in PVDR at the phantom surface, a shorter collimator options would appear optimal in the context of using the LFS. This assumes, of course, that the MSC remains sufficiently thick to block x-rays of the highest energy present in the source spectrum.

Generally speaking, the slit width is a critical parameter in the context of MRT research as it directly governs the resultant microbeam size. While smaller slits are typically considered ideal insofar as PVDR maximization and biological response is concerned, they are also much more difficult to produce, even more so when tight manufacturing tolerances are imposed. The fabrication process is complicated further when using divergent sources, such as the SARRP, as the collimator slits must then be focused to appropriately compensate and still produce a regular array of dose peaks. As such the development of an affordable MSC is inextricably dependent on the ability to either reproducibly and affordably develop micro-slit apertures in high-Z metals or to increase the design tolerances such that compromises can be made that simplify construction without a large detriment to performance.

3.4.4 Slit material

As a means to enable the affordable construction of a divergent MSC, the feasibility of using plastic spacer materials was investigated. The proposed design includes a brass or tungsten frame, fitted within the SARRP nozzle, and allows for improved modularity by sandwiching the spacers between tungsten sheets (septa). To this end, a simulated collimator geometry had its vacated (air) apertures replaced with one of two candidate plastic materials: polypropylene (PP) or polyethylene terephthalate (PET).

PP is a widely-utilized, low-density polymer and PET is a common polyester most notable for its role as the film base in pressure-sensitive tapes. Both polymers were selected for their widespread

application and range of densities. While PP is comprised of simple hydrocarbon monomer chains, PET boasts heavier, oxygen bearing molecular units and is 46% denser by mass.

Comparison of the selected spacer materials revealed a surprising, modestly improved response, albeit at significant cost to the dose rate (Figure 3.8). Specifically, a slight increase in PVDR was observed when using PP or PET at each sampled depth (Figure 3.8b). Such an effect might be attributable to the slight beam hardening that occurs as the beam passes through the material filled slits. Based on this result, use of the low-density spacers appears feasible and may provide a novel means of subtly improving the PVDR while simultaneously supporting the proposed method for MSC fabrication.

Unfortunately, use of either material type reduced the fluence substantially. For PP and PET the output relative to air was reduced by approximately 37% and 47%, respectively. Evidently, PP afforded slightly higher dose rate, largely due to its lower mass density to which the dominant Compton interaction cross-section is proportional, and for that reason it may be considered slightly preferable. Based on these results, it is obvious that using any material spacer will decrease the maximum deliverable MRT dose in vivo; practical countermeasures might include using the LFS to partially offset the peak dose limitation. While the system would suffer a consequent reduction in PVDR, the decreased sensitivity to slit width could also lead to simplifications during production by enabling the use of larger slits.

3D printing has been proposed as a favorable means for spacer fabrication as it would allow for simplified part customization and reduced lead times. Additionally, the desired slit divergence could be achieved by having the spacers themselves printed with a subtle gradient along the beam direction. The added modularity would help improve MSC configurability and remove the need to commit the finely manufactured septa in a single prototype, thereby reducing the financial risk and total cost of production.

Suitable printing modalities have been identified, and one of stereolithographic (SLA) or material jetting are recommended for their ability to produce highly accurate features with superior z-resolution (layer height), on the order of 25 µm. Such fine resolution is necessary to produce the subtle gradients that ultimately create a divergent slit arrangement. Naturally, the choice of technology in this context constrains the available selection of simulated plastics.

The selection of PP in this study was partly motivated by the availability of photopolymer materials applicable to the above-mentioned print modalities. While the exact composition and physical properties of 3D printable analogues would not be identical to those of the polymers simulated here, the densities do fall within the range considered (ρ = 0.95–1.3 g cm^{-3}). Interestingly, using PET, with its moderately (46%) increased material density, resulted in negligible differences to the PVDR and only a 10% reduction in dose rate over the low-density (PP) alternative. Therefore, while a range of 3D printable spacer materials might be expected to reduce the primary fluence, relative to one another the changes in performance are unlikely to be substantial. This outcome would imply that

plastic spacer materials might be chosen based on the desired manufacturing (i.e. print) modality and, perhaps secondarily, on a set of desirable physical properties.

3.4.5 Parallel-slit collimator experiment

The effectiveness of a simple steel, parallel-slit collimator was evaluated to determine the feasibility of MRT delivery on the SARRP as well as provide a preliminary test of the reliability of the validated MC model used in this simulation study.

Irregularities within the MRT film data (Figure 3.9a) may have resulted from a number of entangled factors, including the influence of slit malleability and an uncertain setup configuration. In particular, collimator deformation and tilt within the nozzle, which occurred post-insertion, could not be constrained in our setup and were thus unaccounted for in the MC models. Moreover, as the dimensions of the parallel-slit collimator were not explicitly known during irradiation, it was not possible to perfectly model the MSC. Factors such as these inevitably limit our ability to reconcile differences between the film and MC data sets. Additionally, notable asymmetry had been observed within our 2D film dose distributions (Figure 3.10a) which clearly manifested in the corresponding lateral dose profiles (Figure 3.10c). This effect was not reflected in the MC source model (Figure 10b), which might also account for some of the discrepancy between the MC and experimental results (see Figure 3.9a). For future validation, it will be important to reconcile or at least account for these differences, which we believe may derive from a sensitivity of the distribution to how accurately the focal spot geometry was modelled.

Fortunately, the experimental and MC results were found to agree reasonably well for the maximum intensity peak; the mean valley doses, on the other hand, differed by a factor of 2.7. Qualitative agreement was found between the film and MC profiles, most notably with respect to the relative peak positions. The expected peak and neighboring valley regions were clearly visible in the film data and normalized PDDs demonstrated the expected behavior when compared with MC results, which were everywhere consistent. It is worth noting that the measured valley doses were near the $\sim 10\,\mathrm{cGy}$ lower limit for the film's sensitive dose range and, as such, the confidence in the measured dose data is limited. Longer exposures would be required to achieve more reliable valley, and thus PVDR, results, by ensuring all doses remain well above the film sensitivity threshold.

Our observations underscore the need for a more reliable, rigid and reproducible collimator in future validation efforts on the SARRP system, and has motivated ongoing work in the development of informed collimator designs. Future planned MSC prototypes will benefit from known slit dimensions, tight manufacturing tolerances, and a rigid design that mitigates deformation and tilting of the collimator within the nozzle. Despite the discrepancy between the preliminary experimental and MC results, the work to date serves to indicate the ease with which a small focal spot, broad beam source from a conventional small animal irradiator can be spatially fractionated and provides a foundation for the dosimetric evaluation of future, improved MRT experiments on the SARRP.

3.5 Conclusions

Based on the results of this study, use of the SARRP's 220 kVp therapy beam at a short (i.e. 1 cm) collimator-to-surface distance (CSD) along with the small focal spot (SFS) and minimized slit width proved optimal in terms of maximizing the PVDR. However, the work also highlighted the conditional use of sub-optimal settings, such as the large focal spot (LFS), and design compromises that may help in manufacturing a more cost-effective multi-slit collimator (MSC). For example, while the LFS was found to decrease the PVDR at all depths it also afforded a significant increase in dose rate; moreover, LFS configurations were much less sensitive to changes in slit width when compared to their SFS counterparts. Therefore, in situations where design constraints demand the use of larger slit widths, it becomes increasingly advantageous to employ the LFS to reduce the overall treatment time or enable greater dose escalation. On the other hand, if setup variability or large CSDs are encountered then the SFS should prove more effective, assuming the dose rate remains reasonable, since the SFS configurations appeared less sensitive to changes in CSD. In all cases, however, minimizing the CSD whenever possible will maximize the dose rate and reduce the degree of PVDR degradation resulting from gradual broadening in the microbeam penumbra.

In order to realize a more cost-effective modular MSC design, polypropylene and polyethylene terephthalate were investigated as potential spacer material candidates. Both spacer types reduced the dose rate substantially, but also effected a marginal improvement in PVDR when compared with the air slit configuration. These facts underline the feasibility of using an alternating septal-spacer arrangement in place of solid attenuators with micro-machined apertures. Such a configuration may be paired with the LFS to partly compensate for the beam attenuation within the spacer material itself. Prototypes of this nature would improve production lead times and affordability, potentially costing less than $1000 if a modular configuration can be maintained.

The simulation study presented here has provided quantitative insight that is being used to inform the development of a new, cost-effective MSC capable of reliably delivering MRT on the SARRP. Preliminary experimental results have re-affirmed the challenges of producing a regular array of microbeams and underscore the need for a more precise, divergent collimator before reliable MRT treatments are delivered for future validation work. Second-generation divergent MSCs will leverage a novel, modular design concept able to facilitate efficient and inexpensive modification based on experimental feedback.

3.6 Follow-up: Prototype fabrication and SFRT proof-of-concept

The MC simulation study presented in this chapter served as a basis for verifying reasonably effective dimensions and properties of the proposed divergent MSC, however the initial MRT experiment was completed using only a simple parallel slit (steel septa) collimator, able to fit within the SARRP $1 \times 1\,\text{cm}^2$ treatment nozzle (Figure 3.11).

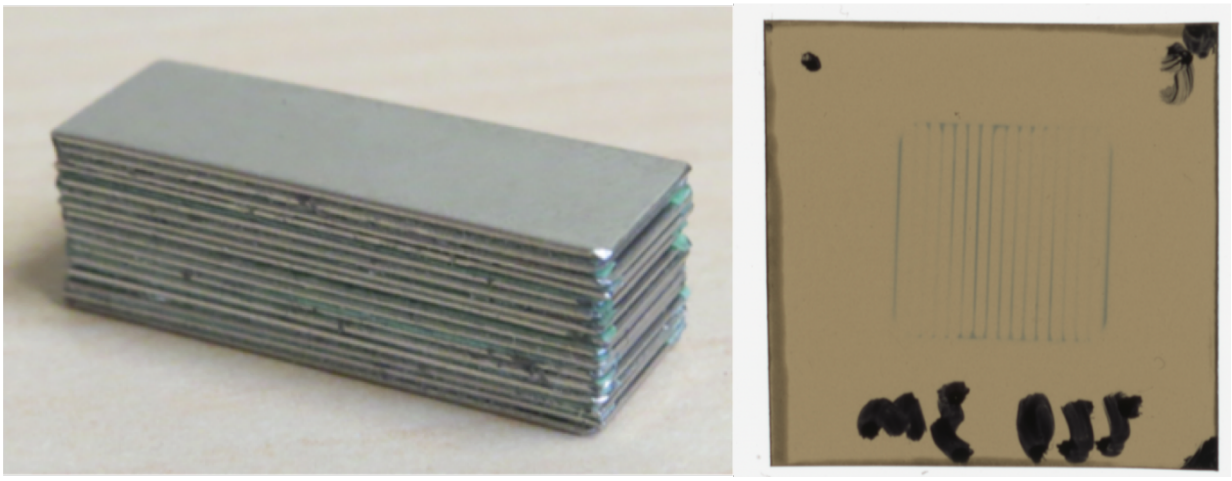

Figure 3.11: A photograph of the initial parallel-slit, steel MSC prototype (left), including installation on the SARRP (inset), and the resulting film for a 3 min irradiation at 220 kV, 2.9 mA, using the small focal spot is also shown (right).[2]

The preliminary results (see Figure 3.9) re-affirmed the difficulties of producing a regular array of microbeams and underscored the need for a more precise, divergent collimator before reliable MRT treatments could be delivered on the SARRP. Particular difficulties were observed in operating within the films less sensitive dose range. Fortunately, the microbeam peak and adjacent valley regions were clearly visible and the normalized PDDs (Figure 3.9b) demonstrated the expected depth-dose behavior. Unsurprisingly ,the PVDR values were highly discrepant as a result of the relatively poor valley-dose agreement between film and MC results. For reference, a difference of as little as ±3 cGy in valley dose was sufficient to change the calculated PVDR by up to a factor of 2. Such observations were strong motivators for developing a more reliable MSC prototype.

In follow up to this body of work, and to facilitate MRT/MBRT on commercial SARRP systems, a portable, cost-effective and modular MSC was fabricated (Figure 3.12). This was accomplished using micro-machining technologies readily available through the Department of Physics and Astronomy Machine Shop at UVic. Rather than leveraging 3D printed spacers, as previously proposed, the design instead comprised two Delrin® (polyoxymethylene) plastic frames with arrays of slits that were capable of accommodating N=15 tungsten septa (300 µm ± 10%). The design of the collimator was informed through the MC optimization work (Section 3.3.1) and the above-mentioned experiments using a parallel-slit MSC prototype [31]. This second-generation MSC comprised 15 mm long tungsten septa in a divergent array and functioned to produce an array of up to 16x200-µm microbeams, separated 500 µm on-center, and may be mounted directly onto the SARRP gantry/nozzle assembly.

A brief characterization of the MSC prototype, capable of fitting within the stock SARRP treatment nozzle, was completed (Figure 3.13). Film irradiations were performed in a 6 cm^3 solid water phantom at 31 cm SSD (i.e. 1 cm CSD). The SARRP 220 kVp, large focal spot (IEC366: 3.0 mm) therapy beam, operating at maximum tube current (13 mA), and with 0.15 mm of added Cu filtration

[2]Steel collimator prototype by Lila Chergui

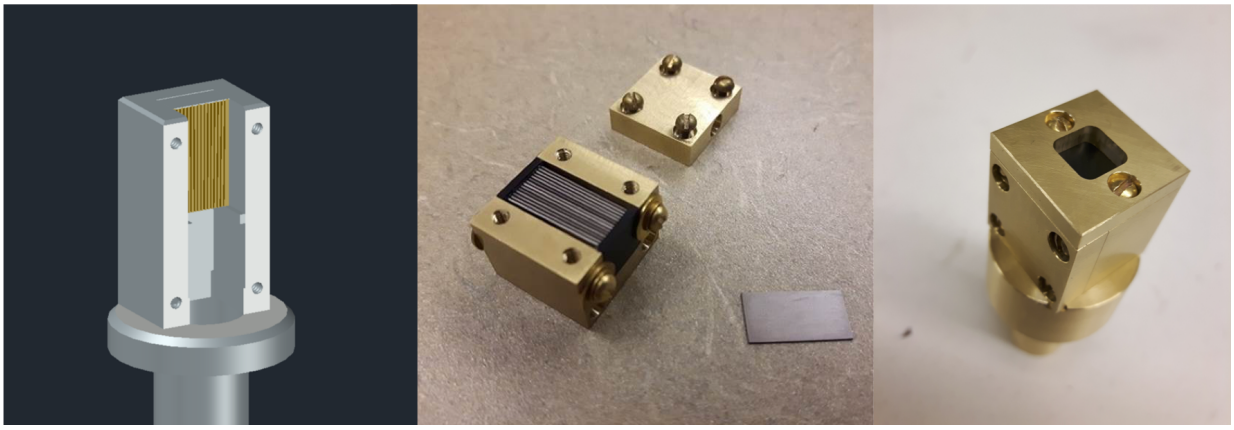

Figure 3.12: CAD model (left) for the theoretical design of a first Tungsten-Air MSC prototype. The pre- and post-assembled prototype MSC is shown in the center and right-hand panels, respectively. The collimator is comprised of 16x 200 µm (air) slits, with 300 µm tungsten septa and supported on either end by a total of 2 mm of Delrin® plastic.

was employed along with a total irradiation time of 1min. The resulting surface dose profiles (Figure 3.13b) indicated that only 9 of the 15 intended micro-beams manifested. This was attributed to a discrepancy in either beam-slit divergence matching or the distance from the focal spot (source) to the collimator, but additional work would be required to rectify this issue. Nevertheless, profiles taken along the Y-axis illustrates the excellent slit regularity in that direction while the overall profile symmetry points to the accuracy of the construction (Figure 3.13c). While a uniform array of beamlets is desire, the partial coverage of the microbeam array is currently sufficient for radiobiological experiments and does not preclude it usefulness, although validation efforts must wait until the underlying issue is identified. Following this initial characterization of the SARRP MSC, alternative strategies for delivering novel spatially micro-fractionated treatments on the SARRP were investigated using GRID-like collimators to produce 2D-array of beamlets; a comparison study for GRID collimation against the divergent-slit SARRP MSC design is presented in Appendix A.1.

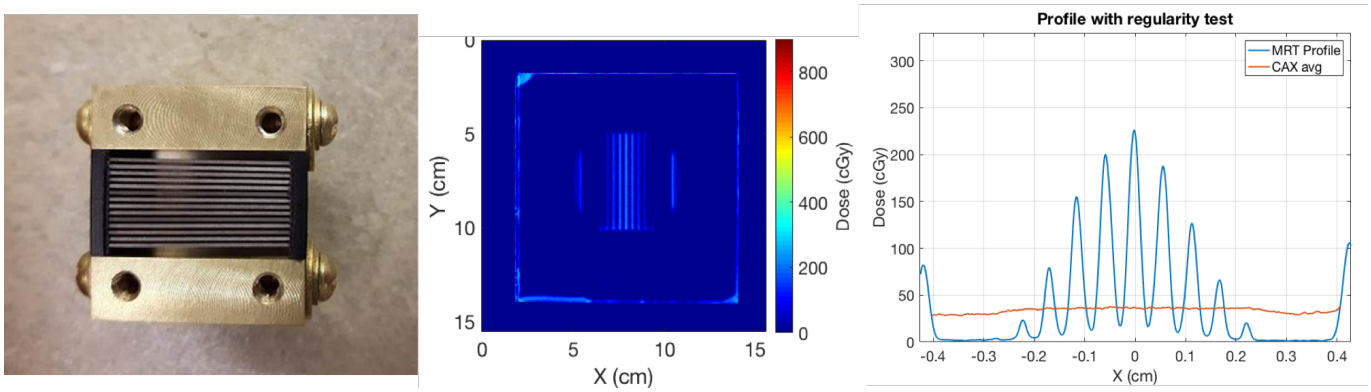

Figure 3.13: Close up of the collimator body (left), including divergent slits in the Delrin® frame. The design was made to be matched to the SARRP beam divergence, but the results of film dosimetry (dose map - center) point to slit divergence being out of tolerance or an erroneous source to collimator distance. The corresponding MRT dose profile, averaged over the full height (Y-axis) of the field, is shown in the right-hand panel.

Chapter 4

Development and validation of 3D-printed mouse phantoms for improved preclinical dosimetry

Manufacturing of a realistic mouse phantom for dosimetry of radiobiology experiments[1]

4.1 Introduction

In the context of small animal radiotherapy and radiobiological research there exists an ongoing demand for standardized, accurate dosimetric practices. Studies have indicated that the dose accuracy in small animal experiments is generally quite poor due, in part, to the small fields and kilovoltage beams that are typically employed [62–64]. Moreover, when dosimetric results are compared across institutions there may be variation derived from differences in measurement technique and available technologies. As such, the ability to fabricate a small-animal phantom that can simulate, as closely as possible, an anatomically-correct mouse model might provide the grounds for more reproducible, cross-institutional measurement procedures and improved dosimetric reliability in pre-treatment verification.

One means of reliably fabricating highly-customizable and specialized phantom geometries has emerged via 3D printing, a cost-effective form of additive manufacturing. Various 3D printing modalities have previously been evaluated for use in the context of radiotherapy and diagnostic imaging [169–171]. Of these, material jetting is found to provide a number of desirable properties well suited to the development of a small, detailed, anatomically-accurate and highly uniform small-animal phantom. Specifically, the technology features the highest available feature resolution and the ability to print a solid model using multiple materials within a single job. Multi-material 3D printing is particularly novel for the reason that it can enable the incorporation of heterogeneities to represent realistic anatomical structures and allow for a modular construction [148, 150]. The high degree of material uniformity and the ability to simulate, at least structurally, highly accurate anatomy should prove useful for radiobiological experiments with potential application to imaging experiments.

Small field dosimetry on commercial small animal irradiators is typically reliant upon two detector

[1] This work was published as a Technical Note in *Medical Physics* [66]. All authors contributed equally to this work.

types – radiochromic films, commonly used for commissioning of conformal small animal irradiators, and small volume dosimeters [61, 172–174]. In order to perform reliable dosimetry, modifications to the design of a 3D printed phantom, in the form of custom apertures, may be used to accommodate any variety of small-field portable dosimeters, including TLD/OSLDs, scintillating detectors, and diamond or pinpoint ion chambers. For the purposes of this study, modifications have been made to accommodate both radiochromic film and a 1-mm plastic scintillator dosimeter (PSD) [166].

To date, mouse phantoms have been conceived for use in optical imaging [175–177] applications and dosimetry with megavoltage sources [178]. However, these phantoms have either been simplistic in their geometry (i.e. cylindrical) or based on a non-realistic anatomy. More recently, groups have found success creating anatomically-accurate mouse phantoms for improved quality assurance in small-animal imaging and therapeutic applications. Welch *et al.* [179, 180] and Wu *et al.* [181] accomplished this by using materials that closely mimicked the physical properties of the corresponding anatomy and precise micro-machining techniques; unfortunately, the proposed methodology remained laborious and costly. Bache *et al.* [182], on the other hand, used comparatively affordable 3D printed molds, based on rat CT data, to form a homogeneous, tissue-equivalent 3D dosimeter out of radiochromic Presage® material with dose readout accomplished via optical-CT. Zhang *et al.* [183] similarly utilized 3D printing to generate accurate bony and superficial (skin shell) anatomy to enable the construction of a heterogeneous mouse phantom compatible with CT, MRI and PET imaging. However, their modular approach required the manual alignment of the printed anatomy in post-production and the use of a synthesized molten hydrogel filler. The present work is thus concerned with the design and fabrication of a realistic, heterogeneous mouse phantom for pre-clinical dosimetry through the exclusive use of multi-material 3D printing technology. It is hoped that the model presented here will help to lay the foundation for more consistent dosimetry by providing a common, cost-effective means of production and a design that may be easily modified and printed by various institutions.

4.2 Materials and Methods

The flowchart of the phantom design process is depicted in Figure 4.1 and will be described in detail in the following sections.

4.2.1 Mouse microCT scanning and organ segmentation

A 32-g anesthetized mouse was scanned in the Small Animal Radiation Research Platform (SARRP, Xstrahl, Surrey, UK). The SARRP standard imaging protocol was applied, which employs a 60 kVp tube voltage, 1.2 mA tube current and a 2-minute imaging time set to acquire 6 frames per second (fps). Images were reconstructed with a voxel size of $(275 \times 275 \times 275)$ µm.

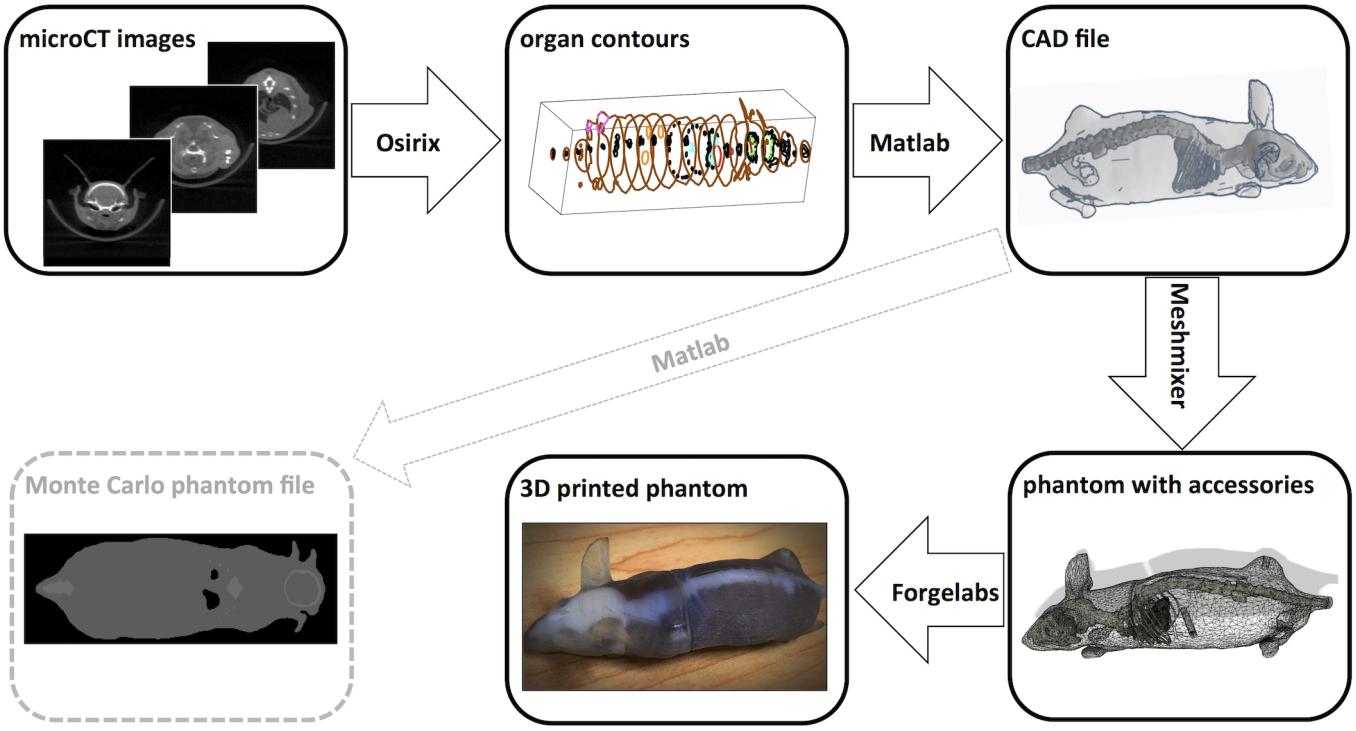

Figure 4.1: Flowchart of phantom design process.

4.2.2 Mouse phantom design

Osirix™ (Pixmeo SARL, Bernex, Switzerland) was used to segment the relevant mouse anatomy using the microCT data. The resulting CSV files were then converted into STL files using a MATLAB® (Mathworks, Nattick, MA) script. The brain, skull, spine, ribs and lung were separately contoured to enable appropriate organ delineation and material specification. Various computer-aided design (CAD) software packages were subsequently used to modify and improve upon the original, contour-derived mouse model. Blender™ (Blender Foundation, Amsterdam, NL) was used refine the geometry mesh so as to allow for improved feature resolution, and thus anatomical accuracy, prior to fabrication. To allow for lung excavation, the phantom model was split into two parts, through the middle of the lungs, using Fusion360™ (Autodesk, San Rafael, CA). Two pegs were additionally added to accommodate the placement of a laser-cut EBT3 Gafchromic® film (Ashland, Bridgewater, NJ) and three 1-mm diameter cavities were included to enable insertion of the PSD. The cavities were located in each of the brain, abdomen and flank subcutaneous tumor and, when not in use, could be plugged with the same material comprising the bulk of the phantom. Lastly, Netfabb™ (Autodesk, San Rafael, CA) was used to ensure the final STL file geometries were watertight for printing. The resulting mouse phantom had dimensions of $(31.95 \times 26.23 \times 98.03)$ mm with a subcutaneous flank tumor $\approx 1\,\text{cm}$ in diameter.

4.2.3 3D printing

The mouse phantom was printed using a Stratasys (Eden Prairie, MN) Connex3 260 Polyjet™ 3D printer at Forge Labs (Vancouver, BC, Canada). The selected 3D printing materials, along with their associated densities and colors, are summarized in Table 4.1. The body and bone were comprised of low-density photopolymer materials selected to best simulate polymethyl methacrylate (PMMA). The lung, designed as a void within the original CAD model, is necessarily filled with support material that must then be excavated; the resulting space may be optionally replaced with cork or, as in our case, polystyrene (PS) to better approximate lung tissue. It should be noted that the printed skeletal structures are not dosimetrically representative of real bone tissue, but were included to facilitate improved setup reproducibility and feature localization by providing radiological contrast, with appropriate window-level settings, in pre-treatment microCT scans. The total cost for commercial phantom printing was $190, which could be greatly reduced if printed in-house.

Table 4.1: Materials and their mass densities and colors used for 3D printing.

Organ	Phantom material	Mass density	Color
Body	VeroClear™ (RGD720)	$1.18\,\mathrm{g/cm^3}$	Translucent
Lung	Support material (to be excavated)	$1.25\,\mathrm{g/cm^3}$	Black
Bone	Rigur™ (RGD450)	$1.20\,\mathrm{g/cm^3}$	White

4.2.4 Phantom evaluation

The quality of the 3D printed phantom and the uniformity its material constituents were evaluated by microCT scanning. The phantom was scanned on the SARRP with the standard imaging protocol, as described previously, with the scan time increased to 4 minutes. Additionally, a QA phantom containing five materials of known densities ranging from $0.00124\,\mathrm{g/cm^3}$ (air) to $1.82\,\mathrm{g/cm^3}$ (bone equivalent material) was scanned with the same protocol and a CT number to mass density calibration curve was calculated. The mouse phantom was analyzed for uniformity and the mass density of each material was evaluated.

4.2.5 Monte Carlo dose calculations

Tissue equivalency of the 3D printed phantom materials, in terms of their use in dose calculations, was evaluated. Monte Carlo (MC) simulations of SARRP treatment dose delivery in the phantom were performed with the EGSnrc/DOSXYZnrc [142, 184] code using a validated MC model of the system [166]. Six MC dose calculations were run in total - for three treatment sites (brain, abdomen, and the subcutaneous tumor) and two tissue classification cases (the 3D-printed PMMA phantom and real mouse tissues). The dose delivered with the SARRP's 220-kVp treatment beam and $3 \times 3\,\mathrm{mm}$

Table 4.2: Summary of physical properties for the simulated mouse tissue and phantom material.

	Mouse Simulation			**Phantom Simulation**		
Organ	Tissue Type	$(Z_{eff})_{sw}$ $[(Z_{eff})_m]$	Mass density ($g\,cm^{-3}$)	Simulated As	$(Z_{eff})_{sw}$ $[(Z_{eff})_m]$	Mass density ($g\,cm^{-3}$)
Body	ICRU-44 Soft tissue	3.81 [3.61]	1.06	PMMA ($C_5O_2H_8$)	3.83 [3.71]	1.18
Lung	ICRU-44 Lung	3.82 [3.61]	0.58	Polystyrene (C_8H_8)	3.64 [3.56]	0.32
Bone	ICRP-23 Bone (Averaged)	5.96 [5.31]	1.60	PMMA ($C_5O_2H_8$)	3.83 [3.71]	1.20

nozzle was calculated for a brain target using a 360°arc at the location of the brain PSD. Dose delivered using the 5×5 mm nozzle was calculated for an abdominal target with three equally spaced coplanar beams at the location of the EBT3 film. Two parallel opposed 5×5 mm beams were used for the treatment of a subcutaneous tumor at the location of the tumor PSD.

The STL file for the printed mouse was converted into a DOSXYZnrc *.egsphant* phantom file using MATLAB. The EBT3 film layer as well as the PSD were modeled as water under the assumption that both dosimeters will be calibrated to measure dose in water. The dose calculation grid was comprised of $(200 \times 200 \times 200)$-µm voxels and the body and bone materials were simulated as PMMA with their respective mass densities (Table 4.1). The lungs were modeled as polystyrene with an averaged mass density of $0.32\,g/cm^3$, determined via microCT scans of the phantom. To subsequently evaluate dose delivery to a real mouse, the phantom materials were replaced by mouse tissues with appropriate densities derived from our previous work [166]. Furthermore, the bony anatomy was modeled as a single, averaged bone tissue (ribs, spine, and cranium). Table 4.2 summarizes the mass densities and effective atomic numbers (Z_{eff}) for these various simulated materials. Energy-dependent Z_{eff} values were determined using the Auto-Zeff software and the methods of Taylor *et al.* [185] were applied to calculate a spectrum-weighted average $(Z_{eff})_{sw}$ along with the value at the spectral mean energy (81 keV) for the SARRP's 220-kVp beam $(Z_{eff})_m$. A lower-than-expected Z_{eff} value for PMMA, and the similarity to soft tissue, is in our case a product of the large energy dependence of Z_{eff} at low energy and the specific energy fluence spectrum of our source. Note, however, that similar Z_{eff} values here point to the similar attenuation, but not necessarily dose deposition, properties of the materials.

All processes relevant for low-energy photon interactions were included in the simulations and kinetic energy cutoff was set to 10 keV for both photons and electrons. Dose calculation statistical uncertainty in high dose regions did not exceed 1.5%.

4.3 Results

4.3.1 Phantom quality

The microCT scan of the 3D-printed mouse phantom revealed excellent uniformity of the body material. No regions were found to contain unwanted air cavities or high-density inclusions, as might be observed in solid water phantoms. Based on scans of a calibration phantom, the mean mass density of the polystyrene lung was determined to be $0.32\,\mathrm{g/cm^3}$. The mass density of the phantom body and bone material was calculated as $1.18\,\mathrm{g/cm^3}$ and $1.20\,\mathrm{g/cm^3}$, respectively, in agreement with the mass densities provided by the manufacturer.

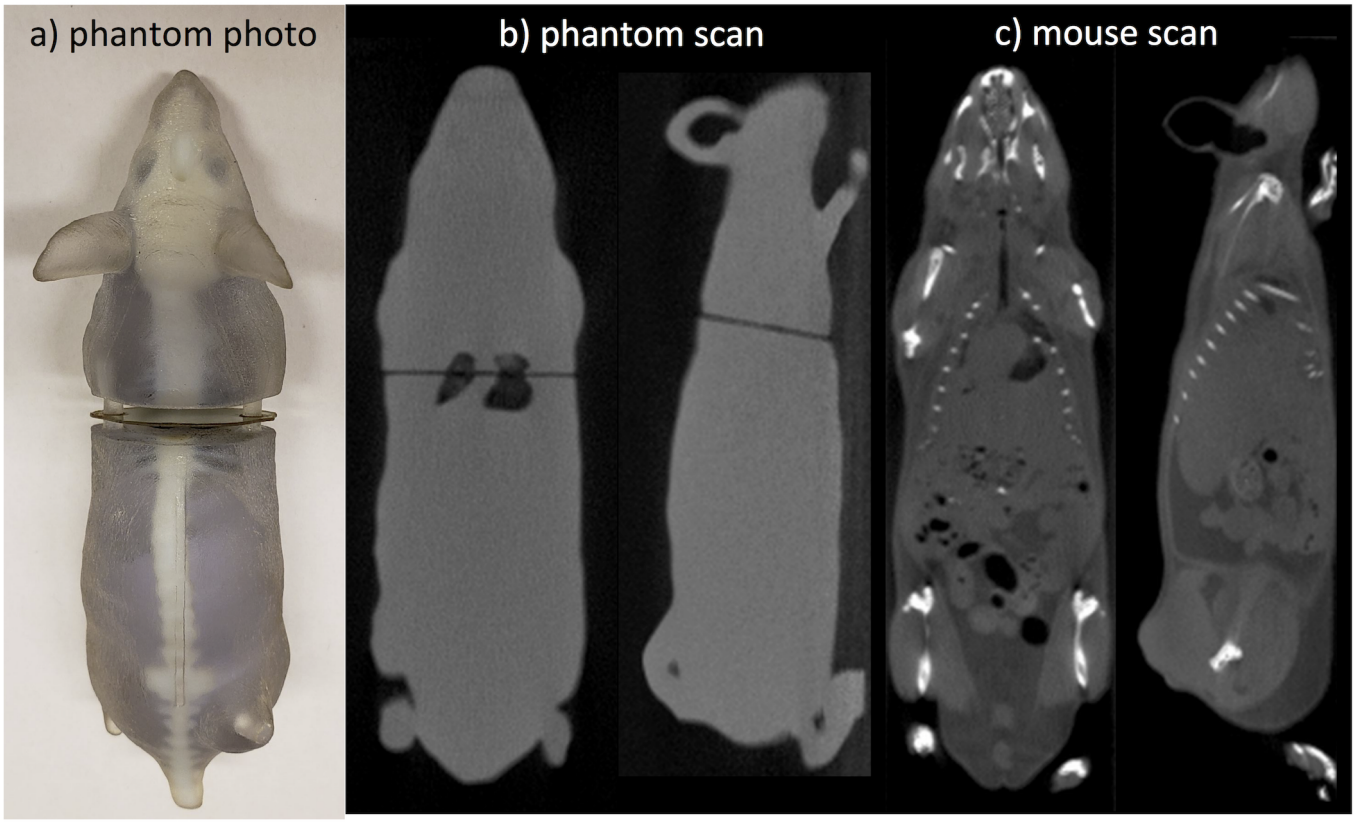

Figure 4.2: Phantom photograph with EBT3 film inserted between the two phantom parts (a) and microCT scans of the phantom (b) and original mouse (c). The air cavity in the subcutaneous tumor is the PSD hole.

4.3.2 MC dose calculations

Dose calculation results for the six investigated MC dose distributions are presented in Figure 4.3. The dose to the PMMA-phantom body was on average 15% lower than the dose to the mouse soft tissue. The brain dose distribution revealed that the dose to the skull was 1.8× higher than the dose to the 3D-printed bone. All dose distributions indicated that the dose to a water-equivalent dosimeter placed in the printed phantom was similar to the dose in mouse soft tissue. The doses to the PSD

and film dosimeters within the PMMA phantom were underestimated with respect to dose to mouse tissue by 5.4%, 3.7%, and 3.2% for the brain, body, and tumor targets, respectively. This 3-5% underestimation is deemed to be an acceptable error assuming the 5% accuracy of radiobiological experiments that is proposed by the AAPM TG-319 task group[2].

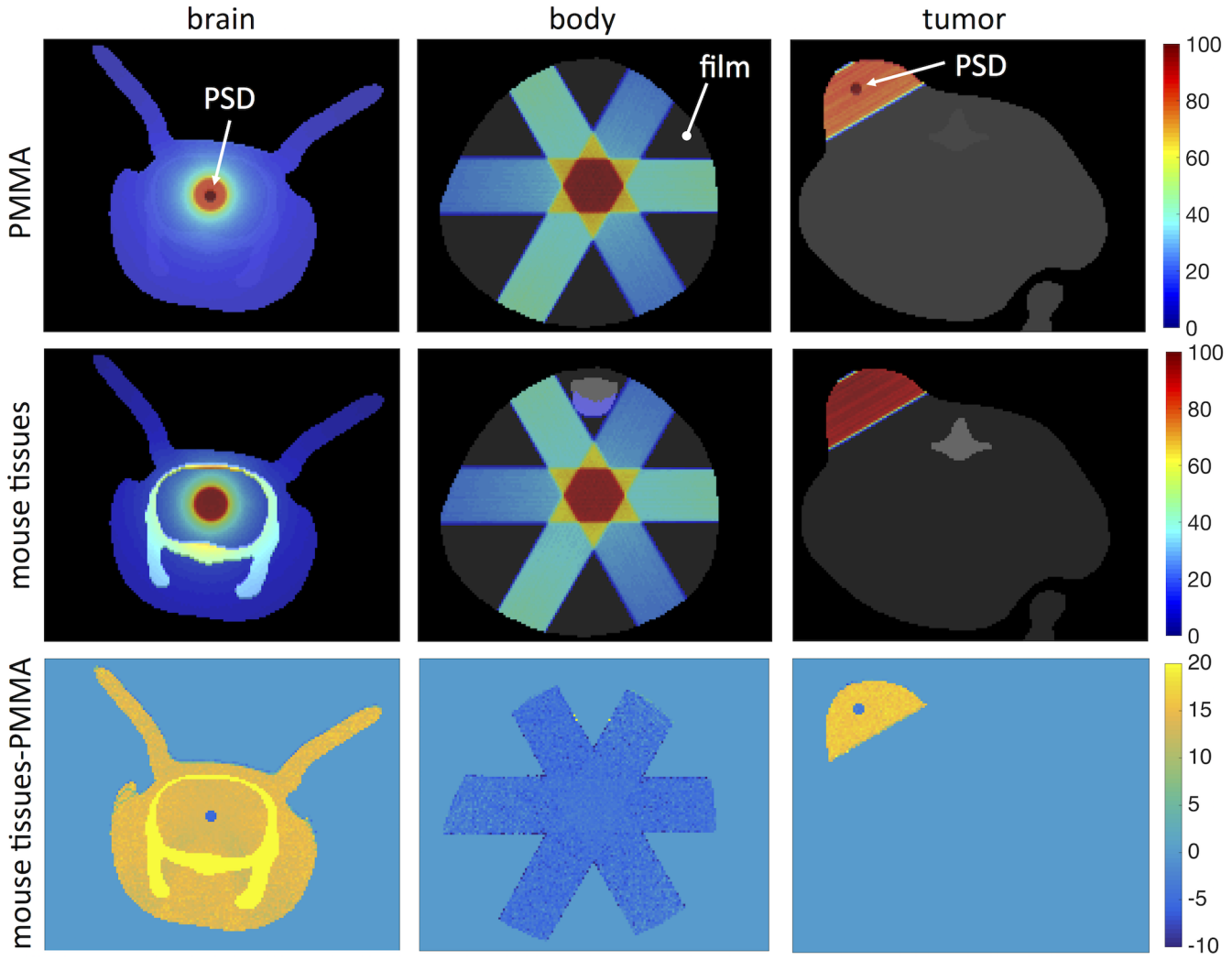

Figure 4.3: MC dose distribution in the PMMA phantom (top row) and in mouse tissue (middle row) for the brain (left column), body in the location of the EBT3 film (middle column), and subcutaneous tumor (right column). Percentage dose differences (tissues – PMMA)/PMMA are shown in the bottom row.

4.4 Discussion

An economical 3D-printed mouse phantom was designed and manufactured with the goal of providing a useful tool for dosimetry in radiobiological experiments. Modifications to the model were made to accommodate reproducible insertion of both radiochromic film and a plastic scintillating detector. Since the phantom was 3D-printed using non-tissue equivalent plastic materials, the expected

[2]Personal Communication. S. Kry (2018)

accuracy of phantom dose measurements with respect to actual doses delivered to small animals was evaluated by means of MC simulations. The PSD and the film were modeled as water in the MC dosimetric evaluation. While these dosimeters are not strictly tissue equivalent, they are commonly calibrated to measure dose to water.

The doses to mouse soft tissue were approximately 15% higher than dose to the phantom material. This was consistent with expectation based on the SARRP 220 kVp energy spectrum-weighted ratio of the mass-energy absorption coefficients for ICRU-44 soft tissue and PMMA and the corresponding value for the beam's mean energy (81 keV), which were calculated to be 1.23 and 1.10 respectively. It is important to note that the increased attenuation in the bone could not be accurately accounted for in the phantom as it did not include bone-mimicking material; for the brain target, specifically, this resulted in an additional 2% dose reduction. However, a cranial target likely presents a worst-case bone-attenuation scenario, in which the beam interacts with the largest thickness of bone found in a mouse body. As such, the overall dosimetric detriment from including the low-density 'bony' (PMMA) anatomy appears tolerable, as evidenced by the small percentage difference in dose delivered to the PSD and film for corresponding target regions of the mouse and PMMA-phantom configurations (Figure 4.3).

Post-fabrication changes to the phantom design can be made by simply altering the requisite CAD (STL) model and re-printing. As such, the model could be modified for increased suitability with imaging experiments. The application of 3D-printing in developing such a mouse phantom was recently demonstrated by Zhang *et al.* [183]. However, their model's material constitution and modular construction method was notably different from ours, requiring post-printing alignment of the component anatomy. The group also used a hydrogel compound and synthesized bone filament in order to more precisely mimic the physical characteristics of mouse tissue. In our phantom, the printed 'bone' material (Table 4.1) was chosen as the highest-density, opaque photopolymer material that was commercially available; this was to ensure that we might visually (Figure 4.2a) and radiologically distinguish the component anatomy (Figure 4.4). While microCT scans confirmed that the printed skeletal material was slightly denser than its transparent, soft-tissue counterpart, it cannot be used to effectively simulate the dosimetric properties of real bone, as noted previously. Furthermore, in the context of the phantom MC simulations, by choosing to omit the PMMA-bony anatomy, we additionally found that there is a negligible difference in the calculated dose between a phantom with or without the printed bone structure. Nevertheless, the inclusion of such distinct anatomy helps to ensure reproducible phantom alignment and pre-treatment setup verification using the SARRP's on-board imaging capabilities.

Future fabrication efforts would naturally benefit from an attempt to more closely replicate bone tissue, possibly by filling skeletal cavities with a suitable mimetic material or using a chemically engineered (printable) resin – methods which were beyond the scope of the present work. In order to maintain the presented methodology, for example, it would be necessary to procure or develop a

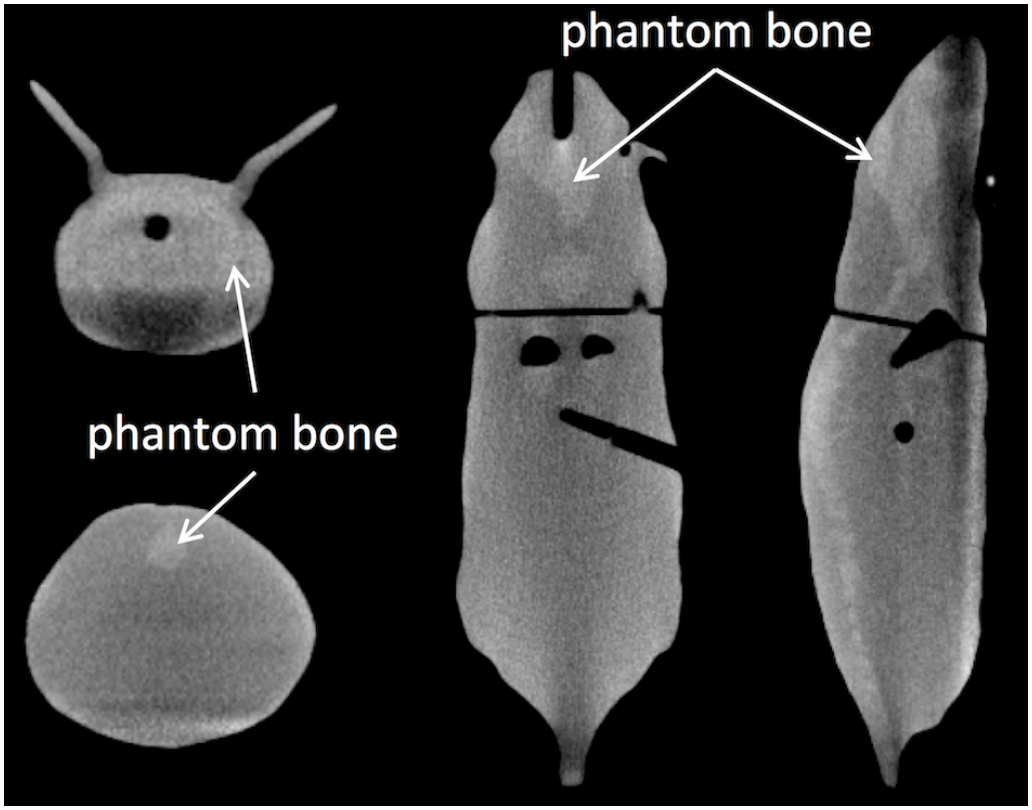

Figure 4.4: Representative microCT image of the printed mouse phantom illustrating the component anatomy made visible with appropriate window-level settings (W/L: 600/330). Such anatomy is used to guide isocentric targeting during on-board pre-treatment imaging. The standard imaging geometry of the SARRP results in a number of beam hardening artifacts that are emphasized when such a narrow window is used.

doped photopolymer filament compatible for use with multi-material 3D printers. In particular, it would be desirable to adopt such a material that boasts a higher mass density and Z_{eff}, the latter being particularly important for low-energy applications, so that we might better represent bone in a realistic small-animal context. On the other hand, a major benefit to the fabrication method utilized in this work is the simplification, cost-effectiveness and ease of adoption of the production modality.

Owing to the convenience of end-to-end construction using commonly available 3D-printing technologies, institutions that adopt the demonstrated methodology could readily share, re-design and re-print any model, including the one presented here. This could potentially help mitigate the chance of cross-institutional variability in dosimetric procedures during treatment verification. Moreover, the anatomical features, print resolution, and selection of available photopolymer materials might be customized to best suit the intended dosimetric application or more effectively simulate a user's specific experimental setup. The determination of optical properties for the printed mouse model might also enable such a phantom to serve as a useful tool in optical and bioluminescence imaging (BLI) research.

4.5 Conclusions

We presented a simple process to manufacture a low-cost 3D printed mouse phantom able to accommodate two types of dosimeters for use in in-vivo radiobiology experiments. Monte Carlo simulations predicted that the dose to water-equivalent dosimeters placed in the brain, middle of the body and a flank subcutaneous tumor would be underestimated by 3-5% compared to the dose delivered to mouse tissues. This phantom can be easily and reproducibly manufactured and may, after careful dosimetric characterization, serve as a valuable tool for dose verification in a range of radiobiology experiments and between independent research groups. Ongoing work is being aimed at the use of radiochromic film and a plastic scintillator dosimeter to validate the phantom and corresponding Monte Carlo model.

Preclinical dose verification using a 3D printed mouse phantom for radiobiology experiments[3]

4.6 Introduction

Dose verification in preclinical radiotherapy is critical for ensuring that the treatments and associated biological outcomes remain accurate, reliable and reproducible. Unfortunately, dosimetry in a small-animal context is particularly challenging owing to small field sizes and steep dose gradients frequently encountered. Furthermore, there is a wide variability in the measurement techniques and technologies used between different institutions based on availability of equipment and the experimental treatment setup in question. While modern, commercially-available small animal irradiators have come equipped with on-board imaging and treatment planning software to improve accuracy, there remains a lack of standardization in the methods of dose determination and dosimetry reporting in a majority of radiobiological publications [62]. Results of recent dosimetry studies further support concerns over the frequency with which inaccurate doses might be reported [62–64]. Pedersen *et al.* [64] found that, across 12 participating institutions, the overall average deviation of dose delivered relative to the target dose was 10.7%, for both radionuclide and x-ray units, while for x-ray irradiator facilities alone the average deviation increased to 17.2%. The survey conducted by Seed *et al.* [63] observed that only four of their seven participating centers (57%), including both radionuclide and orthovoltage units, were able to maintain average dose errors <5% using thermoluminescent (TLD) and optically stimulated luminescence (OSLD) dosimeters. The results of these studies suggest that doses reported in the context of radiobiology research might not be sufficiently accurate for determining the biological effects of radiation exposure. Consequently, the development and validation of technologies able to support precise dosimetric practice, independent of the source or irradiation geometry, represents an important initiative and a primary motivator for the work described herein.

The fabrication of anatomically-accurate small-animal phantoms has emerged as one means of improving the reproducibility of pre-treatment dose verification for preclinical radiotherapy. In contrast with traditional phantoms, which were generally simplistic in their geometry (i.e. cylindrical) or based on a non-realistic anatomy, the increased utilization of 3D printing has facilitated reliable production of realistic, heterogeneous phantom models [148, 171, 186]. Of the available 3D printing technologies, material jetting stands out for having the highest available feature resolution and the ability to print solid models using multiple materials within a single job [148, 169]. Multi-material 3D printing is particularly attractive for the reason that it enables the incorporation of heterogeneities representing structural anatomy and allows for highly accurate, seamless phantom constructions [150]. Moreover, the high degree of material uniformity may prove attractive in the context of image-guided radiotherapy and imaging research. While there remains a need to improve the selection of 3D printing materials boasting favorable radiological properties [148], this limitation

[3]This work was published as an article in *Medical Physics* [67]

does not necessarily preclude the usefulness of representative, small-animal phantoms in improving the reliability of preclinical surrogate dose measurements via preservation of realistic anatomy.

To date, a variety of anatomically accurate phantoms have been produced for both imaging and radiotherapeutic applications [175–183]; few of these, however, have had a comprehensive evaluation with respect to their utility as tools for preclinical dosimetry. Welch *et al.* [179, 180] and Wu *et al.* [181], utilized an anatomically accurate mouse phantom comprised of materials that closely mimicked the physical properties of the component anatomy; however, their phantom was fabricated using less-economical micro-machining techniques which did not preserve the outer contours of the mouse model. Bache *et al.* [182], on the other hand, used comparatively affordable 3D printed molds, based on rat CT data, to form a homogeneous, tissue-equivalent 3D dosimeter out of radiochromic Presage® material with dose readout accomplished via optical-CT. The group utilized radiochromic film and nanocrystal scintillator detector for dose verification, but these dosimeters necessitated post-irradiation modification of the radiochromic rodent-morphic dosimeter, which was itself single-use by nature. Zhang *et al.* [183], on the other hand, found success utilizing 3D printing to generate a heterogeneous mouse phantom well suited to CT, MRI and positron emission tomography (PET) imaging studies, but which was not designed to accommodate radiation dosimeters.

Small field dosimetry on commercial small animal irradiators is often accomplished through the use of radiochromic films or a variety of other small volume dosimeters [61, 172–174]. Owing to the low cost, short lead times and design flexibility of 3D printing, modifications to printed phantoms, in the form of custom apertures, may be used to accommodate a variety of small-field portable dosimeters, including TLD/OSLDs, scintillating detectors, diamond detectors, or pinpoint ionization chambers. To better allow for preclinical dosimetry verification, it is desirable to have a phantom capable of accommodating dosimeters of the aforementioned variety at target sites of interest. This rational fed back into the design of our groups first-generation dosimetric mouse phantom, which was designed to accommodate both radiochromic film and a 1-mm diameter plastic scintillator dosimeter (PSD) [66, 187]. The present work is therefore concerned with the dosimetric validation and verification of conformal treatments with the phantom in question using an image-guided small animal irradiator.

The mouse phantom utilized in the present work leverages a cost-effective, readily customizable model and efficient production modality. Therefore, it is hoped that provision of a fully 3D-printed, anatomically accurate phantom for preclinical dosimetry may provide an accessible means for improving the precision of preclinical dosimetry across various institutions engaged in small-animal radiotherapy research.

4.7 Materials and Methods

4.7.1 Realistic 3D printed mouse phantom

An anatomically realistic mouse phantom was 3D printed based on segmented microCT data of a tumor-bearing 32 g mouse and is described in detail in our previous work [66]. Briefly, The body was comprised of a transparent, PMMA-like material ($\rho = 1.18\,\mathrm{g/cm^3}$) that served as an appropriate surrogate for water at the beam energies of interest while the lungs were packed with porous polystyrene ($\rho = 0.32\,\mathrm{g/cm^3}$) to better represent lung tissue. The mouse's skeletal anatomy was made with a slightly denser ($\rho = 1.20\,\mathrm{g/cm^3}$), opaque, PMMA-like material which, while not dosimetrically representative of real bone, enabled on-board visualization and localization of relevant anatomical targets. The phantom was designed to accommodate both laser-cut EBT3 Gafchromic® film (Ashland Advanced Materials, Bridgewater, NJ) and a plastic scintillator dosimeter (PSD) boasting a 1-mm long, 1-mm diameter polystyrene active element (Figure 4.5a). The films could be rigidly fixed within the mouse thorax, in a plane dividing the lungs, thereby enabling acquisition of 2D spatial and depth dose information simultaneously. The PSD, by contrast, enabled high-resolution point-dose measurements within one of three target sites: the brain, abdomen or a subcutaneous tumor. These targets were chosen considering they would be of interest in the context of the more common radiobiological experiments.

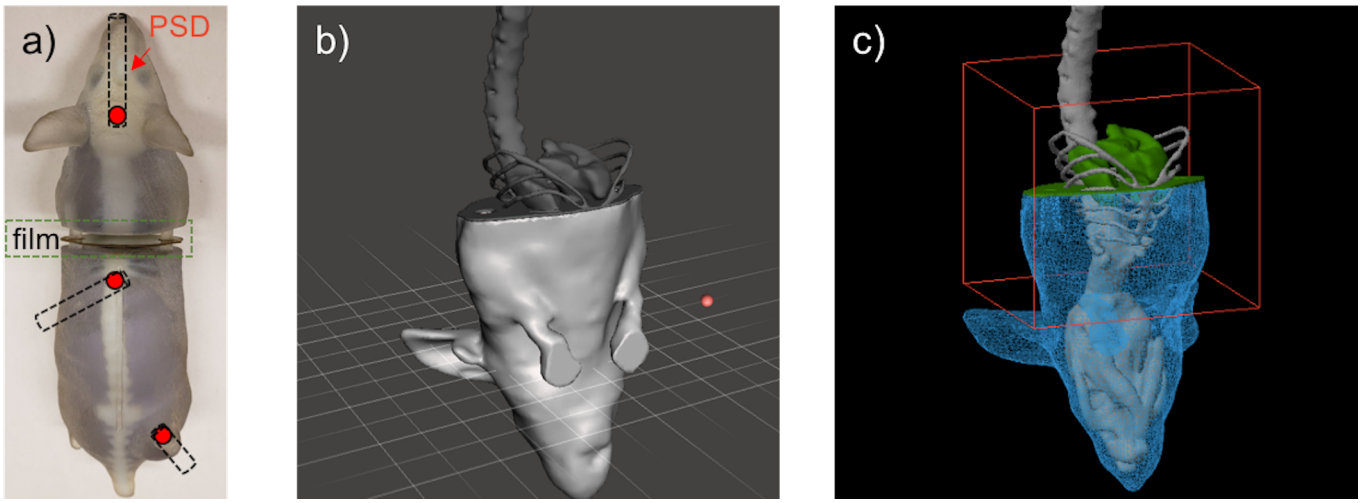

Figure 4.5: Photographic and microCT images (a) of the 3D-printed mouse phantom. The film and PSD sites (1 mm active element in orange, not to scale) are outlined in the left-most panel. A cut away of the computer-aided design (CAD) model (b), used for phantom fabrication, is provided alongside the corresponding geometry after import into TOPAS (c). The material comprising the mouse skeleton, while not dosimetrically representative of real bone, enabled on-board visualization and localization of relevant anatomical targets within the phantom.

4.7.2 Phantom irradiations

All treatments were delivered on the small animal radiation research platform (SARRP, Xstrahl Ltd, Surrey, UK) using the system's 220 kVp therapy beam (mean energy ≈ 80 keV; HVL=0.71 mm Cu). For each treatment, the large focal spot (3.0 mm; IEC366 convention) was employed along with the maximal tube current of 13 mA and an irradiation time of 60 s per beam. Total filtration for the 220 kVp beam included the inherent 0.8 mm Be filter and an additional 0.15 mm of Cu [30].

Seven treatment configurations were utilized in total, including irradiations of both radiochromic film and the PSD, and are summarized in Table 4.3. Beam collimation was varied based on treatment site and was facilitated through use of the SARRP's stock 10×10, 5×5 and 3×3 mm treatment nozzles. All treatments were delivered in an isocentric manner with source-to-isocenter (SID) and collimator-to-isocenter distances (CID) of 35 cm and 5 cm, respectively.

Table 4.3: Summary of treatment configurations along with location of dosimetry target.

Dosimeter	Treatment	Target Site
PSD	$10 \times 10\,mm^2$ (5-beam) $5 \times 5\,mm^2$ POP $3 \times 3\,mm^2$ ARC	Abdomen Subcutaneous Tumor Brain
Film	$10 \times 10\,mm^2$ (3-beam) $10 \times 10\,mm^2$ (single beam) $5 \times 5\,mm^2$ (3-beam) $3 \times 3\,mm^2$ ARC	Thorax/lungs

4.7.3 Film dosimetry

EBT3 Gafchromic® film was used to acquire 2D dose distributions for each of the co-planar deliveries, using three $5 \times 5\,mm^2$ and $10 \times 10\,mm^2$ beams, separated by 120°, a single $10 \times 10\,mm^2$ beam at 0°and a $3 \times 3\,mm^2$ 360°arc (Table 4.3). Prior to irradiation, the SARRP isocenter was localized, as accurately as possible, at the film mid-plane via pre-treatment CBCT imaging. To additionally ensure that the setup could be maintained between irradiations, only half the phantom was fixed to the treatment couch so that the film could be inserted or replaced without having to remove the entire phantom.

The film batch was cross-calibrated with respect to a PTW Farmer® TN30013 (PTW, Freiburg, Germany) ion chamber to measure dose-to-water for the SARRP 220 kVp beam using the AAPM TG-61 protocol [140], as outlined in our previous work [66]. Specifically, twelve calibration films were irradiated to doses ranging from 0 to 8 Gy while preserving the setup of the corresponding ion chamber measurements. The ion chamber calibration, suitable for use with kilovoltage irradiators, is traceable to the standards laboratories of the National Research Council of Canada (NRC). An

aggregate uncertainty of 3% was applied to all profile measurements; this includes the uncertainty from the calibration and film scanning procedure as well as the intrinsic non-uniformity error in the film response, informed through the manufacturer specifications [188].

We have previously verified our dosimetric accuracy through the UW Madison Radiation Calibration Lab (RCL) dosimetry service for which doses, measured using a pinpoint ionization chamber, were delivered both in air and an acrylic phantom and found to agree to within <1% of the prescribed dose.[4]

Irradiated films were scanned 24h after exposure on an EPSON® 10000XL flatbed scanner (Epson America, Long Beach, CA) at a resolution of 200 dpi and in the same orientation as the calibration films. An in-house Matlab® (Mathworks, Nattick, MA) script, previously validated against FilmQA pro® (Ashland Advanced Materials, Bridgewater, NJ), was used to analyze the films using the red-channel data.

4.7.4 PSD dosimetry

Dosimetry using the PSD followed the methods outlined by Johnstone *et al.*, who previously characterized the detector response for the SARRP system [187]. Prior to irradiation, the PSD was aligned to isocenter and cross-calibrated with a PTW Farmer® TN30013 ion chamber according to the in-air dosimetry procedure set out by the AAPM TG-61 protocol. In addition, the PSD was placed on a rigid polystyrene block so as to maintain its positioning at isocenter.

Measured dose to water ($D_{w,M}$) was calculated from electrometer readings ($M_{PSD,M}$), in units of µC, by using the following relation:

$$D_{w,M} = \frac{D_{w,C}}{M_{PSD,C} B_{MC}} M_{PSD,M} = k M_{PSD,M} \tag{4.1}$$

where k is a calibration factor [$k = 0.572\,\mathrm{Gy\,\mu C^{-1}}$], taking into consideration a Monte Carlo (MC) calculated backscatter correction ($B_{MC} = 0.952$) owing to the presence of the above-mentioned polystyrene block. The value of k was calculated from the dose-to-water ($D_{w,C}$) and corresponding in-air electrometer reading ($M_{PSD,C}$) taken under TG-61 calibration conditions, as denoted by the subscripted C. Since the PSD was calibrated for the same beam quality as what was used for all measurements, no additional spectral correction was applied.

Owing to the sensitivity of the PSD response to the potentiometer setting, the calibration and measurement data were taken successively so as to minimize measurement error. The dark current response of the PSD was also measured to be 0.452 pC/s and was subtracted from all subsequent dose measurements. The estimated standard deviation for repeated measurements using the PSD was previously determined to be 0.6% [187].

[4] This important verification study supported the dose accuracy of the validation data used in this work.

PSD irradiations comprised a $3 \times 3\,\text{mm}^2$ brain arc, $5 \times 5\,\text{mm}^2$ parallel-opposed pair (POP) and 5-beam $10 \times 10\,\text{mm}^2$ abdominal co-planar arrangement. Prior to each delivery, the 1-mm diameter active element of the PSD was targeted by using the SARRP's onboard cone beam computed tomography (CBCT) imaging capabilities. Acquisition of high-resolution CBCT images, with a voxel size of 275-µm, helped to ensure precise placement of the treatment isocenter.

4.7.5 Monte Carlo simulations

For each treatment configuration, TOPAS (v3.1.2) [143] Monte Carlo (MC) simulations were employed to verify the absolute doses delivered to the film plane or PSD target site of interest. Input phase-space files, generated using a validated model of the SARRP [166], built in the BEAMnrc [59, 167], were located just above the variable nozzle geometry, 26.55 cm from the source. In addition, each nozzle geometry was modelled according to manufacturer specification and precise measurement data as required. Absolute doses were calculated directly from MC-calculated dose, expressed in Gy/particle, based on beam current and irradiation time per the methods of Johnstone *et al.* [166].

Doses were scored within the relevant measurement geometry, either a voxelized EBT3 film layer or 1-mm diameter PSD active element, each of which was precisely defined using the associated computer-aided design (CAD) data. The stereolithography (STL) files for each phantom component, used for 3D printing, were similarly imported and defined so as to include the same materials and their respective mass densities as the physical phantom (Figure 4.5b, c). Additionally, since the CAD and MC geometries were made to share a common coordinate system, precision targeting of the treatment isocenter could be achieved; specifically, the absolute positions in TOPAS were made to coincide exactly with those defined in our CAD software.

Each dosimeter type was modelled as being made of water since the dosimeters themselves were calibrated to measure dose to water. The film calculation grid consisted of $0.5 \times 0.4 \times 0.3\,\text{mm}^3$ voxels, with the voxel z-dimension defined so that it would encompass the manufacturer-specified $\sim 280-$µm thickness of a single EBT3 film layer.

A physics list suitable for low energy applications was selected from those available (G4EmStandardPhysics_option4) with optional processes enabled or disabled as required. By default, the list leveraged the low-energy Livermore and Penelope models for particle transport, a low-energy Compton scattering model with simulation of Doppler broadening, and atomic de-excitation. Fluorescence and Rayleigh scattering were enabled by default while Auger production was optionally enabled. The global range cut for all particles was set to 1 µm. No other variance reduction techniques were employed and 3.5×10^9 primary histories were simulated for each treatment. The calculated dose uncertainty within the high-dose regions remained below 2% in all cases. All calculations were completed on a high-performance computing cluster using Intel® Broadwell and Skylake CPUs (Intel, Santa Clara, CA) running at 2.1 GHz and the time per simulation ranged from 10-20 hours.

4.7.6 Dosimetry analysis

Experimental and MC-derived film data were co-registered in MATLAB to enable consistent comparison between 2D dose distributions. Dose profiles were calculated for isocentric regions of interest (ROI) defined such that their height conformed to the field size in question – 10 mm, 5 mm and 3 mm for the 10×10, 5×5 and $3 \times 3\,mm^2$ field sizes, respectively – while the width was held constant at 11 mm. Lateral line profiles were computed along the x-axis of these regions with each point representing an average along the corresponding span of the ROI along the y-axis. Mean doses and mean absolute differences were calculated for points with doses above 90% of the dose maximum (D_{max}). Lateral profile comparisons were calculated for each film irradiation, while a depth-dose curve was generated using the single-beam $10 \times 10\,mm^2$ delivery. The same lateral dose criterion used previously ($> 90\%D_{max}$) was applied to sampled depth-dose data for depths between 0.1 and 1.47 cm. These bounds were chosen so as to safely avoid the damaged (laser-cut) edges of the film, which could not be recreated within the calculated distribution. Error maps were also generated and directly associated with dose data on a per-voxel basis and maintained their pixel associations after image registration. The MC-calculated profile error bars therefore represented the absolute standard deviation (in Gy) calculated from ROIs consistent with those described above.

The doses measured by the PSD were compared to the MC-calculated doses for all three treatment sites and relative dose differences were reported.

4.8 Results

Dosimetric analysis of the phantom involved the comparison of the mean dose and dose differences for 2D film profiles and PSD point-dose measurements for each treatment configuration. All measured doses were found to agree to within 5% of the corresponding MC-simulated data and are summarized in detail below.

4.8.1 Film dosimetry

Figure 4.6 shows each of the MC and measured film dose distributions. Each non-registered distribution pair showcases visible agreement, particularly for the dose regions about isocenter. In all cases, the measured film distributions were subject to some rotation owing to slight phantom positioning shifts on the treatment couch and film rotation introduced during scanning. Owing to the unknown nature of the shift, however, this facet was not replicated in the simulated case. Differences in the size of the peg-holes (at Y=0 cm) in the MC and film data resulted from the coarser grid sampling of the STL geometry in TOPAS and the fact that a manufacturing tolerance, added prior to laser-cutting the film, is not reflected in the raw STL files used for simulation.

Approximate analysis ROIs are overlaid on each dose distribution pair and the associated line profiles are depicted in Figure 4.7.

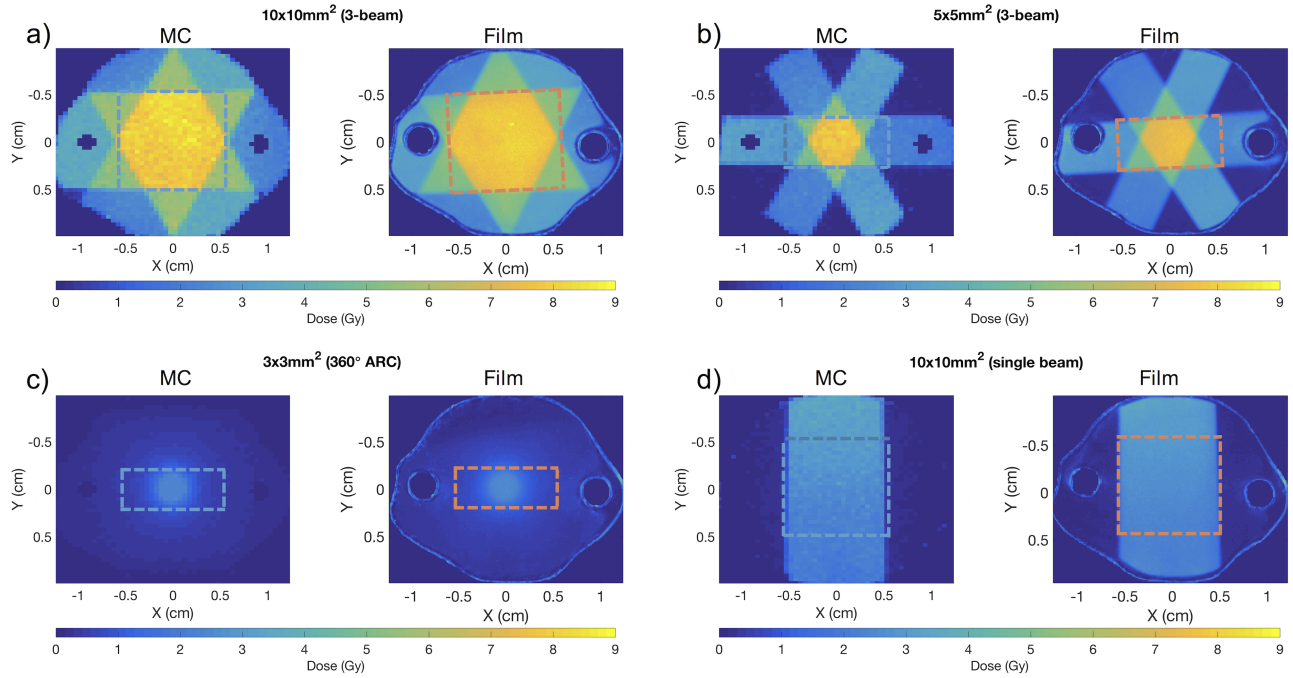

Figure 4.6: Dose maps for each film irradiation with MC and experimental (film) data presented in the left and right-hand panels of each figure, respectively. The $10 \times 10\,\mathrm{mm}^2$ (a) and $5 \times 5\,\mathrm{mm}^2$ (b) configurations comprised three beams, spaced at 120°intervals, while the 360°arc (c) was delivered using the $3 \times 3\,\mathrm{mm}^2$ field size.

The profiles are found to be consistent within the bounds of the associated uncertainties with the exception of the $5 \times 5\,\mathrm{mm}^2$ and $3 \times 3\,\mathrm{mm}^2$ (Figure 4.7b, c) distribution penumbra, wherein points below $\sim 35\%$ of D_{max} begin to diverge. It is apparent that the $10 \times 10\,\mathrm{mm}^2$ and $5 \times 5\,\mathrm{mm}^2$ co-planar configurations (Figure 4.7a, b) feature a slight overestimation, of 1.42% and 2.25% respectively, in the MC dose relative to the measured doses that were $> 90\%$ D_{max} (Table 4.4). This contrasts with the trend observed in the arc and single-beam treatments (Figures 4.7c, d) in which the film doses about isocenter where 1.56% and 1.33% higher, respectively, than the MC results. The mean value of the absolute percentage difference across all film irradiations was found to be 1.64%.

The mean values for the absolute difference between the full MC and measured film profiles were found to be 1.75%, 2.24%, 2.33% and 1.44% for the $10 \times 10\,\mathrm{mm}^2$ co-planar, $10 \times 10\,\mathrm{mm}^2$ single-beam, $5 \times 5\,\mathrm{mm}^2$ co-planar and $3 \times 3\,\mathrm{mm}^2$ arc irradiations, respectively.

These reported dose results largely showcase the agreement within the high-dose regions, sampled by taking points above 90% D_{max}, and not in the penumbra. The $3 \times 3\,\mathrm{mm}^2$ arc distribution, stands as an exception owing to the steep dose gradient about isocenter; in this case, the dose uncertainty was also increased due to the analysis ROI having partially encompassed the penumbra in the y-direction as well.

In all cases, the calculated and measured doses agreed to within 5%, and therefore meet the goal for dose accuracy previously set out by various groups [63, 64], as well as the recently formed TG-319

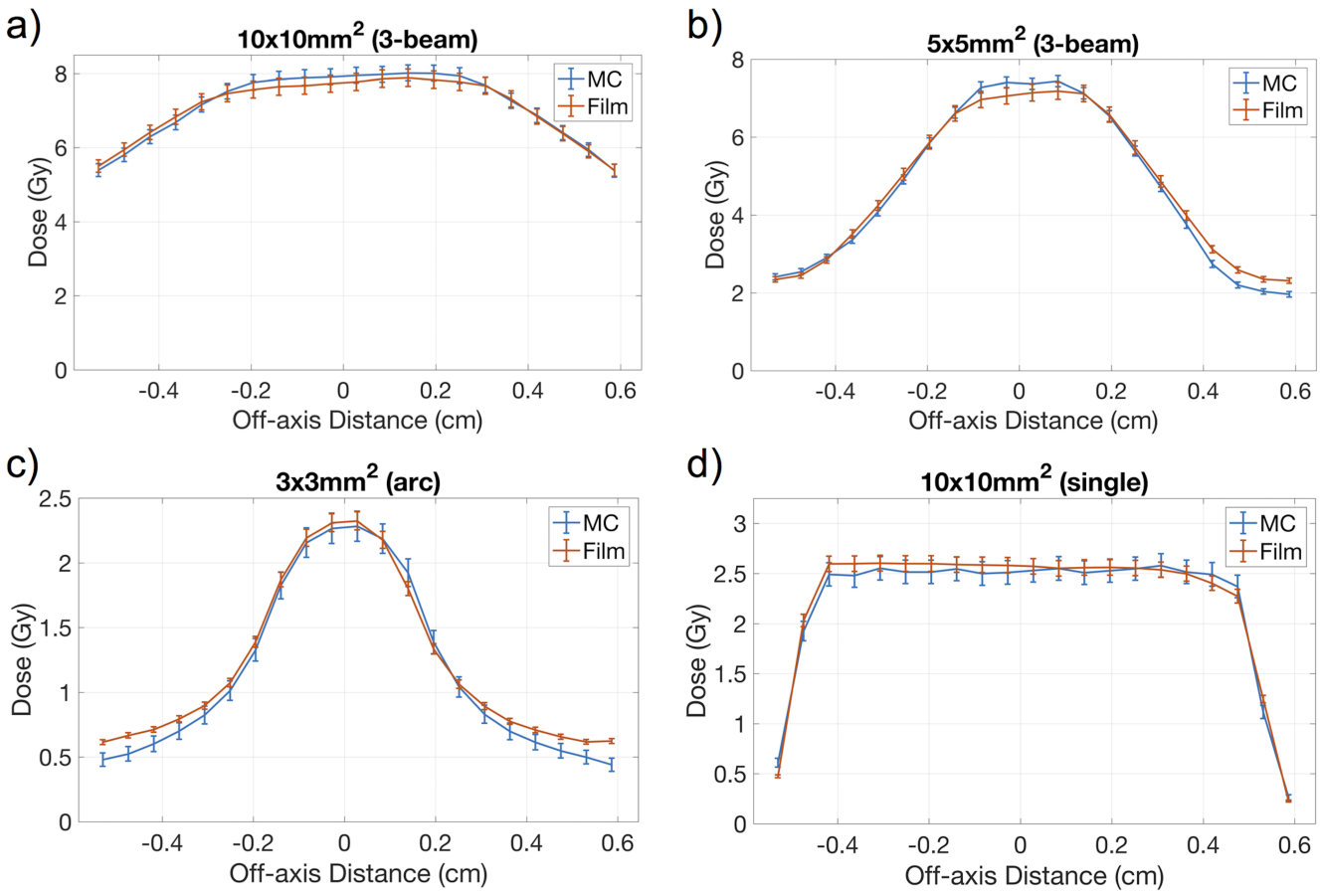

Figure 4.7: Dose profile comparisons for all MC and experimental data sets. Averaged lateral (x-axis) profiles are presented with each point corresponding to the mean of the analysis region of interest along the y-axis.

Table 4.4: Film mean profile doses, for points above 90% of D_{max}, and associated percentage differences. The percentage difference was calculated as $100\% * (MC - Film)/MC_{max}$.

Dosimeter	Treatment	Dose (Gy) MC	Dose (Gy) Film	% difference
Film (Thoracic)	10x10 (3-beam)	7.76 ± 0.07	7.65 ± 0.23	1.42
	10x10 (single)	2.52 ± 0.03	2.56 ± 0.08	-1.56
	5x5 (3-beam)	7.11 ± 0.08	6.95 ± 0.21	2.25
	3x3 ARC	2.22 ± 0.09	2.25 ± 0.07	-1.33

task group[5]. A depth dose profile for the $10 \times 10\,\mathrm{mm}^2$ single-beam distribution (Figure 4.6d) is presented in Figure 4.8.

The depth doses are found to agree well about isocenter, and while the profiles diverge slightly above and below this point, the data remain largely consistent in consideration of the associated

[5]Personal Communication. S. Kry (2018)

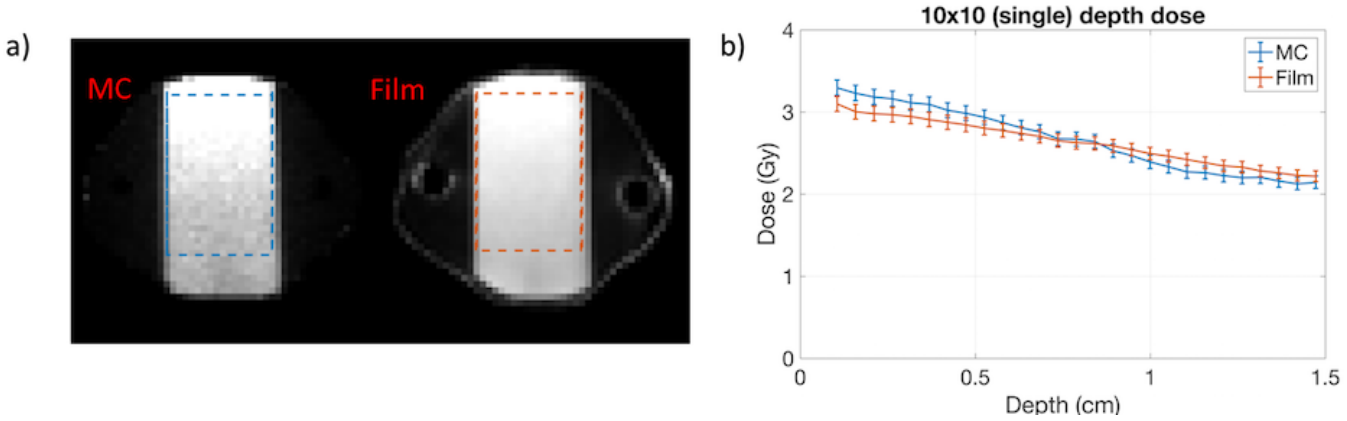

Figure 4.8: Registered film and MC data (a) and depth-dose curves (b) for the single $10 \times 10\,\mathrm{mm}^2$ beam irradiation. A slight decrease in dose at depth is observed for the MC data in regions proximal to the lungs, a feature which is not visibly present in the film data. The regions of interest are consistent between the two registered images.

dose uncertainties. The average deviation between the depth-dose curves was found to be 4.2%. Meanwhile, the mean relative dose difference between the MC and film data, for the full ROI outlined in Figure 4.8a, was only $(0.1 \pm 3.3)\%$. The apparent deviation of the MC curve from the film curve at depths well above or below the treatment isocenter is discussed in detail below.

4.8.2 PSD dosimetry

Table 4.5 summarizes the PSD dose measurement and corresponding MC simulation results along with their percentage differences. For each treatment configuration, the dose difference was found to be less than 5%, with absolute maximum and minimum deviations of 3.17% and 1.33% for the $10 \times 10\,\mathrm{mm}^2$ co-planar and $3 \times 3\,\mathrm{mm}^2$ arc therapies, respectively.

Table 4.5: Mean dose to water and percentage differences for MC and measured PSD data. The percentage difference was calculated as $100\% * (MC - PSD)/MC_{max}$.

Dosimeter	Treatment	Dose (Gy)		% difference
		MC	PSD	
PSD	10x10 Abdomen (5-beam)	12.85 ± 0.23	12.45 ± 0.08	3.17
	5x5 Tumor POP	5.66 ± 0.14	5.58 ± 0.03	1.51
	3x3 Brain ARC	2.45 ± 0.04	2.48 ± 0.02	-1.33

4.9 Discussion

The success of radiobiological studies seeking to determine dose-response relationships inextricably depends upon the quality of the dosimetry and quality assurance methods which precede them. The

motivation for this work therefore pertained to evaluation of a realistic 3D printed mouse phantom that may help in addressing the need for improved dose measurement and reporting procedures in radiobiology experiments [62].

In general, realistic small-animal phantoms for dose verification and quality assurance in preclinical settings are valuable for their ability to improve the dose accuracy, and thus treatment outcomes, of increasingly complex irradiations. The steep dose gradients encountered with kilovoltage sources lends to a strong sensitivity of the dose distribution to the body contours of small-animal models, for example, and limits the utility of the more simplified phantom geometries. Through the use of 3D printed models, however, fine anatomical features may be reliably replicated and treatment sites of interest may be additionally customized to suit the demands of a specific experiment.

In order to assess the utility of our mouse phantom in facilitating accurate dosimetry, a variety of treatment were employed using the SARRP system. Film irradiations of the mouse thorax, and PSD point-dose measurements of the abdomen, brain and a 1-cm flank tumor were completed. Both dosimeter types were calibrated to measure dose-to-water and so the film layer and polystyrene active element of the PSD were both modelled as water in the corresponding MC simulations. The accuracy of simulating dose to water-equivalent dosimeters within our phantom relative to the case where the phantom was comprised of tissue-equivalent material was discussed in our previous work [66].

The agreement between measured and simulated dose distributions in Figure 4.6 was found to be very good overall. Dose distribution profiles presented in Figure 4.7 demonstrate a good agreement in the high-dose regions, where $D > 90\%D_{max}$, such that the mean deviation was $< 3\%$ in all cases. For the $5 \times 5\,\mathrm{mm}^2$ and $3 \times 3\,\mathrm{mm}^2$ treatments, on the other hand, increased dose differences were observed towards the edges of the sampled penumbra, but everywhere remained $< 10\%$. This deviation may have resulted, in part, from skew or rotation in the film distributions relative to the idealized MC data or from interpolation of dose within in high-gradient regions as a result of the registration process.

PSD measurement data were similarly found to agree with the MC-calculated results; a maximum dose difference of 3.17% was observed for the 5-beam $10 \times 10\,\mathrm{mm}^2$ co-planar treatment. The actual PSD boasts a polystyrene active volume, which has an energy dependent response different from water, but the effects were found to be negligible. This was verified, in part, by scoring dose to polystyrene in otherwise identical simulations and applying the spectrum-weighted mass-energy absorption coefficient ratio for water and polystyrene (≈ 1.34) at a nominal depth of interest (1 cm), the results of which were found to be within 1% of the corresponding doses to water.

For the small field sizes under consideration, a high degree of positioning accuracy is required to enable precise PSD measurements. Additionally, rigid positioning of the PSD and maintenance of ambient conditions (i.e. temperature) is vital to ensuring that measurements can be reproduced and reasonably modeled in MC simulations. Fortunately, the 0.2-mm positioning accuracy of the translation stage and high-resolution CBCT-guidance capabilities of the SARRP assist in meeting this demand. For the corresponding MC simulations, use of STL geometry data enabled localization

of targets within the CAD software followed by appropriate translations being effected within TOPAS. The excellent agreement shown for the position-sensitive $3 \times 3\,\mathrm{mm}^2$ arc treatment, in which the dose difference for the PSD active element was $< 1.5\%$, demonstrates the robustness of the targeting capabilities of the SARRP and the methodology used to replicate the delivery in TOPAS.

In the case of the film irradiations, post-alignment motion of the phantom remained a possibility throughout the experiments. To the best of our ability, however, visual inspection of the alignment lasers and physical markers had been used to facilitate reproducible localization of the non-fixed half of the phantom following image-guided isocenter placement. In this way any targeting errors, which would not be reproducible within the MC simulations, could be minimized.

In contrast with the above-mentioned isocentric dose data, depth-dose curves derived from the single $10 \times 10\,\mathrm{mm}^2$ irradiation revealed some marked differences between measured and simulated data. In particular, the depth dose was found to decrease more quickly in the MC data relative to the film measurement (Figure 4.8b). The deviation above and below the treatment isocenter ($\approx 0.95\,\mathrm{cm}$) is believed to derive from the interface with the low-density (polystyrene) lung and higher-density (PMMA) body which were directly contiguous with the film (water) boundary in the simulations, but not in the real phantom. Specifically, it is surmised that the scattered dose contribution increased and decreased, respectively, about these body-film and lung-film interfaces. These interfaces are not present in the physical phantom owing to a small air-gap, of unknown dimension, existing between the film and phantom surfaces. In addition, secondary electrons (i.e. photoelectrons), which deposit substantial dose within the surrounding media, have a very short range and, as pointed out by Welch *et al.* [180], may not be well captured by EBT3 film owing to the $\approx 125\,\mu\mathrm{m}$ polyester layer that encapsulates the film's active layer. The polyester layers were not accounted for in the simulated models; instead, the film active layer was assumed to be 300-µm thick.

Exclusion of both the air-gap and polyester film layers in the MC simulation may have promoted a slight overestimation in dose towards the surface, due to the higher-density (PMMA) material contiguous to the film plane, and underestimation of dose about the lung interface, which extended from $0.95\,\mathrm{cm}$ to the bottom of the analysis ROI (Figure 4.8). However, these trends may be complicated by the potential for the phantom to sag or shift about the film plane throughout treatment, thereby causing variable surface contact about isocenter, and the fact that the polystyrene lung material was packed non-uniformly, in contrast with the MC lung definition. Together, such factors could have also contributed to the observed reduction in penumbral agreement (see Figure 4.7b, c). Inclusion of a well-modeled air-gap and a reduction in MC dose uncertainty would be expected to improve the level of agreement, but would require precise characterization of the air-gap, which is liable to change on a per-treatment basis.

For each MC simulation, the PMMA (body and bone) components were modeled with their appropriate (CT-derived) mass densities; however, the exact chemical composition of the printable photopolymer material was proprietary and thus not fully known. Nevertheless, the agreement

between measurement and MC results serves to indicate the value in simulating the geometry as-is, even with the simplified material definition. To support this in detail, the results of our PMMA mouse simulations were compared against those which considered the most accurate material composition we could derive from MSDS documents; specifically, two cases were considered for which the two primary (i.e. highest mass fraction) constituents were simulated in their maximum and minimum concentrations. It was determined that, even in these extreme cases, the relative dose error due to simplification of the phantom material was $\approx 1\%$ or less - even for the case of the 5-beam thoracic irradiation (see Table 4.5), the measured and new MC-calculated doses were still found to agree to within 5%. Furthermore, the absolute dose differences in all cases were found to be within the bounds of the associated MC dose uncertainty. Based on the results of this investigation, it becomes apparent that defining the phantom bulk material as PMMA should not introduce large errors into the dose calculation process and may in fact promote a simpler simulation procedure – one which does not require users of the phantom to incorporate the uncertain and complicated photopolymer material definitions into their own MC models or treatment planning systems.

It is interesting to note that, while the photoelectric effect (PE) has a strong dependence on the effective atomic number (Z_{eff}), and thus material composition, only a small proportion of the 220 kVp energy spectrum is contained in the energy range for which PE interactions contribute substantially within our (PMMA-like) phantom. Specifically, only 4% of primary photons are found below 40 keV, for which PE comprises $\sim$ 24% of all photon interactions in PMMA [73]. This attenuation behavior is similarly shared amongst other water-like polymeric materials, though not in higher-Z bone-mimicking materials which might be employed in the future. These factors, along with the compositional likeness of polymeric materials, including the above-mentioned photopolymer, and our accurate density determination are believed to be driving factors for the acceptable dose agreement that was observed.

Welch *et al.* (2017) [180] had previously compared radiochromic film measurements in their mouse phantoms with MC simulation results; however, the group was limited in their ability to precisely replicate the physical experiment due to constraints in phantom fabrication and alignment of the film and analysis grid. In the present study, the use of STL-defined models, in place of voxelized geometries, and a high-resolution 3D printed phantom facilitated highly accurate alignment of the simulated and physical setups. Furthermore, our ability to arbitrarily define a dose scoring grid over continuous STL geometries provided flexibility when balancing computational efficiency and spatial resolution without compromising the accuracy of particle transport through the phantom.

While the excellent feature resolution afforded by 3D printing ensured that the physical phantom conformed very well to the digital (STL) model, the skeletal heterogeneities were not made to be dosimetrically representative of real bone. Inclusion of heterogeneities boasting a higher mass density and Z_{eff} would therefore allow for phantom measurements which better represent the dose delivered to real mouse tissue, especially in contexts where attenuation in bone is of concern (i.e. intracranial

targets), and for lower-energy imaging beams where PE interactions become increasingly important. However, we have also demonstrated that replacing the phantom PMMA and polystyrene materials with mouse soft-tissue, bone and lung tissue, where appropriate, results in differences of $\approx 5\%$ or less for dose delivered to a water-equivalent dosimeter at each treatment site [66]. Therefore, considering the agreement between the measured and simulated results presented herein, dose estimates acquired with our current phantom should be sufficiently accurate for estimating dose to mouse soft-tissue within the suggested accuracy limit ($< 5\%$) for small animal dosimetry.

The 3D printed mouse phantom presented in this work has been shown to facilitate precise dose-verification for a variety of treatment configurations. Future work could leverage our phantom design or production methodology to reliably and affordably adapt the phantom for various other dosimetry applications and dose verification procedures on irradiators both with and without image-guidance. Moreover, experiments concerned with optical, bioluminescence or spectral imaging, or those interested in localizing contrast agents in place of a small-volume detector, could be readily accommodated while allowing for dose measurement under the same experimental conditions.

4.10 Conclusions

A realistic, fully 3D-printed mouse phantom was evaluated for use as a tool for precise dosimetry in the context of small-animal radiotherapy and radiobiology research. The phantom was irradiated using a total of seven image-guided treatment configurations. Radiochromic film and a plastic scintillating dosimeter were used to measure dose to the mouse thorax (film), abdomen, brain and a subcutaneous tumor (scintillator). Measured doses were compared to those calculated using a validated MC model of the SARRP system. For all treatments, the mean dose deviation between measured and MC dose data was found to be less than 5%, deemed an acceptable threshold. The results of this study showcase the utility of our 3D printed phantom in facilitating precise preclinical dosimetry, critical to ensuring the reliability of dose-response outcomes in radiobiological experiments, and streamlining the dose verification procedures for increasingly complex preclinical treatments.

Chapter 5

Development of UHDR compatible x-ray sources for FLASH-RT research

On the capabilities of conventional x-ray tubes to deliver ultra-high (FLASH) dose rates[1]

5.1 Introduction

Normal tissue toxicity has long been a key factor limiting the curative potential of radiation therapy (RT). To date, a number of techniques and technologies have been advanced in order to circumvent this limitation - intensity and volumetric modulation, spatial and temporal fractionation, particle therapies, image-guidance and precision techniques among them - yet none so far have been able to foster complete avoidance of normal tissue toxicity [37, 189–192]. Fortunately, renewed exploration into the regime of ultra-high dose rate (FLASH) therapy may be providing a radical new solution towards minimizing long-term effects.

While the concept of high-dose rate therapy is not altogether new [91, 193–195], interest has been rekindled in light of the reduction in normal-tissue toxicity that has been observed following treatment [10,11,38,196]. FLASH therapy is currently characterized by the use of dose rates exceeding 30-40 Gy/s and is notable for its apparent capacity to improve the therapeutic ratio of RT by fostering a differential response between normal and tumoral tissue [38].

Recent preclinical studies have showcased remarkable improvements in treatment outcome following FLASH therapy, owed in large part to the increased normal tissue tolerance (FLASH effect) and maintenance of tumor-control efficacy for a given prescription. In particular, the seminal work of Favoudon *et al.* revealed the isoeffective nature of electron-beam FLASH ($> 40\,\mathrm{Gy/s}$) compared with conventional RT ($< 0.03\,\mathrm{Gy/s}$) for orthotopic lung tumors in mice; moreover, it was observed that FLASH-irradiated mice were free of the severe complications that were otherwise found in all mice exposed to 17 Gy at conventional dose rates [196]. In whole mouse-brain irradiated to 10 Gy, spatial memory was preserved for FLASH dose rates $> 100\,\mathrm{Gy/s}$ and partially preserved down to $\sim 30\,\mathrm{Gy/s}$, while total impairment was observed at conventional (0.1 Gy/s) dose rates [10]. This neurocognitive

[1] This work was published in *Medical Physics* [50]

sparing effect was subsequently observed using synchrotron-generated x-rays delivered with a FLASH-compatible mean dose-rate of 37 Gy/s [44]. In higher mammalian subjects, including mini-pigs and cats, the FLASH effect was again demonstrated by way of a significant reduction in normal-tissue toxicity relative to conventional treatments even as dose escalation was performed. In both subjects, the target normal tissues (pig-skin and cat nasal planum) exhibited improved tolerance when irradiated to high doses with only mild superficial side effects observed (i.e. depilation) for the range of doses considered in the escalation studies [11]. These outcomes point to the opportunity for further dose escalation in FLASH therapy, which could foster improved tumor control or allow for application to cases concerned with radiosensitive organs at risk. Thus, FLASH therapy appears poised to create a paradigm shift in radiotherapy whereby tumor ablation may be achieved in single-fraction, sub-second treatments while promoting a substantial reduction in radiation-induced side effects for exposed healthy tissues.

While these results are tantalizing, an underlying mechanistic understanding remains to be elucidated; as such, there is a fast-growing need for research into the biological foundations of the so-called FLASH effect. To meet this demand, we propose a means of using existing technologies to enable more accessible *in-vitro* FLASH experiments. To date, achieving FLASH-capable dose rates has typically relied upon access to specialized electron sources (i.e. Oriatron eRT6), and few other commercial devices yet exist which are readily suited for FLASH therapy despite the growing demand for preclinical research in this domain [38, 94]. In principal, modern clinical linacs can be made suitable for FLASH therapy, but this requires substantial modification to these clinically-optimized systems [48, 49]. Moreover, while synchrotrons, notable for their superior beam intensities [29, 44, 197], and high-energy cyclotron-accelerated protons are also capable of achieving the requisite dose rates [198], limited accessibility and high costs remain barriers to their widespread application.

The present work investigates the feasibility of using a conventional, high-powered x-ray tube for FLASH therapy experiments. A Monte Carlo model for our x-ray system is presented, along with indirect experimental validation and subsequently used to demonstrate its capacity to deliver $>$ 100 Gy/s at 120 kVp, which would be suitable for both controlled cell studies or superficial treatments in preclinical subjects.

5.2 Materials and Methods

Two x-ray tubes were considered for FLASH dose rate delivery in this work, the Comet MXR-160/22 and MXR-165 (Comet, Flamatt, Switzerland). Both x-ray tubes boasted tungsten anodes and were capable of continuous operation; other main parameters of interest are listed in Table 5.1. The output of an unfiltered 160 kV beam, for both tubes operating at maximum power, was simulated at the tube surface by using Monte Carlo (MC) models for comparison against FLASH dose rates. For MC modeling validation, the dose at depth in a phantom for the 120 kV beam of the MXR-160/22 was

experimentally measured and compared to MC simulations.

Table 5.1: Parameters of the investigated x-ray tubes MXR-160/22 and MXR-165.

	MXR-160/22	**MXR-165**
Maximum tube power (kW)	3	6
Maximum tube voltage (kV)	160	160
Investigated tube voltage (kV)	120, 160	160
Maximum tube current (mA)	18.75	37.5
Large focal spot size IEC (mm)	3.0	3.0
Anode angle (°)	20	30
Beryllium window thickness (mm)	0.8	4.0
Distance from focal spot to tube surface (cm)	3.6	3.5

5.2.1 Monte Carlo simulations

Both x-ray tubes were modeled with the EGSnrc/BEAMnrc MC code (v 2016) [142] based on the tube parameters listed in Table 5.1 and are schematically illustrated in Figure 5.1a. To find the peak output for both x-ray tubes, 10^9 electrons, each with a kinetic energy of 160 keV, were simulated to impinge upon the tungsten anode. Phase-space files, comprised of both photons and electrons crossing a plane just below the lead cone, were then scored; the resulting phase-space files contained 2.6×10^8 and 1.1×10^8 particles for the MXR-160/22 and MXR-165 x-ray tube, respectively. In order to speed up the x-ray beam simulations, Bremsstrahlung directional splitting with a splitting factor of 200 was used [199]. Half-value layers (HVLs) of the x-ray beams were calculated from the x-ray spectra extracted from the phase-space files at the surface of the x-ray tube using the methodology described by Verhaegen *et al.* [200].

The resulting phase-space files were subsequently used for the calculation of dose deposited in a $(5.0 \times 5.0 \times 1.0)\,\mathrm{cm}^3$ water phantom using the DOSXYZnrc code [184]. The surface of the phantom coincided with the surface of the x-ray tube (Figure 5.1b) and the absorbed dose was scored in the phantom with $(1.0 \times 1.0 \times 0.5)\,\mathrm{mm}^3$ voxels. For each x-ray tube, 5×10^8 histories were run resulting in a statistical uncertainty in high-dose regions of less than 0.9%. The MC calculated dose, expressed in Gy/particle, was converted to dose-rate ($\dot{D}$) expressed in Gy/s, assuming that the maximum tube current for both x-ray tubes. This conversion was accomplished by $\dot{D}(Gy/s) = \dot{D}(\mathrm{Gy/particle}) \times I(\mathrm{A})/1.602 \times 10^{-19}(\mathrm{C})$, where I is the x-ray tube current.

The 120 kV beam was also simulated for the MXR-160/22 x-ray tube in order to validate the presented MC simulations using the experiment described below. First, a 120 kV phase-space file was generated in a similar fashion to the 160 kV x-ray beam simulation, described above. Thereafter, the 120 kV beam dose-rate within a $(6.0 \times 6.0 \times 2.1)\,\mathrm{cm}^3$ plastic water (PW) phantom (CIRS, Norfolk, VA) [201], with $(0.1 \times 0.1 \times 0.1)\,\mathrm{mm}^3$ voxels, was calculated using the DOSXYZnrc code. In this

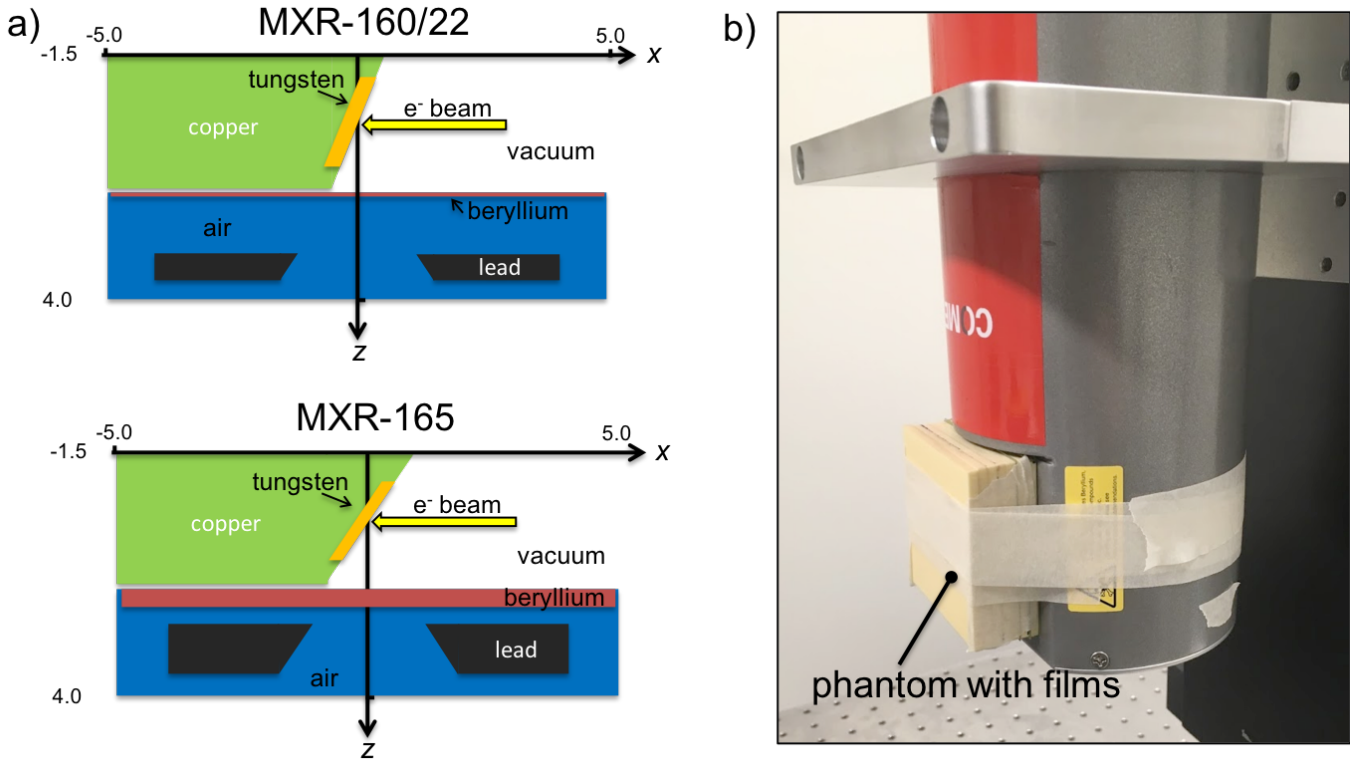

Figure 5.1: BEAMnrc models of the MXR-160/22 and MXR-165 x-ray tubes (a) and photograph of phantom and film dose measurement of the MXR-160/22 tube (b).

case, the experimental absolute dose was calculated, taking into account the tube beam current and irradiation time.

In all MC simulations, the electron and photon kinetic energy cutoffs were set to 5 keV. Low energy physics, such as atomic relaxation, electron impact ionization, and Rayleigh scattering were included. The xcom cross section data was used. All simulations were run on a 2 × 3.06 GHz 6-Core Intel® Xeon computer.

5.2.2 Experimental validation

A $(6.0 \times 6.0 \times 2.1)\,\mathrm{cm}^3$ PW phantom consisting of $(6.0 \times 6.0 \times 0.3)\,\mathrm{cm}^3$ slabs was irradiated with the MXR-160/22 x-ray tube. Dose was measured (Figure 5.1b) with two sheets of Gafchromic EBT3 films (International Specialty Products, Wayne, NJ) placed at depths of 15 and 18 mm in the phantom. The phantom was irradiated for 30 s using a 120 kV beam and the minimum stable tube current of 0.2 mA. The low current was selected so as to minimize the end effect [140] while keeping the dose within the dynamic range of the EBT3 film.

The films were read out by an Epson® flatbed scanner (Expression 10000 XL, Epson, Long Beach, CA) 24 hours post-irradiation according to our film dosimetry protocol. The films were cross-calibrated with a PTW TN30013 Farmer ionization chamber (PTW, Freiburg, Germany), in the

120 kV beam at 2 cm depth in solid water, with beam output measured per the TG-61 protocol [140]. The chamber was previously calibrated for use in a kilovoltage beam by the National Research Council of Canada (NRC). Measured film 2D dose-distribution profiles were compared with those derived from the MC simulations.

5.3 Results

5.3.1 Monte Carlo simulations

The results of MC dose rate calculations for the two x-ray tubes, operated at 160 kV and at their maximum tube currents, are summarized in Figure 5.2. The maximum phantom surface dose-rates were found to be (114.3±0.6) Gy/s and (160.0±0.8) Gy/s for the MXR-160/22 and MXR-165 x-ray tube, respectively. Dose non-uniformity due to the heel effect was evident for both cases (Figure 5.2a). For a 1-cm diameter region of interest (ROI) placed in the high dose region away from the heel effect (shown as a white circle in Figure 5.2a), the dose rate was (110.6±2.7) Gy/s for the MXR-160/22 and (151.9±2.6) Gy/s for the MXR-165 x-ray tube.

Plotting the dose rate as a function of depth demonstrated a steep attenuation of the unfiltered 160 kV x-ray beam (Figure 5.2b). At only 2-mm depth, the dose rate decreased to 23% and 28% of the surface dose rate for the MXR-160/22 and MXR-165 x-ray tube, respectively. Despite the difference in beryllium window thickness (0.8 mm for the MXR-160/22 tube and 4.0 mm for the MXR-165 tube), the energy spectra of the two x-ray tubes extracted from the phase-space files were similar and showed high tungsten L-shell peaks (Figure 5.2c). The 160 kV beam HVLs calculated

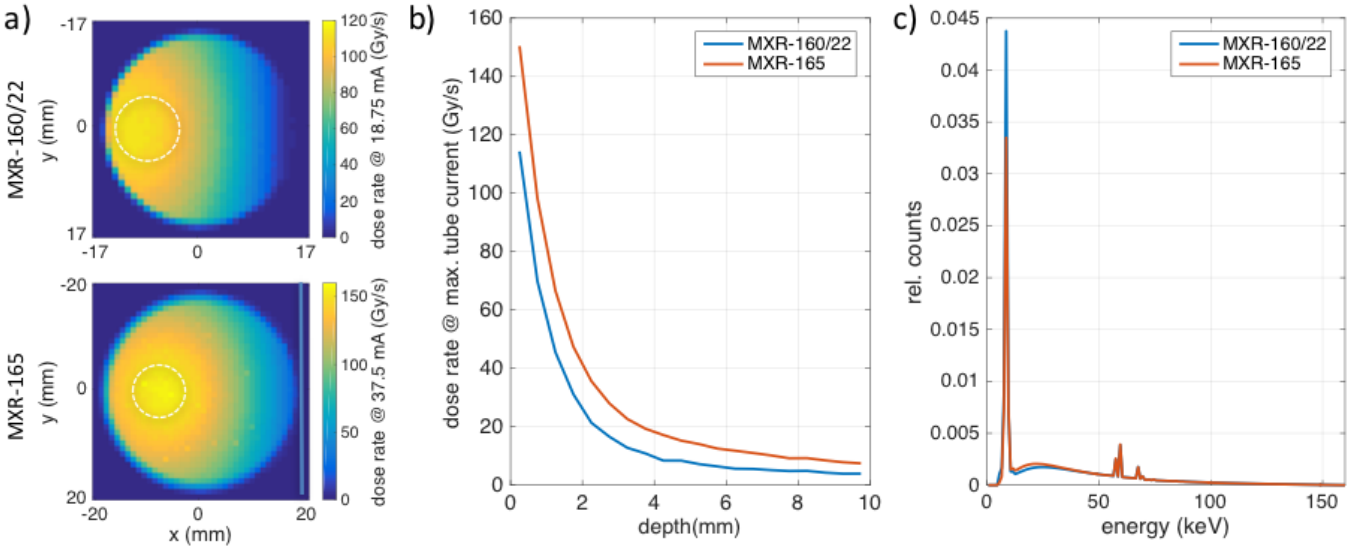

Figure 5.2: Calculated 2D dose rate maps at the surface of a water phantom for the MXR-160/22 and MXR-165 x-ray tubes calculated for a beam energy of 160 kV and maximum tube current. The high-dose 1-cm diameter ROI is shown in white dashed line (a). Dose rate as a function of depth (b) and x-ray energy spectra (c).

from MC spectra scored just below the beryllium window were 77 µm aluminum and 87 µm aluminum for the MXR-160/22 and MXR-165 x-ray tube, respectively.

5.3.2 Experimental validation

The 2D dose distributions measured by films and calculated by MC at depths of 15 and 18 mm are shown in Figure 5.3a. Cross-line (along x-axis) and in-line (along y-axis) profiles are presented in Figure 5.3b. A good agreement between film measurements and MC simulations in the region not affected by the heel effect was found for both phantom depths. The mean x-profile difference, in the -20 mm to 10 mm region, between film measurements and MC simulations was 1.5% and 3.2% at 15 mm and at 18 mm depth, respectively. The mean y-profile difference, in the -20 mm to 20 mm region, between film measurements and MC simulations was 1.5% and 3.5% at 15 mm and at 18 mm depth, respectively. The agreement in the heel-effect region along the x-profile (10 mm to 20 mm) was poorer, however, and the mean difference between film measurements and MC simulations was 10.3% and 17.8% at 15 mm and 18 mm depth, respectively.

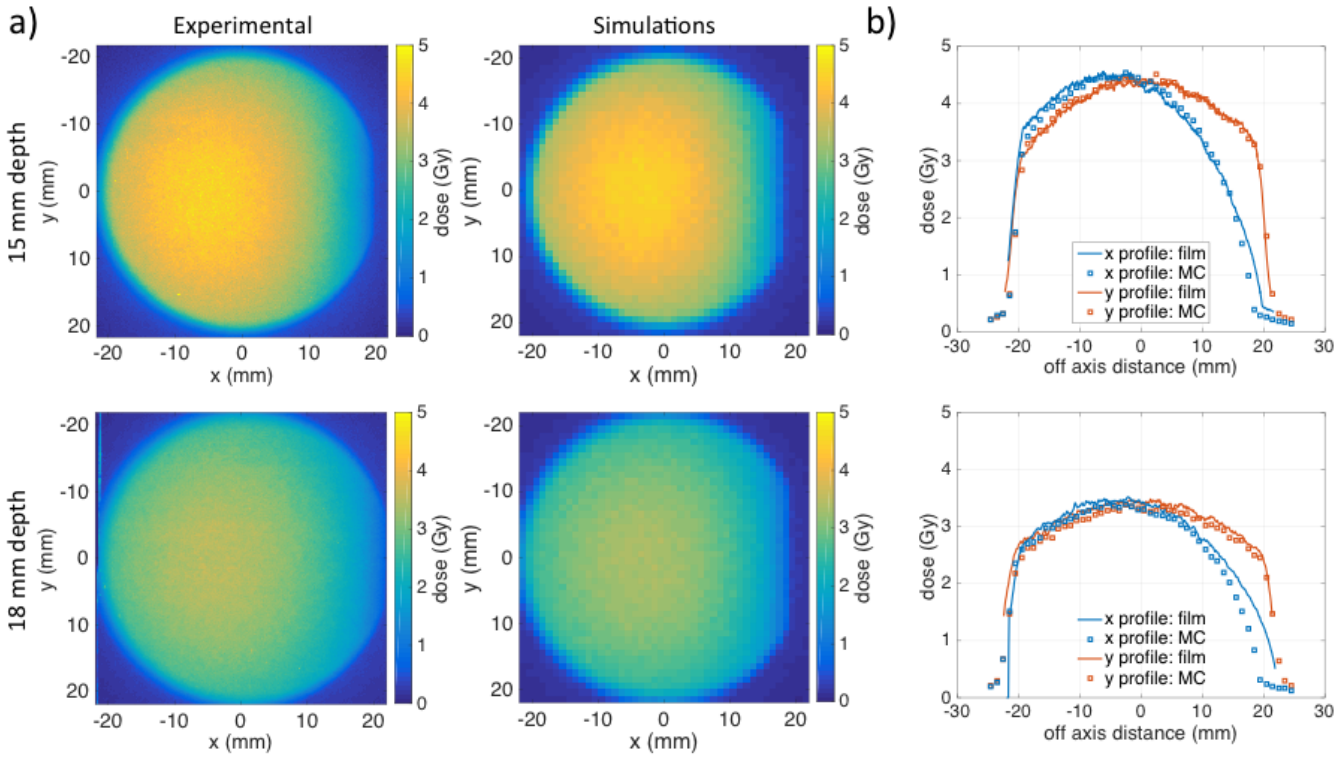

Figure 5.3: Experimental and simulated 2D dose distributions at 15 mm and 18 mm depth in the solid water phantom (a). Comparison of cross-line (x) and in-line (y) dose profiles at the two depths (b).

5.4 Discussion

The maximum dose rate in a phantom placed at the surface of the MXR-160/22 and MXR-165 x-ray tubes was calculated with MC. It was indirectly determined that the dose rates generated by both x-ray tubes were FLASH-capable, exceeding 100 Gy/s on the surface of the phantom. The x-ray beams contained low-energy tungsten L-shell x-rays that are simulated with a ≈4% accuracy in the EGSnrc code[2] [202]. The experimental validation showed that outside of the heel effect region, measured doses at 15 mm and 18 mm depth in phantom agreed with MC simulations to within 3.6%, which was an acceptable level of agreement for our work and demonstrates the capacity for conventional x-ray tubes to deliver FLASH therapy. It is interesting to note that the MC dose was underestimated at both depths, which could potentially be attributed to the x-ray tube end-effect not accounted for in the MC simulations. Gafchromic films have been shown to be dose rate independent up to dose rates of 9×10^{12} Gy/s [121, 127].

The depth dose-rate curves demonstrated a rapid dose rate fall-off for both x-ray tubes (Figure 5.2b). This was the result of attenuation of the soft x-ray beam as well as decreased intensity due to inverse square law that is prominent at such short ≈3.5 cm source-to-surface distances from the focal spot. As a result, the FLASH effect (> 40 Gy/s) can only be achieved at maximum depths of 1.4 and 2.1 mm for the MXR-160/22 and MXR-165 x-ray tube, respectively. At deeper depth, the FLASH effect might not persist. The investigated x-ray tubes might therefore be used for FLASH skin irradiations, FLASH *in vitro* experiments, or to test dose-rate dependence of small-field dosimeters. It should also be emphasized that the dose in a 1-cm diameter ROI is uniform to within 2.5%, which also effectively limits the use of x-ray tubes for FLASH irradiations to small fields.

As noted above, the experimental data were acquired with a long 30-s irradiation time to limit the tube end effect. For FLASH irradiations, doses will likely have to be delivered in sub-second intervals and a shutter mechanism will have to be designed. A simple shutter mechanism will shift the irradiation location by 2-3 mm, which will result in a ≈15% decrease in dose rate. A more complex shutter mechanism recessed between the beryllium window and the tube surface could also be designed, and might avoid decreasing the dose rates demonstrated in this work. Alternatively, the irradiation sample could be placed next to the beryllium window, which is at 1.7 and 2.0 cm from the focal spot. At this location, the dose rate on surface of a phantom was calculated with MC to be 513.2 Gy/s and 493.4 Gy/s for the MXR-160/22 and MXR-165 x-ray tube, respectively.

The presented doses are calculated for a phantom with almost full back-scatter conditions. According to the study by Klevenhagen, our 2.1 cm phantom resulted in 94% fraction of full back-scatter [203]. For radiobiological experiments, comparable scatter conditions should be used so that similar FLASH-like dose rates are achieved. In order to successfully carry out FLASH *in vivo* and *in vitro* studies with conventional x-ray tubes, the experiments must be cautiously designed and

[2] Ernesto Mainegra-Hing (personal communication)

dosimetry carefully performed.

5.5 Conclusions

We have indirectly demonstrated that conventional x-ray tubes can achieve dose rates of $> 100\,\mathrm{Gy/s}$ and may therefore be FLASH-therapy capable. Considering the rapid dose fall-off with depth and 2D dose non-uniformity, the studied x-ray tubes can deliver FLASH irradiations at depths of up to 2 mm for a 1-cm diameter region within the high-dose region. Conventional x-ray tubes therefore appear suitable for *in vitro* FLASH experiments and may henceforth serve as an invaluable tool for investigating the biological mechanisms underlying the FLASH effect.

Design optimization of an electron-to-photon conversion target for ultra-high dose rate x-ray (FLASH) experiments at TRIUMF

5.6 Introduction

In the current scope of radiotherapy research and development there has been a recent revival of interest in ultra-high dose rate irradiation as a potential means of widening the therapeutic window. This attention is owed in no small part to the promising normal tissue sparing effects that have been repeatedly demonstrated through high-dose, sub-second treatment fractions at dose rates typically exceeding $100\,\mathrm{Gy\,s^{-1}}$ which has been broadly dubbed the "FLASH" effect [10, 12, 38, 196]. As a result, the demand for new radiation sources capable of achieving the requisite dose rates has grown substantially and yet relatively few compatible sources exist today. Increasing accessibility to a variety of radiation sources and enabling technologies therefore remains important to facilitate ongoing research aimed at improving our understanding, and thus safe exploitation, of FLASH radiotherapy (FLASH-RT) in pre-clinical trials and beyond.

To date, FLASH-RT literature has been dominated by low-energy electron accelerators [11, 45, 48, 94, 126, 204] and, more recently, proton accelerators [129, 130, 198, 205, 206]. Photon modalities, on the other hand, have seen comparatively limited adoption due to the relative unavailability of ultra-high dose rate (UHDR) x-ray sources capable of achieving clinically-relevant megavoltage (MV) beam energies [13, 207]. Moreover, while FLASH-RT has been successfully delivered using synchrotron-generated kilovoltage (kV) x-rays [44], the limited scalability and accessibility of such sources, low penetration of kV photons and the need to use scanned micro/mini-beams in forming UHDR broad beams, serve as limiters to wider adoption. MV x-rays therefore remain as an attractive modality for a future clinical translation of FLASH-RT owing to their highly penetrating nature and, thus, ability to treat tumors at greater depths in tissue. Established accelerator technologies, intensity modulation techniques and treatment planning software also exist which are specific to high energy x-rays and could be adapted for FLASH assuming multi-directional beam delivery can be implemented. By contrast, the prevailing particle FLASH modalities must overcome major barriers ahead of clinical translation. Electron FLASH, for example, may require the use of compact very-high energy electron (VHEE) accelerators (i.e. high gradient or laser acceleration) to enable treatment at greater depths; such sources exist, but require further development to keep pace with the competing modalities in terms of routine application and reliability. Meanwhile, proton FLASH leverages relatively costly infrastructure, excepting those clinical facilities that may be retrofitted, and is subject to the dosimetric challenges associated with FLASH treatment planning using active scanning techniques [208] or field-size dependent dose-rate limitations in passive scattering systems [13].

To facilitate FLASH-compatible x-ray beam generation, already existing high-power sources can be employed; for example, superconducting electron linear accelerators (e-linacs) may be used to

[2] This work was published in *Medical Physics* [53]

deliver high-intensity MeV electron beams to purpose-built bremsstrahlung conversion targets in order to generate the requisite UHDR photon field, while simultaneously providing access to the highly flexible beam parameter space which is unique to the underlying electron source. The development of a photon conversion target suitable to this application represents a primary motivator for this work.

In general, one of the primary difficulties with high-power MV photon sources relates to the bremsstrahlung conversion of electrons to photons in high atomic number (Z) targets. Due to an inherently low conversion efficiency, however, high-Z bremsstrahlung targets designed for a FLASH-compatible UHDR x-ray source must be capable of withstanding very high (i.e. kW) instantaneous beam power, which produces correspondingly high thermal stresses and associated damage within the converter [13, 209]. Furthermore, the target thickness must be optimized for the beam energy, or energy range, of interest so as to maintain UHDR compatibility by minimizing excessive self-attenuation while maximizing cooling performance and ensuring structural integrity over many thermal cycles (i.e. beam pulses). These considerations ultimately motivate the use of thin, sub-centimetric targets for which thermal strain and fatigue become significant challenges during design optimization and a limiter to achievable beam power. Thin-target photon converters have been used in the context of target design for industrial and food processing irradiators and therefore helped form a basis for the design framework employed herein [210].

In this work, the development of a static tantalum (Ta) conversion target and Aluminum (Al) flange using an explosion-bonded interface [211] has been explored with the goal of optimizing dose-rates within the thermomechanical constraints of the target system. The Ta-Al converter, and ancillary systems, have been developed for use on the high-powered electron linac of the Advanced Rare Isotope Laboratory (ARIEL) at TRIUMF (Vancouver, CA). There, a 10 MeV beam dump is being retrofitted to accommodate the new target flange alongside a preclinical treatment apparatus, while preserving its functionality as a low-power dump for e-linac development. The overarching goal was to develop a UHDR platform that will enable time scales of irradiation and intra-pulse dose-rates which are compatible with the prevailing definition of FLASH (i.e. $t < 0.5\,\mathrm{s}$, UHDR$> 40\,\mathrm{Gy\,s^{-1}}$) [12, 40]. Meanwhile, the driving ARIEL e-linac could allow for flexible variation of these temporal beam parameters, namely the pulse time structure and instantaneous (intra-pulse) dose-rates for a given average dose-rate and prescribed dose.

The primary objective of this study was to design and fabricate a modular, cost-effective, yet robust, static photon converter for a 1 kW FLASH beam. The UHDR x-ray target was designed by way of dose-rate and thermomechanical optimization using Monte Carlo (MC) and finite element analysis (FEA) simulation methods. In what follows, the design process and theoretical performance results of the final prototype will be presented.

5.7 Materials and Methods

The development of the ARIEL UHDR x-ray source and FLASH irradiation platform has centered on the design and optimization of a target flange (converter). In addition, the converter is required operate as a non-UHDR beam dump for the ARIEL e-linac under normal (diagnostic mode) operation, which imposed constraints on the target design unique to its use-case at TRIUMF. Designing a suitable converter geometry was an iterative process (Figure 5.4) in which MC simulations (Section 5.7.1) informed geometric constraints while the detailed design and overall assembly were informed using thermomechanical simulations (Section 5.7.2). A detailed overview of the aforementioned methods is presented in the following sections and a summary of the simulation parameter space is provided in Table 5.2.

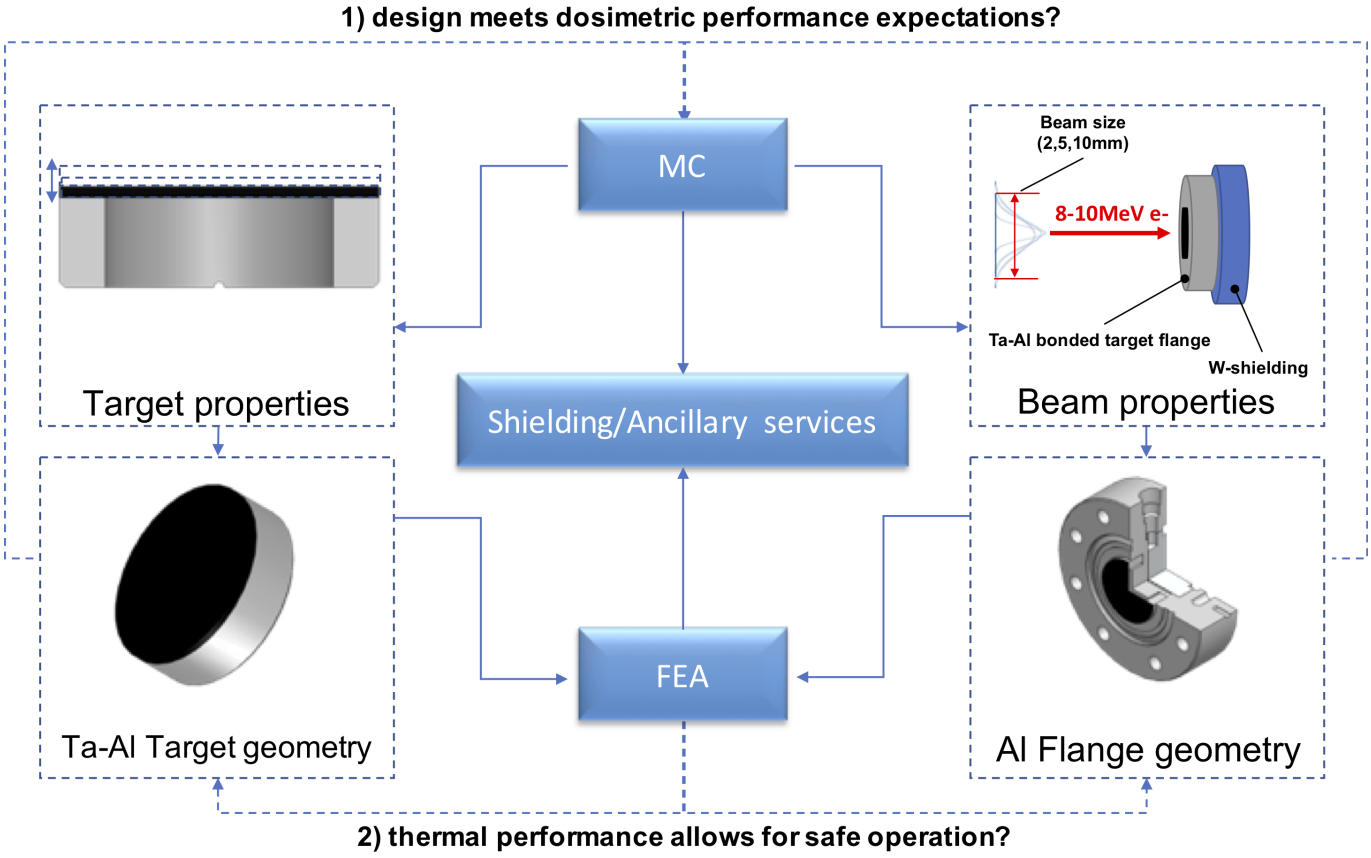

Figure 5.4: Schematic illustration of the ARIEL FLASH converter iterative design process, which included optimization with respect to target thickness, beam energy and size, thermal contacts, water cooling strategy and vacuum interfaces. Design limits were set through dosimetric (1) and thermal (2) performance goals that had to be simultaneously met.

5.7.1 Monte Carlo simulations of x-ray beam production

5.7.1.1 Source Description: The ARIEL e-linac at TRIUMF

The MC simulation of the bremsstrahlung target and resultant dose calculations were completed using a simplified model of the electron beam that will be delivered by the ARIEL superconducting e-linac at TRIUMF (Vancouver, BC).

The ARIEL e-linac is capable of delivering a high-powered megavoltage (MV) electron beam to experiments with excellent flexibility in the choice of physical beam parameters. The time-structure of the beam is nominally characterized by the injector frequency of 650 MHz that produces a continuous (CW) beam, to which a user-specified duty factor between 0.05% and 100% may be applied [97]. Specification of the duty factor allows for varying the average electron beam current over a wide range to enable both conventional and UHDR irradiations and, when paired with a low bunch charge (i.e. 0.15 pC), mitigates the need for re-tuning of e-linac parameters between modes.

At the location of the FLASH conversion target flange, an existing beam dump is being retrofitted for FLASH radio-biological experiments (Figure 5.5). Here, an electron beam can be delivered at energies between 300 keV and 10 MeV, using an average beam power of up to 1 kW, and the emitted x-ray field propagates through the vacuum flange to the ambient air immediately downstream. Operation in a CW diagnostic mode shall be preserved for beam development at a maximum average beam power of 200 W.

For the purposes of MC simulation, the time-structure of the beam was considered to be continuous beam neglecting any possible duty factor. For each simulated case, the electron beam was assumed to be perfectly monoenergetic with the beam spot size modeled as an axisymmetric 2D-Gaussian with a corresponding size characterized by the profile 2σ. At the location of the converter, a zero dispersion beam can theoretically be tuned while maintaining a nearly circular beam ($Y_{rms} = X_{rms}$) for $2\sigma \in [2, 10]$ mm [212] which justifies the use of the aforementioned simplifying assumptions regarding the electron beam properties.

5.7.1.2 Target Description: The electron-to-photon converter

The FLASH photon-converter flange presented here has been designed for routine, modular installation at the end of a horizontal beamline on the ARIEL e-linac, while considering the various space-limiting and safety constraints placed therein. The design included use of a tantalum thin-target "window" (Figure 5.6a) and aluminum body assembled by way of an interference (shrink) fit between an explosion bonded Ta-Al target insert (plug) and a water-cooled T6-tempered Al-6061 flange (Figure 5.6b,c). Aluminum was removed from the plug after explosion bonding, thereby creating the aluminum cylindrical interface (corona) attached to the tantalum layer.

One major requirement for converter design was to ensure that the primary electrons entering the flange would be stopped fully to avoid an excessive electron surface dose in the phantom. To

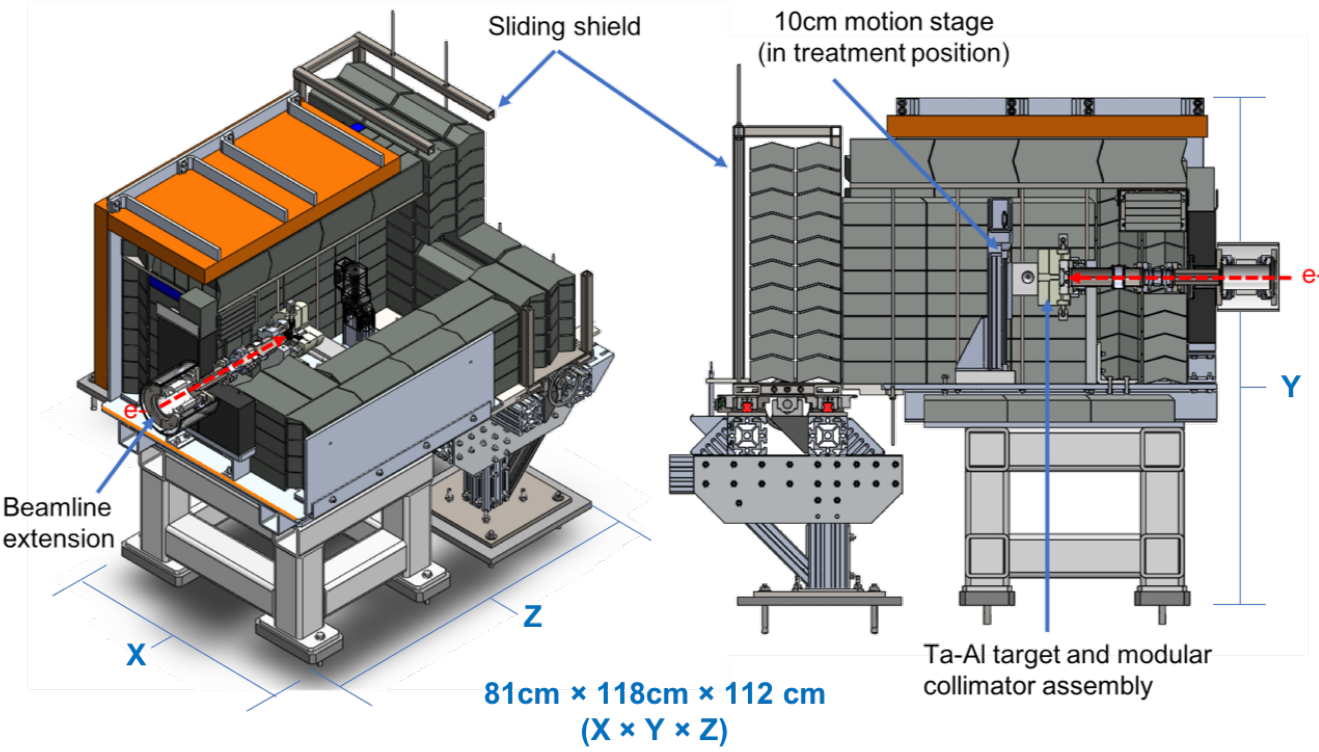

Figure 5.5: Computer-aided design (CAD) model of the ARIEL FLASH irradiation platform at TRIUMF. A retrofitted beam dump is leveraged to support a new, modular small-animal treatment apparatus which includes: Ta-Al target flange (which is also the vacuum window), modular x-ray collimator, electron collimator and target protection system, insulated beamline extension (for real-time current readback), sliding shield and access hatch, 10 cm vertical-motion treatment stage, and small-animal (i.e. mouse) localization/immobilization assembly.

achieve this, the combined thickness (t) of the tantalum target and aluminum flange body in the beam direction exceeded the CSDA range of the highest (10 MeV) energy electrons [i.e. at 10 MeV: $R_{CSDA,Ta} = 0.3728\,\text{cm}$; $R_{CSDA,Al} = 2.1716\,\text{cm}$]. Mathematically this condition can be described as follows [210]:

$$\left(\frac{t}{R_{CSDA}}\right)_{Ta} + \left(\frac{t}{R_{CSDA}}\right)_{Al} > 1.0 \tag{5.1}$$

It should be noted that, for all MC simulations presented herein, the aluminum flange thickness was fixed at 1.9 cm based on practical manufacturing considerations. For a nominal 1-mm tantalum target thickness, the left-side of Eq. 5.1 equates to 1.14, a value which exceeds unity and therefore satisfies the condition that the left-hand side exceeds unity. The implications of target thickness will be discussed in the context of the simulation results (Section 5.8.1).

The selection of tantalum for the target was predicated on the need for a high-Z material that would maximize the bremsstrahlung x-ray conversion efficiency, while also providing favorable thermomechanical properties, most notably a high melting point and excellent ductility. The robustness of tantalum under high heat loads, good tolerance to radiation damage, and long lifetime under cyclic

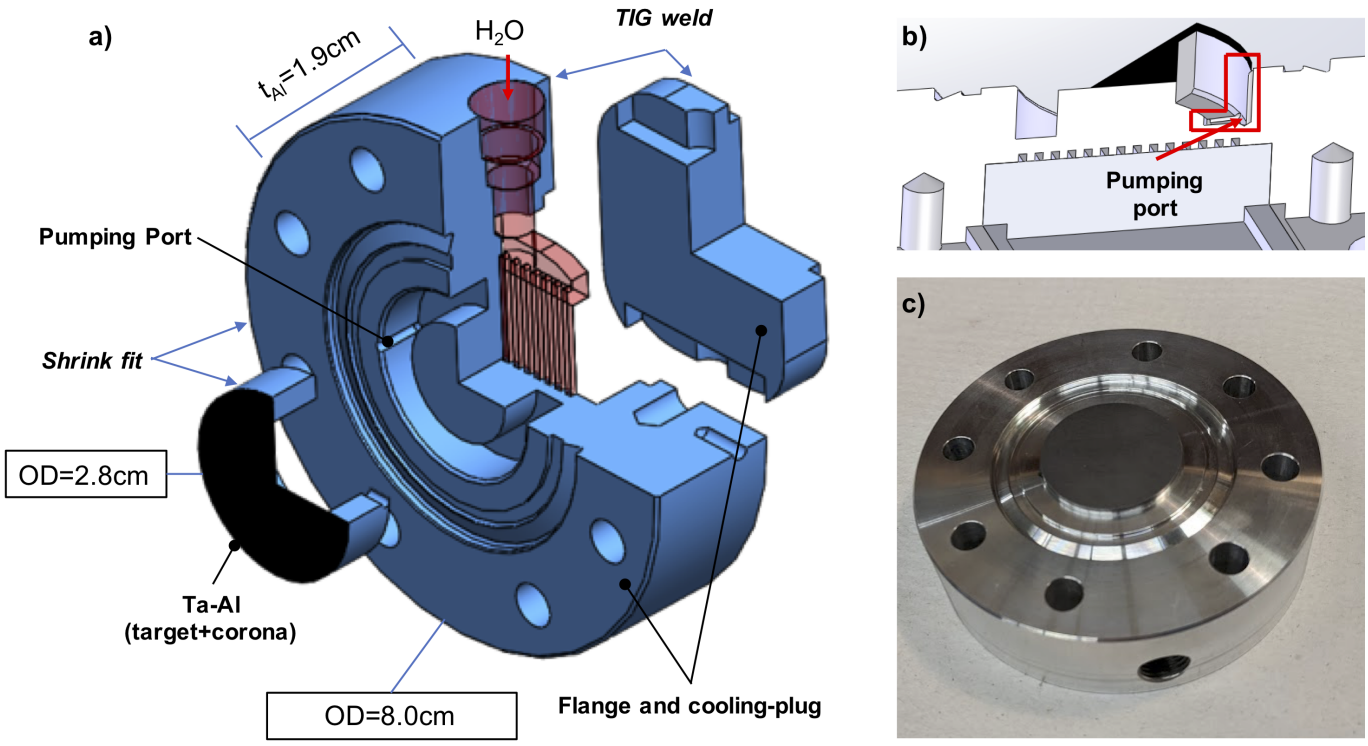

Figure 5.6: Sectioned and exploded CAD model for the conversion target (a) in which the various components (bold text) and assembly methods (italicized) are outlined. Included are the tantalum target (black), aluminum corona and flange (blue) and cooling water channels (red). A close-up view of the target 'window' is shown (b) with the vacuum (conductance-limited) pumping port labelled. The assembled prototype, which is currently undergoing thermal benchmarking, is also pictured (c). [TIG=tungsten inert gas welding; OD=outer diameter; t_{Al}=flange thickness]

thermal loads supports the material as an effective choice for the thin-target design [213, 214]. As compared to tungsten, which is commonly used in transmission x-ray targets, tantalum benefits our unique application by having a much lower ductile-to-brittle transition temperature that is important for maintaining ductility over the wide range of operational temperatures that it will be expected to withstand [107, 215–217]. The use of aluminum 6061 in the flange, by contrast, is motivated by the comparatively low Z and photon interaction cross-section of the material, which also boasts high thermal and electrical conductivity to allow for improved heat transport.

The computer-aided design (CAD) models for the entire converter geometry (Figure 5.6), alongside ancillary beamline components (Figure 5.5), were designed in SolidWorks® Professional 2020 (Dassault Systemes, Vélizy-Villacoublay, France) and were directly imported into the subsequent thermal and mechanical finite element analysis (FEA) simulations (Section 5.7.2). For the purposes of this work, the final prototype and associated simulation outputs will be presented.

5.7.1.3 Dose calculations and simulation geometry

MC dose calculations were employed to establish the theoretical performance of the converter based on identification of optimal target and beam parameters that ensure the performance goals of the project could be met within the thermomechanical constraints of the system. To this end, the converter flange assembly (Figure 5.7) was modeled in EGSnrc/BEAMnrc(v 2020) [142].

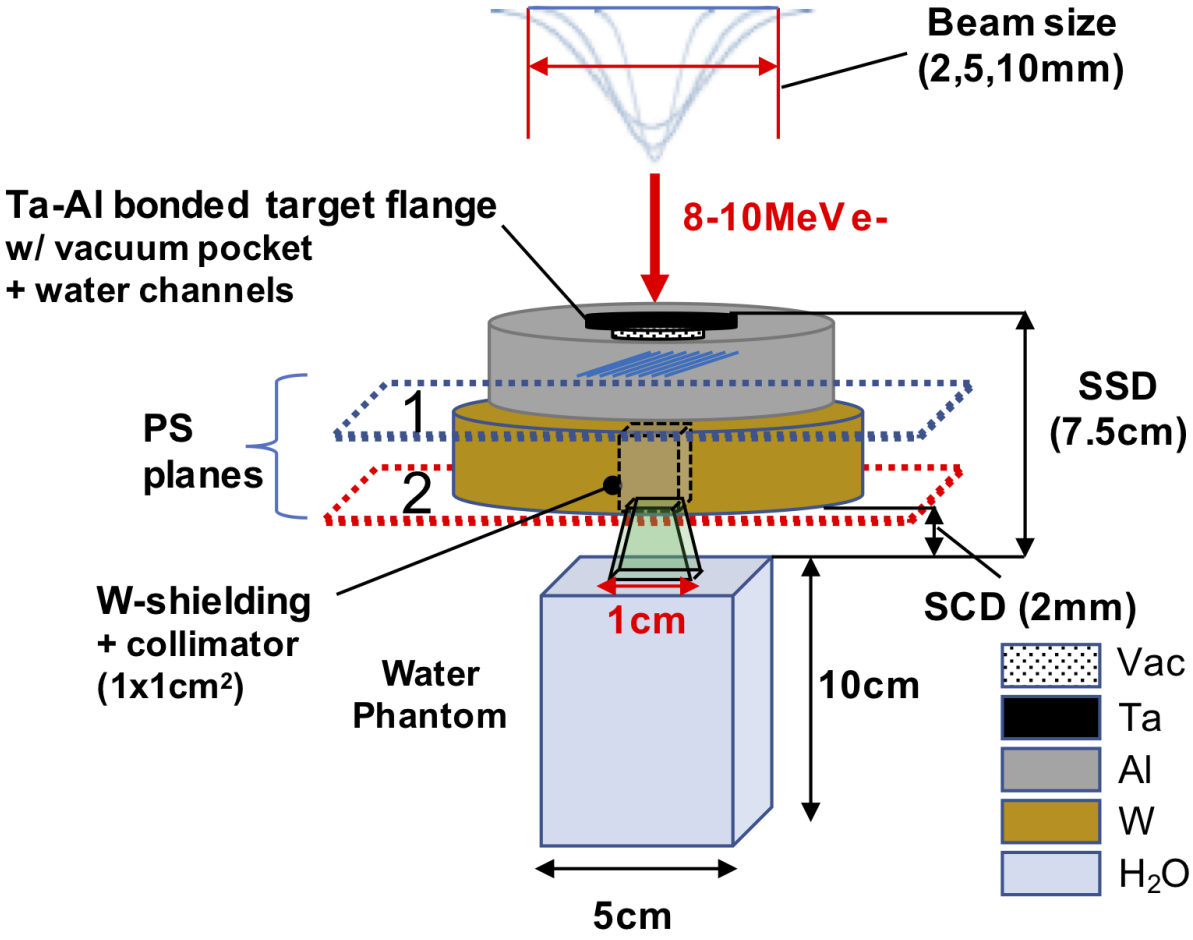

Figure 5.7: Schematic illustration of the water-cooled converter simulation geometry modeled in the EGSnrc MC codes. Phase-space (PS) scoring planes were located between the Al flange and W collimator, and at the $1 \times 1\,\text{cm}^2$ collimator exit. The $5 \times 5 \times 10\,\text{cm}^3$ phantom was located at a nominal distance of 7.5 cm for all DOSXYZnrc phantom simulations using files from PS#2 (red plane) as source inputs with the exception of the open field simulation, which used files from PS#1. The source-to-collimator distance (SCD) was fixed for all simulations at 2 mm, excepting the mouse phantom simulation (Section 5.7.1.4) for which an SCD of 7 mm was used. The $1 \times 1\,\text{cm}^2$ collimator was used to define the field size.

To study the influence of target geometry and beam parameters on dose rate, a discrete set of parameters were investigated in the course of the target design optimization based on informed constraints. Specifically, the effect of target thickness (t = 500, 1000 and 1500 µm), electron beam size (2σ =2, 5, 10 mm) and beam energy (E = 8, 10 MeV) were considered (Table 5.2). The limited energy

range was chosen for practicality with the converter design and suitability to MV UHDR irradiations. Note that beam size shall everywhere refer to the size of the primary electron beam, whereas field size refers uniquely to the x-ray beam and is defined by the downstream tungsten collimator. In all simulations, the x-ray fields were shaped by the $1 \times 1\,\mathrm{cm}^2$ collimator unless otherwise specified (i.e. for an open field).

Table 5.2: Summary of MC simulation parameters to be optimized in this work.

Power	1 kW
Energy	8, 10 MeV
Electron Beam Size	2, 5, 10 mm
Target Thickness	0.5, 1.0, 1.5 mm

In a first simulation step, the impinging electron beam was transported through the Ta-Al target and flange geometry. For each simulated configuration (Table 5.1), 10^6 electrons with initial kinetic energies of either 8 or 10 MeV were made to impinge upon a thin Tantalum film – the target 'window' – and transported through the water-cooled flange which comprised a 2-cm thick aluminum body (flange) and fifteen $1\times1\,\mathrm{mm}^2$ square cross-sectional water channels. The 5-cm thick, $1\times1\,\mathrm{cm}^2$ field-size tungsten collimator was additionally included (Figure 5.7) in order to produce a more representative treatment field size, and conformal dose distribution, along the beam central axis (CAX). Phase-space files were scored at various interfaces in order to facilitate the analysis of relevant beam properties (PS#1,2; Figure 5.7).

In order to improve the efficiency of the x-ray beam simulations, directional bremsstrahlung splitting with a splitting factor of 200 was used together with a bremsstrahlung cross-section enhancement factor of 20 in the tantalum target. To improve contaminant electron statistics, $e-/e+$ splitting was activated for the aluminum flange which was modelled using the FLATFILT geometry and included the cooling water channels and vacuum pocket.

In a second simulation step, the phase-space files generated in BEAMnrc were used as source inputs for depth-dose simulations in a $(5\times5\times10)\,\mathrm{cm}^3$ water phantom using the DOSXYZnrc code [184]. The phantom thickness was selected to ensure full backscatter conditions in a 10 MV beam rather than be representative of pre-clinical models. Each phase-space source contained $> 10^7$ particles. The phantom was located at a source-to-surface distance (SSD) of 7.5 cm and the absorbed dose was scored in uniform $0.2\,\mathrm{mm}^3$ voxels. The SSD was fixed at 7.5 cm, so as to represent the nearest location for the surface of small-animal models which will be placed in an irradiation jig (not shown) located immediately downstream of the collimator assembly. The air gap between the collimator exit surface and water phantom surface, or collimator-to-surface (CSD), was fixed at 2 mm unless otherwise specified.

For each DOSXYZnrc simulation, the full phase-space was run, without any recycling of particles, resulting in a statistical uncertainty within high-dose regions of less than 0.9%. The calculated dose,

expressed in Gy/particle, was converted to dose-rate ($\mathrm{Gy\,s^{-1}}$) by assuming the maximum beam current, for each beam energy, that would correspond to an average power of 1 kW (i.e. 0.1 mA for 10 MeV). The dose conversion was accomplished by way of the following formula: $dD/dt(\mathrm{Gy\,s^{-1}}) = dD/dt(\mathrm{Gy\ particle^{-1}}) \times I(\mathrm{A})/1.602 \times 10^{-19}\,\mathrm{C}$, where I is the time-invariant electron beam current in $\mathrm{C\,s^{-1}}$. Unless otherwise specified, all PDD dose-rates are calculated as averaged values in a $0.5\,\mathrm{cm^2}$ ROI about the CAX at each depth. Beam penumbra are calculated as the interpolated lateral distance between points on the beam dose profile which correspond to 80% and 20% of the maximum dose at a treatment depth of 1 cm.

For all EGSnrc simulations, the electron and photon kinetic energy cutoffs were set to 150 keV and 5 keV, respectively. Low energy physics, such as atomic relaxation, and Rayleigh scattering were included, while electron impact ionization was ignored. The xcom cross section data was used. The remaining EGSnrc input parameters were set to their default values. All simulations were run on 3.06 GHz 6-Core Intel® Xeon processors using a local high-performance computing cluster. The BEAM simulation time was between 39-50 hrs while each DOSXYZnrc simulation completed in < 5 hrs.

5.7.1.4 *in vivo* dose distribution using a rodent-morphic 3D-printed mouse phantom

A brief MC study of the dose distribution in a sample mouse lung-irradiations was completed to demonstrate the theoretical dose distributions that might be expected for unidirectional, single-fraction irradiation of a mouse model *in vivo*. The material properties of the phantom are such that there is negligible energy-dependence for x-ray beam energies > 1 MeV based on the effective atomic number and predominance of the Compton scattering cross-section [66,67]. However, for the purposes of this study, the materials in the lung and bone were selected to be that of a biological mouse as opposed to the polymeric materials comprising the 3D-printed phantom to be used for treatment dose verification ahead of planned irradiation campaigns. Specifically, ICRU Report 44 [218] densities were used for bone ($\rho = 1.6\,\mathrm{g/cm^3}$), lung ($\rho = 0.58\,\mathrm{g/cm^3}$) and soft tissue ($\rho = 1.06\,\mathrm{g/cm^3}$) body for the MC simulated mouse geometry.

For the purposes of this work, a single unidirectional lung irradiation was simulated in the mouse phantom using the reference 10 MV FLASH beam, generated in BEAMnrc (Section 5.7.1.3) assuming a 5-mm electron beam size and a 1000-um thick tantalum target. The voxelized geometry data for the phantom was imported directly into DOSXYZnrc as an .egsphant file and the dose-rate for a 1 kW exposure was calculated for the $1 \times 1\,\mathrm{cm^2}$ collimated field (scored at PS2, Figure 5.6) using the dose conversion specified in the previous section. A nominal treatment SSD of 8 cm (SCD=7 mm, see Figure 5.7) was used as it corresponded to the closest position for the irradiation and jig and motion stage assembly (Figure 5.5). The beam was incident on the mouse right flank with beam isocenter assigned to the geometric center of the mouse lung. Dose contours were visualized using the online VICTORIA [219] software while the dose-rate profiles are calculated for a central $0.5\,\mathrm{cm^2}$ ROI about the CAX from which lateral and depth-dose distributions could be derived.

5.7.1.5 Converter energy deposition and material activation

To provide accurate heat inputs to thermomechanical converter simulations (Section 5.7.2) the FLUKA MC code (version 2020.0) was employed to score volumetric energy deposits throughout the flange and target geometries. These results were then used, with appropriate re-formatting, as power inputs to FEA simulations (Section 5.7.2). FLUKA was employed in this capacity due to the existence of a well-developed pipeline that couples MC and downstream FEA simulations, along with flexible scoring options within the target geometry and calculations not available to EGSnrc, such as neutron transport and photo-activation.

For each electron beam size, 10^7 primary histories (8 or 10 MeV electrons) were transported through a model of the shielded irradiation platform (Figure 5.5). The simulated converter geometry was as described in Section 5.7.1.3, excepting the target thickness which was fixed at 1000 µm for the results presented herein. Three-dimensional energy deposition maps were scored in $0.5 \times 0.5 \times 1\,\mathrm{mm}^3$ voxels, and results were output in terms of power density ($\mathrm{W\,cm^{-3}}$) with statistical uncertainties of less than 2% for all voxels with power densities $> 1\,\mathrm{W\,cm^{-3}}$, including everywhere within the beam impingement region. Photo-fission and subsequent neutron activation within the entire irradiation station was simulated to evaluate the resultant activation and inform safe handling according to the possible equivalent dose to personnel. Equivalent dose was scored in $\mathrm{mSv\,hr^{-1}}$ at a distance of 0.5 m from the target center after 1 week of continuous CW irradiation at 1 kW and 10 MeV, equivalent to FLASH mode operation at 100% duty factor; this is opposed to the more realistic low-frequency scenario with < 1 s beam-ON time and a low total number of irradiations (< 50) lasting less than 1 week. Results assumed emission from a point source at the location of the target and without any self-attenuation in, or shielding of, the activated components for added conservatism.

For all FLUKA simulations, the transport energy threshold for delta rays (electrons) were set to 200 keV. Optional physics models that were implemented to include evaporation, coalescence, electro-magnetic dissociation (projectile and target), heavy-ion direct pair production. The standard cross-section libraries were used and no variance reduction was applied. Simulations were run on a quad-core i7-6700 CPU at 3.4 GHz and completed within 12 hrs.

5.7.2 FEA thermal and structural simulations of the electron-to-photon converter

Thermomechanical simulations were employed to establish an efficient and practical design for the compact photon converter flange. The FEA software package ANSYS® [2020 R2] (Canonsburg, PA) and, specifically, the static and transient Mechanical and Thermal modules in Workbench 2020 R2 were used to simulate the steady-state and transient thermomechanical responses. The parameterized design study considered the same configurations as for MC simulations (Table 5.2). In addition, all FEA simulations utilized conservative assumptions as relates to physics inputs, including convection coefficients, water flow rates, and thermal conductance values by applying a safety factor of 2 in

each case. In this way, an engineering safety margin could be built in while maintaining additional confidence in the robustness of the final design (Table 5.3). Temperatures (°C), von Mises stress (MPa) and elastic/plastic strain (m/m) distributions were evaluated for each case. The von Mises stress applies to a yield criterion which states that where this stress is equal or greater than the yield strength of a material, defined under uniaxial tension, the material will yield. The von Mises yield criteria and subsequent stress-strain analyses were considered suitable to the ductile nature of the critical metallic target components.

SolidWorks® CAD geometries were imported into the ANSYS® design modeler while power density inputs, as calculated in FLUKA (Section 5.7.1.5). An unstructured tetrahedral mesh, with element sizes of 0.7–1.5 mm, was used for the aluminum flange body while the Tantalum target plug was modeled using a hybrid hexahedral mesh, with element sizes of 0.25–0.5 mm, for improved regularity and accuracy; default mesher settings were otherwise employed. The resulting geometry comprised 4.07×10^5 elements. All interfaces (Ta-Al, and Al-Al) used in the downstream mechanical simulations were assumed to be bonded while the Al-Al shrink fit interface was assigned a manually-input thermal conductance of $4720\,\mathrm{W\,m^{-2}\,K}$, extrapolated from experimental data examining cylindrical Al interfaces under similar conditions [114]. In this case, the lowest temperature regime, modest (1000 psi) contact pressures, and a 65 microinch (root-mean square) RMS surface roughness were assumed. The cooling channels were assigned a convective heat transfer coefficient (h) of $3.2 \times 10^4\,\mathrm{W\,m^{-2}\,K}$, calculated based on the dittus Boelter correlation [113] for water in square cross-sectional channels with 1 mm hydraulic diameter; this value was verified using ANSYS computational fluid dynamic simulations (CFD module) which included the same water-cooling channel design as in the Mechanical simulations while assuming a water flow-rate of 4.5 lpm and bulk temperature of 30 °C. Thermal radiation effects for the target were included by setting a conservative emissivity of 0.1 on the tantalum surface. It is worth noting that both the heat transfer coefficient and Al-Al thermal conductance values used were input as 50% of their calculated values in order to elicit a safety factor of at least 2 (see Table 5.3). In all structural simulations, engineering material data, including temperature-dependant ultimate tensile and yield strengths, linear expansion coefficients, density, elastic moduli, and conductivities, were taken from standard libraries or compiled reports on material properties such as for 6061-T6 aluminum [220, 221] and tantalum [222, 223].

Fatigue analysis in the flange was approached separately for the tantalum and aluminum materials. The calculation of fatigue life in the tantalum layer followed from the assumption of a purely elastic stress-strain model and used the ANSYS fatigue tool's parameterized strain-life equations with Morrow mean-stress correction. The coefficients for the model were derived for the highest temperature data (1350°F) in argon available from LaForce *et al.* (1971) [213]. It is worth noting that tantalum plasticity was modeled in an identical set of simulations, without fatigue modelling, where the stress and corresponding plastic strain within the entire flange geometry could be evaluated. For estimating the fatigue behavior of the aluminum parts, an empirical fit to ASME-derived

stress-cycle curve data was used as the basis for estimating the fatigue life, or number of cycles (N), in the Al-6061 bodies [224, 225]. The governing equation, which assumes fully reversed loading and thus requires the Goodman mean-stress corrected stress amplitude (S) as input, takes the following form:

$$S = \frac{14479}{\sqrt{N}} + 96.5\,\text{MPa} \tag{5.2}$$

In the above formalism, S was calculated from the Goodman equation $S = S'/(1 - S_m/S_u)$, wherein S_m is the mean stress, or half the sum of the stress amplitude and shrink-fit pre-stress as calculated from the corresponding ANSYS simulation, S_u is the ultimate tensile strength taken from the literature and S' is the stress amplitude for the case of non-fully reversed loading. Given that steady-state diagnostic operation at lower beam power accounts for the largest contributor to cyclic thermal loading, the aluminum corona is assumed to act as the fatigue-life limiting material, whereas for high-power FLASH (pulsed) operation, the fatigue life of the tantalum becomes relevant, particularly in off-normal condition use (i.e. accidental power spikes or beam trip). Radiation-induced embrittlement is not accounted for and oxidation is ignored due to the extremely low oxygen and hydrogen partial pressures in the UHV (10^{-9} mbar) beamline. However, it is recognized that pressures behind the target window may be elevated (up to 10^{-4} mbar)[3] due to the reduced pumping speed afforded by the conductance-limited pumping port in the converter (Figure 5.6) and may contribute a possible oxidation risk[4].

Table 5.3: Summary of custom FEA simulation and material parameters of relevance to thermal and structural (static and transient) modules. Quoted quantities are set to 50% of their calculated values, equivalent to applying a safety factor of 2.

Convective heat transfer coefficient (for water channels)	$16\,000\,\text{W m}^{-2}$
Thermal conductance (Al-Al, shrink fit)	$2360\,\text{W m}^{-2}$
Thermal conductance (Ta-Al)	Ideal, bonded
Emissivity (Ta)	0.1
Interference fit (Al-Al, contact gap)	-1×10^{-5} m
Strain-life model (Ta)	LaForce *et al.* 1971 [213]

The time required for convergence during steady-state thermal simulations, which employed a single simulation step, was approximately 1 min, while transient thermal simulations utilized adaptive time stepping over a 3 s of simulated time and converged within 30 min. Static structural simulations were completed using 10 substeps and converged in $<$ 30 min while transient simulations used the same time stepping parameters as the transient thermal analyses, converging within 6 hrs. All simulations were run in parallel (4 threads) on a quad-core i7-6700 CPU at 3.4 GHz.

[3] This presented a worst case assessment of the analysis that was conducted. Vacuum simulations including a more representative model of the vacuum pressure is presented in Appendix A.4 and A.4.2

[4] Subject is explored in some detail in Appendix A.4

5.8 Results

The results of MC simulations in a homogeneous water phantom are presented in the forthcoming section (Section 5.8.1). These results were used to motivate the selection of beam and target parameters for future irradiations and provided a basis for selecting the more conservative beam configurations for use in subsequent thermomechanical simulations (Section 5.8.2). All MC results presented herein were simulated according to the methods outlined in Section 5.7.1.

5.8.1 Monte Carlo simulation of x-ray beam production

The effects on depth-dose rates due to variation of the tantalum target thickness for both beam energies, keeping the electron beam size constant, is presented in Figure 5.8. The 500 µm target showcases a large dose enhancement of up to 48% at shallow depths ($z < 1$ cm) for the 10 MV beam. This feature, absent in the 8 MV beam data, is contributed by an increase in low-energy primary electron transmission amounting to an 86.7% increase in electron energy fluence compared to the cases where only secondary electrons were present. This enhancement is illustrated via the electron energy fluence spectra for the 500 µm target at the surface of the water phantom for the 5 mm electron beam (Figure 5.8b). The 1000 µm target, by contrast, proved capable of removing the primary electron fluence and leaving only secondary electrons which were generated within the flange body (Al) and W-collimator and are primarily responsible for the lack of a depth-dose build-up region.

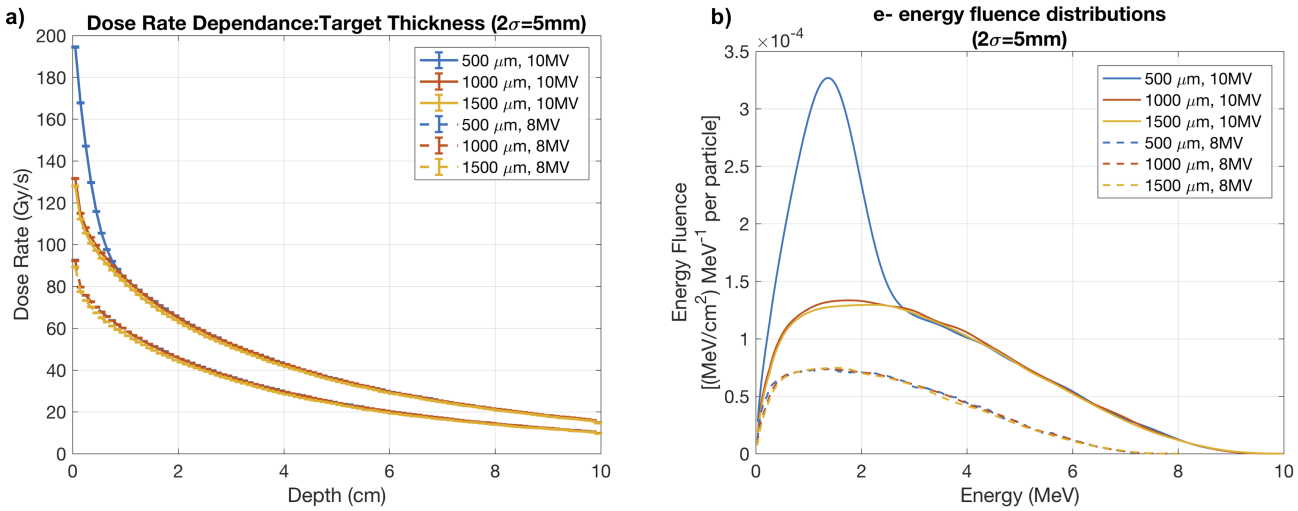

Figure 5.8: The effect of Ta target thickness on the dose-rates as a function of depth for both candidate beam energies (a) and field size of $1 \times 1\,\text{cm}^2$. A demonstration of the primary electron transmission in the 500 µm target configuration at 8 and 10 MeV is shown (b) by way of the electron energy fluence spectra which is normalized by the field size, energy bin width and number of primary histories.

The effects of changing electron beam size and energy were also considered for the 1000 µm tantalum target (Figure 5.9). Figure 5.9a showcases the changes in dose-rate with an electron beam

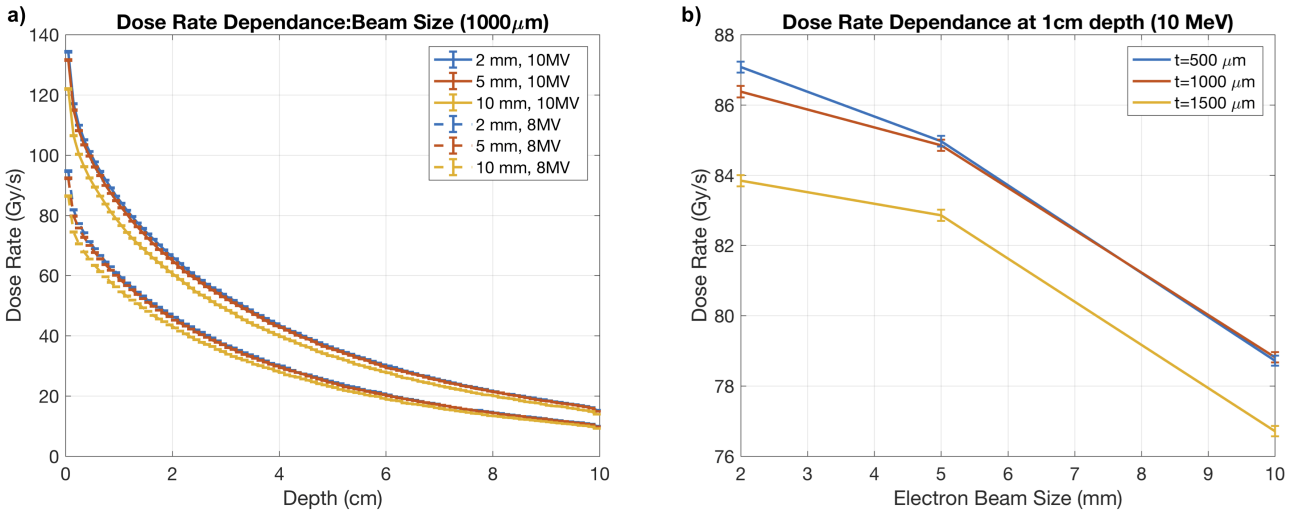

Figure 5.9: The effect of electron beam size (Gaussian 2σ) on the depth dose-rates for both candidate beam energies (a) on a 1 mm Ta target. A summary of the dose-rate dependence of the $1 \times 1\,\mathrm{cm}^2$ 10 MV beam on target thickness and beam size, at a representative treatment depth of 1 cm in the water phantom, is presented in b). The sample depth was selected for its relevance to pre-clinical treatments and to avoid the possibility of the dose-rate varying due to differences in the contaminant electron dose observed at the phantom surface.

size across both candidate energies (8, 10 MeV). At 10 MV, a 6.8% depth-averaged increase in dose-rate is found by reducing the beam size from 10 mm to 5 mm; this difference is slightly reduced at 8 MV, with average difference of 6.0%. In contrast, there is only a marginal increase (1.4%) in dose-rate when further reducing beam size to 2 mm for both beam energies. Moreover, an incoming electron beam energy of 10 MeV yielded 31.7% higher dose-rates when compared to an 8 MeV beam, providing a clear incentive to employing the higher beam energy during FLASH irradiations.

A summary of the dose-rate dependence on electron beam size and target thickness are summarized by way of Figure 5.9b for a 10 MV FLASH beam at the treatment SSD (7.5 cm) and depth ($z = 1$ cm) within the homogenous water phantom. The dose-rate plot in figure 5.9b shows low sensitivity to changes in target thickness between 500 µm and 1000 µm, and to changes of beam size between 2 mm and 5 mm. The 500 µm target provides a marginal dose-rate increase for the smallest beam size (2 mm) only and the 1500 µm target is everywhere sub-optimal with respect to dose-rate. Hence, the nominal operational conditions comprise a target thickness of 1000 µm to minimize primary electron contamination, while maximizing dose rates, and a 5 mm beam size to keep temperatures in the tantalum low, as will be shown in Section 5.8.2.

The largest impact of changing target thickness is observed in a 'filtration' of the spectrum, predominantly below the pair-production peak at 511 keV (Figure 5.10). A summary of the change in relative energy content for beam spectra produced by the 500 µm and 1000 µm or 1500 µm targets is summarized in Table 5.4, where the energy integral differences are calculated from the energy fluence spectra in Figure 5.10b. The photon mean energies of the various beam configurations, scored in a

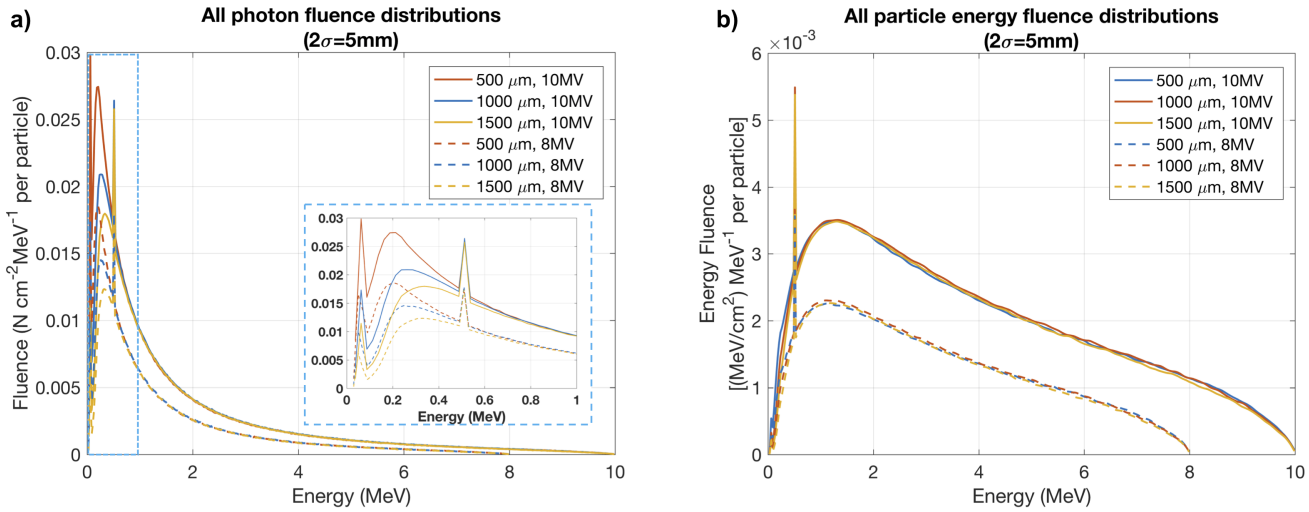

Figure 5.10: Normalized photon fluence (a) and total (all particle) energy fluence spectra (b) for beam configurations of interest in this work. The inset in (a) highlights the spectral range up to 1 MeV and illustrates the low-energy sensitivity of the electron beam spectra to changes in target thickness. All beams assumed the 5-mm (2σ) beam size. Spectral quantities are normalized by the field size, energy bin width and number of primary histories.

$1 \times 1\,\text{cm}^2$ area along the CAX at the location of the phantom surface (at 7.5 cm SSD), are shown in Table 5.5.

Table 5.4: Integrated 10 MV all-particle energy fluence (relative) differences between target thickness configurations and for various energy ranges [spectral ranges: < 511 keV, > 511 keV, or full spectrum]. All spectra were evaluated at the collimator exit (PS#2, Figure 5.7).

	10 MV			**8 MV**		
[A,B][a]	< 511 keV	> 511 keV	Full	< 511 keV	> 511 keV	Full
[500,1000]	15.36%	-1.11%	-0.47%	10.26%	-1.17%	-0.74%
[1000,1500]	13.25%	2.05%	2.42%	9.31%	2.02%	3.20%

[a] The spectral differences between the target thickness configurations are calculated as the following integral ratio (R): R=(A-B)/max(A,B) where A and B are integrals over the energy fluence curves designated by the target thicknesses (in µm) under consideration.

The 2D dose profiles corresponding to each electron beam size, at the phantom surface and a depth of 1 cm, are shown in Figure 5.11 for a 1000 µm thick target and the 10 MV beam. While smaller beam spots confer an advantage in dose-rate and a sharper beam penumbra (see Table 5.6), they produce higher thermal stresses within the tantalum layer and are thus detrimental to the converter's design life, as will be demonstrated in the following section 5.8.2.

Figure 5.12 illustrates the effects of removing the collimator, and thereby allowing for samples to be placed closer to the tantalum target - to within 3.5 cm SSD. The dose maps of Figure 5.12(b,c)

Table 5.5: Mean photon beam energies for a $1x1\,\mathrm{cm}^2$ collimated field evaluated at the phantom surface.

Target thickness (µm)	10 MV	8 MV
500	1.63 MeV±0.05%	1.39 MeV±0.05%
1000	1.76 MeV±0.05%	1.42 MeV±0.05%
1500	1.84 MeV±0.04%	1.56 MeV±0.04%

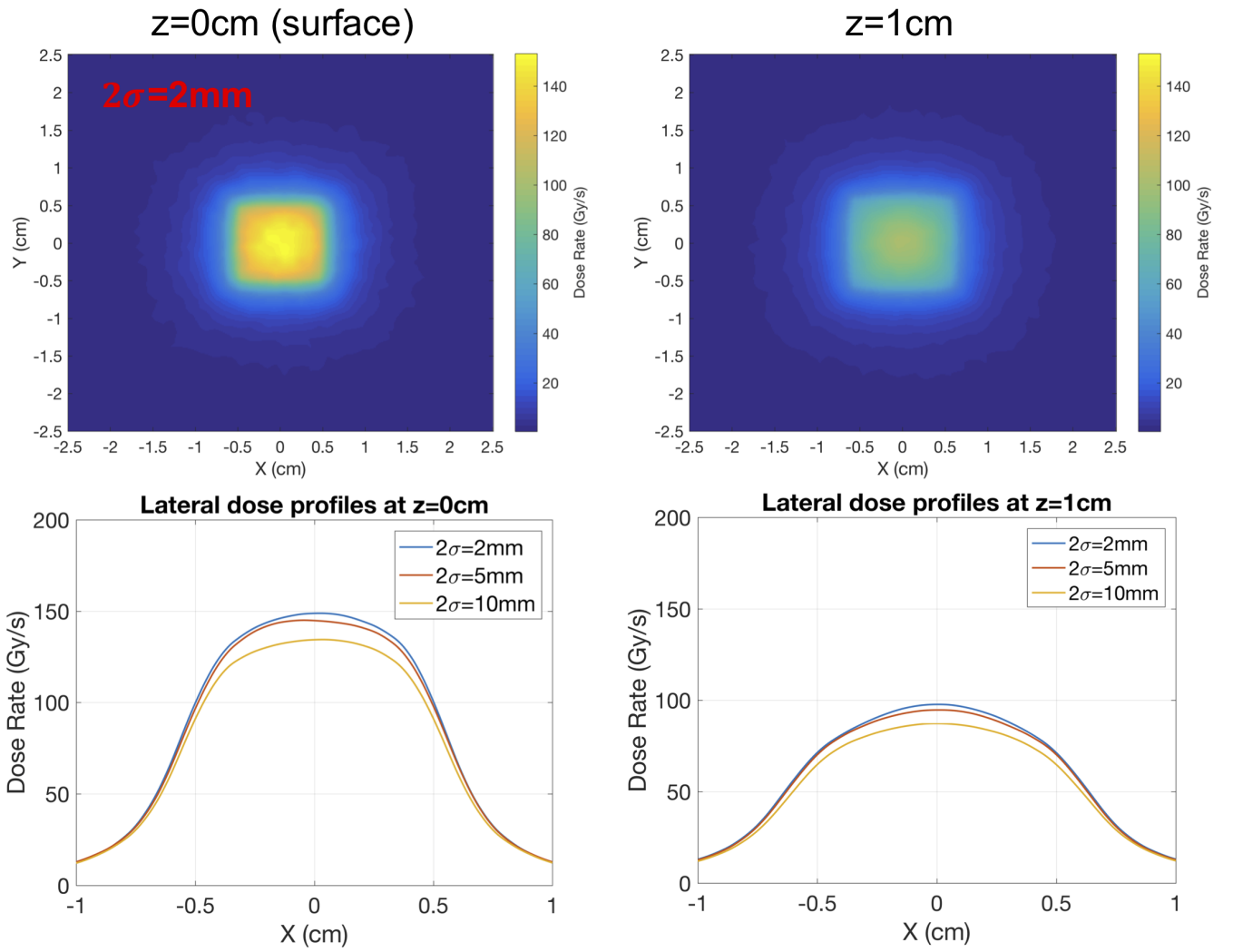

Figure 5.11: Representative 2D dose maps for the $1 \times 1\,\mathrm{cm}^2$ collimated x-ray field produced by a 10 MeV electron beam (Gaussian size: $2\sigma = 2\,\mathrm{mm}$) impinging on a 1000 µm Ta-target. Doses at the surface (left column) and at 1 cm depth (right column) in the homogeneous water phantom are shown for a treatment SSD of 7.5 cm.

showcase the tradeoff in dose-rate and field conformality at the phantom surface for with and without the $1 \times 1\,\mathrm{cm}^2$ collimator at SSDs of 7.5 and 3.5 cm, respectively. The corresponding PDDs are shown in Figure 5.12d while the normalized beam half-profiles, which highlight relative changes in the lateral dose distribution, are shown in Figure 5.12e. Evidently, the collimator succeeds in producing

Table 5.6: 80-20 beam penumbra (in mm) for all electron beam sizes for the $1 \times 1\,\mathrm{cm}^2$ collimated 10 MV beam at 7.5 cm SSD. The values in square brackets correspond to the FWHM (in cm) for the same beam profiles.

2σ Beam Size (mm)	80-20% penumbra (mm) [FWHM (cm)]	
	Surface	z=1-cm depth
2	3.012 [1.161]	4.235 [1.256]
5	3.011 [1.141]	4.046 [1.266]
10	3.043 [1.136]	3.984 [1.271]

a $1\,\mathrm{cm}^2$ square field size comprised of dose-rates $> 40\,\mathrm{Gy\,s^{-1}}$, as required, with only a slight (≈ 1 mm) broadening at the nominal 1 cm treatment depth. The open field, on the other hand provides peak dose-rates in excess of $600\,\mathrm{Gy\,s^{-1}}$, but with significant beam broadening and an increased depth-dose gradient. For example, at 1-cm depth the gradients are found to be $\dot{dD}/dx = -22.7$ and -164.7 $\mathrm{Gy\,s^{-1}\,cm^{-1}}$ for the collimated and open-field beams at 10 MV, respectively. At 8 MV these gradients are correspondingly increased to $\dot{dD}/dx = -17.2$ and $-135.6\,\mathrm{Gy\,s^{-1}\,cm^{-1}}$.

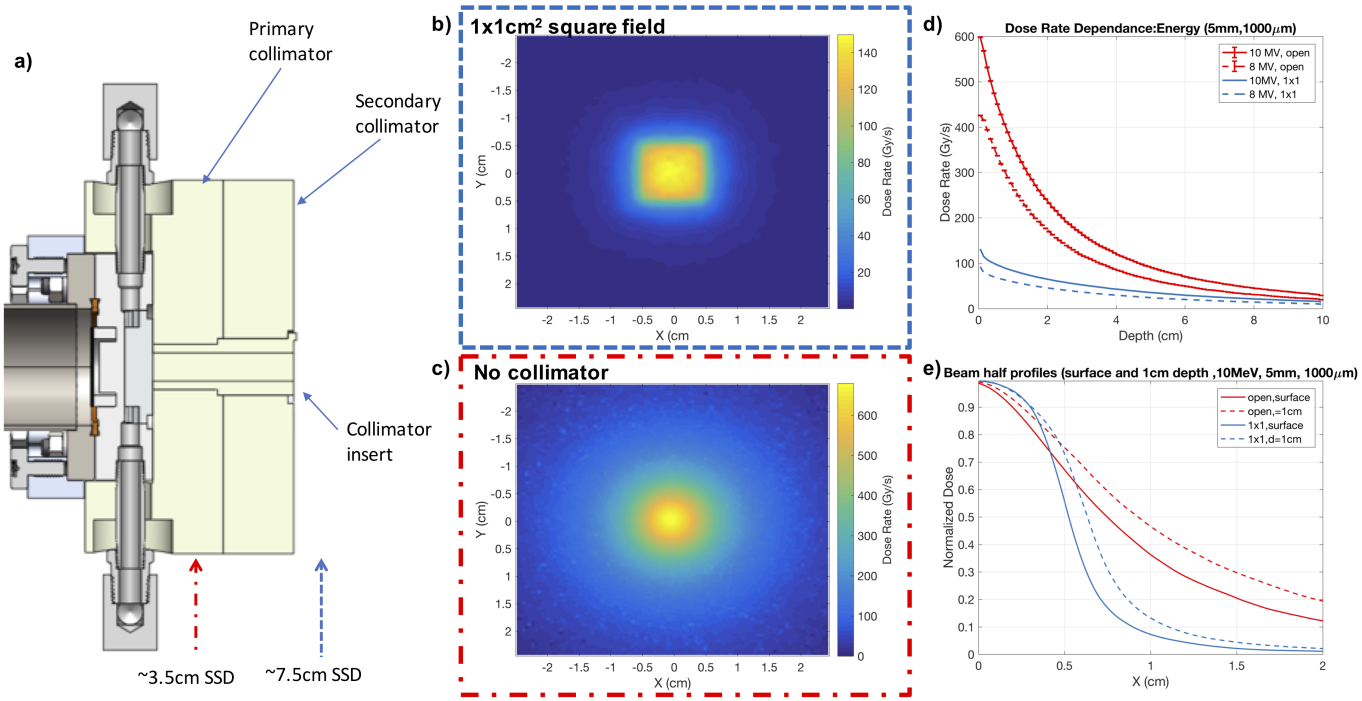

Figure 5.12: Cutaway model of the modular W-collimator assembly (a) which allows for flexible selection of field size depending on whether the primary and secondary collimators are mounted. A set of 3D-printed tungsten inserts can allow for custom field shaping or flattening filter insertion based on use-case. The collimated (b) and open (c) fields are illustrated to showcase the dose-rate enhancement afforded by the latter. The treatment SSD of the open (SSD=3.5 cm) and collimated (SSD=7.5 cm) fields is annotated in a) and color matched to the dose maps (blue=$1\,\mathrm{cm}^2$; red=open beam). Corresponding PDD (d) are included for both field types as well as lateral half-profile plots (e) for depths of 0 cm and 1 cm in the water phantom, for which the dose is normalized to the maximum dose for that depth.

A brief outline of the critical dosimetric performance considerations of the FLASH converter are highlighted in Table 5.7. Clearly, the threshold dose-rate of 40 Gy s^{-1} has been exceeded, even at the nominal SSD (7.5 cm), field size (1×1 cm^2) and treatment depth ($z = 1$ cm) for both beam energies, with a clear benefit being demonstrated for using the higher energy (10 MeV) beam for improved bremsstrahlung conversion efficiency and, as will be discussed later, reducing target strain and thus preserving design life.

Table 5.7: Primary dosimetric goals for the FLASH converter and simulated results for a 1×1 cm^2 x-ray field size and 1 kW average electron beam power.

Parameter	Goal	Calculated
FLASH dose-rates (7.5 cm SSD, 1-cm depth in water)	> 40 Gy s^{-1}	10 MV: 84 Gy s^{-1} 8 MV: 59 Gy s^{-1}
Primary e- transmission	$< 0.001\%$	$< 0.0006\%$ ($t_{Ta} > 500$ µm)

5.8.1.1 *in vivo* dose distribution using a rodent-morphic 3D-printed mouse phantom

Figure 5.13 illustrates the MC-calculated dose distribution in a 3D-printed mouse phantom, validated previously for use in kV treatment beams.

Using the VICTORIA dose visualization application [219], the in-phantom dose contours are made visible in Figure 5.13a, while averaged lateral and depth-dose profiles (Figure 5.13b,c) are also included. The dose distributions verify that the beam profile maintains its sharp distribution even at depth and the dose-rate throughout the entirety of the lung (the target organ of interest) remains well above 40 Gy s^{-1} and is expected to be compatible with treatment times of $< 10^{-2}$ s to facilitate single-fraction treatments customary of small-animal FLASH experiments that have been conducted to-date [40, 226].

5.8.1.2 Simulated converter activation, prompt and residual doses

The total equivalent dose at a distance of 0.5 m from the tantalum target, assuming no self-attenuation of the emitted radiations following 1 week of CW irradiation at 1 kW and 10 MeV, is summarized in Table 5.8. It should be noted that neutron radiation transport is considered in the activation analysis and converter energy deposition studies performed with FLUKA, but is not available in EGSnrc MC simulations. Due to our simplifying albeit conservative assumption of isotropic emission, the dose can be scaled to any arbitrary distance with an inverse-square correction to the tabulated values.

The primary activation products of interest are ^{180}Ta, produced in the tantalum target through the ^{181}Ta$(\gamma, n)^{180}$Ta reaction, along with the photo-fission products ^{185}W and ^{182}Ta produced in the W-collimator. While ^{185}W contributes the highest dose-rate, it only emits low-energy beta

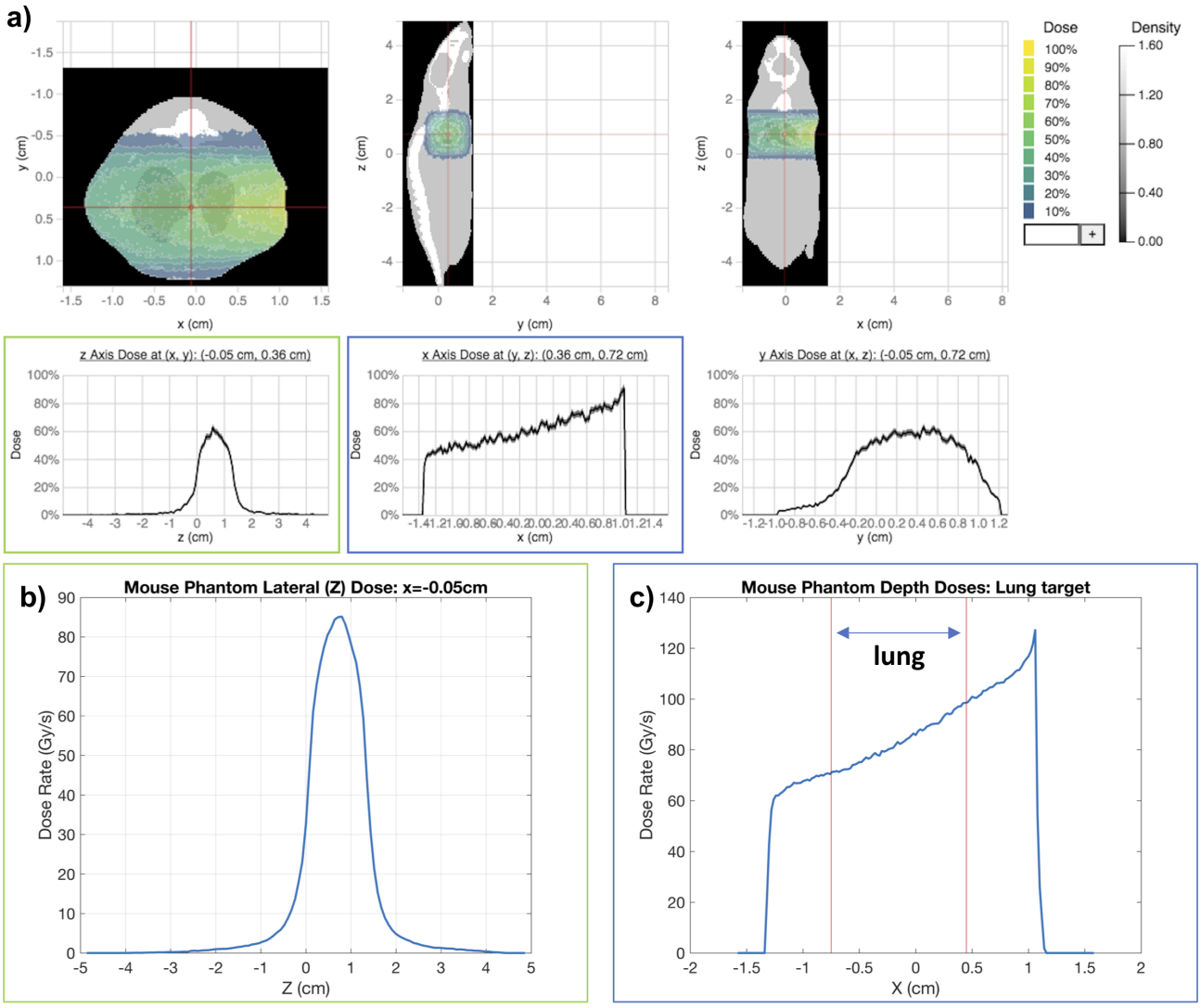

Figure 5.13: Doses to a realistic 3D-printed mouse phantom visualized using the web-based VICTORIA dose-viewer(a). Note that 100% dose here corresponds to an absolute maximum dose-rate of 142.4 Gy s^{-1}. Area-averaged (0.5 cm^2) lateral (b) and depth dose-rate profiles (c) for the $1 \times 1 cm^2$ 10 MV x-ray treatment beam generated by using the 1 kW, 5-mm electron beam at a 8-cm source-to-surface distance. The lung region of the averaged depth-dose (c), which in this case is delineated along the X-axis, showcases ultrahigh dose-rates (> 40 Gy s^{-1}) throughout the entire organ and is of relevance to planned lung irradiation studies using this MV source.

particles or gammas from the metastable state, whereas ^{180}Ta and ^{182}Ta, both beta emitters, may exist in metastable states which are capable of producing high-energy (> 1 MeV) gamma rays. ^{179}Ta and fast-decaying ^{179}W were only produced in negligible quantities, less than the associated error in yield, while the ^{28}Al produced in the Al-flange itself is another short-lived weak beta emitter. Residual doses, in practice, should be much lower than those quoted in Table 5.8 due to the reduced beam uptime under routine steady-state use, and will become lower still during low-frequency, short duration FLASH experiments. For reference, the worst-case estimate for total equivalent dose under

Table 5.8: Summary of activation products within the various converter components and the resulting equivalent dose-rates (in µSv hr^{-1}) at a distance of 0.5 m from the target. The target is considered as the point source for decay radiations and self-attenuation is omitted. Radioactive decay of the long-lived products is demonstrated through the dose-rate evolution at various times following end-of-beam (EoB).

	EoB	**5 m**	**1 h**	**1 d**	**10 d**	**100 d**
Tantalum target						
^{180}Ta	8.56	8.50	7.87	1.11	1.18×10^{-8}	0
W shield						
^{179}Ta	1.10×10^{-1}	1.11×10^{-1}	1.11×10^{-1}	1.11×10^{-1}	1.10×10^{-1}	9.99×10^{-5}
^{182}Ta	9.35×10^{-1}	9.35×10^{-1}	9.35×10^{-1}	9.29×10^{-1}	8.80×10^{-1}	5.11×10^{-1}
^{179}W	5.77×10^{-2}	5.25×10^{-2}	1.88×10^{-2}	1.15×10^{-13}	0	0
^{181}W	4.27×10^{-1}	4.27×10^{-1}	4.27×10^{-1}	4.25×10^{-1}	4.04×10^{-1}	2.41×10^{-1}
^{185}W	1.29	1.29	1.29	1.28	1.18	5.12×10^{-1}
Al flange						
^{28}Al	3.02×10^{-1}	6.46×10^{-2}	2.72×10^{-9}	0	0	0
TOTAL	11.6	11.3	10.5	3.75	2.46	1.26

1 kW CW irradiation amounted to 32 µSv hr^{-1} at EoB, if activation in the lead shielding surrounding the platform were also included; therefore, FLASH mode residual doses will always remain below this value. Given that the peripheral lead shielding is setup specific, and much farther from the sample/animal jig when compared with the converter flange, it was omitted for the preceding analysis of Table 5.8.

Considering the short time-scale of FLASH irradiations, prompt doses results for the same simulation geometry were found to produce a very small radiological hazard for occupied areas outside of the electron accelerator hall, with the most severe conditions corresponding to 6.2 µSv hr^{-1} when operating the beam in CW mode for beam diagnostics at 200 W and 10 MeV. The equivalent prompt dose-rates scale with beam power and uptime, while beam quality remains the same, and thus the corresponding dose during FLASH mode would reduce to 2 µSv hr^{-1} assuming a maximum of 4 FLASH macro-pulses per minute, in order to allow thermal stabilization between pulses.

5.8.2 FEA thermal and structural simulations of the electron-to-photon converter

This FLASH target will be used in two operational modes:

1. **FLASH** — during FLASH experiments, a maximum beam power of 1 kW will impinge on this target for a maximum of one second with maximum electron beam energy of 10 MeV.

2. **Diagnostic** — during regular electron linac development, the electron beam can be delivered to the converter with a maximum power of 200 W for indefinite time.

The 1 s upper-limit to the FLASH operational mode is consistent with the above-mentioned total irradiation times customary of FLASH and also presents the most severe thermal condition expected

for our targets. Practical irradiation times will be less than a full 1 s and therefore the implications of varying the irradiation time, assuming a 100% duty factor, on the temperature distribution within the target flange have also been presented in the forthcoming section. The need to preserve beam dump functionality using a low-power CW beam for arbitrarily long time periods provided unique requirements for our design, independently of the FLASH mode, and thus steady-state results for the diagnostic mode are also included here.

5.8.2.1 Summary of steady-state (diagnostic mode) and transient (FLASH mode) thermomechanical results

Figures 5.14 and 5.15 highlight the temperature, von Mises stress distributions within the flange for the steady-state (Figure 5.14 CW mode) and transient (Figure 5.15, FLASH mode) simulations, respectively. An extended data set which includes the elastic strain (relative deformation) may be found in the Supplementary Material (Figure A.17, A.18). For steady-state simulations, a more conservative beam energy of 8 MeV was considered as it induced higher temperatures and stresses in the aluminum components near the tantalum interface, due to the higher power deposition per unit length. To aid in clarity of presentation, the top rows (a,b) in each figure highlight the aluminum components only, which feature lower extrema compared to the target, which is included in the bottom figure rows (c,d). It should be noted that plastic strain within the flange (not shown) was non-zero within the tantalum target, but localized to the beam impingement region only; for reference, the maximum values of plastic strain in the tantalum are also summarized in Table 5.9.

According to the von Mises yield criterion, wherever the von Mises stress exceeds the material yield strength, the material will begin to yield plastically (i.e. deform irreversibly). The maximum elastic and plastic strains derived from the calculated stresses are summarized in Table 5.9. Importantly, the degree of deformation in aluminum everywhere remains elastic, while plasticity in tantalum is deemed tolerable based on the ductility characteristics reported in the literature for the temperatures observed.

Table 5.9: Elastic and plastic strain components for 200 W steady-state and 1 kW transient simulations for the reference simulation using a 5 mm electron beam size and 1000 µm target thickness. Transient data are sampled at 1 s, the time of simulated beam OFF in FLASH mode.

Beam type	Elastic Strain (Al, max)	Plastic Strain (Ta, max)	Total (max)
200 W steady-state (8 MeV)	0.0022	0.0028	0.0038
1 kW transient (8 MeV)	0.00559	0.0574	0.0579
1 kW transient (10 MeV)	0.0062	0.0435	0.0439

Note that the total strain is not simply the summation of the elastic and plastic components in Table 5.9 values as the distributions are spatially dependent. The largest plastic strains were

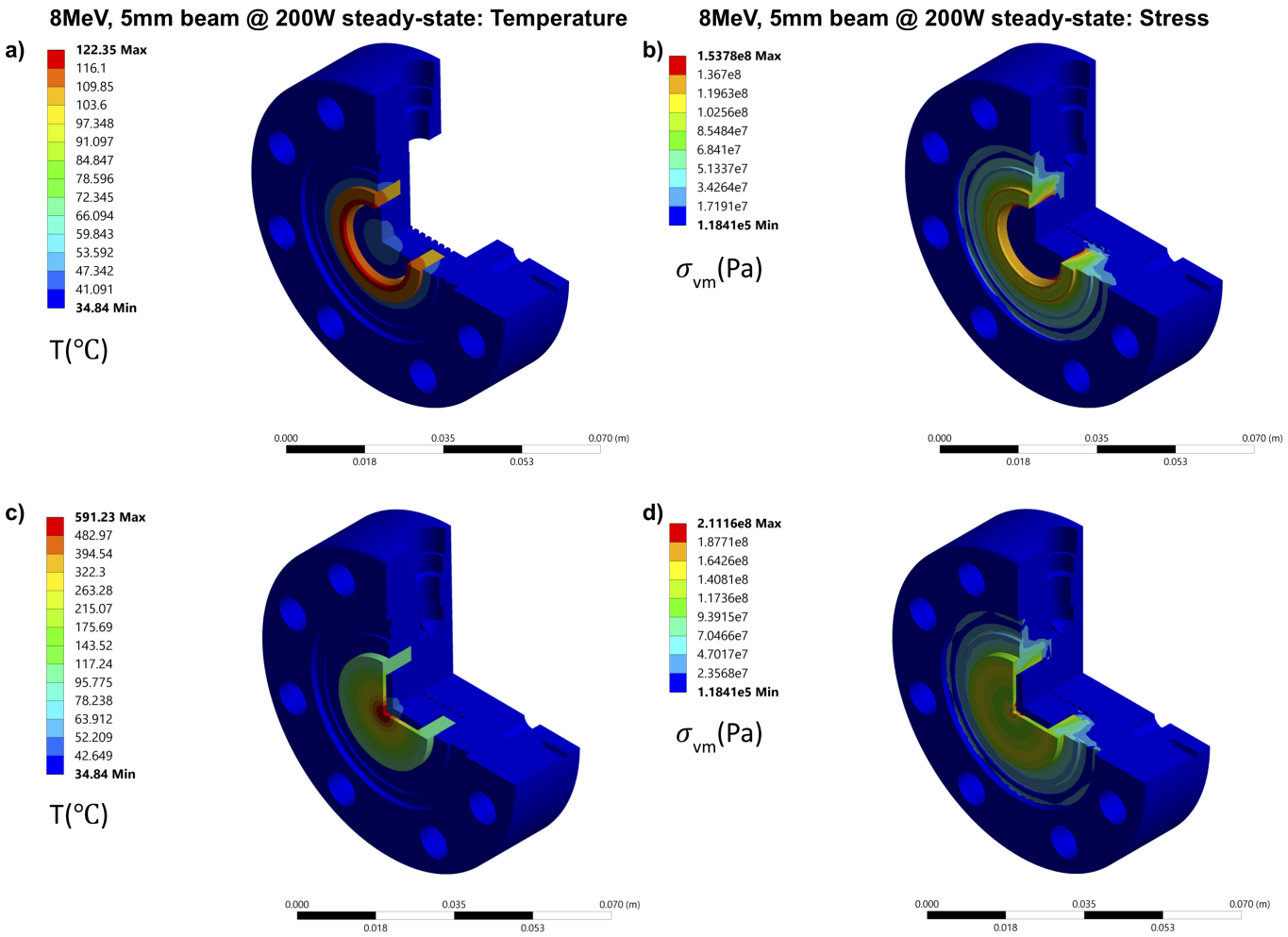

Figure 5.14: Summary of steady-state ANSYS FEA simulation results for the 8 MeV CW beam with a 5 mm electron beam size and 200 W average power. The temperature (T) (a,c) and von Mises stress (σ_{vm}) (b,d) distributions are shown in aluminum-only (a,b) and full target (c,d) views.

observed in the case of transient irradiations at 1 kW, as expected, due to the extreme temperatures reached within the tantalum.

A subset of the fatigue analyses, with the number of cycles to failure (N), is presented in Table 5.10. It includes the ANSYS peak alternating stresses, the mean stress – accounting also for the estimated shrink-fit pre-stress of 50 MPa and 17 MPa on the inner (plug) and outer (flange) cylindrical surfaces of the interference interface – and corresponding Goodman mean-stress corrected stress amplitude for use with Equation 5.2.

The two power values compared in Table 5.10 (200, 250 W) help to demonstrate the detriment of using higher beam power due to the increased stress amplitudes and higher mean stresses experienced over the many steady-state thermal cycles (i.e. beam ON until beam OFF) that are required of the CW (diagnostic) mode. It would be reasonable to operate a CW beam at electron beam power of 200 W or lower, for beam sizes larger than 2 mm, assuming a design-life requirement of 3000 thermal

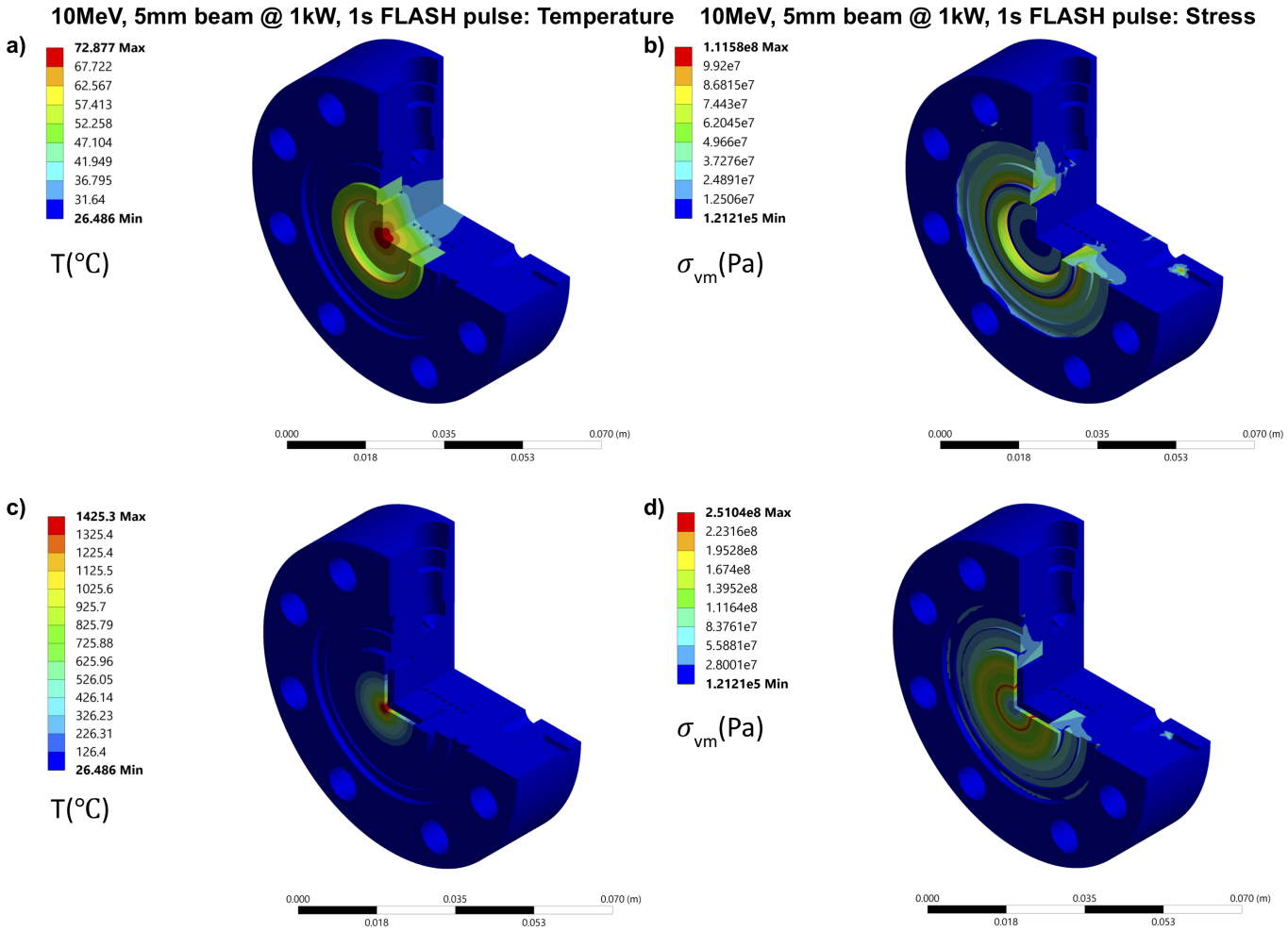

Figure 5.15: Summary of transient ANSYS FEA simulation results for the 10 MeV FLASH (pulsed) beam with a 5 mm electron beam size and 1 kW average power operating for 1 s. The temperature (T) (a,c) and von Mises stress (σ_{vm}) (b,d) distributions are shown in aluminum-only (a,b) and full target (c,d) views. All data are generated at the end of a 1 s electron beam pulse.

(beam) cycles over 5 years of operation. The selection of 200 W as the benchmark steady-state power follows from this fatigue evaluation for the CW electron beam of the ARIEL e-linac, which is typically employed during routine beam development.

The ANSYS tantalum fatigue results yielded values of N in excess of 10^4 under the same conditions and are therefore not included in the design life analysis for steady-state operation. For 1 kW FLASH irradiation at 10 MeV, however, the length of beam ON has a drastic impact on the life of the tantalum due to the rapid heating and extreme temperatures; importantly, the value of N decreases from 16310 at 0.1 s (max $T_{Ta} = 557\,^{\circ}$C) to 811 at 1 s, where the maximum TTa can reach 1425°C, based on conservative thermal parameters (Table 5.3).

The detailed temperature evolution of the 10 MV, 1 kW transient (FLASH mode) irradiations are shown in Figure 5.16 for the 5 mm electron beam size.

The temperature time-evolution over 100 ms, a timescale of interest for FLASH-RT, is visualized

Table 5.10: Fatigue analysis for the life-limiting Al components in 8 MV CW beam configurations using a 1000 µm target and for each electron beam size (2σ). The 8 MV case is the most conservative for this fatigue analysis and hence is presented here. S_u and S_y, the ultimate tensile strength of Eq. 5.2 for Al-6061 and the yield stress, respectively, are temperature dependent[a].

2σ	**Power (W)**	**Temp** (°C)	S' **(MPa)**	S_m **(MPa)**	**S (MPa)**	S_y **(MPa)**	S_u **(MPa)**	N **(cycles)**
10	250	146	196	125	422	217	237	1981
	200	123	159	107	292	239	264	5460
5	250	145	192	123	406	218	239	2192
	200	122	154	104	278	240	265	6378
2	250	122	153	104	275	240	265	6585
	200	103	124	89	200	259	287	19385

[a] S_u and S_y data are interpolated from tables taken from the ASM handbook [220]. For added conservatism, the value of S_u used in Eq. 5.2 is taken as the lower of two bounding values for any given temperature rather than the interpolated value shown here - i.e. if $T_{sim} \in (T_{ASM,1}, T_{ASM,2})$ then $S_u(T_{sim}) = S_u(T_{ASM,2})$

in Figure 5.16c. The extremely rapid heating rate within the Ta as compared to the aluminum and water channels, which exhibit comparatively slow temperature variations over time, demonstrates the ability of the flange to remove the deposited heat as it equilibrates (Figure 5.16d). Whereas TTa increases to 1425 or 1905 °C within 1 s of beam ON at 10 MeV and 8 MeV, respectively, the conductive aluminum corona only sees a corresponding increase of 45–49°C within that same period. 8 MeV results here reaffirm the benefit to using higher beam energy from a thermal perspective, namely to achieve lower peak temperatures and smaller gradients in the tantalum and aluminum components which lend to lower stress rates, thermal strain and thus a longer life for the Ta target layer.

5.8.2.2 Overview of thermomechanical design limits and calculated extreme values

An overview of the thermomechanical design limits and the calculated values are shown in Table 5.11. All goals were met and, together with achievement of the dosimetric performance goals outlined in Table 5.7, constitute a full acceptance criteria for the prototype fabrication, which has since been successfully completed.

5.9 Discussion

The ARIEL converter flange is being developed to provide an ultrahigh dose-rate (UHDR) x-ray source, suitable for FLASH radiobiological experiments, based on the conversion of the high powered electron beam delivered by the ARIEL e-linac. This achievement requires a target that is capable of withstanding high instantaneous power (1 kW) over many thermal cycles for UHDR irradiations while routinely serving as a diagnostic beam dump under lower-power (200 W) steady-state (CW beam) irradiation - a unique requirement of our platform. MC and FEA thermomechanical simu-

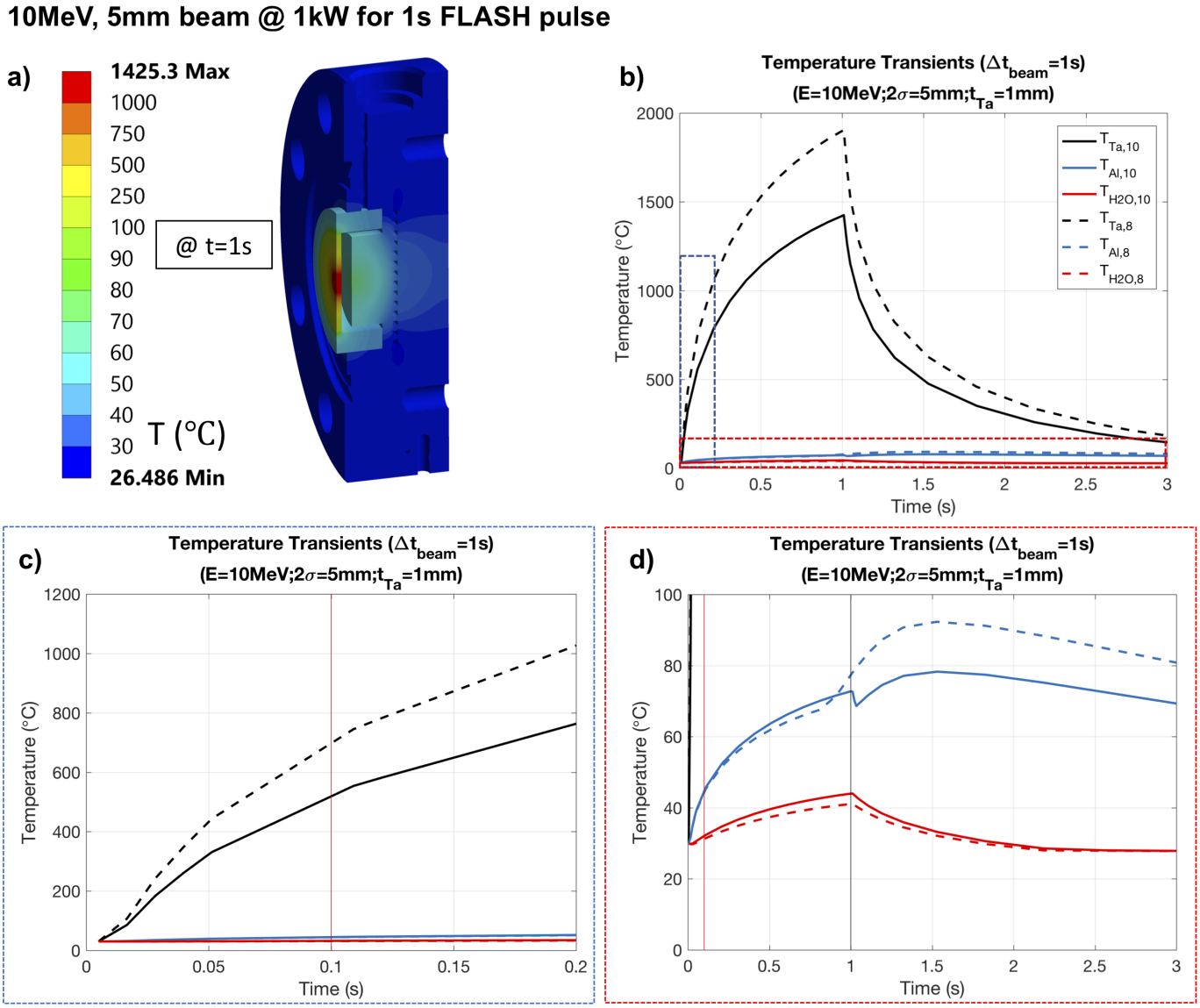

Figure 5.16: Transient temperature evolution of the 5 mm, 10 MeV FLASH reference beam. The FEA result (a) samples this data at $t = 1$ s. A non-linear colorbar scale is used to visualize the beam-induced heating across the converter CAX. The temperatures in each of the converter materials are plotted as a function of each time step in b). Ta temperature evolution on short (< 0.2 s) timescales (c) and the comparatively cool Al and water bodies (d) are also brought into focus.

lations have been used to inform flange optimization directly using an iterative design framework (Figure 5.4). Reasonable design limits were set based on dosimetric and thermal performance goals which must be simultaneously met along with acceptable manufacturing practices. Moreover, the dosimetric performance during UHDR (FLASH mode) irradiations had to be evaluated within practical and thermomechanical constraints identified for safe operation of the target during steady-state (diagnostic mode) irradiation. A prototype based on a design informed through the methodology presented here has since been fabricated.

The final target prototype leverages a novel thin-target design motivated by the need to implement

Table 5.11: Mechanical design limits and simulated results of the final converter prototype. Stress-strain limits are evaluated for the 8 MeV steady-state (SS) beam while transient temperatures (FLASH) are evaluated after a full 1 s FLASH mode irradiation in order to represent the most intensive conditions for each parameter to afford a more conservative design.

Parameter[a]	**Mode**	**Design limit**	**Calculated**
T_{Ta}	FLASH (transient)	< 2000°C	< 1905°C
T_{Al}	SS	< 200°C	< 122°C
T_{H_2O} (channel interface)	FLASH	< 100°C	< 60°C
Ta plastic strain	SS	< 0.02	< 0.005
Al plastic strain	All	< 0.02	~ 0
SS design life – steady-state (N cycles before failure, Al)[b]	SS	$> 3,000$	> 6000 (at 200 W)

[a] Peak temperatures are evaluate for the transient 8 MeV, 1 kW beam simulations at $t = 1$ s using a 5 mm electron beam size and 1000 µm target. This represents the nominal FLASH mode treatment beam configuration under the more intensive thermal conditions afforded by the lower beam energy.
[b] Target design life was limited by the Al parts in the case of a 200 W steady-state beam.

a small (space-saving), thermally efficient and static photon converter. High thermal and mechanical stresses are inevitably generated within the converter as a result of the enormous thermal load deposited by the impinging high-energy electron beam. To remove heat from the system, the high-Z bremsstrahlung target requires reliable and persistent contact with an actively water-cooled backing material. This was facilitated by interfacing Al-6061 with a tantalum target layer using explosion bonding (welding) processes which maximizes heat conduction across the laminated Ta-Al interface. In order to limit temperatures in the aluminum, especially at the interfacial boundary, the bonded aluminum within the region of e-beam impingement was removed, thereby creating an aluminum cylindrical interface (corona) axially bonded to the tantalum 'window' (Figure 5.6a,b). In order to realize this design, without creating water-leak paths into the ARIEL particle-free UHV beamline, the target was assembled by adopting a two-piece shrink fitting approach whereby the bonded Ta-Al layer was fashioned into a 'plug', cooled in liquid nitrogen, and inserted into the water-cooled Al-6061 flange (Figure 5.6c). The subsequent expansion (at room temperature) within a precision machined flange creates a contact interference between 5 and 26 µm which affords excellent thermal conductance across the aluminum-to-aluminum (coronal to flange) interface, limited predominantly by the microscopic surface roughness (65 micro-inches RMS) and manufacturing (i.e. cylindricity) tolerances. A higher conductance leads to reduced temperatures and thermal strain, thereby offering improved target longevity as well as a potential to deliver higher power and, in turn, increased dose-rates.

The use of the Ta-window design has helped to reduce the stresses at the critical Ta-Al interface and no plastic deformation, a key factor in the low-cycle design life, was observed within the simulated aluminum geometries. Secondly, the robustness of the explosion bonded Ta-Al joint was inferred from

literature. In the previous work by Egoriti *et al.* (2020), a sample of explosion-bonded tantalum to Al-6061 was irradiated with an electron beam at 300 keV at the ARIEL converter test stand (CTS) [211]. The temperature and stresses resulting from this reference test at the Ta-Al interface were higher than those seen in the FLASH converter; hence, the delamination risk from the design presented in this work was considered to be retired.

Other notable modifications to the converter include a 1-mm diameter vacuum pumping port, which was added to allow for degassing within, and evacuation of, the vacuum pocket during bake-out, while simultaneously reducing the pressure differential across the tantalum target layer (Figure 5.6b). Maintaining UHV within the vacuum pocket also minimizes the risk of oxygen exposure at the interior tantalum surface, which can otherwise lead to target oxidation and embrittlement, which would pose and as yet uncertain detriment to target life. The precipitation hardened 6061 flange body (T6 re-tempered) was selected for its resistance to erosion-corrosion effects and the improved tensile strength of the T6 condition, both of which help to maintain a leak-free connection to the rest of the steel beamline. It should be noted that the effects of radiation embrittlement may be of relevance to a thin target design, but were beyond the scope of this work. Fortunately, tantalum targets have previously been found to remain ductile even after prolonged periods of intense, high-energy irradiation using heavier particles capable of imparting substantial recoil energy to the knock-on atom precursors of damage cascades within the target material [214, 227]. While the literature on this subject is sparse, successful multi-year operating experience, for example with tantalum clad ISIS targets, may imply a reasonable preservation of thin Ta-targets even in the absence of a dedicated study on electron irradiation-mediated damage [112,214]. The aforementioned ARIEL CTS results at TRIUMF have also reaffirmed the robustness of Ta-Al explosion bonded targets in UHV conditions whereby experimental evidence failed to demonstrate radiation-damage assisted failure modes in the target, even at high operating temperatures ($T_{max,Ta}$ = 658 °C; $T_{max,Al}$ = 236 °C) under CW irradiation over long time periods (500 h, 50 cycles) [211].

Since a primary goal of target optimization was to maximize dose-rates, the results indicated that the small target thicknesses might be preferable due to the higher surface dose-rates and loss of build-up owing primarily to secondary electron dose (Figure 5.8). However, these observations had to be made considering the requirement that we must stop all primary electrons in the target (Table 5.7), a condition which was not met for the 500 µm target. Bearing this electron transmission constraint in mind, the optimal target thickness was selected to be 1000 µm, as it maximized the dose rates at all depths while mitigating primary electron transmission at 10 MeV, as demonstrated in Figure 5.8b. Moreover, allowing the tantalum layer to be as thick as possible, without compromising dosimetric performance, improved its mechanical resistance against stresses and buildup of potential surface oxide layers that may occur at high temperatures. Due to manufacturing constraints and the surface defects which follow the explosion-bonding process, thickness tolerances below 500 µm would be difficult to realize and this in turn supported a coarser optimization of target thickness

using increments of 500 µm.

While it lies beyond the intended application scope of the FLASH converter, a surface dose enhancement may provide an interesting opportunity for those interested in mixed radiation beams; in that case, it would be possible to greatly increase doses down to a depths < 1 cm using thinner targets and by exploiting the primary-electron dose deposition. For the thicker targets (> 1000 µm), on the other hand, the contaminant electron dose is derived from secondaries generated in the flange and the W-collimator (Figure 5.8b), exacerbated by their close proximity (CSD< 5 cm) to the water phantom. For the 1000 µm target and 5 mm beam size, secondary electrons generated in the 10 MV field contribute up to 72% of the surface dose, quickly decaying to $< 10\%$ at $z = 1$ cm depth and $< 2\%$ by $z = 2$ cm; contributions are reduced at 8 MV for all depths in water. Superficial dose due to these low-energy electrons ($\bar{E}_{10MV} = 1.3$ MeV) should therefore be taken into consideration for *in vivo* surface dosimetry or where measurement devices mounted on the irradiation jig may be exposed (i.e. at SSD=7.5 cm). Our simulated beam is somewhat unique in that it delivers MV x-rays while avoiding a superficial build-up region where dose-rates might otherwise fall below a UHDR threshold for FLASH, which we assume here to be 40 Gy s^{-1}. This depth-dose feature is shared by synchrotron (kV) x-ray or low-energy electron FLASH sources used to date, but it should be noted that the implications of mixed low-energy electron and MV photon beams on the FLASH effect have not been studied. Additionally, the mixed field might pose challenges for accurate dosimetry. Design modifications for thinner targets could be relevant to lower-energy beams better suited to other UHDR applications, especially keV spatially-fractionated modalities such as micro-/mini-beam radiotherapy. However, if these low beam energies are desired, then our 500 µm lower limit for the Ta-target thickness may preclude the use of the target-window design presented here.

Using a higher energy photon beam offered an obvious improvement in dose-rates (Figures 5.8a,5.9a) for each target thickness configuration and all beam sizes, even when disregarding the enhanced secondary electron fluence – this can be observed in the depth-dose differences for depths $z > 1$ cm. For example, in Figure 5.8a the relative dose-rate difference between 8 and 10 MV beams (normalized to the 10 MV data), for depths > 1 cm, ranged between 29% and 34% across all simulated configurations and increased with depth in the water phantom.

The converter together with the collimator assembly has been designed such that > 40 Gy s^{-1} could be achieved for a 1×1 cm^2 field size at a nominal SSD of 7.5 cm, as demonstrated in Figure 5.12. This field size was selected as being typical for small-animal irradiators and suitable to mouse lung irradiations for which the ARIEL FLASH system is being designed [59]. However, because of the W-collimator modularity, it can also accept a number of 3D-printed collimator inserts with common form factors, as long as they fit within the 2-cm diameter aperture of the secondary collimator, which itself defines the largest collimated field size (see Figure 5.12a). Alternatively, the primary and secondary collimators can be removed from the beam path entirely. This latter configuration might be of interest, for example, where exceptionally high dose-rates (> 600 Gy s^{-1}) are required

without the need for field conformality, possibly outside of small-animal experiments. Removal of all collimators (open beam) was found to increase the available dose-rate by a factor of 4.56 and 4.62 for the 10 and 8 MV beams ($2\sigma = 5$ mm, 1000-µm thick target), respectively, for the shortest SSD of 3.5 cm achievable without collimation. Optimizations for improved field conformality and transversal characteristics are being considered for future collimation strategies; for example, we are considering 3D-printed flattening filters to compensate and flatten the x-ray field.

Given that the dose attributable to both contaminant electrons and x-rays at the surface of small-animal models may have dosimetric implications, the transport of the electrons through the entire aluminum flange had to be considered. This was necessary to accurately model the secondary electron shower and promote bremsstrahlung x-ray production within the flange itself. To this end, the electron transport threshold for the BEAMnrc simulations was set to a low value of 150 keV and electron range rejection was not employed. As an example, the mean electron energy upon exiting the aluminum flange (SSD=2 cm) was approximately 1.5 MeV at which point the radiative yield is 13.7% of that in tantalum at the same energy and this value increases for the higher energy electrons which enter the flange after the Ta target.

To ensure that the performance of the system meets the prescribed design goals (Tables 6 and 10), the quantities of interest, namely UHDR dose-rates and converter temperatures, were evaluated under a conservative set of assumptions. From a thermomechanical perspective, important heat transport parameters were reduced by a safety factor of 2 in order to assure operation at 1 kW remained tenable. Furthermore, treatment dose-rates were evaluated against the threshold (40 Gy s^{-1}) at a depth of 1 cm in water, which is of relevance to planned small-animal irradiations. The maximum target temperatures, meanwhile, were evaluated after a full 1 s of irradiation, despite the expected beam ON time for a typical FLASH biological irradiation being an order of magnitude less ($\approx$ 100 ms). This increased time to beam OFF (1 s) has the important implication that the corresponding thermomechanical results reflect a more extreme, but less likely, operating condition compared to that of a 0.1 s long irradiation, as evidenced by the large temperature increase, from 510 to 1425 °C at 10 MeV, between 0.1 s and 1 s total irradiation times (Figure 5.16).

The combined results of the MC and FEA simulations are illustrated in Figure 5.17. The improved dose-rates and reduced peak tantalum temperatures are immediately evident at higher beam energy together and with beam sizes > 5 mm.

The results of the combined MC and transient FEA simulations (Figure 5.17) illustrate that the design goals (Tables 5.7 and 5.11) have been met, with the added margin of safety discussed above. There were clear benefits to dose-rate from selecting the higher beam energy, besides the improved depth of penetration, as previously noted (see Figures 5.9). For example, using an electron beam energy of 10 MeV and spot size of 5 mm beam, the dose rates could be increased by up to 41.4% relative to an 8 MeV beam of the same size and power at 1 cm depth, while generating peak transient tantalum temperatures (T_{Ta}) which were a factor of 25.7% lower after 1 s (Figure 5.17a). Use of smaller beam

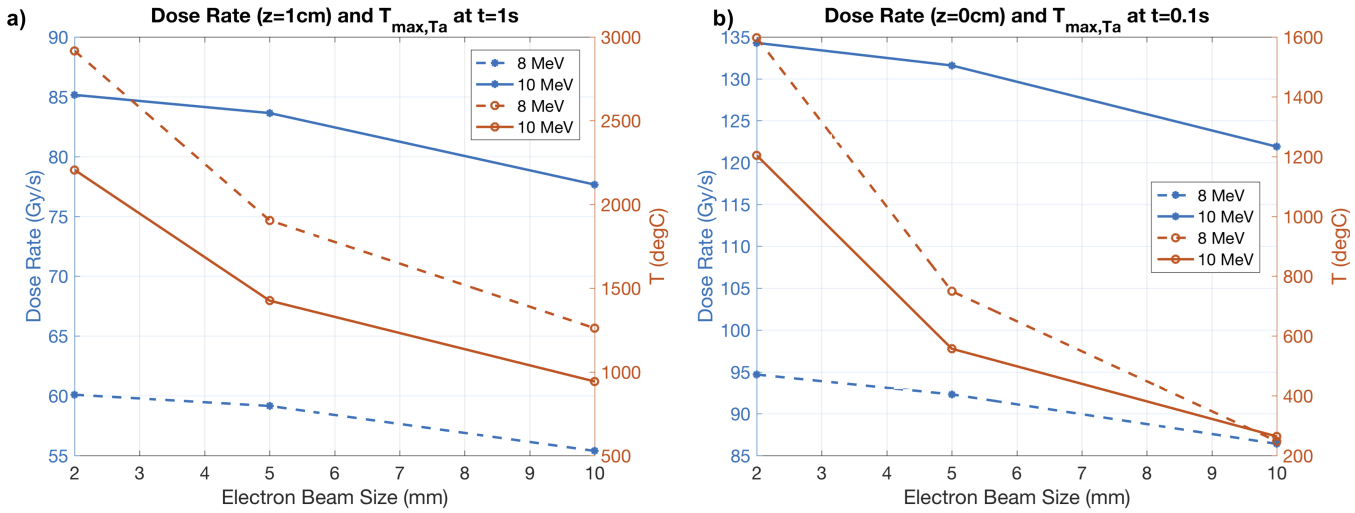

Figure 5.17: Combination plots for simulated dose-rate and peak Ta temperatures (T_{Ta}) for the $1 \times 1\,\mathrm{cm}^2$ FLASH-mode treatment x-ray beam. A Ta-target thickness of 1000 µm is simulated with a 5-mm electron beam size and an average power of 1 kW at 8 MeV (0.125 mA) and 10 MeV (0.1 mA). Data are shown for 1 full 1 s irradiation at a depth (z) of 1 cm in water phantom (a), reflecting a more extreme set of conditions which were compared against the design goals. Data evaluated at the phantom surface for a typical FLASH irradiation time of 0.1 s is also included (b) to reflect a more practical treatment scenario.

sizes, meanwhile, appeared beneficial for increasing peak dose-rate, due largely to geometric factors improving transmission of forward-directed x-rays, but with a trade-off in target protection given that TTa would increase substantially given the higher power density on the tantalum target. For example, in the 10 MeV beam TTa increased by 64.3% when decreasing the beam size from 5 mm to 2 mm, in exchange for a dose-rate increase of only 2.1% (Figure 5.17a). The importance of minimizing the peak temperatures while pursuing maximal dose-rates is of critical importance to the viability and longevity of the target design. Altogether, the implication is that for a 1000 µm target, using the higher beam energy (10 MeV) together with a 5 mm electron beam size offers the best compromise between dose-rate and peak temperatures at the time scales of interest in FLASH-RT and has become the reference configuration.

In the interest of designing a flange capable of both FLASH (low-cycle) and routine diagnostic (high-cycle) usage, the fatigue life of the converter had to be estimated. The use of safety factors on the life of the material helps to account for and mitigate added risk owing to the design life uncertainty. We estimated that the converter would be capable of surviving at least 6378 cycles under steady-state 5 mm beam irradiation, limited by fatigue in the aluminum corona of the target plug rather than the thin tantalum target itself. This is substantiated by the observation that negligible plastic strain was observed in the tantalum for a 200 W CW irradiation (Table 5.9) and the fact that the ductility of tantalum affords it long life under largely elastic (reversible) cyclic strain [228–230]. Furthermore, tantalum endurance limits – the fully-reversed stress amplitudes to survive 2×10^8 cycles – taken from high-cycle fatigue literature are generally higher than the worst-case stress amplitudes

reported here (Table 5.10); although, there may be notable variations depending on the material conditioning and testing frequency [112, 228]. Under the extreme conditions of FLASH irradiation, by contrast, the impact of increased strain on design life is important under the cumulative damage theory [104] whereby the percent of life expended under FLASH irradiation is carried over to the case of lower power, and less destructive, steady-state. Fortunately, the design life for the tantalum target under the 1 kW FLASH mode, assuming that the irradiations are short (≈ 0.1 s), far exceeds that of even the aluminum corona at an estimated 16310 cycles. However, in the event of an off-normal (> 1 s) irradiation at 1 kW, the target life would be reduced due to the extreme temperatures and stresses experienced to approximately 811 cycles. In such a case, it would only take ≈ 405 off-normal exposures to reduce the life by half, the equivalent of running 3189 cycles at 200 W steady-state. These considerations are important to inform accelerator operators about the timeline for replacement and how this may be modified by accidental events.

The converter has been shown to produce a negligible increase in radiological hazards to personnel on the basis or activation and prompt doses (Section 3.1.2). Activation in the target at 10 MeV is present, but the resulting radioactive isotopes (Table 5.8) together generate equivalent dose-rates at a nominal personnel distance (0.5 m) that would be unlikely to pose a risk, especially considering the short-duration access required of the irradiation platform. Moreover, the calculated values assume no component self-attenuation as well as impractically long CW irradiation at 1 kW, which is not possible given the operational power limit of the flange design (i.e. CW at 200 W only). Activation in the target and collimator geometries are also the primary contributors to non-therapeutic doses to experimental animal models. This is of particular relevance due to the close proximity of the converter to the location of the irradiated sample, device or small animal (in the irradiation jig). The activities and doses in calculated in FLUKA assumed 1 week of continuous CW irradiation at 1 kW, which is unlikely to occur considering the design limitations of the flange, but provides a very conservative estimate to re-affirm the safety of operating the converter under high-powered irradiation using 10 MeV electrons, which are also capable of producing a very low neutron flux [231, 232]. The reduced uptime, lower beam power and converter shielding/collimation will together greatly reduce the radiation hazard in spite of the close proximity of small animals restrained by the irradiation jig located at ~ 7.5 cm SSD.

The target flange will ultimately be used to enable small-animal (rodent) FLASH-RT research at TRIUMF. Along with the provision of UHDR for < 1 s single-fraction mono-directional treatments, the field should have qualities that allow for reasonable beam conformality and mean dose-rates above 40 Gy s^{-1} at the nominal treatment depth of 1 cm. MC simulations of a realistic mouse phantom irradiations using the 10 MV treatment beam (1000 µm target, 5 mm 2σ), representative of an experimental lung irradiation (Figure 5.13), were used to illustrate the successful collimation strategy and > 40 Gy s^{-1} UHDR delivery at depths throughout the entirety of the mouse thorax that is intersected by the beam (Figure 5.13c). The beam was not substantially divergent within the

phantom and the requisite dose-rates are achieved in a $1 \times 1\,\mathrm{cm}^2$ field at all depths. A substantial increase in dose-rate can be effected by positioning an animal, or any other sample of interest, near to the converter flange (Al face) without collimation at the expense of the conformality afforded to the collimated fields (Figure 5.12). It is interesting to note that at MeV electron energies the x-ray production efficiency is such that the power requirements for achieving UHDR with our target ($\approx 1\,\mathrm{kW}$) are lower when compared to a UHDR functionalized static anode x-ray tube (i.e. 3-6 kW) [32, 50] and at least an order of magnitude lower than modern high-performance rotating anode x-ray tubes (60-100 kW) [233].

The importance of developing a static target design capable of UHDR x-ray irradiation derives from the fundamental difference in the delivery requirements of FLASH-RT compared to conventional dose-rate therapies. Specifically, the sub-second nature of single fraction FLASH-RT is incompatible with conventional, gantry-mediated intensity modulation (IMRT, VMAT) techniques, and instead lends itself well to stationary accelerator beamline and target setups, not unlike the source considered in the present work. To then enable multi-directional intensity modulated fields, the use of multiple beamlines nigh-simultaneously could provide the desired solution; this is the approach proposed for the 10 MV SPHINX system to deliver FLASH RT with MV x-ray beams [52]. To enable such a deliver system, however, each individual beamline target would be required to withstand only a very short, pulsed exposure period compatible with the FLASH-RT definition ($< 1\,\mathrm{s}$), rather than using a continuous beam. The robustness against short duration, high-powered pulses of the design presented in this work might therefore be relevant to future development efforts towards UHDR-capable MV bremsstrahlung sources and enabling a clinical translation of x-ray FLASH. To date, only a single demonstration of a MV UHDR x-ray source suitable to FLASH-RT has been published, namely using the PARTER system located at the Chengdu terahertz free electron laser facility (CTFEL; Chengdu, China), which leverages a rotating target to distribute heat deposited by the incident electron beam circumferentially around the target, in a manner similar to a rotating-anode x-ray tube [207]. The benefit of instead working towards a static target design relates to the comparative affordability and suitability to compact, multi-directional treatment machines, particularly if combined with electron beam rastering capabilities. Owing to the different target design combined with lower beam energy, the PARTER system offered depth-dose distributions which were well-suited to small-animal experiments. By comparison, a key limitation of the static target design presented in this work is the steep depth-dose gradient, resulting largely from the use of very short treatment SSDs. In pre-clinical subjects (Figure 5.13c) this can manifest as dose non-uniformity and presents a shortcoming when compared to, for example, the PARTER MV x-ray beam or proton beams employing a shoot-through method. This may be of some concern if the treatment dose is at the center of a larger subject requiring over-dosing of the more superficial tissues, possibly beyond a tolerable threshold for toxicity. Conversely, at greater tissue depths this might result in an inability to reach a supposed lower dose threshold for initiating the FLASH effect during the treatment of shallower sites.

In the course of the ARIEL FLASH project, following online beam commissioning of the converter presented herein, the authors endeavor to offer a first demonstration of FLASH at this key treatment energy. Higher beam powers, up to 10 kW, may also be theoretically possible and limited only by the thermal tolerances of the components associated with the planned FLASH irradiation station, including the converter presented herein. Conversely, a lower beam power enables conventional (low dose-rate) irradiations on a common platform, using the same irradiation conditions and beam spectra. The beam quality can be theoretically maintained by modifying the electron beam power via the duty factor without the need for retuning of e-linac running parameters. Furthermore, single (macro) pulses with widths between 0.5 and 1000 ms allow for variable instantaneous dose-rates to be delivered in a FLASH-pulse operational mode by setting the duty factor to $< 100\%$ while maintaining a 1 kW average beam power. The eventual irradiation platform will facilitate a first exploration of FLASH-RT in pre-clinical models using MV x-rays delivered using a static bremsstrahlung target design.

5.10 Conclusions

A photon conversion target for the high-power ARIEL electron linac at TRIUMF has been successfully designed to satisfy a series of conservative performance thresholds suitable to UHDR irradiations and, eventually, FLASH radiobiological studies. Dose rates in excess of 80 $\mathrm{Gy\,s^{-1}}$ at 1-cm depth in a water phantom were simulated for all beam configurations considered, well above the 40 $\mathrm{Gy\,s^{-1}}$ design lower limit. Meanwhile, temperatures and resulting thermal stresses were everywhere tolerable based on the intended practical limits set according to intended use cases, including total strain and design life requirements, and therefore supports the robustness of the final converter design. The prototype is currently being validated/evaluated through offline thermal testing and will be refined, if needed, ahead of commissioning with the 10 MeV ARIEL electron beam.

Author contributions: This chapter comprised a large, multi-disciplinary collaboration and as such the published work has relied upon significant contributions from the co-authors which are acknowledged herein. **Section 5**: Magdalena Bazalova-Carter (MBC) and Nolan Matthew Esplen (NME) contributed equally to the work and writing of the manuscript published as [50]. NME conducted the experimental verification experiments and analysis and MBC conducted the MC modelling and validation. **Section 5.6**: NME was responsible for writing the manuscript and producing the figures for the manuscript published as [53]. NME conducted the dosimetric MC simulations, transient FEA thermal and coupled mechanical fatigue analysis. Luca Egoriti (LE) performed the steady-state thermo-mechanical and fatigue calculations, activation analyses and ambient dose equivalent safety assessment. NME and LE contributed equally to the design and fabrication of the FIRST irradiation platform, including target concept, beamline modifications, and related ancillary services. All authors contributed to editing of the manuscript and provided technical expertise and project guidance instrumental to the realization of delivering x-ray FLASH-RT at TRIUMF.

Chapter 6

Dosimetric Characterization for radiobiological experiments on a novel UHDR megavoltage x-ray source

6.1 Introduction

The normal tissue sparing potential of UHDR irradiation has been demonstrated using electron linacs in radiobiological studies spanning the past 40 years [13,39,131]. Since then, the concept of ultrahigh dose-rate RT has been re-established, driven by the exciting demonstration of a differential (FLASH) effect between tumor and normal tissue and sophisticated new accelerators have emerged which are capable of delivering pulsed beams with a wide variety of temporal configurations.

Unfortunately, the ability to deliver UHDR radiation for the purposes of FLASH-RT research is currently restricted by the poor availability of high intensity sources across all radiation modalities routinely employed for curative RT. At present, low-energy electrons ($E < 10\,\text{MeV}$) predominate the literature, but are of limited benefit to clinical translation owing to their limited depth of penetration [12,13,38]. UHDR compatible VHEE [234,235] and synchrotron (keV) x-ray sources [29,44] have also drawn attention for FLASH research, but suffer from poor accessibility due to the limited number of research systems available worldwide, and current lack of compact alternatives. Conventional x-ray tube sources may address the need for accessibility but are limited in application due to the extremely soft beams produced [32, 33, 50], though emerging compact x-ray technologies may help to alleviate this [34]. Protons, meanwhile, have attracted substantial interest in terms of FLASH development due to their favorable physics properties, but remain comparatively costly and rely upon established infrastructure in order to support more widespread adoption.

In contrast to the above-stated particle modalities, megavoltage (MV) x-rays offer the ability to treat deep-seated tumors while requiring comparatively modest accelerator specifications. The development of MV x-rays therefore presents a high priority niche for future FLASH source research and development. Presently, systems capable of delivering UHDR (i.e. FLASH-compatible) x-rays at MV energies are at the developmental stage commercially [52]. Otherwise, only two experimental MV x-ray FLASH beamlines exist globally at the time of writing - the Chengdu CTFEL and the TRIUMF ARIEL facilities [53, 131]. A primary limiter to UHDR MV source development relates to

the significant engineering challenges associated with the design and fabrication of practical targets for Bremsstrahlung conversion of sufficiently high-power electron driver beams. Consequently, the newly commissioned UHDR x-ray source installed at TRIUMF (Vancouver, BC) stands as a unique platform for FLASH radiobiological experiments at heretofore unexplored energies (10 MV) and with dose rates in excess of 100 Gy/s [53].

As an extension of the pre-requisite target development effort (Section 5.6), the aim of this work was to employ the new FLASH Irradiation Research Station at TRIUMF (FIRST) in a pre-clinical study of FLASH effects in healthy lung of male C57Bl6 mice. To enable these experiments, it was necessary to first asses the system's capabilities and characterize the beam under treatment conditions using established dosimetric techniques. For UHDR radiobiological research, in general, accurate dosimetry is of critical importance in order to establish both reliable FLASH-RT delivery strategies and support reliable correlation between treatment methodologies and biological outcomes, especially in view of future translational research. Notably, careful consideration must be given to detector selection that is compatible with the temporal nature (i.e. pulsed or continuous) of the radiation source being employed [13, 125, 236, 237].

For the purposes of our small-animal irradiations at TRIUMF, radiochromic films (type EBT3) were selected for their demonstrated dose-rate independence over the range relevant to our UHDR x-ray source (i.e. 10^{-2} to 10^{2}) [13, 127]. This quality is especially important for the estimation of *in-vivo* doses in the absence of validated treatment planning systems or Monte Carlo models, and for experiments which consider a large range in dose rate (i.e. FLASH and CONV). The high spatial-resolution and energy independence of films at MeV beam energies [132, 135], for both photons and electrons, was also well-suited to the ARIEL photon beam which boasts a broad energy spread, a small ($\approx 1 \times 1\,\mathrm{cm}^2$) field size and mixed photon/electron contribution down to $\simeq 2\,\mathrm{cm}$ depth in water [53].

To date, small-animal experiments for FLASH have been conducted for a range of animal models using electrons, protons, photons and carbon ions [11, 43, 44, 206, 207]. However, the mechanisms which drive the observed normal-tissue sparing (FLASH) effect remain to be elucidated. A number of theories have been proposed, with the prevailing oxygen depletion hypothesis having originated during the pioneering experiments of the late 1960s. This mechanism would ascribe the FLASH effect to a transient hypoxia induced by radiolytic oxygen depletion under UHDR irradiation [91, 92, 238]. In the context of modern FLASH-RT research, however, updated knowledge based in oxygen depletion data and consideration of physiological oxygen tension has since prompted a number of competing or complementary mechanistic explanations, whether they be physico-chemical, cellular (i.e. redox biology) or immunologic in nature [239]. In order to better understand the limitations of FLASH, identify the pre-requisite beam delivery parameters and highlight the driving mechanisms, there yet remains a need to pursue *in-vivo* research under a much wider range of experimental conditions. For example, beam micro-structure and depth of anesthesia may have effects on the transient and

persistent oxygenation status in tissue, respectively. How such factors might modulate observed FLASH outcomes are open questions which we might be better positioned to answer using emerging experimental systems such as FIRST (Section 5.6). The ARIEL e-linac is particularly attractive for the proposed application owing to the range of applicable energies (300 keV to 30 MeV) and the ability to utilize highly flexible modes of current delivery, in contrast with the few other potentially FLASH-capable x-ray sources. FIRST therefore enables delivery of UHDR beams with precise control over a number of source parameters of interest such as the (macro) pulse repetition frequency (PRF), peak (instantaneous) current (i.e. instantaneous dose rate ($\dot{D}_p$)), beam energy and average power ($P \propto \bar{\dot{D}}$).

This work represents the culmination of an effort to enable FLASH-RT research using MV x-rays in Canada and deliver a world-first irradiation at 10 MV with a UHDR bremsstrahlung source. Moreover, the successful completion of preclinical experiments with mouse models at TRIUMF represents a valuable institutional milestone, and may provide reference for future *in-vivo* radio-biological work at TRIUMF and capabilities for irradiation experiments on the ARIEL e-linac.

In the forthcoming chapter, the first demonstration of UHDR MV x-ray irradiations at TRIUMF is presented via dosimetry results from beam characterization and commissioning under both UHDR (FLASH mode) and conventional dose-rate (CONV mode) operation. Lastly, the results of film dosimetry from the ongoing mouse radio-biological study will be summarized.

6.2 Methods and Materials

6.2.1 Source Description

The TRIUMF ARIEL superconducting electron linac is described in Section 5.7.1.1. For the purposes of commissioning and subsequent radio-biological irradiations, only a subset of the available beam parameters were employed. Specifically, the electron beam energy was fixed at 10 MeV in order to maximize dose rates and target longevity [53], while the beam (peak) current was nominally set between $95--105\,\mu$A (i.e. $0.1\,\text{mA} \pm 5\%$). Current, and therefore dose, variation were unavoidable to due limitations with source stability [240]; the current variance appeared to increase at peak currents much lower than the e-gun design specification (10 mA) such as those required for $P \leq 1kW$ operation. To contend with this limitation, beam parameters were verified ahead of each irradiation and online adjustments made, as necessary, according to a standard procedure depending on the delivery mode (see Section 6.2.4). The e-linac has been commissioned to operate in either FLASH or CONV mode, which allowed for beam delivery using a single (macro) pulse or a defined PRF, respectively (see Table 6.1). To allow dose rate variation within either beam mode, the average beam current ($\propto P_{ave}$) was controlled using the duty factor (DF) of the beam (Figure 6.1). These source parameters enabled FLASH and CONV irradiation under identical experimental conditions and without perturbing the quality/spectrum of the beam.

Table 6.1: Summary of beam parameters available for FLASH and CONV irradiation on the ARIEL e-linac and those used for the dosimetry and *in-vivo* irradiation campaigns.

Parameter	Design Values	Experimental Values (nominal)
Energy	8,10 MeV	10 MeV
Average Current	$\leq 100\,\mu$A ($\pm$10%)	$95 - 100\,\mu$A
Duty Factor (DF) [Frequency (PRF)]	0.05-100% [1-100 Hz]	CONV: 0.055% [100 Hz] FLASH: 100% [1 Hz]
e-beam size (2σ)	1-10 mm	$\approx$5 mm

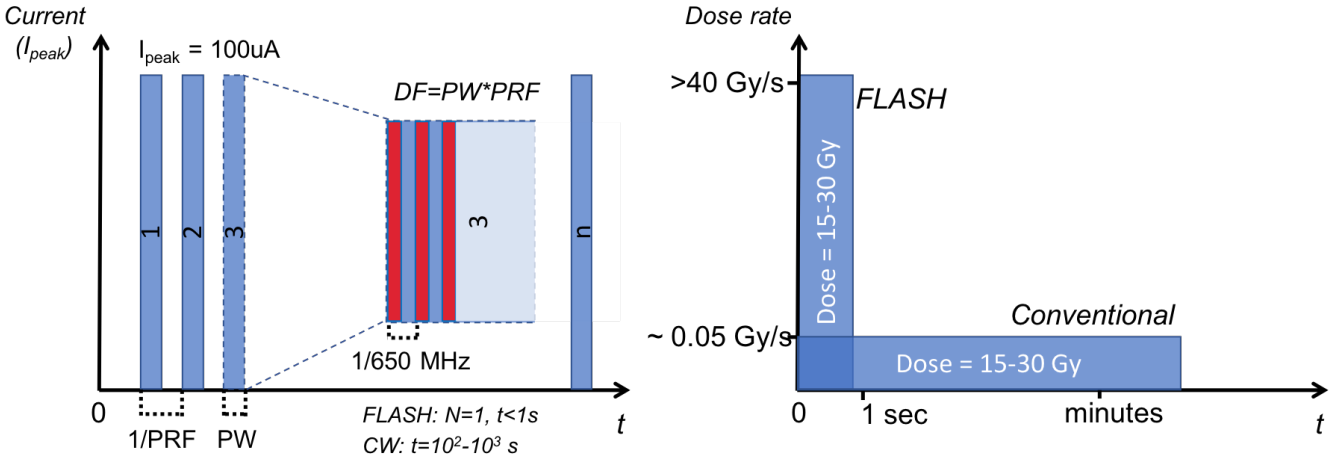

Figure 6.1: Beam time structure for conventional and ultra high dose-rate (FLASH mode) delivery.

The approximate mean energy of the photon beam produced under either mode of operation was 1.76$\pm$0.05% MeV, based on previous MC calculations [209]. The beam optics settings were established using beam envelope calculations [212] from which the beam size (Gaussian 1σ) was found to be 2.27 mm in X and 2.79 mm in Y (Figure 6.2). The goal was to obtain a $2\sigma \approx$ 5mm beam with zero dispersion at the location of the target and ensure that a maximally parallel and Gaussian electron beam could be delivered. This is ensured by minimizing the beam-size perturbation term in the dipole bending plane (X transverse plane), for which $\Delta X \propto D * \delta_p$, where D is the dispersion parameter (m) and δ_p the relative momentum spread as a percentage (dp/p). An energy spread of $< 1\%$ was maintained and phase shift adjustments to EINJ were applied as necessary to ensure the beam position and emittance remained consistent.

6.2.2 Film calibration and dosimetry

Owing to their superior spatial registration and established dose-rate independence [13, 127], EBT3 Gafchromic® (Ashland Advanced Materials, Bridgewater, NJ) films were employed for the dose

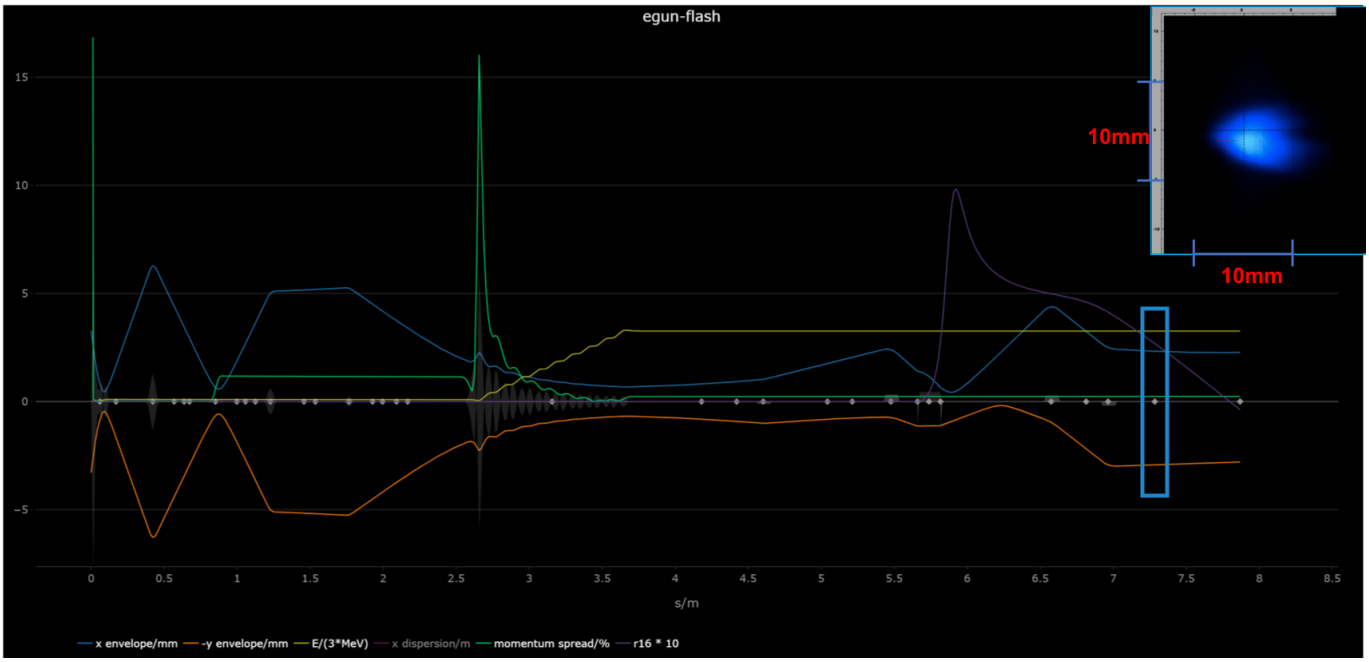

Figure 6.2: TRANSOPTR [212] beam optics summary for the final ARIEL FLASH beam tune. The beam size is defined by the last datum which corresponds to $\sigma_x = 2.27\,\text{mm}, \sigma_y = 2.79\,\text{mm}$, or $2\sigma \approx 5\,\text{mm}$. The inset shows the beam visualized on the scintillating VS within the diagnostic box (grey diamond) located in the region demarcated by the blue rectangle

measurements used throughout the FLASH campaign at TRIUMF. Prior to their first use for absolute dosimetry, the film batch was cross-calibrated against a reference 0.6cc ionization chamber (Farmer TN30010, PTW, Freiburg, Germany) and SuperMAX$^{\text{TM}}$ electrometer (Standard Imaging, Middleton, USA) whose calibration is traceable to the standard laboratories of the National Research Council of Canada (NRC). The film calibration was handled according to supplier recommendations and TG-55 guidelines [241] while the absolute dose measurement was conducted according to the procedure set out by AAPM's TG-51 protocol [139]. The films were located at a depth of 10 cm from the phantom surface at 100 cm SAD and the chamber reading was therefore scaled to the film depth by applying a previously measured tissue-maximum ratio conversion that was also verified at the time of irradiation[1].

In all, 18 calibration films were irradiated to doses ranging from 0 to 35 Gy using a 10 MV clinical photon beam delivered on a Varian TrueBeam STx (Varian, Palo Alto, USA). The feasibility of using EBT3 film beyond 20 Gy has been previously demonstrated [138, 242] though future work would benefit from the use of EBT-XD with enhanced dose sensitivity and accuracy out to $\approx 30 - 40$ Gy [134, 242].

Irradiated films were scanned at least 24h after exposure using an EPSON® 10000XL flatbed scanner (Epson America, Long Beach, CA) at a resolution of 200 dpi. A Matlab® (Mathworks, Nattick, MA) script was written to process the scanned films using both red and green color channels,

[1]Calibration conducted at BC Cancer-Vancouver assisted by Dr. Tania Karan and Claudia Mendez

from which the absorbed dose was interpolated for each channel independently. Red channel responses were used for $\leq$15 Gy dose to exploit the improved dynamic range and reduced variance while for >15 Gy irradiations the green channel was instead used. The red and green channel calibration data are shown in Figure 6.3 along with the second-order rational function fit.

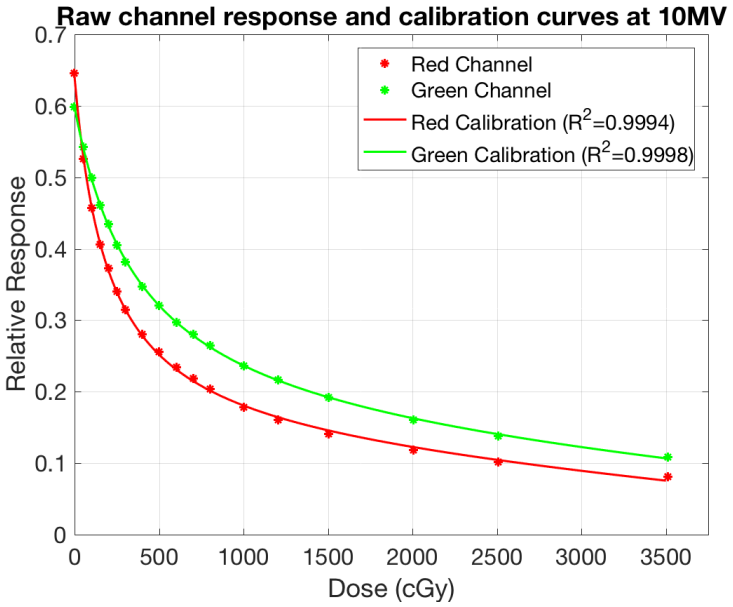

Figure 6.3: EBT3 calibration for the red and green channels including the R^2 goodness of fit metric for the rational function fits (solid lines) which model the film response $R = f(D)$. Doses for all films in this work were calculated based on interpolation from these calibration curves. Note that the relative channel response ($RR(D) = R(D)/65535$) is shown here instead of the usual optical density [$OD = -ln(R(D)/R(0Gy))$].

6.2.3 The FIRST irradiation platform and phantom setup

The target and supporting infrastructure is the culmination of a multi-year collaborative effort to design and fabricate a robust, cost-effective UHDR photon source (i.e. > 40 Gy/s) with the goal of enabling MV x-ray FLASH radiotherapy research in Canada (Figure 6.4).

Following fabrication and prototype offline testing (see Appendix A.3), the UHDR target system was commissioned for both UHDR pulsed (FLASH mode) and low dose-rate (CONV mode) delivery. A key advantage of the system was the ability to switch between modes and dose rate (DR) regimes by simply changing the DF, keeping all other beam properties constant.

Notable commissioning milestones for FIRST included installation of a new AC current transformer (ACCT), updated beam-dump (EMBD) and electron collimator (COL) current read-backs, temperature (K-type thermocouple) read-backs, cooling-water flow-rate monitoring[2], and the establishment of a zero dispersion beam tune[3]. Flow rates were set to ~7 lpm and beam current on

[2]Requirement specifications developed together with Luca Egoriti
[3]Beam tunes (see Figure 6.2) developed and commissioned by Drs. Stephanie Rädel and Thomas Planche

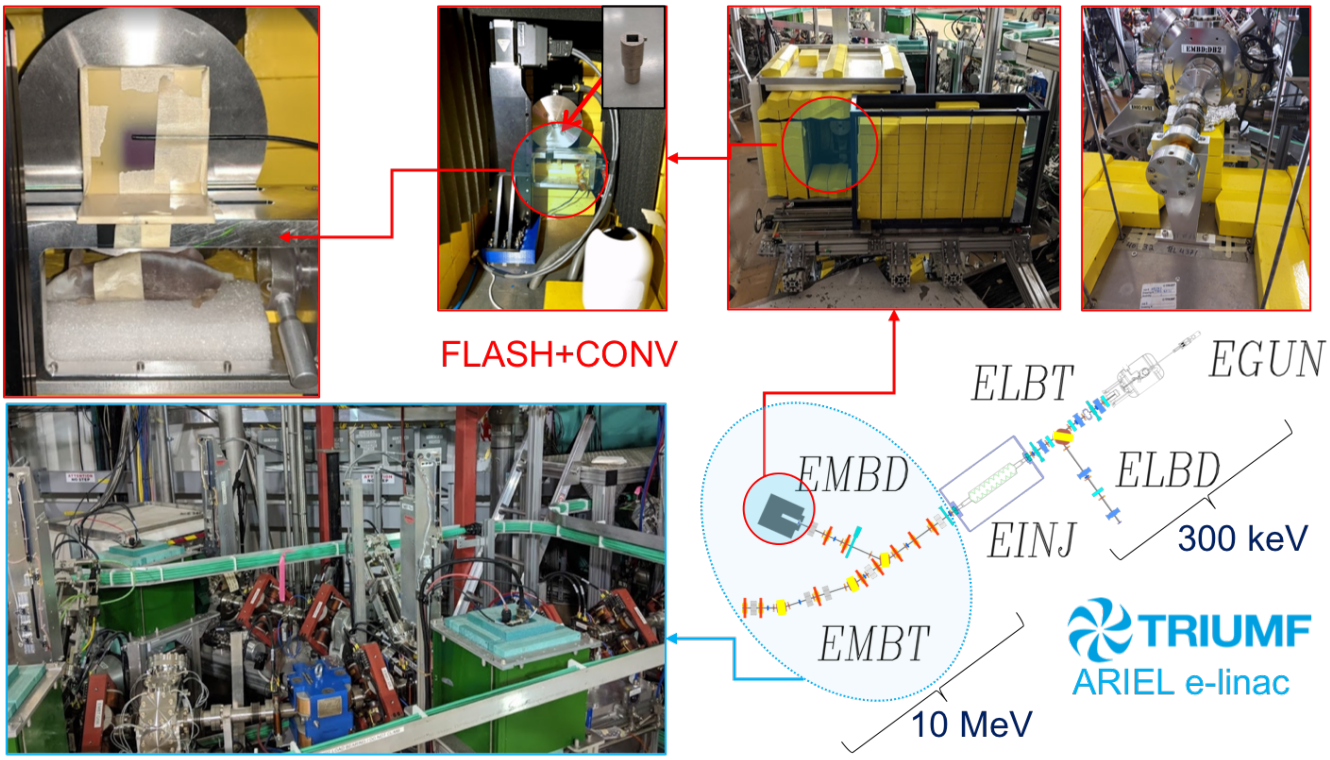

Figure 6.4: The ARIEL electron linac and new FIRST 10 MV x-ray FLASH platform (outlined in red) has been installed in the medium energy section (EMBD, blue outlines) following the injector cryomodule (EINJ). Film and real-time dosimetry was conducted in solid-water phantoms and a water-filled Falcon tube registered with the mouse treatment position (top left).

the target/dump assembly was consistently between 105-120 μA, consistent with conservative beam power (heat) load limitations considered in the previous design work [53].

Diagnostics upstream of the target included a fluorescent viewscreen (VS) and non-intercepting beam position monitors (BPMs) for online beam centering and size verification, Faraday Cups (FC) for steady-state beam current measurement, and a calibrated AC current transformer (ACCT) for pulsed beam current measurement. While FCs are simple integrating charge collection devices, the ACCT presented a critical addition for measurement of the ultra-fast current transients which the FCs could not detect owing to the limitations of their associated readout electronics. Fundamentally, the ACCT functioned as an in-air induction toroid which detected changes in the current passing through it's center on a ms time scale by using a precision (70-300 MHz) 1.25 GSa/s RTB2004 oscilloscope (Rhode&Schwarz, Munich, Germany). The relative position of these components within the linac structure is illustrated schematically in Figure 6.5.

6.2.3.1 Solid water and Falcon tube phantoms

Film measurements were conducted in both a solid water (SW) stack and a water-filled 50 mL Falcon tube. For SW measurements, depth-dose profiles were acquired perpendicular to the beam direction

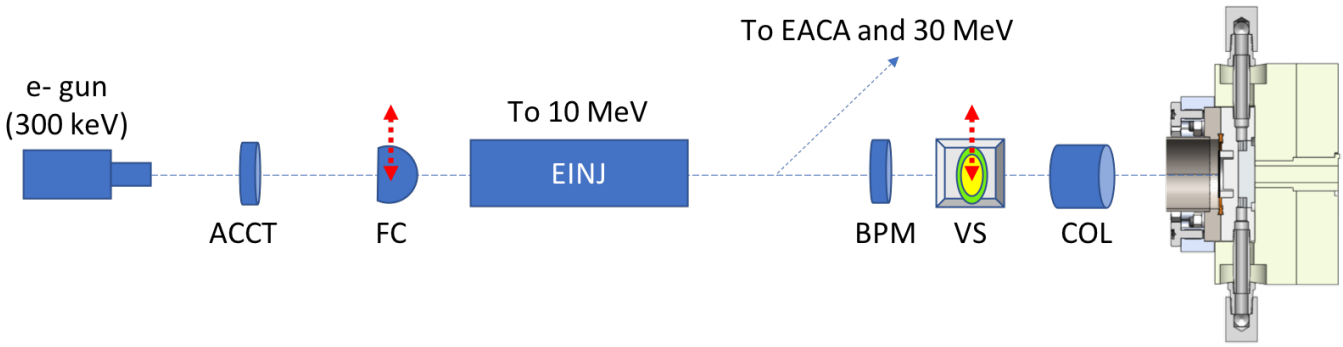

Figure 6.5: Beamline schematic for the ARIEL e-linac. Various diagnostics and important transport devices for FLASH and CONV delivery are denoted at their relative position (not to scale) along the beam path. Current was monitored for FLASH (single pulse) operation at the ACCT, while current and integrated charge was measured for CONV (continuous) at the e-to-γ conversion target-flange assembly (i.e. EMBD current). An insulated electron collimator with an internal diameter of 2 cm (0.8") is used to ensure the beam is tripped in the case of operation steering error or a kick that might otherwise result in beam impingement on sensitive, non-cooled structures downstream. [VS=viewscreen; BPM-beam position monitor; FC=Faraday Cup; ACCT=AC current transformer; COL=electron collimator]

at various depths within a $(5.8 \times 5.8 \times 3)\,\mathrm{mm}^3$ phantom composed of 3-mm thick slabs. Alternatively, continuous depth-doses could be acquired by aligning the films parallel to the beam direction [243]. In either case, the phantom was placed on the top of the mouse compartment, owing to space constraints, and carefully aligned by means of taking 'scout' films and measuring the required position shifts. A stepper-motor driven, 10-cm travel motion stage (Zaber, Vancouver, Canada) was capable of vertically positioning the phantoms to within an accuracy of $25\,\mu m$; meanwhile, the phantom position was localized horizontally using fiducials located 1 cm from the front edge of the mouse holder, which corresponded to an SSD of $\sim$ 8.5 cm. This setup was used to align the SW 1-cm depth-dose film with the location of the Falcon tube centra-axis, which would in turn corresponded to the mouse mid-sagittal plane.

To more closely reproduce the treatment setup of the mouse, and verify the validity of reference doses measured within the SW stack, films were carefully cut to fit within a water-filled polypropylene Falcon tube. Film submersion was limited to no longer than 1 hr to avoid affecting results away from the taped film edges [122, 244]. The results in this setup better reflected actual treatment conditions as the films could be positioned within the Falcon tube at the water depth representative of the mouse lung, $\sim$ 1 cm assuming a nominal mouse diameter of 2 cm. The Falcon tube provided an additional 1 mm water-equivalent thickness due to the tube wall. In practice, this would have resulted in a reduction in electron skin dose for the mouse based on the steep dose-falloff at shallow depths observed in MC simulations [53]. The full dosimetry setup is shown in Figure 6.6.

Because doses could not be measured *in-situ* for mouse irradiatons, the 1-cm depth-dose (D_{1cm}) in the Falcon tube was correlated with dose delivered to films (D_{win}) located in-air upstream of the tube/mouse position. The holder and films were thus rigidly fixed between the collimator at

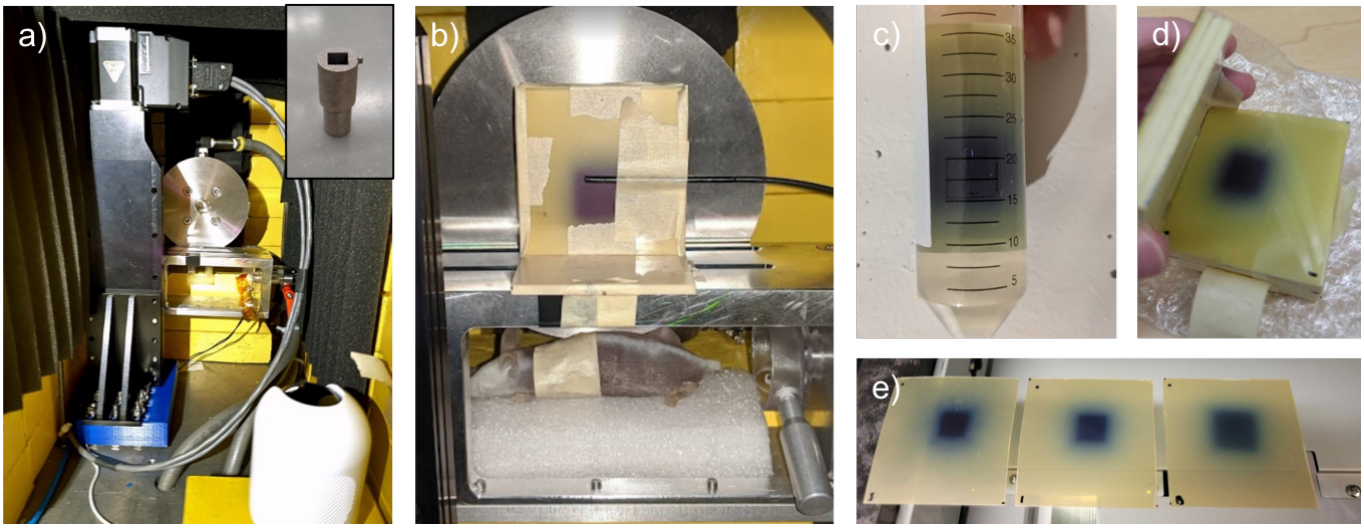

Figure 6.6: UHDR/FLASH irradiation station interior (a) and experimental setup for simultaneous EBT3 film and fiber optic scintillator test measurements (b). Films irradiated within the Falcon tube (c) or solid-water (SW) stack (d) are shown. Perpendicular SW films were affixed to an 18-mm thick SW phantom comprising $5.8 \times 5.8 \times 3.0\,\mathrm{cm}^3$ slabs at depths of 0, 9 and 18 mm, representative of entrance, lung and exit planes for a 2-cm diameter small-animal (e). The source-to-surface distance was 8.5 cm and the field size was defined by a $1 \times 1\,\mathrm{cm}^2$ 3D-printed tungsten collimator insert (see (a) inset). A 3D-printed mouse phantom (b) containing laser-cut thoracic films revealed that body doses in the lowered (bunkered) stage position were below the detectable limit of the film (D <10cGy) [118].

Falcon tube (i.e. SSD≈ 8.5 cm; see Section 6.2.5). The window-to-D_{1cm} conversion factor ($WR = D_{win}/D_{1cm}$) was determined separately for each prescription dose (15 or 30 Gy) due to the mixed beam quality at the window-film location; in this case, the 10 MV (photon) film calibration (6.2.2) was not assumed to hold for the electron dose component ($\bar{E}_e = 1.3\,MeV$) for the ARIEL beam [53]. On the other hand, WR was not found to change between beam tunes at constant energy or between CONV and FLASH mode.

During beam setup, samples were removed from beam via vertical motion stage (see Figure 6.6a,b) to limit radiation dose to <10 cGy prior to delivery and mitigate risk of accidental exposure. The sample holder was moved to a pre-defined treatment position once the beam was readied. In addition, the mouse holder was designed to accommodate a 25 kg lead brick on top of the motion stage adapter (max. cantilevered load = 120 Nm) to further reduce the dose to samples in the bunker (lower) position.

6.2.4 Irradiation procedure for UHDR and CONV delivery on the ARIEL e-linac

A summary of the procedure for delivering both 10MV FLASH and CONV beams to the irradiation station are described herein. In all cases, the e-beam is provided by the thermionic e-gun at 300 keV and accelerated to 10 MeV through the injector cryomodule (EINJ, Figure 6.4 and 6.5). In all cases the peak current was set near to a nominal value of 100 µA (0.1 mA) and time or charge

integration corrections, as is appropriate to FLASH and CONV respectively, were made online based on deviations from a calibration value. A schematic summary of the irradiation delivery workflow is shown in Figure 6.7.

6.2.4.1 UHDR (FLASH) Irradiation Procedure

Beam was delivered at UHDR ($\sim 10^{-2}$ Gy/s) by ensuring the linac was set for 'single pulse' operation, in which the PRF was set to 1 Hz. In this mode the variable DF effectively modulated the total pulse length (irradiation time), up to a maximum of 1 s. A limit on the pulse length was set at 500 ms to limit the risk of beam trips due to occasional vacuum spikes resulting from spurious over-current on the target or electron collimator. The average power was limited to 1 kW based on thermomechanical and fatigue life limitations [53] and corresponded to an average beam current of 0.1 mA at 10 MeV.

Ahead of irradiation, the peak current was first measured by an upstream FC under steady-state (i.e. normal mode) conditions. Once a stable beam current had been set-up on the FC, it was imperative to evaluate the single-pulse peak current and shape. To accomplish this, a single shot was delivered with the FC inserted while the the ACCT oscilloscope recorded the pulse transient as voltage over time (see Figure 6.7, bottom-left). The raw pulse data was immediately processed using a custom MATLAB (Mathworks, Nattick, MA) script[4] to determine the average current (I_{ACCT}) and pulse width of the recovered signal. Since I_{ACCT} was proportional to the mean pulse DR ($\bar{\dot{D}}$), the pulse width - and thus the FLASH irradiation time - was scaled in accordance with the measured ACCT current using a pre-calibrated DR-to-I_{ACCT} conversion factor (in Gy µC^{-1}):

$$f_{FLASH} = \frac{\bar{\dot{D}}}{I_{ACCT}} \tag{6.1}$$

The irradiation time (t) required to deliver a prescribed dose to 1-cm depth (D_{1cm}) was calculated as:

$$t = D_{1cm}/(f_{FLASH} * I_{ACCT}) \tag{6.2}$$

Before delivering to the target, the electron beam centering on the target was verified by using the upstream VS while the samples were in a retracted (shielded) position. Moreover, if the ACCT signal shape was not uniform, adjustments to cathode heater voltage were made to help stabilize and flatten output curves and thus minimize dose-rate variations within the pulse. When ready, the FLASH single-pulse mode was selected to deliver a single (macro) pulse in under 500 ms.

6.2.4.2 CONV Irradiation Procedure

Beam was delivered at low dose-rates ($\bar{\dot{D}} \sim 10^{-2}$Gy/s) by ensuring the linac was set for 'normal' mode operation, in which the DF - and thus pulse width - as well as pulse repetition frequency were

[4] Adapted from the transfer function and code developed by Dr. Hui-Wen Koay.

freely variable but were constrained by a maximum average beam power of 200 W, as determined by the following relation: $P_{ave} = (I_p \cdot E \cdot DF) < 200\,W$, where I_p is the peak current in mA, E is the beam energy in MeV and DF is the duty factor which represents the proportion of the time that the beam is on (see Figure 6.1).

In contrast to FLASH, CONV deliveries require much longer irradiation times at lower dose rates. This was accomplished by using a low duty factor and fixed 100 Hz PRF. However, due to potential for current drift, it was insufficient to calculate *a priori* the treatment time based on current measurements. Instead, a procedure was developed to deliver a prescribed dose based on the total integrated charge measured on the target/beam dump (EMBD). A dose-to-charge conversion factor was first calculated by delivering beam for a set amount of time and taking the mean ratio between film dose and the corresponding EMBD integrated charge according to the following formulation:

$$f_{CONV} = D_{1cm}/C_{EMBD} \tag{6.3}$$

where C is the total integrated charge at the EMBD (i.e. on target). Thereafter, the charge (C) required to reach the desired dose to 1-cm depth in water could be determined from:

$$C_{EMBD} = D_{1cm}/f_{CONV} \tag{6.4}$$

Figure 6.7 (bottom-right) shows an example of the (peak) current signal monitoring (red line and inset) and the corresponding integrated charge (blue line) that dictates when delivery is terminated, namely after reaching the prescribed value (dashed line). The DF was nominally set to 0.05% for all irradiations which corresponded to a dose-rate of approximately 0.05 Gy/s (see Section 6.3).

For phantom and animal irradiations, the current on the upstream FC was measured to verify the peak current, as for FLASH mode. Thereafter, sample irradiation would proceed as the beam current was integrated in real-time on the target read-back (EMBD).

In the event that a FLASH/single pulse is to be delivered immediately before or after CONV, an ACCT-to-EMBD current calibration (transmission) factor (TF) of 1.1 (0.6 for the 15 Gy cohort) - representing the mean current-ratio measured between the ACCT to the EMBD readings - could be applied to ensure reliable charge, and thus dose, consistency for back-to-back irradiations despite changes in dose rate. A set of *drosophila* larvae experiments demonstrated the feasibility of this procedure as well as highlight the beam quality constancy between beam modes under identical conditions; PDDs are included in Appendix A.7.

6.2.5 First UHDR and comparative CONV mouse irradiations at 10 MeV

In a first small-animal study, four mouse cohorts each comprising six healthy male C57Bl6 mice (Jackson Laboratory, Sacramento, CA, United States) were prescribed with single-fraction 15 Gy or 30 Gy total-lung (thoracic) irradiations using either FLASH (> 40 Gy/s) or CONV(< 0.05 Gy/s)

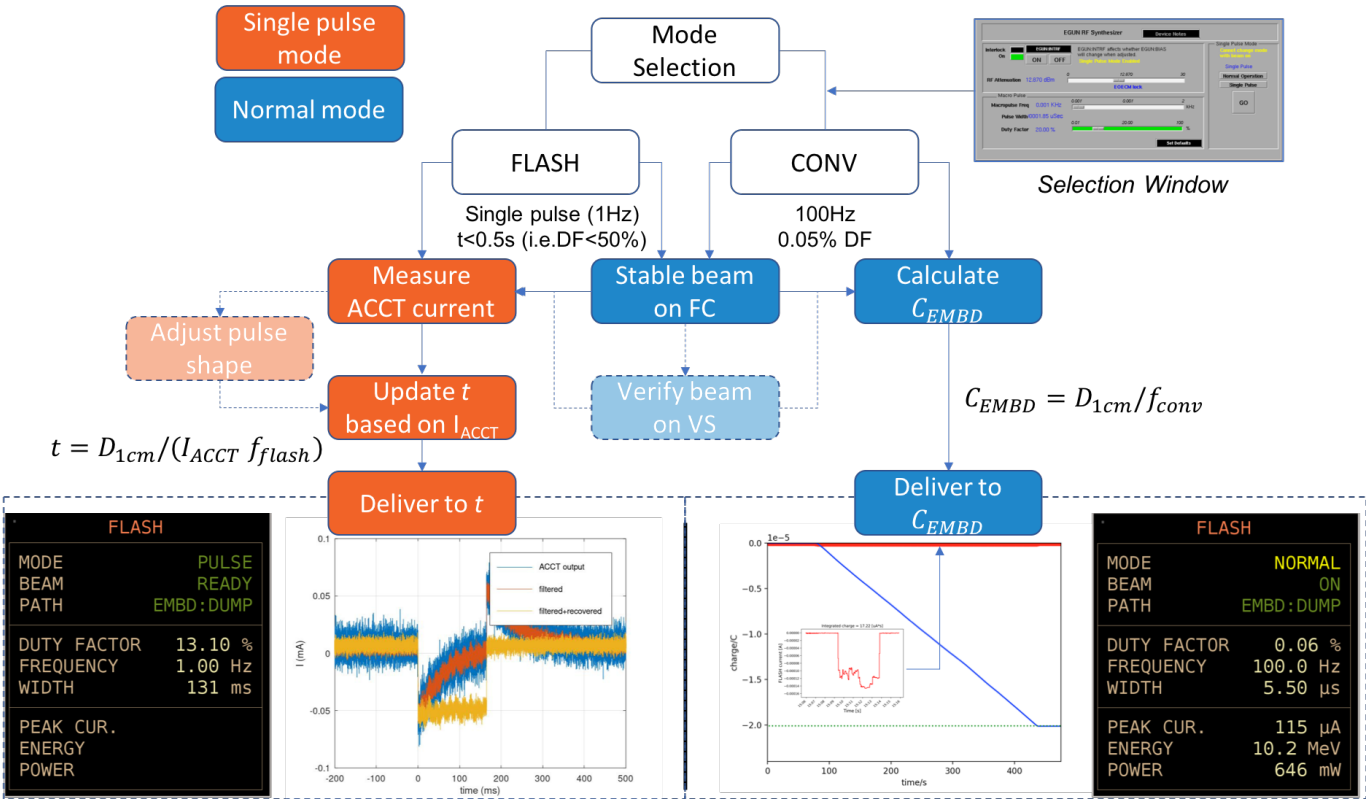

Figure 6.7: Beam delivery and monitoring workflow based on mode selection (CONV or FLASH) for radiobiological experiments on the ARIEL e-linac. The single-pulse (FLASH) or normal mode (CONV) operational elements are highlighted in orange or blue, respectively. Procedures with dotted lines denote aspects of beam delivery which are optionally followed based on operational needs. An inset (top-right) shows the controls screen for beam mode selection and beam temporal parameter adjustment. Examples of current monitoring outputs are shown in the bottom insets for FLASH/pulsed (bottom-left; ACCT) and continuous/CONV delivery (bottom-right; EMBD), including screenshots of the respective beam parameter summary screens.

beam modes and a $1 \times 1\,\mathrm{cm}^2$ field size. In all, 12 mice were irradiated for each modality with N = 6 per dose group, namely the 15 or 30 Gy FLASH (FLASH-15/30) or 15 and 30 Gy CONV (CONV-15/30). A control (sham irradiated) group (N = 4) was included and received only the injected anesthesia comprising Alfaxalone (40-60 mg/kg), Dexmedetomidine (0.15 mg/kg), and Butorphanol (2 mg/kg), delivered by subcutaneous injection.

All mice were aged 10-12 weeks at the time of treatment and were housed at housed and monitored at the Centre for High-Throughput Phenogenomics (University of British Columbia, Vancouver, CA) where baseline (pre-IR) and follow-up micro computed tomography (CT) scans were conducted (at 2, 4, 6, 9 and 12 weeks post-IR). With the exception of the control group, treated mice were anesthetized on-site by a trained technician prior to transport to the e-linac bunker for installation on the FIRST platform. In all cases, mice were localized within a perforated 50 mL Falcon tube which was placed horizontally within the beam path (see Figure 6.8). Mice were kept in a bunker position (by retracting the motion stage) until beam was ready for delivery; this procedure mitigated any risk of accidental

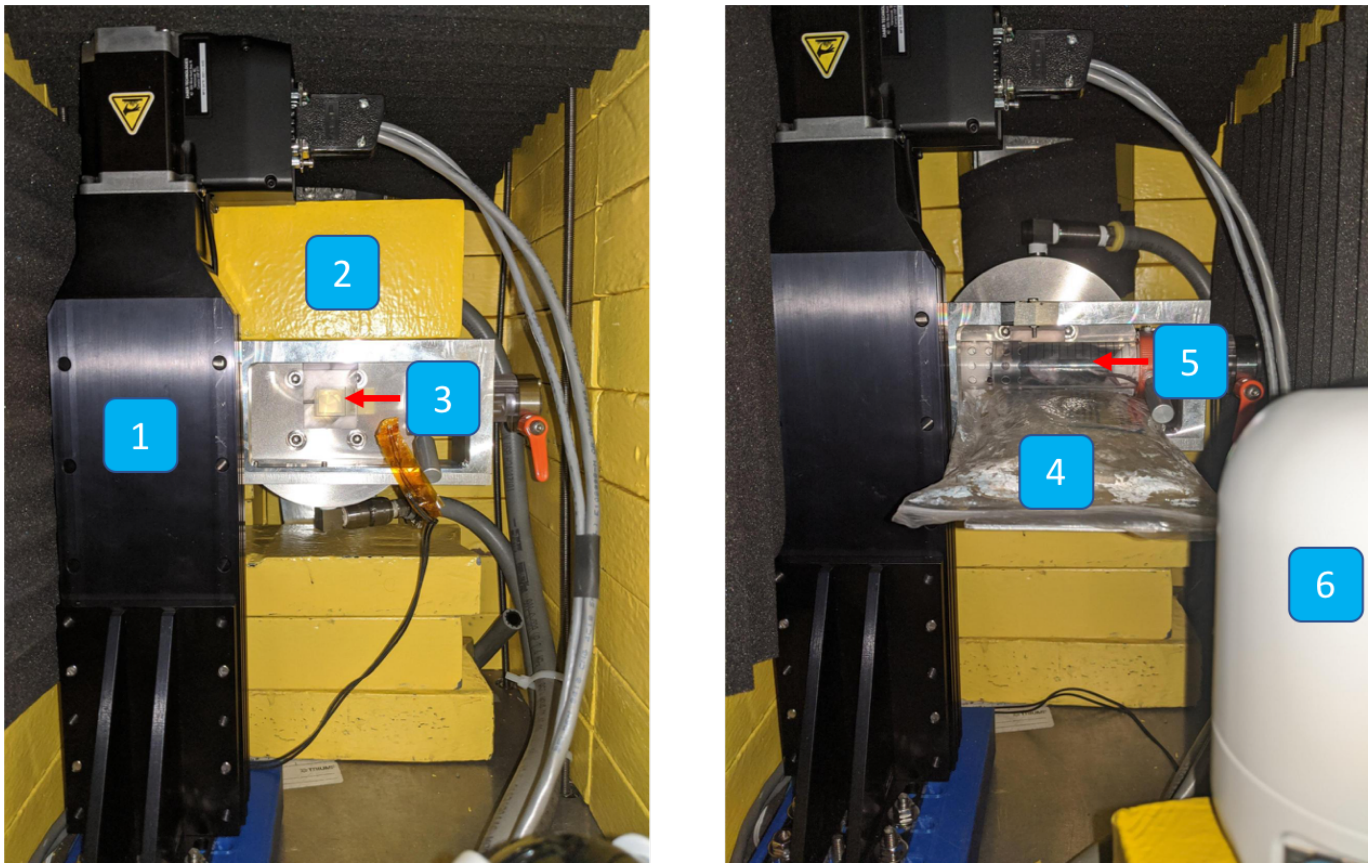

Figure 6.8: Notable setup features of the FIRST x-ray irradiation platform on the ARIEL beamline. The motion stage (1) enables transport of the sample holder and any shielding payload (2) over a travel distance of 10 cm. The window film holder is shown in (3). The mice were installed in the 50 mL Falcon tubes (5) that could be rigidly located within the mobile holder assembly along with liquid heating pads (4) for maintenance of animal temperature. A networked IR camera (6) could be used to monitor for animal movement and respiratory distress in the low-light conditions of the enclosure during treatments.

exposure and allowed for safe low-power tuning with beam on target determined through previous phantom measurements under identical setup conditions.

The doses to mouse lung following irradiation were calculated using the entrance (window) film doses calibrated against depth-dose measurements acquired under identical setup conditions (WR; Section 6.2.3.1). A schematic/CAD illustration is provided in Figure 6.9. FLASH irradiations were delivered as single $< 0.5s$ pulses while CONV was delivered using continuous (100 Hz) beam and a 5.5% duty factor. The summary of dosimetric results for this small-animal study as well as the average delivery parameters - including dose, DR, delivery time and charge measurements - is presented in section 6.3.

Prior to animal irradiations, ethics approval was obtained through the UBC animal care committee, in compliance with the Canadian Council on Animal Care (CCAC) assessment, for the experimental protocol (#A21-0060) under which all animal procedures were conducted.

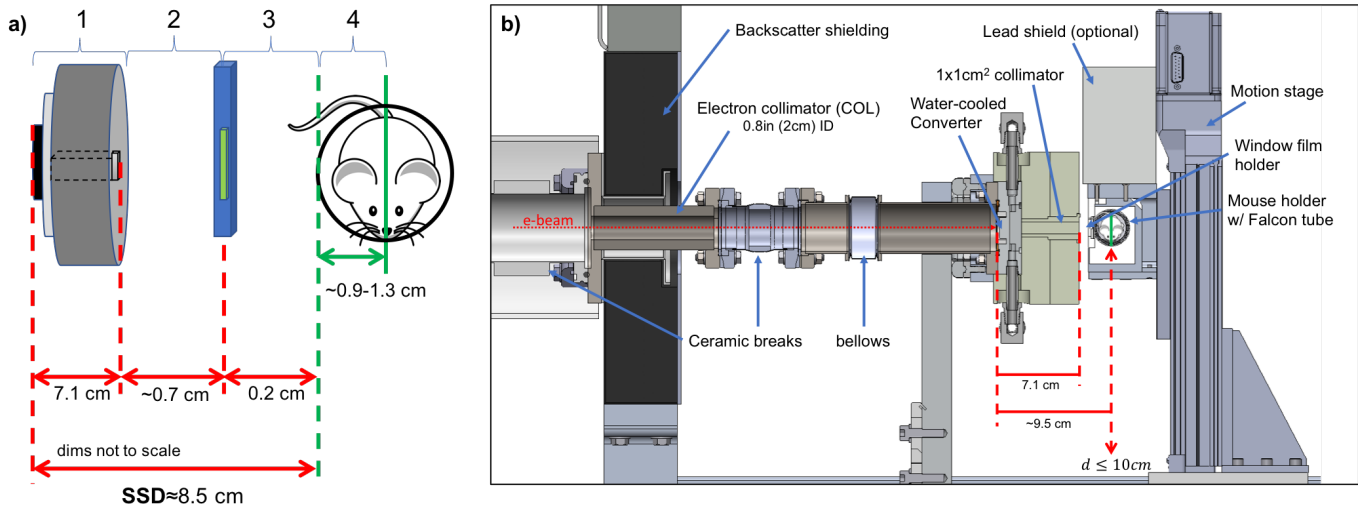

Figure 6.9: Schematic illustration of the treatment setup for mice at ARIEL FIRST (a). Distance annotations include the relative position of the collimator exit from the source (1), of the window films used for *in-vivo* dosimetry verification (2), the Falcon tube surface (3), and the approximate mouse mid-plane (4). The position of the motion stage, as well as the mice and their effective diameters were variable and so a range has been estimated. In b) a CAD cross-sectional view from the target to the motion stage and holder assembly is included along with to-scale dimensions for reference.

6.3 Results

6.3.1 Characterization of the ARIEL (FIRST) FLASH irradiation platform

Dose rates measured in sets of films in SW demonstrated the achievement of ultra-high dose rates on the ARIEL e-linac at 10 MeV and with a nominal beam power of 1 kW (Figure 6.10). Dose-per-charge ratios were calculated from the film doses and the associated charge-per-pulse, found by integrating the recovered ACCT response. Examples of the ACCT pulse signal are shown in Figure 6.11a for different same-day irradiations.

Table 6.2 summarizes the outcomes of the various UHDR Falcon tube irradiations for doses $\geq$ 24 Gy, including the film-derived doses and ACCT measurements. All irradiations had a pre-set time and the ACCT current was recorded twice in rapid succession, with beam first on the FC (ACCT pre) and then the target (ACCT actual). This provided a measure of I_{ACCT} variation that might be expected for the pre-treatment (planning) and treatment beam delivery. By using window-film doses acquired concurrently during tube irradiation, the 15 (Table 6.3) and 30 Gy (Table 6.2) WR factors were also calculated to be 1.25±0.95% and 1.22±6.23% (see Section 6.2.3.1). Also included are the dose-rates normalized to 100 µA (0.1 mA) peak beam current.

Conventional dose-rate (normal mode) irradiations were conducted under identical conditions as for the FLASH beam mode, but used the peak-current integration procedure outlined in Section 6.2.4.2. In order to establish the requisite f_{CONV} conversion factor, fixed-length (300 s) irradiations at 100 Hz and 0.055% DF were conducted with film-loaded Falcon tubes or SW phantoms, with results

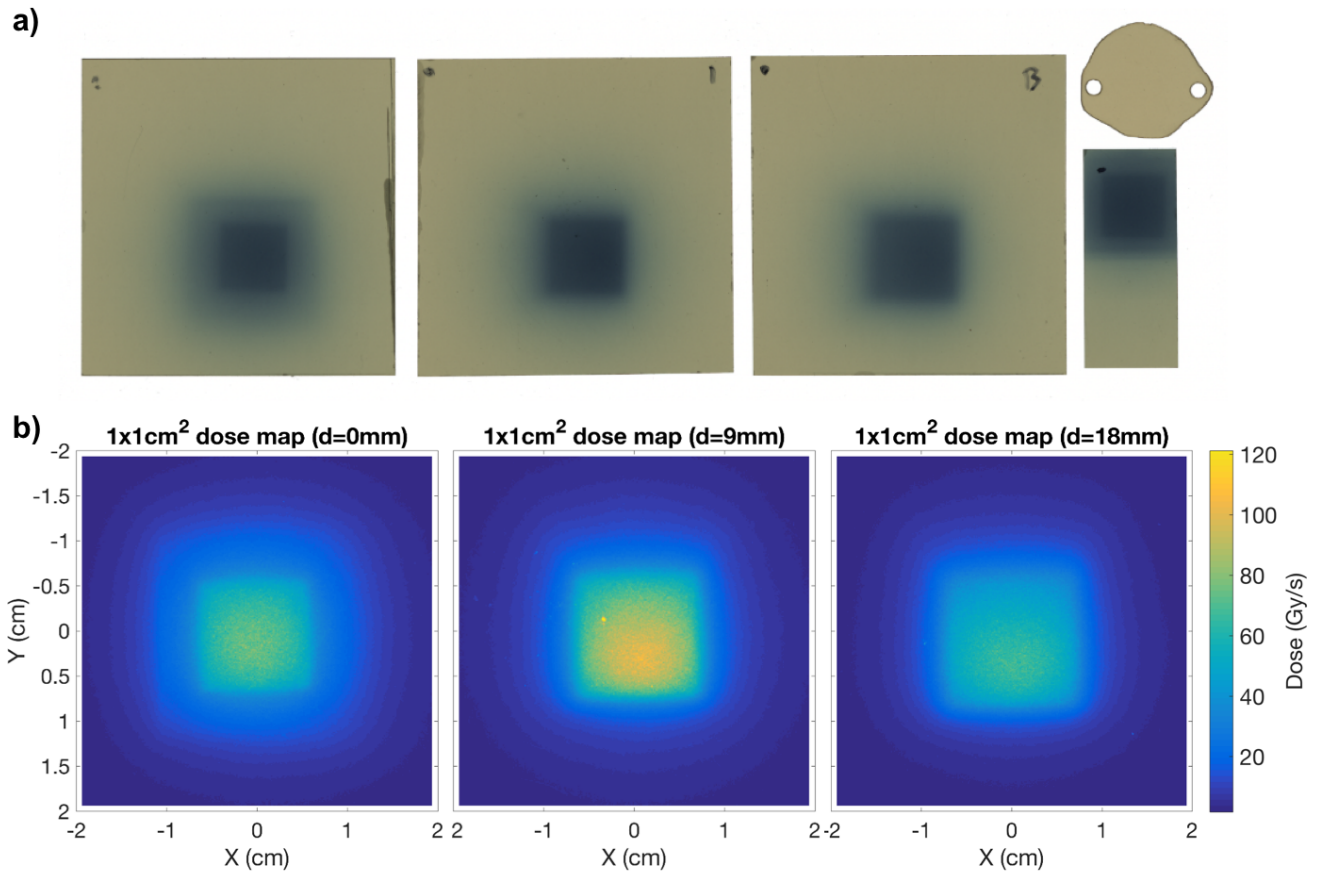

Figure 6.10: Example of UHDR (FLASH mode) irradiated EBT3 films (a) at three depths (0, 9, 18 mm) in solid water, a window (reference) film (bottom right), and a laser-cut film that was placed within the 3D-printed mouse phantom thorax in the bunker position (top right). The window film is irradiated in-air and used to determine the ratio (WR) of the window-film dose to that at 1-cm depth in water (i.e. prescription depth). The corresponding dose-rate maps, based on the film dose-calibration (Figure 6.2) are included in b) which demonstrated achievement of UHDR conditions for a single 165-ms long FLASH-mode pulse.

summarized in Tables 6.3 and 6.4, respectively. Simultaneous integration of the ACCT current enabled calculation of the ACCT-EMBD transmission factor ($TF \approx 1.1$), which appeared to be inconsistent with the apparent agreement between f_{FLASH} and f_{CONV}.

Table 6.2: Summary of UHDR (FLASH mode) results for high-dose Falcon tube film irradiations (≥ 24 Gy) delivered to 1-cm depth in water. ACCT currents were recorded with beam delivered to the FC (ACCT pre) or to the target (ACCT actual) and the dose on the reference window films are included for calculation of WR. Mean values for the ratio quantities (Normalized DR, *f*, WR) are included with the % standard deviation.

Sample name	Dose (Gy)	σ_{std}	Time (ms)	Dose rate (Gy/s)	ACCT pre (μA)	ACCT actual (μA)	Normalized DR* (Gy/s)	f_{FLASH} (Gy/μC)	Window dose (Gy)	WR
FT_1	34.52	3.4%	300	115.06	215	155	81.82	0.74	42.14	1.22
FT_2	36.18	3.1%	300	120.59	155	162	82.04	0.74	43.88	1.21
FT_3	24.00	3.0%	225	106.68	149	143	82.22	0.75	31.75	1.32
FT_4	30.68	3.1%	300	102.28	140	134	84.13	0.76	34.89	1.14
						mean ± σ	82.55±1.29%	0.75±1.29%	—	1.22±6.23%

*dose-rate (DR) is normalized to 100 μA as measured at the target (EMBD)

Perpendicular film-stack measurements, for both the initial (i.e. for FLASH-15/CONV-15) and final beam tune (for FLASH-30/CONV-30) are included in Table 6.4. It is important to note that the f_{FLASH} factors differ by a factor of ≈ 1.6 for the two beam tunes primarily due to changes in the ACCT calibration, and not due to significant changes in electron transport efficiency along the beamline. This is exemplified by the CONV results presented in Table 6.3 above, where a decrease in the ACCT-EMBD TF by a factor of 1.83 is observed between the two tunes, contrasting with a smaller (10%) change in f_{CONV}, and implies only a comparatively modest improvement in transport efficiency for the the new beam (tune2).

Parallel SW films for PDD and depth-profile measurements were analyzed and a dose map is shown in Figure 6.12a. The PDD results (Figure 6.12b) are compared against the discrete (N=8) depth measurements from perpendicular data sets, a subset of which were included in Table 6.4. Good agreement was found between the parallel and mean perpendicular data evidenced by corresponding depth-doses agreeing to within the bounds of the associated uncertainty down to a water-depth of 18 mm. At this point, a drop off in the perpendicular data appears due to the relative lack of backscatter in the 2-cm thick, perpendicular film phantom as compared to the parallel configuration for which the phantom thickness was 5.8 cm. Notable are the relatively low d_{max} (0.57 cm) relative to clinical 10 MV beams ($d_{max} \approx 2$ cm) which resulted from both the small field size, and reduced skin-sparing effect (higher superficial dose); the latter contribution is due to reduced (target) self-attenuation and beam filtration in the converter, as well as contaminant electrons generated predominantly in the

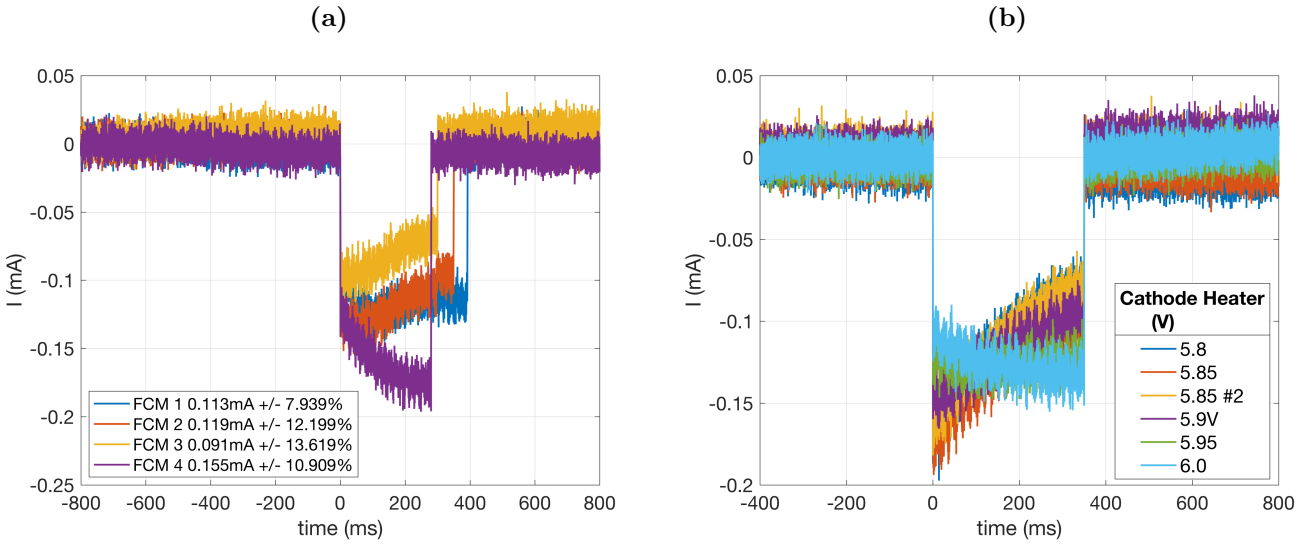

Figure 6.11: Reconstructed ACCT (current) signal outputs (a) used to calculate the required FLASH treatment time (Equation 6.2). The sensitivity of the pulse shape, and thus intra-pulse dose-rate (DR), to cathode heater setting in a single lockup is clearly demonstrated in b). The plots illustrate the source-related limitation of dose-rate constancy within a single (macro) pulse for a selected peak current (as measured on the FC, Figure 6.5). To minimize the effects of pulse DR variation in preclinical subjects, the pulse shape was checked ahead of each UHDR irradiation and cathode heater settings were adjusted to rectify highly irregular pulses (i.e. those with large transients).

Table 6.3: Summary of conventional, low-DR (CONV mode) results for low dose Falcon tube film irradiations ($\geq 10\,\mathrm{Gy}$) delivered to 1-cm depth in water. The EMBD and ACCT currents were integrated over the course of beam delivery, which was terminated at a prescribed time (300 s), in order to provide total charge values and ACCT-EMBD transmission factors (TF). Film irradiation using the initial beam tune (FT_CW0) is included, wherein italicized quantities indicate those for which significant changes were found between tunes. Mean values for the ratio quantities (Normalized DR, *f*, WR) are included with the % standard deviation.

Sample name	Dose (Gy)	σ_{std}	Time (s)	Dose rate (Gy/s)	EMBD charge (μC)	ACCT charge (μC)	TF†	Normalized DR* (Gy/s)	f_{CONV} (Gy/μC)	Window dose (Gy)	WR
FT_CW1	12.70	2.3%	300	4.23×10^{-2}	16.7	17.178	1.03	4.18×10^{-2}	0.76	15.77	1.24
FT_CW2	10.43	2.4%	300	3.48×10^{-2}	14.54	17.0955	1.18	3.95×10^{-2}	0.72		
						mean ± σ	1.10±9.44%	4.06×10^{-2}±4.10%	0.74±4.10%	—	—
FT_CW0	13.48	3.4%	300	4.49×10^{-2}	20.1	*12.09*	*0.60*	3.69×10^{-2}	0.67	16.97	1.26

*dose-rate (DR) is normalized to 100 μA as measured at the target (EMBD)
† the transmission factor (TF) is defined as the ratio of the ACCT charge and EMBD (target) charge readings

collimating structures. The lack of build-up was expected due to the large electron dose component although it was less pronounced compared to MC simulations, which was attributed to the increased treatment SSD (≃8.5cm) [53].

Lateral (Y) dose profiles at relevant depths of d_{max} and at 1 cm (prescription depth) are shown in Figure 6.13a. While the consistency of the beam full-width at half-maximum (FWHM) and lateral penumbra is qualitatively apparent, there is an obviously limited degree of flatness about the central-axis. The depth-dependence ($d \in [0, 5.8]\,\mathrm{cm}$) of the beam 80-20% beam penumbra and FWHM is presented in Figure 6.13b. In addition, the full-width at 80% of dose-maximum (FW80) is shown, which encompasses the $0.5\,\mathrm{mm}^2$ region of interest (ROI) over which peak dose-rates were evaluated; this region was considered to be sufficiently flat for the purposes of dose prescription. A representative set of penumbra width measurements was taken from a perpendicular film set (SW_FLASH; see Table 6.4). The point of intersection between each full-width measurement and the nominal 40 Gy/s FLASH threshold dose-rate was calculated (F40W) and is included in Table 6.5. Notably, the inter-

Table 6.4: Solid water phantom depth-dose result summary for FLASH (initial and final tune) and CONV irradiation. Data are derived from perpendicular film dose measurements for a $5\,\mathrm{mm}^2$ ROI with irradiation time and current measurements at the ACCT or EMBD. Italicized current values represent those calculated using the ACCT-EMBD TF from Table 6.3.

	Depth (mm)	Dose (Gy)	σ_{ROI}	time (s)	Dose Rate (Gy/s)	ACCT current (μA)	EMBD current (μA)	Integrated EMBD charge (μC)	Normalized DR* (Gy/s)	*f*† (Gy/μC)
SW_CONV (tune2)	0	10.24	1.7%	300	3.41×10^{-2}			20.1	2.80×10^{-2}	0.51
	3	14.95	2.8%	300	4.98×10^{-2}	*134.3*	121.8	20.1	4.09×10^{-2}	0.74
	9	14.43	2.6%	300	4.81×10^{-2}			20.1	3.95×10^{-2}	0.72
SW_FLASH (tune2)	0	17.63	2.5%	0.22	80.12			—	62.19	0.56
	3	24.06	2.8%	0.22	109.36	141.0	*127.9*	—	84.88	0.77
	9	22.61	2.7%	0.22	102.75			—	79.76	0.72
	18	16.46	2.9%	0.22	74.80			—	58.06	0.53
SW_FLASH (tune1)	0	11.30	2.0%	0.162	71.24			—	55.69	0.91
	3	15.63	3.0%	0.162	100.07	77.0	*128.0*	—	78.22	1.25
	9	13.76	2.7%	0.162	88.00			—	68.79	1.10
	18	10.82	2.3%	0.162	68.40			—	53.47	0.87

*dose-rate (DR) is normalized to 100 μA as measured at the target (EMBD)
† dose-per-charge, where charge is measured via the ACCT or EMBD for FLASH and CONV modes, respectively

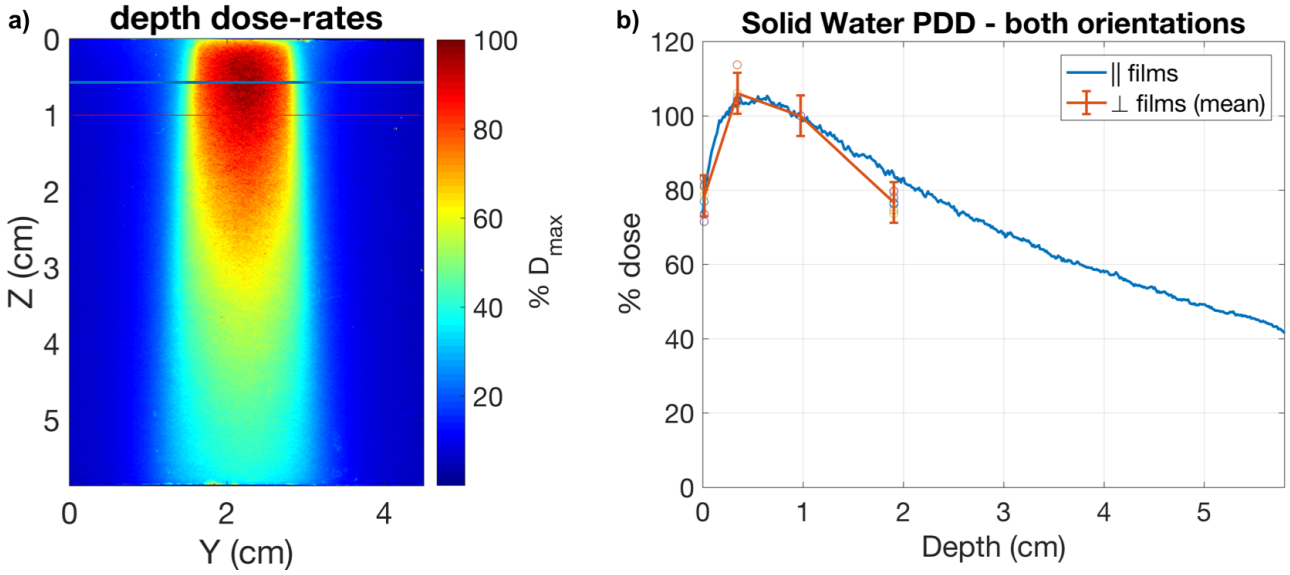

Figure 6.12: Parallel film dose map (a) and corresponding PDD (b) normalized at 1 cm depth. Results from 4 sample depths (at d=0,3,9,18 mm) using 8 sets of perpendicular films (N=8), adjusted for the approximate film thickness ($\approx$ 0.3µm), are plotted as open circles. Errorbars are included for the averaged depth-dose result at each depth and correspond, as a percentage, to the standard deviation in the mean. The PDD data in b) are normalized to the dose at 1 cm (treatment depth) in water, rather than d_{max} used in a).

section depth for FW80% (3.6 cm) provides an indication of the depth in water-equivalent media to which the beam is effective at providing sufficient dose coverage (FW80%=1.25 cm) at UHDR (i.e. $\bar{\dot{D}}$ >40 Gy/s).

To illustrate the Gaussian-like symmetry of the produced x-ray field using the film data, X- and Y-profiles, averaged over the complementary direction, were calculated for the central 5 mm^2 ROI. The results are shown for a perpendicular SW film sets in Figure 6.14, for the initial and final (Figure 6.2) beam tune respectively, which help to qualitatively illustrate the degree of symmetry.

If the beam had been noticeably off-centre along either axis then it would have appeared as a skew in the dose distributions. Aside from the surface dose distribution, which is dominated by the broadly distributed electron component of the beam, the profiles in Figure 6.14a show some asymmetry at depth. This is particularly obvious in the initial beam tune and corroborates the apparent shift in the central peak of the 2D dose distribution within the raw film data (see Figure 6.10). In the refined

Table 6.5: Depths of intersection between the FWHM or FW80% and the full-width at which the mean dose-rate is equal to 40 Gy/s (FW40), derived from the curves in Figure 6.13.

FW metric	Width (cm)	FW40 intersection depth (cm)
FWHM	1.47	1.35
FW80%	1.25	3.60

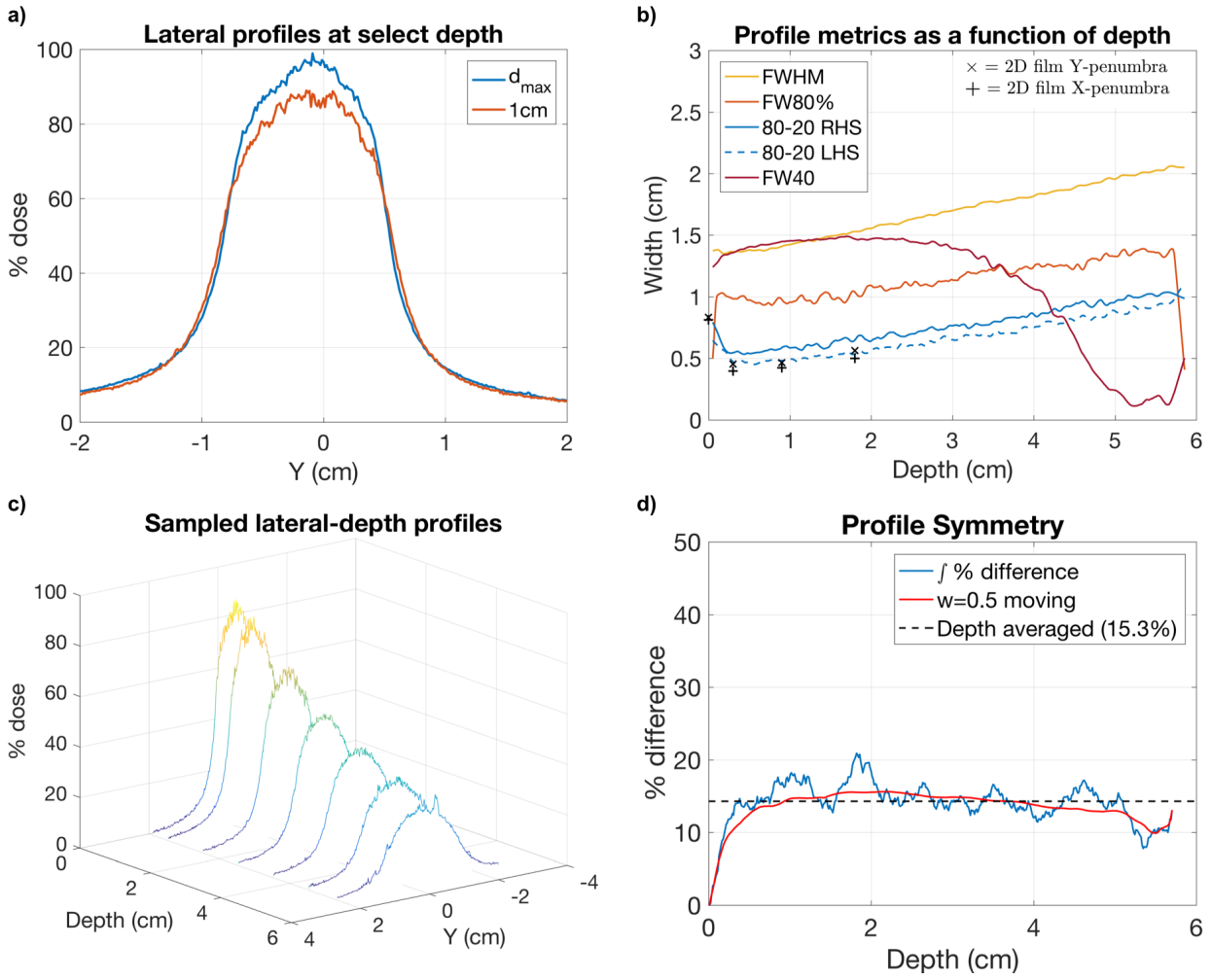

Figure 6.13: Depth-dose profile characterization of the 10 MV x-ray beam based on parallel film dosimetry results. Lateral profiles for d_{max}(0.57 cm) and at the nominal treatment depth of 1 cm in solid water are shown in a). The continuous depth-profile metrics are summarized in b) including the full-width at half-maximum (FWHM), full-width and $0.8D_{max}$ (FW80%), the 80–10% beam penumbra and full-width at 40 Gy/s (FW40). The penumbra are calculated separately for the left (LHS) and right-hand sides (RHS). The mean penumbra values calculated from perpendicular film data are plotted for the Y and X dimensions denoted by the **x** and + symbols, respectively. Data showcasing the depth-evolution of the lateral profile and peak doses (c) as well profile symmetry determined from the Y-axis 80-20 penumbra (d) are included. Depth-symmetry data was also smoothed using a 0.5 span (w) moving-average filter in MATLAB.

beam tune developed for the 30 Gy mouse cohort (see Section 6.3.2), symmetry was visibly improved in the profiles of Figure 6.14b,d. The degree of beam symmetry for the final tune was also quantified by taking the integral for the 80-10 penumbral domain on either side of the FW80% domain (X_{FW80}) for the parallel-film depth-dose profile (Figure 6.12), where X_{FW80} : $[x(0.8D_{max,1}), x(0.8D_{max,2})]$. This amounted to integrating between $[x(0.2D_{max,1}), x(0.8D_{max,1})]$ and $[x(0.8D_{max,2}), x(0.2D_{max,2})]$ and computing the percentage difference. The symmetry as a function of depth in water is shown in Figure 6.13d. The mean value across all depths was 15.3 +/- 59%. Given that this degree of asymmetry was not apparent in the central (FW80) region of the averaged X and Y lateral profiles,

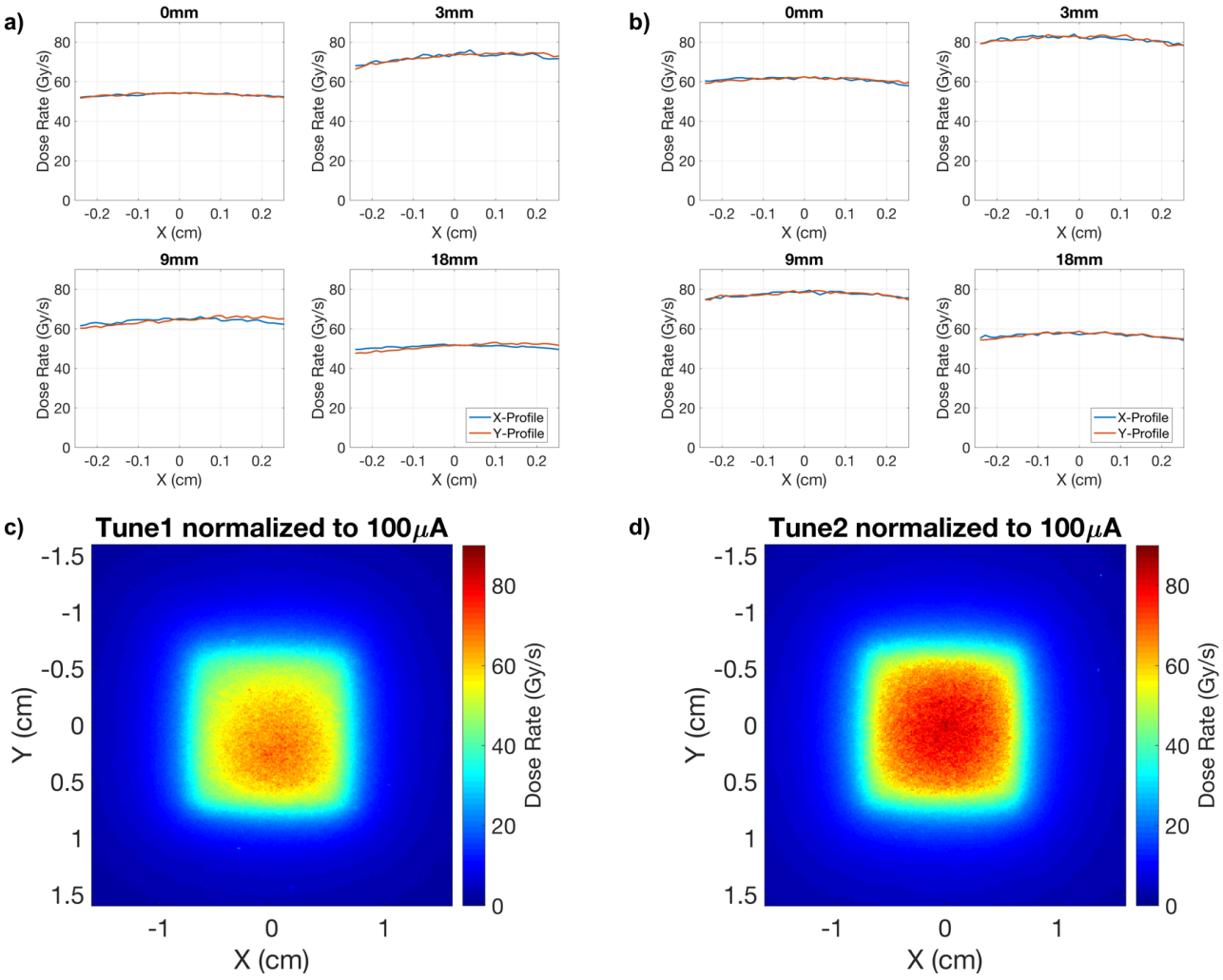

Figure 6.14: Lateral dose-rate profiles along X (blue lines) and Y (red line) axes. Data are averaged over the complementary direction for a CAX ROI of 5 mm^2. The results for the initial beam (a) and final (b) beam tunes are included at depths of 0, 3, 9 and 18 mm in the solid-water phantom. 2D dose-rate maps for films at 1-cm depth, and normalized to an EMBD current of 100 µA, are shown in the bottom row for both data sets.

depicted in Figure 6.14, it is suggested that the degree of symmetry within the treatment ROI domain ($X_{ROI} : [x(0.8D_{max,1}), x(0.8D_{max,2})]$) is better than for the penumbra regions ($x \notin X_{ROI}$).

Table 6.6: Comparison of representative dosimetry quantities. The mean dose-rate ($\bar{\dot{D}}$), time to 15Gy (t_{15Gy}),and f factors, are provided for both FLASH and CONV mode irradiations assuming that 100 µA (1 kW) is delivered to the target.

Mode	$\bar{\dot{D}}$ (Gy/s)	t_{15Gy} (s)	f (Gy/µC)
FLASH*	82.6	0.181	0.75
CONV†	4.40×10^{-2}	341	0.74

* single pulse (PRF=1 Hz; DF=100%)
† PRF=100 Hz; DF=0.055%

6.3.2 Mouse irradiation dosimetry

The dosimetric results - including dose, DR, irradiation times along with the measured charge and experimental dose/charge conversion (f) factors - for the first *in-vivo* study of x-ray FLASH-RT at TRIUMF are summarized in Tables 6.7 and 6.8 for the 15 Gy FLASH (FLASH-15) and CONV (CONV-15) cohorts, respectively. Tables 6.9 and 6.10 correspondingly report the results for the 30 Gy FLASH (FLASH-30) and CONV (CONV-30) cohorts. A visual summary of doses delivered for each cohort is included in Figure 6.15.

Table 6.7: Dosimetric result summary of FLASH-15 irradiated mouse cohort ($N = 6$, $D_{1cm} = 15$ Gy).

Mouse (M_#)	Window Dose (Gy)	D_{1cm} (Gy)	% difference*	Time (ms)	Dose rate (Gy/s)	ACCT actual (μA)[b]	Integrated charge (μA s)[b]	f_{FLASH} (Gy/μC)[b]
1	16.74	13.40	8.05	165.00	81.19	74.96	12.37	1.08
2[a]	16.16	14.76	1.30	154.00	95.83	*76.00*	*11.70*	*1.26*
3	18.73	14.99	2.87	165.00	90.83	75.70	12.49	1.20
4	18.10	14.49	0.58	171.00	84.71	71.90	12.29	1.18
5	17.58	14.07	3.43	162.00	86.85	74.70	12.10	1.16
6	19.64	15.72	7.89	171.00	91.93	76.90	13.15	1.20
mean	18.16	14.57	4.02	164.67	88.56	75.03	12.35	1.18
$\pm\,\sigma$ (%)	6.08	5.46	80.36	3.85	6.01	2.29	3.87	4.92

* The % difference is calculated as $(D - \bar{D})/max\{D, \bar{D}\}$.
[a] beam trip; dose delivered as two consecutive shots (82 ms and 72 ms resp.), and current is the time-weighted average current.
[b] Italicized, greyed-out cells indicate the quantities calculated for beam trips or in cases where a measurement was missed.

Table 6.8: Dosimetric result summary of CONV-15 irradiated mouse cohort ($N = 6$, $D_{1cm} = 15$ Gy).

Mouse (MCW_#)	Window Dose (Gy)	D_{1cm} (Gy)	% difference*	Time (s)	Dose rate (Gy/s)	EMBD current (μA)[b]	Integrated charge (μA s)[b]	f_{CONV} (Gy/μC)[b]
1	14.65	11.73	0.11	366.00	3.20×10^{-2}	101.09	20.35	0.58
2	14.76	11.81	0.64	303.00	3.90×10^{-2}	121.21	20.20	0.58
3	13.68	10.95	6.73	322.00	3.40×10^{-2}	114.23	20.23	0.54
4	13.59	10.88	7.33	327.00	3.33×10^{-2}	112.04	20.15	0.54
5	15.22	12.18	3.77	302.00	4.03×10^{-2}	121.79	20.23	0.60
6	16.10	12.89	9.77	360.00	3.58×10^{-2}	102.42	20.28	0.64
mean	14.65	11.74	4.72	330.00	3.57×10^{-2}	112.13	20.24	0.58
$\pm\,\sigma$ (%)	7.23	6.46		8.33	9.24	7.94	0.34	6.32

*the % difference is calculated as $(D - \bar{D})/max\{D, \bar{D}\}$

For both the 15 and 30 Gy groups, measured DRs at 1-cm water-depth for the 10 MV beam were >80 Gy/s and >0.03 Gy/s for FLASH and CONV modes, respectively. This verifies the successful delivery of UHDR treatment, as well as sufficiently low-DR for CONV.

In the 15 Gy group, the FLASH cohort received, on average, 14.6 Gy±5.5%, while the CONV cohort received a lower 11.7 Gy±6.5% dose. A spurious dose-rate drop prior to CONV initially resulted in the lower dose delivered; this is evidenced in the substantial reduction in f_{CONV} compared to the calibration data (cf. FTCW_O in Table 6.3). This lower dose prescription was intentionally maintained across all subjects in order to allow consistent evaluation of toxicity effects within the

Table 6.9: Dosimetric result summary of FLASH-30 irradiated mouse cohort ($N = 6$, $D_{1cm} = 30\,\text{Gy}$).

Mouse (M_#)	Window Dose (Gy)	D_{1cm} (Gy)	% difference*	Time (ms)	Dose rate (Gy/s)	ACCT actual (µA)[b]	Integrated charge (µA s)[b]	f_{FLASH} (Gy/µC)[b]
1	36.23	29.61	0.14	259.00	114.33	150.00	38.85	0.76
2	33.33	27.24	8.12	336.00	81.08	*113.00*	*37.97*	*0.72*
3	37.73	30.84	4.02	336.00	91.80	121.00	40.66	0.76
4[a]	*36.50*	*29.84*	*0.63*	333.00	*89.50*	*122.42*	*40.81*	*0.73*
5	38.78	31.70	6.90	292.00	108.55	*137.00*	*40.00*	*0.79*
6	35.08	28.68	3.29	269.00	106.60	146.00	39.27	0.73
mean	36.86	29.65	3.85	304.17	98.64	131.57	39.59	0.75
$\pm\,\sigma$ (%)	3.87	5.31		11.65	13.19	11.36	2.79	3.69

*the % difference is calculated as $(D - \bar{D})/max\{D, \bar{D}\}$
[a] beam trip; dose delivered as two consecutive shots (97 ms and 236 ms resp.), and current is the time-weighted average current.
[b] Italicized, greyed-out cells indicate the quantities calculated for beam trips or in cases where a measurement was missed

Table 6.10: Dosimetric result summary of CONV-30 irradiated mouse cohort ($N = 6$, $D_{1cm} = 30\,\text{Gy}$).

Mouse (MCW_#)	Window Dose (Gy)	D_{1cm} (Gy)	% difference*	Time (s)	Dose rate (Gy/s)	EMBD current (µA)[b]	Integrated charge (µA s)[b]	f_{CONV} (Gy/µC)[b]
1	40.24	32.89	0.10	630.00	5.22×10^{-2}	116.88	40.50	0.81
2	39.58	32.35	1.54	598.00	5.41×10^{-2}	122.86	40.41	0.80
3	40.66	33.23	1.15	627.00	5.30×10^{-2}	117.27	40.44	0.82
4	39.98	32.68	0.54	499.00	6.55×10^{-2}	147.75	40.55	0.81
5	40.03	32.72	0.40	555.00	5.90×10^{-2}	132.91	40.57	0.81
6	40.69	33.26	1.22	600.00	5.54×10^{-2}	122.52	40.43	0.82
mean	40.32	32.86	0.83	584.83	5.65×10^{-2}	126.70	40.48	0.81
$\pm\,\sigma$ (%)	0.84	1.06		8.54	8.82	9.33	0.17	1.11

*the % difference is calculated as $(D - \bar{D})/max\{D, \bar{D}\}$

CONV-15 cohort. Mean delivery times were 163 ms for the FLASH pulses and 5.5 min for the CONV irradiations.

Similarly, for the 30 Gy group, the FLASH cohort received, on average, 29.7 Gy±5.3% for FLASH, and the corresponding CONV doses were 32.8 Gy±1.1%. Evidently, there was a noticeable reduction in dose variance for the CONV-30 cohort relative to either CONV-15 of either of the FLASH cohorts, which is ascribed to improved procedures following the experiences with the 15 Gy group. Moreover, rather than underdosing as for CONV-15, an ≈ 10% overdose relative to the 30 Gy prescription was observed. This was due to an under-estimation of the f_{CONV} conversion factor, as evidenced by the increased value inferred from the mouse irradiations (Table 6.10).

6.4 Discussion

This work concerns the first recorded demonstration of an ultra-high dose rate, sub-second irradiation delivered with 10 MV x-rays on the new target station and FIRST platform for FLASH radiobiological experiments at the TRIUMF ARIEL e-linac. Film dosimetry and real-time measurements were used to offer high spatial and temporal resolution to demonstrate the system's compatibility with delivering a clinically-relevant 10 MV photons beam at dose rates > 40 Gy/s suitable for FLASH-RT research.

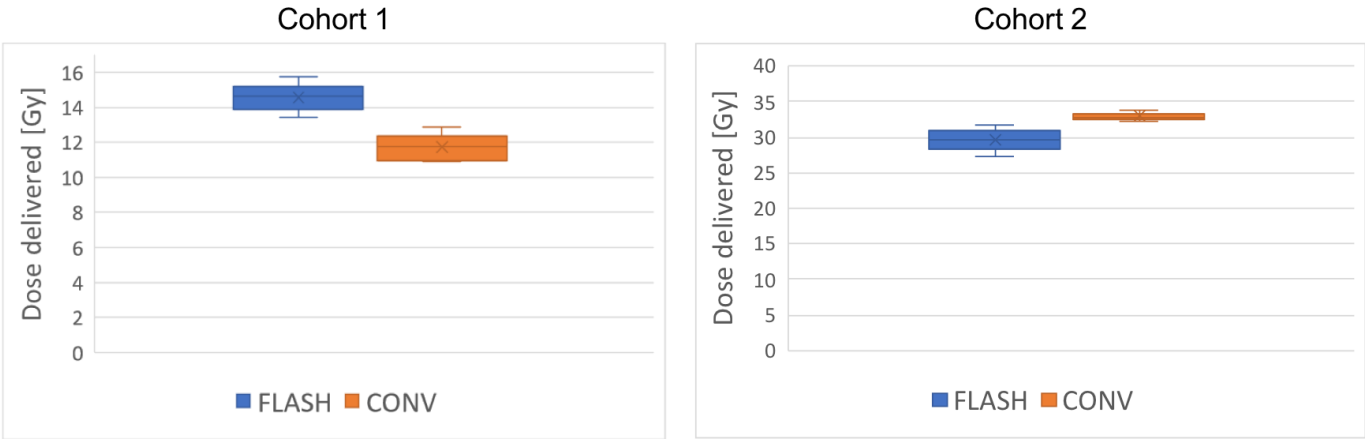

Figure 6.15: Box and whisker plots summarizing actual doses delivered for the 15 Gy (left) and 30 Gy (right) irradiations for two C57BL6 mouse cohorts and both FLASH and CONV modalities. The box represents the interquartile range, within which the median (line) and mean (x) are denoted, while the whiskers extend to the set maximum values. N = 6 per group (12 per cohort).

For UHDR (FLASH mode) irradiations, dose-rates in excess of 80–100 Gy/s, for the typical range in beam current, were consistently demonstrated (Table 6.2). By contrast, dose rates < 0.1 Gy/s were achieved in CONV mode at 100 Hz delivery using a low 0.05% DF. From subsequent mouse irradiations, it was demonstrated that doses could be delivered to within 10% of the prescription using the developed delivery strategy outlined in this work. In general, delivery of FLASH and CONV was predicated on careful pre-treatment dose measurements, whose uncertainties were dominated by variability in the source output and of the film dosimetry itself. Unfortunately, because the beam tune, gun behaviour and ACCT calibration were changed following a facility shutdown between the 15 and 30 Gy cohorts, it was necessary to re-characterize the beam and, specifically, the calculation of the dose-charge calibration factors (f) for each delivery mode. Due to limited beam time availability, the final data were limited in sample size, especially for the CONV beam calibration.

For all absolute and relative dosimetry, EBT3 Gafchromic films were employed alongside sensitive real-time systems for irradiation time and pulse shape diagnostics. Due to the high doses employed, a reduction in film dynamic range and dose sensitivity was expected for the prescribed doses of our mouse experiments. This prompted the use of the green color channel as well as the red channel, typically used at doses <10 Gy [137,245]. To improve the consistency and minimize dose errors across the range of doses used, both channels were evaluated given their comparable dose resolution at 15 and >25Gy [246]. It was determined that the red and green channel results, on average, agreed to within 1% for $D \in [25, 36]$ Gy and the green channel was utilized for the highest recorded doses, including for FLASH/CONV-30; conversely, only the red channel was employed for FLASH/CONV-15 irradiations due to the improved dynamic range and observation of reduced variance observed relative to the green channel at lower doses.

In general, dose results were found to agree well between the solid water phantom results and

Falcon tube measurements ($< 3\%$ difference). These data sets were thus taken together when calculating the average dose-current conversion factor for the mouse treatments. Falcon tube measurements closely replicated the treatment conditions and provided a consistent means of evaluating the window-dose ratio (D_{win}/D_{1cm}), while SW data provided access to surface and depth-dose information. While a full MC validation was not performed, it is interesting to note that the MC results for the dose rate (0.5 mm^2 ROI) at 1 cm depth in a 3D-printed mouse phantom ($\approx$ 86 Gy/s) [53] agreed to within 3.5% of the mean experimental dose-rate (83 Gy/s) at 1 cm depth, calculated from the aggregate Falcon tube and SW measurements. The experimental value in this case has been normalized to 1 kW average power and does not account for uncertainty in setup SSD, nominally set as 8.5 cm instead of 8 cm as used in the MC simulation.

It was determined that the pulse shape and current stability was dependent upon the ambient conditions of the gun and RF power supplies with a dependence that was not, at the time of writing, known or characterized. In particular, the cathode should be able to remain stable with modest temperature variation, but it was found that there was day-to-day variation in the cathode heater voltage required to provide an optimal (square) pulse shape, seemingly independent of RF input parameters or beam tune (see Figure 6.11b). Moreover, in CW mode, the e-gun emission behaviour, per the ACCT, was found to be dependent on the RF stability which itself was tied to the RF power supply temperature. Active cooling with air-conditioning helped to mitigate temperature swings during the irradiation campaign and thus improve pulse-to-pulse reproducibility. Improvements to RF stability could be observed in CONV mode through a reduction in signal noise measured on the ACCT oscilloscope and improved stability in the shape and height of between consecutive macro-pulses.

All mouse irradiations were successfully conducted for both FLASH and CONV groups in each of the 15 and 30 Gy cohorts, except for one mouse in each of the two FLASH groups which had to receive a split dose due to an accidental beam trip. The consequences of the split dose delivery for FLASH irradiation is not known and while it complicates the assessment of outcomes for those mice, it also represents an opportunity to note any differences worthy of follow-up. In terms of treatment reliability, improved precision in dose delivery (reduced standard deviation) was generally observed for the CONV groups, particularly after refinement of the irradiation protocol ahead of the 30 Gy cohort. FLASH irradiations, in contrast, were more accurate but featured larger standard deviation in the doses delivered, which reflected the inherent fluctuations in peak current and therefore charge per pulse. It is important to highlight that the afore-mentioned maintenance period necessitated significant e-gun conditioning and beam tune revision. This, in turn, meant that the beam for the 15 Gy experiments was unavoidably different from that used with the 30Gy cohort and had to be re-characterized ahead of the FLASH-30 and CONV-30 irradiations. The final beam tune used for the 30 Gy cohorts, including demonstration of the beam size (1σ) and near-zero dispersion (at the target location) is shown in Figure 6.2.

Some notable difficulties arose in the delivery of CONV irradiation for both dose cohorts. Firstly, in the 15 Gy mouse cohort doses was under CONV irradiations were 19% lower than the FLASH doses. This was attributed to an initial overestimation of the dose-rate. Moreover, instead of correcting the total charge delivered, the decision was made to retain the sample size (N=6) by prioritizing the delivery of the same dose to all members within the group. Despite this, aberrant beam behaviour resulted in variations in the dose-per-charge ($f_{m15,CONV}$) for the same integrated charge and exceeded what might be readily explained by uncertainty in film dosimetry alone ($\sim$ 5%). This degree of variation was not seen after the shutdown period and might therefore be attributable to source instability, possibly aggravated from a recent vacuum loss event which occurred during the 15 Gy campaign, or minor tuning changes that were required to avoid spurious beam trips.

After shutdown, re-characterization of dose-charge (f) conversion factors and beam behavior was required due to substantial changes in the ACCT calibration and beam tune. The extra refinement and improvements to source stability were reflected in the results for the 30 Gy cohort as a whole (Tables 6.9 and 6.10). The 9.5% mean over-dose observed for the CONV-30 mice was attributed to an under-estimation of the dose-per-charge factor measured for the CONV mode. Interestingly, the measured ACCT-EMBD transmission factor ($TF = C_{ACCT}/C_{EMBD}$ $\approx$1.10) had previously enabled successful dose-matching between FLASH and CONV mode during a single lockup, as demonstrated in preliminary drosophila larvae experiments (see Appendix A.7), and suggests that the beam transmission factor (TF) between the ACCT and EMBD had been well-estimated by our method of measurement. Moreover, this value for TF was corroborated through the results of the 30 Gy group for which $TF \approx f_{m30,CONV}/f_{m30,FLASH} = 1.11$. Taken together, these observations would imply that there had been some unaccounted for factor affecting conversion efficiency at the target. For example, a drift in beam energy, and therefore beam position on the target, had been observed following CONV phantom irradiations. As a result, there was an estimated 0.5 cm e-beam offset which could have contributed changes in transport manifesting as a reduced CAX dose for the converted x-ray beam. This could also explain why the CONV-30 conversion factor ($f_{m30,CONV}$) is approximately the expected value if the ACCT-EMBD TF were applied to the FLASH-30 conversion factor (i.e. $f_{m30,FLASH} * 1.1 \approx f_{m30,CONV}$) derived from phantom measurements. This might be understood by the fact that the beam current would still be collected on the converter body, but with reduced x-ray transmission through the collimator geometry in the event of substantial transport changes. Future studies could include a characterization of the effect that electron beam position has on dose rate, and estimating the uncertainty that can be ascribed to current instabilities.

It is important to note that the window film doses for the 35 Gy mouse cohort were generally near the end of the calibration range for the EBT3 film (35 Gy). Moreover, all window films are subject to a mixed radiation beam with a large electron dose contribution, especially at the surface, which is not accounted for during calibration. For these reasons, window doses were only used as relative output measurements, whereby a given window film OD was associated with dose at

the treatment depth (nominally 1cm) based on previous calibration measurements. Nevertheless, dose-per-charge values inferred from the window-film doses taken for the 30 Gy FLASH mouse irradiations (0.73 Gy/µC±5.2%) agreed with measurements for the 15 Gy Falcon Tube FLASH data (0.75 Gy/µC±1.3%), which would not have been expected had these window films failed to perform as intended at the higher doses.

While *in-vivo* dosimetry results indicated that dose could be consistently delivered with a precision and accuracy of better than 10%, they also point to a need for improved dose-charge calibration based on a more complete understanding of the accelerator parameters and their sensitivity to various conditions. For example, the beam was liable to change between lockup, and thus between samples/mice. In particular, the FLASH pulse shape was sensitive to cathode heater setting (Figure 6.11b), and the CONV peak-current instability was observed to be sensitive to klystron power-supply cooling and high ambient temperatures. For longer irradiations, changes in gun stability or ambient conditions might conceivably change beam output mid-delivery or between deliveries. While the quality of the beam tune and energy drift could be assessed visually using BPM and VS position verification, it was also difficult to know how transmission through EINJ might be changing in time. A second ACCT in the EMBD would be ideal or else additional dose measurements and more rigorous evaluation of the EMBD/ACCT transmission ratio under various conditions should be conducted.

These sources of output variability for the e-linac and the obvious discrepancies in the phantom and mouse dosimetry, particularly for CONV (i.e. normal mode) operation, stresses the importance of re-characterizing the beam ahead of each biological experiment. Unfortunately, due to constrained beam time and resources, small perturbations in beam position or shape were addressed only if outside of a pre-defined range which was identified as posing a significant risk for a beam trip. Ideally, a calibrated real-time dose measurement outside of the beamline (such as a permanent scintillation detector) would be used to notify user of any perturbation in the beam downstream of the ACCT position, which currently stands as the only tool for online dose/dose-rate correction.

Owing to manual targeting inconsistencies of the mouse thorax, it is likely that the treated mice received varying degrees of field coverage within the total lung. This was firstly due to the fact that our targeting was established using mechanical localization of the mouse position by means of the Falcon tube rather than direct immobilization. Specifically, while the field area had a well-defined location within the Falcon tube holder, the mice were manually placed by a registered animal technician and therefore subject to inter-subject variability in the absence of on-board imaging. Secondly, even for a well-centered beam, the limited beam flatness and symmetry (Figures 6.14 and 6.13) would still introduce some degree of dose non-uniformity throughout the treatment volume. This might in turn result in some part of the irradiated target volume receiving sub-UHDR (< 40) Gy/s DR. Moreover, because the lung volume for mice changes rapidly under injectable anesthesia, the situation is further complicated for FLASH pulses with lengths shorter than the respiration period. In effect, sub-second treatment would likely 'freeze' each mouse's lung motion at different points within the breathing

cycle. Unfortunately, this cannot be compensated for without beam gating and represents an inherent limitation to FLASH studies concerned with ultra-fast irradiation of organs subject to physiological motion, such as the lung or heart. Finally, in the present study, manual targeting focused on the diaphragm (i.e. as a physical fiducial) and not the location of the lung during expiration phase, which could not be determined *in situ* without imaging capabilities; this could introduce further inter-mouse variability and organ coverage depending on the respiration phase.

While it lies beyond the scope of this work, a radiobiological study for the aforementioned *in-vivo* irradiations is ongoing, with follow-up time points currently scheduled at 2, 4, 6, 9 and 12 weeks, and an extended monitoring period of 6 months. Pre- and post-IR respiratory-gated micro-CT scans are facilitating dynamic non-invasive tracking of side-effect evolution (i.e. pneumonitis). The resulting data is expected to provide broad insight into relative toxicity for each modality and dose group across various endpoints using histological and micro-CT image analysis. For example, lung and tidal volume evolution and changes in CT number which accompany physiological changes are being monitored to assess transient changes in side-effect progression between each dose and modality configuration.

One of the primary limitations to the ARIEL FIRST platform is the sample throughput, bound by the infrastructure and accelerator hall access routine. Currently, only 1 sample/phantom pair ($N = 2$) or a single animal (to preserve bunker position use), can be irradiated every $\approx$45 min accounting for a full installation/lockup, delivery and access/retrieval. This limited also our feasible cohort size (statistical power) and demanded greater depth of anesthesia using injectables along with associated experimental risk. Fortunately, no animals awoke in their holders during irradiation, and the mice were monitored throughout the procedure on an IR camera with no movement was observed during beam delivery. The long time under anesthesia also poses an interesting question regarding induction of the FLASH effect, namely that there may exist changes in oxygenation status of animals under anesthesia, potentially eliciting an acute state of hypoxia, and driven in part by the change in respiration rate and altered metabolic activity [247, 248].

In future experiments with the ARIEL x-ray source, combined film and organic scintillator dosimetry may be used to provide independent means of diagnosing unexpected behaviour in beam delivery [249]. It will be important to diagnose the underestimation in dose-per-charge during CONV (f_{CONV}) and the intermittent loss of dose-rate scaling linearity with DF (Tables 6.4 and 6.6). Specifically, there appeared to be a $\simeq$ 11% reduction in the expected dose-rate for CONV relative to FLASH under otherwise identical conditions during phantom measurements by assuming power scaling according to the ratio in DF. It is unknown if this may have resulted from an aspect of beam delivery that differs between modes, and possibly depending upon heretofore unknown ambient influences. On the other hand, the DRs inferred from the CONV-30 mouse data would suggest that the DR did scale correctly with DF (and power), as seen by current-normalized DR for FLASH after scaling by DF (0.044 Gy/s at 100μA for DF=0.055%), as compared to CONV at 100μA (0.045 Gy/s). In any

case, in the future, access to a consistent means of measuring the current or charge would be helpful; for example, a second ACCT after EINJ could be added, optimally near the target, or upgrades made to the EMBD electronics to enable measurement of FLASH pulses.

From a source development perspective, the ability to reliably deliver treatments compatible with FLASH radiobiological experiments depends on reproducible beam delivery and reliable calibration. In this first campaign with the new FIRST user platform at ARIEL, good success was found employing a correction scheme, as exemplified by the relatively low dose variance amongst irradiated subjects in spite of changing beam conditions (see Tables 6.7-6.10). Unfortunately, reproducibility is still challenged by the unexpected transmission changes between modes, FLASH-pulse instability (Figure 6.11a), noise in the e-gun current and energy drift. Together, these factors limited our ability to base delivery parameters on previously measured benchmarks and higlights the importance of implementing real-time dose measurement capabilities. In addition to additional ACCT monitors after EINJ in the EMBD beamline, implementing active dosimetry and in-air beam imaging, such as through the use scintillating screens or fiber-optic dosimeters, might provide substantial improvements to our understanding of the x-ray source and improve planning capabilities for future experiments.

6.5 Conclusion

Research concerned with the normal-tissue sparing effects of ultra-high dose rate (FLASH) radiotherapy is of high importance/impact to the oncological community, but few sources exist globally which are capable of achieving the requisite dose-rates. The ARIEL UHDR x-ray conversion target and irradiation platform for FLASH-RT research was the first of its kind in North America, and the first to reach the clinically-relevant energy of 10 MV worldwide. The modular experimental platform has been made suitable for dosimetric and biological irradiations and commissioned for both UHDR pulsed (FLASH mode) and low dose-rate (CONV mode) delivery. Future stability improvements and a more flexible pulsed beam mode system could allow investigators to exploit the large beam parameter space (i.e. time structure) made available by the ARIEL e-linac. In this first experiment on the new ARIEL FLASH system, UHDR x-ray beams were delivered with dose rates in excess of 100 Gy/s. Following a shutdown period mid-campaign, refinements to the beam tune and irradiation procedure further improved the beam properties, including average dose-rate and profile symmetry. Mouse total-lung irradiations were carefully conducted using the best available dosimetry measurements and facilitated dose delivery to within 10 % of the prescription at 1-cm depth. Assessment of treatment outcomes will be subject to follow-up which was ongoing at the time of writing.

Chapter 7

Conclusions and Future Directions

Radiation therapy (RT) continues to underpin curative cancer care around the world, and thus advancements in technology and treatment optimization remain critical to drive improvements to patient outcomes. Nevertheless, dose-limiting normal-tissue side-effects and long-term complications pursuant to the cytotoxic and oncogenic nature of radiation demands that emergent modalities be developed which are capable of reducing radiation-induced toxicity without compromising overall treatment effectiveness. In the course of completing this dissertation, an exploration of myriad subjects evolved with a common goal of developing supporting technologies for preclinical research concerning novel forms of radiotherapy with the propensity for reducing toxicity and, thus, increasing the therapeutic ratio.

The two modalities which stand at the heart of this work, spatially-fractionated RT (SFRT) and FLASH-RT, employ spatial-fractionation and ultra-high dose rates (UHDR), respectively, in order to effect an apparent reduction in deleterious outcomes following high-dose administration in small-animal models. In pursuit of improving source accessibility for SFRT research, a compact multi-slit collimator (MSC) configuration was designed based on Monte Carlo (MC) performance assessment of key dosimetry metrics, such as the peadk-to-valley dose ratio (PVDR) and dose-rate (Chapter 3). Consequently, an affordable and modular collimator assembly suitable for installation on the commercial small-animal radiation research platform (SARRP) was fabricated. Owing to the comparatively ubiquitous nature of small-animal irradiators compared to high-brilliance kV x-ray sources (i.e. synchrotrons), such a gantry-mounted solution provides a comparatively accessible option for treatment planning integration, albeit at the expense of longer treatment times and loss of UHDR capabilities.

Important among the many challenges associated with developing SFRT and FLASH treatments is the increased complexity and non-standard nature of dose measurement under the extreme delivery conditions - namely, micro-scale measures in both spatial and temporal domains. The demand for precise dosimetry under sensitive measurement conditions is challenged by inter-institutional variation in terms of the techniques and technologies employed. For emerging modalities such as SFRT and FLASH-RT, where there is a gap in mechanistic knowledge, poor standardization introduces a

significant source of uncertainty for outcomes data. The 3D-printed rodent-morphic phantom developed in Chapter 4 helps to address this challenge by providing an open-source tool for treatment verification and an opportunity for rodent-specific treatment customization using a methodology for CT-derived phantom construction. The materials used in the experimental prototype were verified as being sufficiently water-equivalent across a range of energies employed by orthovoltage and, implicitly, megavoltage x-ray sources. Moreover, a treatment validation for both simple multi-beam and arc therapies was performed using the SARRP and plastic scintillation with plastic scintillator and radiochromic film dosimeters. Both the phantom and dosimeters in questions serve not only as useful tools for improving the accuracy of dose verification procedures relevant to small-animal dosimetry, but to the development of novel therapies within preclinical models.

The final component of the thesis regards the development of UHDR-compatible sources for FLASH-RT research on both accessible and advanced radiation sources. In the former case, the proof-of-concept for FLASH experiments using a conventional x-ray tube was demosntrated in a succinct study demonstrating the theoretical and then measured capacity for UHDR x-ray irradiations at low (kV) beam energy. This work has since served as a driver for other researchers to investigate and develop their own x-ray tube driven FLASH experimental platforms, consistent with the overarching motivation and theme of this dissertation (Chapter 5). Looking instead to the development of megavoltage (MV) sources in support of translational x-ray FLASH research, the second key contribution involved the fabrication of an electron-to-photon target converter driven by a high-powered superconducting electron linear accelerator (e-linac) at TRIUMF (Vancouver, BC). The FLASH x-ray irradiation platform was successfully constructed and commissioned on the Advanced Rare Isotope Laboratory (ARIEL) e-linac based on the design optimization work summarized in Chapter 5. The target design was predicated on conservative assumptions about thermo-mechanical, physical and operational parameters and yielding a robust design that was verifiably tolerant to sufficiently high (1 kW) instantaneous power load at 10 MeV - of relevance to high-current (UHDR), micro-second pulses characteristic of FLASH. Currently, by providing access to 10 MV UHDR x-rays at ARIEL, TRIUMF is uniquely positioned to probe the relative improvement in treatment outcomes resulting from UHDR irradiation in FLASH radiobiological experiments. Furthermore, analysis of outcomes data from a first preclinical (mouse) experiment, beyond the scope of this dissertation, may further demonstrate the side-effect reduction of FLASH-RT relative to conventional dose-rate therapy. Notably, this body of work comprises the first treatment using UHDR x-rays, with dose-rates in excess of 40 Gy/s, at the clinically-relevant beam energy of 10 MV and has facilitated a first small-animal experiment - a milestone on an institutional and international level.

In the future, FLASH and SFRT might provide a sustainable means of achieving improved clinical outcomes and lower complication rates among Canadian cancer patients undergoing RT. Moreover, it may be that a combination of the two techniques could produce a similar or even greater, synergistic effect, offering also an opportunity for future exploration. It is hoped that the body of work presented

provides, at the very least, inspiration, if not direct avenues, for increasing the accessibility and thus adoption rates of these novel new therapies in order to accelerate an possibility of clinical translation – an important step towards side-effect free radiation therapy.

7.1 Future work

SFRT future work

The development of the MSC for the SARRP (Chapter 3 and Appendix A) has demonstrably enabled divergent microbeam collimation and a cross-fire delivery technique, in which a multi-beam treatment plan could be readily implemented with the SARRP gantry mounted x-ray source. However, a prudent first step to pursue MBRT on the SARRP at UVic involves modification of the MSC geometry (either the SCD or collimator/slit focus) to ensure divergence matching of the source and the MSC. This would allow for a more uniform dose (peak) profile and PVDR; as a result, it might then be possible to apply existing treatment planning tools for the SARRP together with measured and MC-calculated output factors. At present, it is not possible to fully account for irregularities and asymmetry within the MRT dose distributions and, in turn, disallows any MC-based validation and treatment planning. Fortunately, given the modular MSC construction, adjustments may be effected by re-construction of two inexpensive Delrin spacers or, alternatively, 3D-printing a suitable insert, such as a plastic frame, to accommodate the existing tungsten sheets. Advancements in metal 3D-printing (see Chapter 2) have also allowed for comparatively cost-effective additive manufacturing of precise MSC-like collimators, albeit without the intrinsic capacity for re-configuration. For example, a $500\,\mu m$ divergent MSC was made for the ARIEL system as a proof-of-concept to enable future UHDR-SFRT delivery (beyond the scope of this work) and was expanded upon in a design study for effective 2D microbeam (GRID) collimation using divergent MV x-rays [27].

With a functional SARRP MSC installed, it would be possible to simulate more complex treatment scenarios and perform plan verification on the SARRP. For example, by using cross-fired arrays of microbeams and target models boasting physiologically relevant dimensions, users could investigate the degree of coverage along with various dose-volume statistics for a theoretical multi-beam treatment. Furthermore, it would be valuable to investigate how consequent beam overlap might mitigate the dose fall off observed at depth in tissue/water for a kilovoltage radiation source. Additional effort might be expended in an attempt to improve the quality of *in-vitro* dosimetry data, which is otherwise lacking in the present literature.

Phantom future work

Should MC validation of MRT irradiations on the SARRP become possible, MC based planning might be subsequently verified by incorporating the CT-derived rodent-morphic phantom and procedures developed in Chapter 4. The extension of MRT studies on the SARRP therefore provides just one of many possible future applications of the 3D-printed mouse phantom described in this dissertation. More generally, any preclinical treatment simulation, dosimetric verification and quality

assessment for complex fields or experimental setups might be practicable. For example, it would be interesting for users to be able to pursue *in-vivo* measurements in complex conditions where it might be impractical to model every scattering element within an experimental setup, particularly for low-energy sources such as with the SARRP and other cabinet irradiators, or for areas where unaccounted dose contamination factors (activation, neutron dose) or imaging procedures might accumulate additional dose. In cases where dose calculation engines (planning software) or validated MC models are unavailable, 3D-printed phantoms may be used to support the planning and dose prescription for advanced delivery techniques.

UHDR future work

Presently, the technology, infrastructure and methods discussed in Chapters 5 and 6 for the ARIEL e-linac means that FLASH radiobiology experiments might continue to be explored at TRIUMF by interested users, or for other scientific applications where UHDR x-rays might be of use in probing system responses (i.e. of materials, detectors). The scientific mission of the ARIEL e-linac necessitates that beam time be used in accordance with beam development priorities and thus the possibilities for using the FLASH irradiation platform are unknown. Nevertheless, the commissioned systems as well as technical and logistical procedures have been implemented such that future use-cases might be more readily accommodated. However, re-characterization of the beam would be necessary for any planned experiment requesting requiring changes to commissioned beam parameters. Moreover, even should the FLASH tune highlighted in Chapter 6 be preserved, there are outstanding questions regarding the uncertainty in the dose-per-charge calibration which should be addressed and a systematic re-measurement would be important. The currently installed target has an expected fatigue life of 5 years under nominal (beam dump) operation, but replacement targets were fabricated to ensure the longevity of any potential user program for UHDR x-ray irradiation at ARIEL or on any other beamline extension which might be envisioned assuming the power and beam energy constraints are maintained.

Bibliography

[1] GLOBOCAN. The Global Cancer Observatory - All cancers. *International Agency for Research on Cancer - WHO*, 419:199–200, 2020.

[2] Geoff Delaney, Susannah Jacob, Carolyn Featherstone, and Michael Barton. The role of radiotherapy in cancer treatment: Estimating optimal utilization from a review of evidence-based clinical guidelines. *Cancer*, 104(6):1129–1137, 2005.

[3] Scott Tyldesley, Chris Boyd, Karleen Schulze, Hugh Walker, and William J Mackillop. Estimating the need for radiotherapy for lung cancer: an evidence-based, epidemiologic approach. *International Journal of Radiation Oncology, Biology, Physics*, 49(4):973–985, 3 2001.

[4] Rajamanickam Baskar, Kuo Ann Lee, Richard Yeo, and Kheng Wei Yeoh. Cancer and radiation therapy: Current advances and future directions. *International Journal of Medical Sciences*, 9(3):193–199, 2012.

[5] Natacha Leroi, François Lallemand, Philippe Coucke, Agnès Noel, and Philippe Martinive. Impacts of ionizing radiation on the different compartments of the tumor microenvironment. *Frontiers in Pharmacology*, 7(MAR):1–9, 2016.

[6] D N Slatkin, P Spanne, F A Dilmanian, J.-O Gebberst, and J A Laissue. Subacute neuropathological effects of microplanar beams of x-rays from a synchrotron wiggler. *Medical sciences*, 92(September):8783–8787, 1995.

[7] F. Avraham Dilmanian, Yun Qu, Ludwig E. Feinendegen, Louis A. Peña, Tigran Bacarian, Fritz A. Henn, John Kalef-Ezra, Su Liu, Zhong Zhong, and John W. McDonald. Tissue-sparing effect of x-ray microplanar beams particularly in the CNS: Is a bystander effect involved? *Experimental Hematology*, 35(4 SUPPL.):69–77, 2007.

[8] Jeffrey C. Crosbie, Robin L. Anderson, Kai Rothkamm, Christina M. Restall, Leonie Cann, Saleela Ruwanpura, Sarah Meachem, Naoto Yagi, Imants Svalbe, Robert A. Lewis, Bryan R G Williams, and Peter A W Rogers. Tumor Cell Response to Synchrotron Microbeam Radiation Therapy Differs Markedly From Cells in Normal Tissues. *International Journal of Radiation Oncology Biology Physics*, 77(3):886–894, 2010.

[9] Yolanda Prezado, Sukhena Sarun, Silvia Gil, Pierre Deman, Audrey Bouchet, and Geraldine Le Duc. Increase of lifespan for glioma-bearing rats by using minibeam radiation therapy. *Journal of Synchrotron Radiation*, 19(1):60–65, 2012.

[10] Pierre Montay-Gruel, Kristoffer Petersson, Maud Jaccard, Gaël Boivin, Jean François Germond, Benoit Petit, Raphaël Doenlen, Vincent Favaudon, François Bochud, Claude Bailat, Jean Bourhis, and Marie Catherine Vozenin. Irradiation in a flash: Unique sparing of memory in mice after whole brain irradiation with dose rates above 100 Gy/s. *Radiotherapy and Oncology*, 124(3):365–369, 2017.

[11] Marie-Catherine Vozenin, Pauline De Fornel, Kristoffer Petersson, Vincent Favaudon, Maud Jaccard, Jean-François Germond, Benoit Petit, Marco Burki, Gisèle Ferrand, David Patin, Hanan Bouchaab, Mahmut Ozsahin, François Bochud, Claude Bailat, Patrick Devauchelle, and Jean Bourhis. The Advantage of FLASH Radiotherapy Confirmed in Mini-pig and Cat-cancer Patients. *Clinical Cancer Research*, 25(1):35–42, 1 2019.

[12] Jean Bourhis, Pierre Montay-Gruel, Patrik Gonçalves Jorge, Claude Bailat, Benoît Petit, Jonathan Ollivier, Wendy Jeanneret-Sozzi, Mahmut Ozsahin, François Bochud, Raphaël Moeckli, Jean François Germond, and Marie Catherine Vozenin. Clinical translation of FLASH radiotherapy: Why and how? *Radiotherapy and Oncology*, 139:11–17, 2019.

[13] Nolan Esplen, Marc S. Mendonca, and Magdalena Bazalova-Carter. Physics and biology of ultrahigh dose-rate (FLASH) radiotherapy: A topical review. *Physics in Medicine and Biology*, 65(23):23TR03, 2020.

[14] Jean A. Laissue, Stefan Bartzsch, Hans Blattmann, Elke Bräuer-Krisch, Alberto Bravin, Dominique Dalléry, Valentin Djonov, Albert L. Hanson, John W. Hopewell, Barbara Kaser-Hotz, Jani Keyriläinen, Pierre Philippe Laissue, Michiko Miura, Raphaël Serduc, Albert E. Siegbahn, and Daniel N. Slatkin. Response of the rat spinal cord to X-ray microbeams. *Radiotherapy and Oncology*, 106(1):106–111, 2013.

[15] F. Avraham Dilmanian, Terry M. Button, Géraldine Le Duc, Nan Zhong, Louis A. Peña, Jennifer A.L. Smith, Steve R. Martinez, Tigran Bacarian, Jennifer Tammam, Baorui Ren, Peter M. Farmer, John Kalef-Ezra, Peggy L. Micca, Marta M. Nawrocky, James A. Niederer, F. Peter Recksiek, Alexander Fuchs, and Eliot M. Rosen. Response of rat intracranial 9L gliosarcoma to microbeam radiation therapy. *Neuro Oncology*, 4(1):26–38, 2002.

[16] Y. Prezado, M. Dos Santos, W. Gonzalez, G. Jouvion, C. Guardiola, S. Heinrich, D. Labiod, M. Juchaux, L. Jourdain, C. Sebrie, and F. Pouzoulet. Transfer of Minibeam Radiation Therapy into a cost-effective equipment for radiobiological studies: a proof of concept. *Scientific Reports*, 7(1):17295, 2017.

[17] Audrey Bouchet, Elke Bräuer-Krisch, Yolanda Prezado, Michèle El Atifi, Léonid Rogalev, Céline Le Clec'h, Jean Albert Laissue, Laurent Pelletier, and Géraldine Le Duc. Better Efficacy of Synchrotron Spatially Microfractionated Radiation Therapy Than Uniform Radiation Therapy on Glioma. *International Journal of Radiation Oncology Biology Physics*, 95(5):1485–1494, 2016.

[18] Soha Bazyar, Christina R Inscoe, E Timothy O Brian, Otto Zhou, and Yueh Z Lee. Minibeam radiotherapy with small animal irradiators ; in vitro and in vivo feasibility studies. *Physics in Medicine and Biology*, 62(23):8924–8942, 2017.

[19] Stefan Bartzsch, Craig Cummings, Stephan Eismann, and Uwe Oelfke. A preclinical microbeam facility with a conventional x-ray tube. *Medical Physics*, 43(12):6301–6308, 2016.

[20] Raphaël Serduc, Audrey Bouchet, Elke Bräuer-Krisch, Jean A. Laissue, Jenny Spiga, Sukhéna Sarun, Alberto Bravin, Caroline Fonta, Luc Renaud, Jean Boutonnat, Erik Albert Siegbahn, François Estève, and Géraldine Le Duc. Synchrotron microbeam radiation therapy for rat brain tumor palliation - Influence of the microbeam width at constant valley dose. *Physics in Medicine and Biology*, 54(21):6711–6724, 2009.

[21] Jean A. Laissue, Gabrielle Geiser, Per O. Spanne, F. Avraham Dilmanian, Jan Olaf Gebbers, Marianne Geiser, Xiao Ye Wu, Michael S. Makar, Peggy L. Mica, Marta M. Nawrocky, Darrel D. Joel, and Daniel N. Slatkin. Neuropathology of ablation of rat gliosarcomas and contiguous brain tissues using a microplanar beam of synchrotron-wiggler-generated X rays. *International Journal of Cancer*, 78(5):654–660, 1998.

[22] H. Nettelbeck, G. J. Takacs, M. L.F. Lerch, and A. B. Rosenfeld. Microbeam radiation therapy: A Monte Carlo study of the influence of the source, multislit collimator, and beam divergence on microbeams. *Medical Physics*, 36(2):447–456, 2009.

[23] F Avraham Dilmanian, Zhong Zhong, Tigran Bacarian, Helene Benveniste, Pantaleo Romanelli, Ruiliang Wang, Jeremy Welwart, Tetsuya Yuasa, Eliot M Rosen, and David J Anschel. Interlaced x-ray microplanar beams: a radiosurgery approach with clinical potential. *Proceedings of the National Academy of Sciences of the United States of America*, 103(25):9709–14, 2006.

[24] Yolanda Prezado, Pierre Deman, Pascale Varlet, Gregory Jouvion, Silvia Gil, Céline Le Clec 'h, Hélène Bernard, Géraldine Le Duc, Sukhena Sarun, Y Prezado, G Gil, Le Clec 'h, C Bernard, Le Duc, and G Sarun. Tolerance to Dose Escalation in Minibeam Radiation Therapy Applied to Normal Rat Brain: Long-Term Clinical, Radiological and Histopathological Analysis. *Radiation Research*, 184(August):314–321, 2015.

[25] Audrey Bouchet, Raphäel Serduc, Jean Albert Laissue, and Valentin Djonov. Effects of microbeam radiation therapy on normal and tumoral blood vessels. *Physica Medica*, 31(6):634–641, 2015.

[26] Nolan Esplen, Luca Egoriti, Alex Gottberg, and Magdalena Bazalova. Strategies for the delivery of spatially fractionated radiotherapy using conventional and FLASH-capable sources. In *COMP2019 Annual Scientific Meeting*, Kelowna, BC, Canada, 2019.

[27] Nathan Clements, Magdalena Bazalova-Carter, and Nolan Esplen. Monte Carlo optimization of a GRID collimator for preclinical megavoltage ultra-high dose rate spatially-fractionated radiation therapy. *Physics in Medicine and Biology*, 67(18), 9 2022.

[28] Jayde Livingstone, Jean François Adam, Jeffrey C. Crosbie, Chris J. Hall, Jessica E. Lye, Jonathan McKinlay, Daniele Pelliccia, Frédéric Pouzoulet, Yolanda Prezado, Andrew W. Stevenson, and Daniel Häusermann. Preclinical radiotherapy at the Australian Synchrotron's Imaging and Medical Beamline: Instrumentation, dosimetry and a small-animal feasibility study. *Journal of Synchrotron Radiation*, 24(4):854–865, 2017.

[29] Lloyd M.L. Smyth, Jacqueline F. Donoghue, Jessica A. Ventura, Jayde Livingstone, Tracy Bailey, Liam R.J. Day, Jeffrey C. Crosbie, and Peter A.W. Rogers. Comparative toxicity of synchrotron and conventional radiation therapy based on total and partial body irradiation in a murine model. *Scientific Reports*, 8(1):1–11, 2018.

[30] John Wong, Elwood Armour, Peter Kazanzides, Iulian Iordachita, Erik Tryggestad, Hua Deng, Mohammad Matinfar, Christopher Kennedy, Zejian Liu, Timothy Chan, Owen Gray, Frank Verhaegen, Todd McNutt, Eric Ford, and Theodore L. DeWeese. High-Resolution, Small Animal Radiation Research Platform With X-Ray Tomographic Guidance Capabilities. *International Journal of Radiation Oncology Biology Physics*, 71(5):1591–1599, 2008.

[31] Nolan M Esplen, Lila Chergui, Chris D Johnstone, and Magdalena Bazalova-carter. Monte Carlo optimization of a microbeam collimator design for use on the small animal radiation research platform (SARRP). *Physics in Medicine & Biology*, 63, 2018.

[32] Daniel D Cecchi, François Therriault-Proulx, Simon Lambert-Girard, Alexander Hart, Andrew Macdonald, Mike Pfleger, Mark Lenckowski, and Magdalena Bazalova-Carter. Characterization of an x-ray tube-based ultrahigh dose-rate system for in vitro irradiations. *Medical Physics*, 48(11):7399–7409, 11 2021.

[33] Mohammad Rezaee, Iulian Iordachita, and John W. Wong. Ultrahigh dose-rate (FLASH) x-ray irradiator for pre-clinical laboratory research. *Physics in Medicine and Biology*, 66(9), 2021.

[34] Stefan Bartzsch and Uwe Oelfke. Line focus x-ray tubes - A new concept to produce high brilliance x-rays. *Physics in Medicine and Biology*, 62(22):8600–8615, 2017.

[35] I. Martínez-Rovira, G. Fois, and Y. Prezado. Dosimetric evaluation of new approaches in GRID therapy using nonconventional radiation sources. *Medical Physics*, 42(2):685–693, 2 2015.

[36] Consuelo Guardiola and Yolanda Prezado. High-Energy Charged Particles for Spatially Fractionated Radiation Therapy. *Frontiers in Physics*, 8, 10 2020.

[37] Cole Billena and Atif J. Khan. A Current Review of Spatial Fractionation: Back to the Future? *International Journal of Radiation Oncology Biology Physics*, 104(1):177–187, 2019.

[38] M. C. Vozenin, J. H. Hendry, and C. L. Limoli. Biological Benefits of Ultra-high Dose Rate FLASH Radiotherapy: Sleeping Beauty Awoken. *Clinical Oncology*, 31(7):407–415, 2019.

[39] Joseph D. Wilson, Ester M. Hammond, Geoff S. Higgins, and Kristoffer Petersson. Ultra-High Dose Rate (FLASH) Radiotherapy: Silver Bullet or Fool's Gold? *Frontiers in Oncology*, 9(January):1–12, 2020.

[40] Pierre Montay-Gruel, Munjal M. Acharya, Patrik Gonçalves Jorge, Benoît Petit, Ioannis G. Petridis, Philippe Fuchs, Ron Leavitt, Kristoffer Petersson, Maude Gondre, Jonathan Ollivier, Raphael Moeckli, François Bochud, Claude Bailat, Jean Bourhis, Jean François Germond, Charles L. Limoli, and Marie Catherine Vozenin. Hypofractionated FLASH-RT as an effective treatment against glioblastoma that reduces neurocognitive side effects in mice. *Clinical Cancer Research*, 27(3):775–784, 2021.

[41] Charles Fouillade, Sandra Curras-Alonso, Lorena Giuranno, Eddy Quelennec, Sophie Heinrich, Sarah Bonnet-Boissinot, Arnaud Beddok, Sophie Leboucher, Hamza Umut Karakurt, Mylène Bohec, Sylvain Baulande, Marc Vooijs, Pierre Verrelle, Marie Dutreix, Arturo Londoño-Vallejo, and Vincent Favaudon. FLASH irradiation spares lung progenitor cells and limits the incidence of radio-induced senescence. *Clinical Cancer Research*, 26(6):1497–1506, 2020.

[42] Brita Singers Sørensen, Mateusz Krzysztof Sitarz, Christina Ankjærgaard, Jacob G. Johansen, Claus E. Andersen, Eleni Kanouta, Cai Grau, and Per Poulsen. Pencil beam scanning proton FLASH maintains tumor control while normal tissue damage is reduced in a mouse model. *Radiotherapy and Oncology*, 175:178–184, 10 2022.

[43] Walter Tinganelli, Uli Weber, Anggraeini Puspitasari, Palma Simoniello, Amir Abdollahi, Julius Oppermann, Christoph Schuy, Felix Horst, Alexander Helm, Claudia Fournier, and Marco Durante. FLASH with carbon ions: Tumor control, normal tissue sparing, and distal metastasis in a mouse osteosarcoma model. *Radiotherapy and Oncology*, 175:185–190, 10 2022.

[44] Pierre Montay-Gruel, Audrey Bouchet, Maud Jaccard, David Patin, Raphael Serduc, Warren Aim, Kristoffer Petersson, Benoit Petit, Claude Bailat, Jean Bourhis, Elke Bräuer-Krisch, and Marie Catherine Vozenin. X-rays can trigger the FLASH effect: Ultra-high dose-rate synchrotron light source prevents normal brain injury after whole brain irradiation in mice. *Radiotherapy and Oncology*, 129(3):582–588, 2018.

[45] Danielle A. Simmons, Frederick M. Lartey, Emil Schüler, Marjan Rafat, Gregory King, Anna Kim, Ryan Ko, Sarah Semaan, Selena Gonzalez, Melissa Jenkins, Pooja Pradhan, Zion Shih, Jinghui Wang, Rie von Eyben, Edward E. Graves, Peter G. Maxim, Frank M. Longo, and Billy W. Loo. Reduced cognitive deficits after FLASH irradiation of whole mouse brain are associated with less hippocampal dendritic spine loss and neuroinflammation. *Radiotherapy and Oncology*, 139:4–10, 2019.

[46] Kristoffer Petersson, Gabriel Adrian, Karl Butterworth, and Stephen J. McMahon. A Quantitative Analysis of the Role of Oxygen Tension in FLASH Radiation Therapy. *International Journal of Radiation Oncology Biology Physics*, pages 1–9, 2020.

[47] Jia Ling Ruan, Carl Lee, Shari Wouters, Iain D.C. Tullis, Mieke Verslegers, Mohamed Mysara, Chee Kin Then, Sean C. Smart, Mark A. Hill, Ruth J. Muschel, Amato J. Giaccia, Borivoj Vojnovic, Anne E. Kiltie, and Kristoffer Petersson. Irradiation at Ultra-High (FLASH) Dose Rates Reduces Acute Normal Tissue Toxicity in the Mouse Gastrointestinal System. *International Journal of Radiation Oncology Biology Physics*, 111(5):1250–1261, 12 2021.

[48] Michael Lempart, Börje Blad, Gabriel Adrian, Sven Bäck, Tommy Knöös, Crister Ceberg, and Kristoffer Petersson. Modifying a clinical linear accelerator for delivery of ultra-high dose rate irradiation. *Radiotherapy and Oncology*, 139:40–45, 2019.

[49] Emil Schüler, Stefania Trovati, Gregory King, Frederick Lartey, Marjan Rafat, Manuel Villegas, A. Joe Praxel, Billy W. Loo, and Peter G. Maxim. Experimental Platform for Ultra-high Dose Rate FLASH Irradiation of Small Animals Using a Clinical Linear Accelerator. *International Journal of Radiation Oncology Biology Physics*, 97(1):195–203, 2017.

[50] Magdalena Bazalova-Carter and Nolan Esplen. On the capabilities of conventional x-ray tubes to deliver ultra-high (FLASH) dose rates. *Medical Physics*, 46(12):5690–5695, 2019.

[51] Annalisa Patriarca, Charles Fouillade, Michel Auger, Frédéric Martin, Frédéric Pouzoulet, Catherine Nauraye, Sophie Heinrich, Vincent Favaudon, Samuel Meyroneinc, Rémi Dendale, Alejandro Mazal, Philip Poortmans, Pierre Verrelle, and Ludovic De Marzi. Experimental Set-up for FLASH Proton Irradiation of Small Animals Using a Clinical System. *International Journal of Radiation Oncology Biology Physics*, 102(3):619–626, 2018.

[52] Peter G. Maxim, Sami G. Tantawi, and Billy W. Loo. PHASER: A platform for clinical translation of FLASH cancer radiotherapy. *Radiotherapy and Oncology*, 139:28–33, 2019.

[53] Nolan Esplen, Luca Egoriti, Bill Paley, Thomas Planche, Cornelia Hoehr, Alexander Gottberg, and Magdalena Bazalova-Carter. Design optimization of an electron-to-photon conversion target for ultra-high dose rate x-ray (FLASH) experiments at TRIUMF. *Physics in Medicine and Biology*, 67(10), 5 2022.

[54] Emil Schuler, Kjell Eriksson, Elin Hynning, Steven L. Hancock, Susan M. Hiniker, Magdalena Bazalova-Carter, Tony Wong, Quynh Thu Le, Billy W. Loo, and Peter G. Maxim. Very high-energy electron (VHEE) beams in radiation therapy; Treatment plan comparison between VHEE, VMAT, and PPBS. *Medical Physics*, 44(6):2544–2555, 2017.

[55] Bianey Palma, Magdalena Bazalova-Carter, Björn Hårdemark, Elin Hynning, Bradley Qu, Billy W. Loo, and Peter G. Maxim. Assessment of the quality of very high-energy electron radiotherapy planning. *Radiotherapy and Oncology*, 119(1):154–158, 2016.

[56] Magdalena Bazalova-Carter, Bradley Qu, Bianey Palma, Björn Hårdemark, Elin Hynning, Christopher Jensen, Peter G. Maxim, and Billy W. Loo. Treatment planning for radiotherapy with very high-energy electron beams and comparison of VHEE and VMAT plans. *Medical Physics*, 42(5):2615–2625, 2015.

[57] Y. Glinec, J. Faure, V. Malka, T. Fuchs, H. Szymanowski, and U. Oelfke. Radiotherapy with laser-plasma accelerators: Monte Carlo simulation of dose deposited by an experimental quasimonoenergetic electron beam. *Medical Physics*, 33(1):155–162, 2006.

[58] A. Subiel, V. Moskvin, G. H. Welsh, S. Cipiccia, D. Reboredo, P. Evans, M. Partridge, C. DesRosiers, M. P. Anania, A. Cianchi, A. Mostacci, E. Chiadroni, D. Di Giovenale, F. Villa, R. Pompili, M. Ferrario, M. Belleveglia, G. Di Pirro, G. Gatti, C. Vaccarezza, B. Seitz, R. C. Isaac, E. Brunetti, S. M. Wiggins, B. Ersfeld, M. R. Islam, M. S. Mendonca, A. Sorensen, M. Boyd, and D. A. Jaroszynski. Dosimetry of very high energy electrons (VHEE) for radiotherapy applications: Using radiochromic film measurements and Monte Carlo simulations. *Physics in Medicine and Biology*, 59(19):5811–5829, 2014.

[59] Magdalena Bazalova, Geoff Nelson, John M. Noll, and Edward E. Graves. Modality comparison for small animal radiotherapy: A simulation study. *Medical Physics*, 41(1):5–7, 2014.

[60] P. V. Granton, F. Wittkamper, A. Gasparini, F. Verhaegen, J. Hermans, P. E. Lindsay, R. Clarkson, J. Kaas, S. Jelveh, J.-J. Sonke, S. van Hoof, and D. A. Jaffray. Multi-institutional dosimetric and geometric commissioning of image-guided small animal irradiators. *Medical Physics*, 41(3):031714, 2014.

[61] Mihaela Ghita, Stephen J. McMahon, Hannah F. Thompson, Conor K. McGarry, Raymond King, Sarah O.S. Osman, Jonathan L. Kane, Amanda Tulk, Giuseppe Schettino, Karl T. Butterworth, Alan R. Hounsell, and Kevin M. Prise. Small field dosimetry for the small animal radiotherapy research platform (SARRP). *Radiation Oncology*, 12(1):1–10, 2017.

[62] Marc Desrosiers, Larry DeWerd, James Deye, Patricia Lindsay, Mark K Murphy, Michael Mitch, Francesca Macchiarini, Strahinja Stojadinovic, and Helen Stone. The Importance of Dosimetry Standardization in Radiobiology. *Journal of Research of the National Institute of Standards and Technology*, 118:403–418, 2013.

[63] Thomas M. Seed, Shiyun Xiao, Nancy Manley, Janko Nikolich-Zugich, Jason Pugh, Marcel Van den Brink, Yoko Hirabayashi, Koji Yasutomo, Atsushi Iwama, Shigeo Koyasu, Ivo Shterev, Gregory Sempowski, Francesca Macchiarini, Kei Nakachi, Keith C. Kunugi, Clifford G. Hammer, and Lawrence A. DeWerd. An interlaboratory comparison of dosimetry for a multi-institutional radiobiological research project: Observations, problems, solutions and lessons learned. *International Journal of Radiation Biology*, 92(2):59–70, 2015.

[64] Kurt H. Pedersen, Keith A. Kunugi, Clifford G. Hammer, Wesley S. Culberson, and Larry A. DeWerd. Radiation Biology Irradiator Dose Verification Survey. *Radiation Research*, 185(2):163–168, 2016.

[65] Mohamad B. Dabjan, Carolyn M.S. Buck, Isabel L. Jackson, Zeljko Vujaskovic, Brian Marples, and Julian D. Down. A survey of changing trends in modelling radiation lung injury in mice: Bringing out the good, the bad, and the uncertain, 9 2016.

[66] Nolan Esplen, Eisa Alyaqoub, and Magdalena Bazalova-Carter. Technical Note: Manufacturing of a realistic mouse phantom for dosimetry of radiobiology experiments. *Medical Physics*, 46(2):1030–1036, 2 2019.

[67] Nolan Esplen, François Therriault-Proulx, Luc Beaulieu, and Magdalena Bazalova-Carter. Pre-clinical dose verification using a 3D printed mouse phantom for radiobiology experiments. *Medical Physics*, 46(11):5294–5303, 11 2019.

[68] E Podgorsak. *Radiation Oncology Physics: A Handbook for Teachers and Students*. IAEA, Vienna, 2005.

[69] F.H. Attix. Charged-Particle and Radiation Equilibria. In *Introduction to Radiological Physics and Radiation Dosimetry*, pages 61–79. Wiley, Hoboken, NJ, 11 1986.

[70] F.H. Attix. Exponential Attenuation. In *Introduction to Radiological Physics and Radiation Dosimetry*, pages 38–60. Wiley, Hoboken, NJ, 11 1986.

[71] F.H. Attix. Gamma- and X-Ray Interactions in Matter. In *Introduction to Radiological Physics and Radiation Dosimetry*, pages 124–159. Wiley, Hoboken, NJ, 11 1986.

[72] IAEA. Handbook on Photonuclear Data for Applications Cross-sections and Spectra, IAEA-TECDOC-1178. Technical report, IAEA, Vienna, Austria: IAEA, 2000.

[73] J.H. Hubbell and S.M. Seltzer. Tables of X-Ray Mass Attenuation Coefficients and Mass Energy-Absorption Coefficients (version 1.4). Technical report, National Institute of Standards and Technology, Gaithersburg, MD, 2004.

[74] F.H. Attix. Charged-Particle Interactions in Matter. In *Introduction to Radiological Physics and Radiation Dosimetry*, pages 160–202. Wiley, Hoboken, NJ, 11 1986.

[75] Dermott E. Cullen. A Survey of Electron Cross Section Data for use in EPICS2017, IAEA-NDS-226. Technical Report September, Vienna, Austria: IAEA, 2107.

[76] M.J. Berger, J.S. Coursey, M.A. Zucker, and J. Chang. ESTAR, PSTAR, and ASTAR: Computer Programs for Calculating Stopping-Power and Range Tables for Electrons, Protons, and Helium Ions (version 1.2.3). Technical report, National Institute of Standards and Technology, Gaithersburg, MD., 2005.

[77] Maria Grazia Ronga, Marco Cavallone, Annalisa Patriarca, Amelia Maia Leite, Pierre Loap, Vincent Favaudon, Gilles Créhange, and Ludovic De Marzi. Back to the future: Very high-energy electrons (vhees) and their potential application in radiation therapy. *Cancers*, 13(19), 10 2021.

[78] Eiji Tanabe, John Ford, Oncology Systems, Varian Associates, Hansen Way, and Palo Alto. ADVANCES IN MEDICAL ELECTRON ACCELERATOR THECHNOLOGY. In *Proceedings of the 1994 International Linac Conference*, pages 591–593, 1994.

[79] Leticia M. Nogueira, Ahmedin Jemal, K. Robin Yabroff, and Jason A. Efstathiou. Assessment of Proton Beam Therapy Use Among Patients With Newly Diagnosed Cancer in the US, 2004-2018. *JAMA Network Open*, 5(4):e229025, 4 2022.

[80] M R Cleland. Industrial applications of electron accelerators. pages 383–416, 2006.

[81] B W Raaymakers, I M Jürgenliemk-Schulz, G H Bol, M Glitzner, A N T J Kotte, B van Asselen, J C J de Boer, J J Bluemink, S L Hackett, M A Moerland, S J Woodings, J W H Wolthaus, H M van Zijp, M E P Philippens, R Tijssen, J G M Kok, E N de Groot-van Breugel, I Kiekebosch, L T C Meijers, C N Nomden, G G Sikkes, P A H Doornaert, W S C Eppinga, N Kasperts, L G W Kerkmeijer, J H A Tersteeg, K J Brown, B Pais, P Woodhead, and J. J.W.

Lagendijk. First patients treated with a 1.5T MRI-Linac: clinical proof of concept of a high-precision , high- First patients treated with a 1.5T MRI-Linac: clinical proof of concept of a high-precision, high-field MRI guided radiotherapy treatment. *Physics in Medicine & Biology*, 62(L41), 2017.

[82] Yuenan Wang, Stephen B. Easterling, and Joseph Y. Ting. Ion recombination corrections of ionization chambers in flattening filter-free photon radiation. *Journal of Applied Clinical Medical Physics*, 13(5):262–268, 2012.

[83] Y. S. Lee, G. J. Kim, S. H. Kim, J. H. Lee, I. S. Kim, Y. W. Choi, J. I. Kim, J. H. Hwang, A. R. Kim, J. N. Kim, J. S. Shin, Y. J. Seol, T. G. Oh, Y. A. Oh, and Y. N. Kang. Development of side coupled X-band medical linear accelerator for radiotherapy. *Proceedings of the 29th Linear Accelerator Conference, LINAC 2018*, pages 139–141, 2020.

[84] Masahiro Hiraoka, Takashi Mizowaki, Yukinori Matsuo, Mitsuhiro Nakamura, and Dirk Verellen. The gimbaled-head radiotherapy system: Rise and downfall of a dedicated system for dynamic tumor tracking with real-time monitoring and dynamic WaveArc, 12 2020.

[85] Karolina Kokurewicz, Enrico Brunetti, Alessandro Curcio, Davide Gamba, Luca Garolfi, Antonio Gilardi, Eugenio Senes, Kyrre Ness Sjobak, Wilfrid Farabolini, Roberto Corsini, and Dino Anthony Jaroszynski. An experimental study of focused very high energy electron beams for radiotherapy. *Communications Physics*, 4(1), 12 2021.

[86] S Koscielniak, F Ames, R Baartman, R Dawson, J Drozdoff, Y Bylinsky, K Fong, A Hurst, D Karlen, R Keitel, R Laxdal, F Mammarella, M Marchetto, L Merminga, A K Mitra, K Reiniger, T Ries, R Ruegg, I Sekachev, G Stinson, and V Verzilov. ARIEL and the TRIUMF E-Linac Initiative, a 0.5 MW Electron Linac for Rare Isotope Beam Production. In *Proceedings of LINAC08*, 2008.

[87] M Marchetto, F Ames, Z Ang, R.A. Baartman, I. Bylinskii, Y.C. Chao, and D Dale. COMMISSIONING AND OPERATION OF THE ARIEL ELECTRON LINAC AT TRIUMF. In *Proceedings of the 6th International Particle Accelerator Conference, IPAC2015*. JACoW, 2015.

[88] Peter Michel. ELBE Center for High-Power Radiation Sources. *Journal of large-scale research facilities JLSRF*, 2:1–7, 2016.

[89] A. S. Meigooni, S. A. Parker, J. Zheng, K. J. Kalbaugh, W. F. Regine, and M. Mohiuddin. Dosimetric characteristics with spatial fractionation using electron grid therapy. *Medical Dosimetry*, 27(1), 2002.

[90] Ali S. Meigooni, Kai Dou, Navid J. Meigooni, Michael Gnaster, Shahid Awan, Sharifeh Dini, and Ellis L. Johnson. Dosimetric characteristics of a newly designed grid block for megavoltage

photon radiation and its therapeutic advantage using a linear quadratic model. *Medical Physics*, 33(9):3165–3173, 2006.

[91] R. J. BERRY. EFFECTS OF RADIATION DOSE-RATE: From Protracted, Continuous Irradiation to Ultra-High Dose-Rates from Pulsed Accelerators. *British Medical Bulletin*, 29(1):44–47, 1973.

[92] A. H.W. Nias, A. J. Swallow, J. P. Keene, and B. W. Hodgson. Survival of hela cells from 10 nanosecond pulses of electrons. *International Journal of Radiation Biology*, 17(6):595–598, 1970.

[93] Ning Wen, Bo Zhao, Jinkoo Kim, Karen Chin-Snyder, Maria Bellon, Carri Glide-Hurst, Kenneth Barton, Daiquan Chen, and Indrin J. Chetty. IMRT and RapidArc commissioning of a TrueBeam linear accelerator using TG-119 protocol cases. *Journal of Applied Clinical Medical Physics*, 15(5):74–88, 9 2014.

[94] Maud Jaccard, Maria Teresa Durán, Kristoffer Petersson, Jean François Germond, Philippe Liger, Marie Catherine Vozenin, Jean Bourhis, François Bochud, and Claude Bailat. High dose-per-pulse electron beam dosimetry: Commissioning of the Oriatron eRT6 prototype linear accelerator for preclinical use. *Medical Physics*, 45(2):863–874, 2018.

[95] K. Petersson, M. Jaccard, M.C. Vozenin, P. Montay-Gruel, F. Trompier, T. Buchillier, J.F. Germond, F. Bochud, J. Bourhis, and C. Bailat. Dosimetry of ultra high dose rate irradiation for studies on the biological effect induced in normal brain and GBM. *Radiotherapy and Oncology*, 118:S84, 2016.

[96] Raphaël Moeckli, Patrik Gonçalves Jorge, Veljko Grilj, Roxane Oesterle, Nicolas Cherbuin, Jean Bourhis, Marie Catherine Vozenin, Jean François Germond, François Bochud, and Claude Bailat. Commissioning of an ultra-high dose rate pulsed electron beam medical LINAC for FLASH RT preclinical animal experiments and future clinical human protocols. *Medical Physics*, 48(6):3134–3142, 6 2021.

[97] F. Ames, Y. Chao, K. Fong, S. Koscielniak, N. Khan, A. Laxdal, L. Merminga, T. Planche, S. Saminathan, D. Storey, and C. Sinclair. The TRIUMF ARIEL RF modulated thermionic electron source. *Proceedings of the 28th Linear Accelerator Conference, LINAC 2016*, 21(1):310–312, 2016.

[98] S. V. Kutsaev, R. Agustsson, A. Arodzero, R. Berry, S. Boucher, A. Diego, D. Gavryushkin, J. J. Hartzell, R. C. Lanza, A. Yu Smirnov, A. Verma, and V. Ziskin. Linear accelerator for security, industrial and medical applications with rapid beam parameter variation. *Radiation Physics and Chemistry*, 183, 6 2021.

[99] Jerrold T Bushberg, Anthony J Seibert, Edwin M Leidholdt, and John M Boone. *The essential physics of medical imaging; 3rd ed.* Lippincott Williams & Wilkins, Philadelphia, PA, 2012.

[100] H.E. Johns and J.R. Cunningham. *The physics of radiology.* American lecture series-publications ; no1054. Charles C. Thomas, Springfield, Ill., U.S.A, 4th ed. edition, 1983.

[101] J.D. Jackson. *Classical Electrodynamics.* Wiley, Hoboken, NJ, 3 edition, 1998.

[102] Walter Ramberg and William R. Osgood. Description of Stress-Strain Curves by Three Parameters, Technical Note No. 902. Technical report, NACA, NACA, 1943.

[103] Richard Budynas and Keith Nisbett. *Shigley's Mechanical Engineering Design.* McGraw Hill, New York City, 11 edition, 2020.

[104] Flake C Campbell. Fatigue Elements of Metallurgy and Engineering Alloys. Technical report, ASM International, Materials Park, OH: ASM International, 2008.

[105] A. V. Babak and E. I. Uskov. High-temperature embrittlement of tungsten. *Problemy Prochnosti*, 5:65–69, 1983.

[106] T. E. Tietz and W. Wilson, Jess. *Behavior and Properties of Refractory Metals.* Stanford University Press., Stanford, 1965.

[107] K. Farrell, A. C. Schaffhauser, and J. O. Stiegler. Recrystallization, grain growth and the ductile-brittle transition in tungsten sheet. *Journal of The Less-Common Metals*, 13(2):141–155, 1967.

[108] A. Suslova, O. El-Atwani, D. Sagapuram, S. S. Harilal, and A. Hassanein. Recrystallization and grain growth induced by ELMs-like transient heat loads in deformed tungsten samples. *Scientific Reports*, 4:1–11, 2014.

[109] O.S. Oen. Cross sections for atomic displacements in solids by fast electrons (ORNL-4897). Technical report, Oak Ridge National Laboratory (ORNL), Oak Ridge, TN: ORNL, 8 1973.

[110] G S Was and R S Averback. 1.07 - Radiation Damage Using Ion Beams. In Rudy J M Konings, editor, *Comprehensive Nuclear Materials*, pages 195–221. Elsevier, Oxford, 2012.

[111] C Abromeit. Aspects of simulation of neutron damage by ion irradiation. *Journal of Nuclear Materials*, 216:78–96, 1994.

[112] Dan Wilcox, Peter Loveridge, Tristan Davenne, Leslie Jones, and David Jenkins. Stress levels and failure modes of tantalum-clad tungsten targets at ISIS. *Journal of Nuclear Materials*, 506:76–82, 2018.

[113] F P Incropera, D P DeWitt, T L Bergman, and A S Lavine. *Fundamentals of Heat and Mass Transfer*. Hoboken, NJ: Wiley, Hoboken, NJ, 6 edition, 2006.

[114] Martin E Barzelay, Kin Nee Tong, and George F Holloway. Effects of Pressure on Thermal Conductance of Contact Joints (TN-3295). Technical report, NACA, NACA: Washington, 1955.

[115] Joseph R Stephens. Thermal Aging Effects in Refractory Metal Alloys (NASA-TM-87210). Technical report, Lewis Research Center, Cleveland, OH: NASA, 1986.

[116] K J Leonard. 4.06 - Radiation Effects in Refractory Metals and Alloys. In Rudy J M Konings, editor, *Comprehensive Nuclear Materials*, pages 181–213. Elsevier, Oxford, 2012.

[117] G. Bruggmoser, R. Saum, A. Schmachtenberg, F. Schmid, and E. Schüle. Determination of the recombination correction factor kS for some specific plane-parallel and cylindrical ionization chambers in pulsed photon and electron beams. *Physics in Medicine and Biology*, 52(2), 2007.

[118] GafchromicTM dosimetry media, type EBT3 Specifications, 12 2022.

[119] Alexandra Rink, David F. Lewis, Sangya Varma, I. Alex Vitkin, and David A. Jaffray. Temperature and hydration effects on absorbance spectra and radiation sensitivity of a radiochromic medium. *Medical Physics*, 35(10):4545–4555, 2008.

[120] A. D. Koulouklidis, S. Cohen, and J. Kalef-Ezra. Thermochromic phase-transitions of GafChromic films studied by z-scan and temperature-dependent absorbance measurements. *Medical Physics*, 40(11), 2013.

[121] Magdalena Bazalova-Carter, Michael Liu, Bianey Palma, Michael Dunning, Doug McCormick, Erik Hemsing, Janice Nelson, Keith Jobe, Eric Colby, Albert C. Koong, Sami Tantawi, Valery Dolgashev, Peter G. Maxim, and Billy W. Loo. Comparison of film measurements and Monte Carlo simulations of dose delivered with very high-energy electron beams in a polystyrene phantom. *Medical Physics*, 42(4), 2015.

[122] Daniela Poppinga, Rafael Kranzer, Wilfrid Farabolini, Antonio Gilardi, Roberto Corsini, Vanessa Wyrwoll, Hui Khee Looe, Björn Delfs, Lukas Gabrisch, and Björn Poppe. VHEE beam dosimetry at CERN Linear Electron Accelerator for Research under ultra-high dose rate conditions. *Biomedical Physics and Engineering Express*, 7(1), 11 2020.

[123] J. C. Crosbie, I. Svalbe, S. M. Midgley, N. Yagi, P. A.W. Rogers, and R. A. Lewis. A method of dosimetry for synchrotron microbeam radiation therapy using radiochromic films of different sensitivity. *Physics in Medicine and Biology*, 53(23):6861–6877, 2008.

[124] Elke Bräuer-Krisch, Jean Francois Adam, Enver Alagoz, Stefan Bartzsch, Jeff Crosbie, Carlos DeWagter, Andrew Dipuglia, Mattia Donzelli, Simon Doran, Pauline Fournier, John Kalef-Ezra, Angela Kock, Michael Lerch, Ciara McErlean, Uwe Oelfke, Pawel Olko, Marco Petasecca, Marco Povoli, Anatoly Rosenfeld, Erik A. Siegbahn, Dan Sporea, and Bjarne Stugu. Medical physics aspects of the synchrotron radiation therapies: Microbeam radiation therapy (MRT) and synchrotron stereotactic radiotherapy (SSRT). *Physica Medica*, 31(6):568–583, 2015.

[125] Stefan Bartzsch, Stéphanie Corde, Jeffrey C. Crosbie, Liam Day, Mattia Donzelli, Michael Krisch, Michael Lerch, Paolo Pellicioli, Lloyd M.L. Smyth, and Moeava Tehei. Technical advances in x-ray microbeam radiation therapy. *Physics in Medicine and Biology*, 65(2), 2020.

[126] Patrik Gonçalves Jorge, Maud Jaccard, Kristoffer Petersson, Maude Gondré, Maria Teresa Durán, Laurent Desorgher, Jean François Germond, Philippe Liger, Marie Catherine Vozenin, Jean Bourhis, François Bochud, Raphaël Moeckli, and Claude Bailat. Dosimetric and preparation procedures for irradiating biological models with pulsed electron beam at ultra-high dose-rate. *Radiotherapy and Oncology*, 139:34–39, 2019.

[127] Maud Jaccard, Kristoffer Petersson, Thierry Buchillier, Jean François Germond, Maria Teresa Durán, Marie Catherine Vozenin, Jean Bourhis, François O. Bochud, and Claude Bailat. High dose-per-pulse electron beam dosimetry: Usability and dose-rate independence of EBT3 Gafchromic films. *Medical Physics*, 44(2):725–735, 2017.

[128] E. Bräuer-Krisch, H. Requardt, T. Brochard, G. Berruyer, M. Renier, J. A. Laissue, and A. Bravin. New technology enables high precision multislit collimators for microbeam radiation therapy. *Review of Scientific Instruments*, 80(7):1–7, 2009.

[129] Manuela Buonanno, Veljko Grilj, and David J. Brenner. Biological effects in normal cells exposed to FLASH dose rate protons. *Radiotherapy and Oncology*, 139:51–55, 2019.

[130] Elke Beyreuther, Michael Brand, Stefan Hans, Katalin Hideghéty, Leonhard Karsch, Elisabeth Leßmann, Michael Schürer, Emília Rita Szabó, and Jörg Pawelke. Feasibility of proton FLASH effect tested by zebrafish embryo irradiation. *Radiotherapy and Oncology*, 139:46–50, 2019.

[131] Feng Gao, Yiwei Yang, Hongyu Zhu, Jianxin Wang, Dexin Xiao, Zheng Zhou, Tangzhi Dai, Yu Zhang, Gang Feng, Jie Li, Binwei Lin, Gang Xie, Qi Ke, Kui Zhou, Peng Li, Xuming Shen, Hanbin Wang, Longgang Yan, Chenglong Lao, Lijun Shan, Ming Li, Yanhua Lu, Menxue Chen, Song Feng, Jianheng Zhao, Dai Wu, and Xiaobo Du. First demonstration of the FLASH effect with ultrahigh dose rate high-energy X-rays. *Radiotherapy and Oncology*, 166:44–50, 2022.

[132] Thomas A.D. Brown, Kenneth R. Hogstrom, Diane Alvarez, Kenneth L. Matthews, Kyungmin Ham, and Joseph P. Dugas. Dose-response curve of EBT, EBT2, and EBT3 radiochromic

films to synchrotron-produced monochromatic x-ray beams. *Medical Physics*, 39(12):7412–7417, 2012.

[133] Bijan Arjomandy, Ramesh Tailor, Aman Anand, Narayan Sahoo, Michael Gillin, Karl Prado, and Milos Vicic. Energy dependence and dose response of Gafchromic EBT2 film over a wide range of photon, electron, and proton beam energies. *Medical Physics*, 37(5):1942–1947, 2010.

[134] Suphalak Khachonkham, Ralf Dreindl, Gerd Heilemann, Wolfgang Lechner, Hermann Fuchs, Hugo Palmans, Dietmar Georg, and Peter Kuess. Characteristic of EBT-XD and EBT3 radiochromic film dosimetry for photon and proton beams. *Physics in Medicine and Biology*, 63(6), 2018.

[135] Petri Sipilä, Jarkko Ojala, Sampsa Kaijaluoto, Ilkka Jokelainen, and Antti Kosunen. Gafchromic EBT3 film dosimetry in electron beams - energy dependence and improved film read-out. *Journal of Applied Clinical Medical Physics*, 17(1):360–373, 2016.

[136] Pierre Lansonneur, Vincent Favaudon, Sophie Heinrich, Charles Fouillade, Pierre Verrelle, and Ludovic De Marzi. Simulation and experimental validation of a prototype electron beam linear accelerator for preclinical studies. *Physica Medica*, 60(November 2018):50–57, 2019.

[137] Valeria Casanova Borca, Massimo Pasquino, Giuliana Russo, Pierangelo Grosso, Domenico Cante, Piera Sciacero, Giuseppe Girelli, Maria Rosa La Porta, and Santi Tofani. Dosimetric characterization and use of GAFCHROMIC EBT3 film for IMRT dose verification. *Journal of Applied Clinical Medical Physics*, 14(2):158–171, 2013.

[138] S. N. Chen, M. Gauthier, M. Bazalova-Carter, S. Bolanos, S. Glenzer, R. Riquier, G. Revet, P. Antici, A. Morabito, A. Propp, M. Starodubtsev, and J. Fuchs. Absolute dosimetric characterization of Gafchromic EBT3 and HDv2 films using commercial flat-bed scanners and evaluation of the scanner response function variability. *Review of Scientific Instruments*, 87(7), 2016.

[139] Peter R. Almond, Peter J. Biggs, B. M. Coursey, W. F. Hanson, M. Saiful Huq, Ravinder Nath, and D. W.O. Rogers. AAPM's TG-51 protocol for clinical reference dosimetry of high-energy photon and electron beams. *Medical Physics*, 26(9):1847–1870, 1999.

[140] C. M. Ma, C. W. Coffey, L. A. DeWerd, C. Liu, R. Nath, S. M. Seltzer, and J. P. Seuntjens. AAPM protocol for 40-300 kV x-ray beam dosimetry in radiotherapy and radiobiology. *Medical Physics*, 28(6):868–893, 2001.

[141] J. Eduardo Villarreal-Barajas and Rao F.H. Khan. Energy response of EBT3 radiochromic films: Implications for dosimetry in kilovoltage range. *Journal of Applied Clinical Medical Physics*, 15(1):331–338, 2014.

[142] D W O Rogers, B Walters, and I Kawrakow. *BEAMnrc users manual Report No. PIRS-0 509(A), rev. L*. 2017.

[143] J Perl, J Shin, J Schumann, B Faddegon, and H Paganetti. TOPAS : An innovative proton Monte Carlo platform for research and clinical applications. *Med. Phys.*, 39(November):6818–37, 2012.

[144] M. Ady. *MONTE CARLO SIMULATIONS OF ULTRA HIGH VACUUM AND SYNCHROTRON RADIATION FOR PARTICLE ACCELERATORS*. PhD thesis, EPFL, Lausanne, 2016.

[145] M Ady, M Hermann, R Kersevan, G Vandoni, D Ziemianski, and DZiemianski Cern. Leak Propagation Dynamics for the HIE-ISOLDE Superconducting Linac. In *IPAC14*, Dresden, Germany, 2014.

[146] R Kersevan, M Ady, and Geneva Switzerland. RECENT DEVELOPMENTS OF MONTE-CARLO CODES MOLFLOW+ AND SYNRAD+. In *10th International Particle Accelerator Conference*, 2019.

[147] K.H. Huebner, D.L Dewhirst, D.E. Smith, and T.G. Byrom. *The Finite Element Method for Engineers*. Wiley, New Jersey, USA, 4th edition, 2001.

[148] Valeria Filippou and Charalampos Tsoumpas. Recent advances on the development of phantoms using 3D printing for imaging with CT, MRI, PET, SPECT, and ultrasound. *Medical Physics*, 2018.

[149] Gregory Von White, Rajan Tandon, Lysle Serna, Mat Celina, and Robert Bernstein. An Overview of Basic Radiation Effects on Polymers, SAND2013-8003P. *Technical Report Sandia National Laboratories*, SAND2013-8:1–35, 2013.

[150] Elizabeth George, Peter Liacouras, Frank J. Rybicki, and Dimitrios Mitsouras. Measuring and Establishing the Accuracy and Reproducibility of 3D Printed Medical Models. *RadioGraphics*, 37(5):1424–1450, 2017.

[151] D. N. Slatkin, P. Spanne, F. A. Dilmanian, and M. Sandborg. Microbeam radiation therapy. *Medical Physics*, 19(6):1395–1400, 1992.

[152] F Avraham Dilmanian, Gerard M Morris, Nan Zhong, Tigran Bacarian, James F Hainfeld, John Kalef-Ezra, Laura J Brewington, Jennifer Tammam, and Eliot M Rosen. Murine EMT-6 carcinoma: high therapeutic efficacy of microbeam radiation therapy. *Radiation research*, 159(5):632–641, 2003.

[153] Yumiko Ohno, Masami Torikoshi, Masao Suzuki, Keiji Umetani, Yasuhiko Imai, Kentaro Uesugi, and Naoto Yagi. Dose distribution of a 125 keV mean energy microplanar x-ray beam for basic studies on microbeam radiotherapy. *Medical Physics*, 35(7):3252–3258, 2008.

[154] E. A. Siegbahn, J. Stepanek, E. Brauer-Krisen, and A. Bravin. Determination of dosimetrical quantities used in microbeam radiation therapy (MRT) with Monte Carlo simulations. *Medical Physics*, 33(9):3248–3259, 2006.

[155] Daniel Brönnimann, Audrey Bouchet, Christoph Schneider, Marine Potez, Raphaël Serduc, Elke Bräuer-Krisch, Werner Graber, Stephan Von Gunten, Jean Albert Laissue, and Valentin Djonov. Synchrotron microbeam irradiation induces neutrophil infiltration, thrombocyte attachment and selective vascular damage in vivo. *Scientific Reports*, 6(May):1–10, 2016.

[156] John William Hopewell and Klaus Rüdiger Trott. Volume effects in radiobiology as applied to radiotherapy. *Radiotherapy and Oncology*, 56(3):283–288, 2000.

[157] Genro Kashino, Takeshi Kondoh, Nobuteru Nariyama, Keiji Umetani, Takuji Ohigashi, Kunio Shinohara, Ai Kurihara, Manabu Fukumoto, Hiroki Tanaka, Akira Maruhashi, Minoru Suzuki, Yuko Kinashi, Yong Liu, Shin ichiro Masunaga, Masami Watanabe, and Koji Ono. Induction of DNA Double-Strand Breaks and Cellular Migration Through Bystander Effects in Cells Irradiated With the Slit-Type Microplanar Beam of the Spring-8 Synchrotron. *International Journal of Radiation Oncology Biology Physics*, 74(1):229–236, 2009.

[158] Audrey Bouchet, Benjamin Lemasson, Géraldine Le Duc, Cécile Maisin, Elke Bräuer-Krisch, Erik Albert Siegbahn, Luc Renaud, Enam Khalil, Chantal Rémy, Cathy Poillot, Alberto Bravin, Jean A. Laissue, Emmanuel L. Barbier, and Raphaël Serduc. Preferential effect of synchrotron microbeam radiation therapy on intracerebral 9l gliosarcoma vascular networks. *International Journal of Radiation Oncology Biology Physics*, 78(5):1503–1512, 2010.

[159] Sara Sabatasso, Jean Albert Laissue, Ruslan Hlushchuk, Werner Graber, Alberto Bravin, Elke Bräuer-Krisch, Stéphanie Corde, Hans Blattmann, Guenther Gruber, and Valentin Djonov. Microbeam radiation-induced tissue damage depends on the stage of vascular maturation. *International Journal of Radiation Oncology Biology Physics*, 80(5):1522–1532, 2011.

[160] Raphaël Serduc, Pascale Vérant, Jean Claude Vial, Régine Farion, Linda Rocas, Chantal Rémy, Taoufik Fadlallah, Elke Brauer, Alberto Bravin, Jean Laissue, Hans Blattmann, and Boudewijn Van Der Sanden. In vivo two-photon microscopy study of short-term effects of microbeam irradiation on normal mouse brain microvasculature. *International Journal of Radiation Oncology Biology Physics*, 64(5):1519–1527, 2006.

[161] R. C.U. Priyadarshika, J. C. Crosbie, B. Kumar, and Peter A.W. Rogers. Biodosimetric quantification of short-term synchrotron microbeam versus broad-beam radiation damage to mouse skin using a dermatopathological scoring system. *British Journal of Radiology*, 84(1005):833–842, 2011.

[162] Mike Hadsell, Guohua Cao, Jian Zhang, Laurel Burk, Torsten Schreiber, Eric Schreiber, Sha Chang, Jianping Lu, Otto Zhou, Mike Hadsell, Guohua Cao, Jian Zhang, Laurel Burk, and Torsten Schreiber. Pilot study for compact microbeam radiation therapy using a carbon nanotube field emission micro-CT scanner Pilot study for compact microbeam radiation therapy using a carbon nanotube field emission micro-CT scanner. *Medical Physics*, 061710(6):1–11, 2014.

[163] Kerry Babcock, Narinder Sidhu, Vijayananda Kundapur, and Kaiser Ali. Collimator design for experimental minibeam radiation therapy. *Medical Physics*, 38(4):2192–2197, 2011.

[164] E. Bräuer-Krisch, R. Serduc, E. A. Siegbahn, G. Le Duc, Y. Prezado, A. Bravin, H. Blattmann, and J. A. Laissue. Effects of pulsed, spatially fractionated, microscopic synchrotron X-ray beams on normal and tumoral brain tissue. *Mutation Research - Reviews in Mutation Research*, 704(1-3):160–166, 2010.

[165] A. Vassantachart, Y. He, R.C. Tailor, A. Dilmanian, and S. Krishnan. Orthovoltage X-Ray Minibeam Therapy of Moving Targets. *International Journal of Radiation Oncology Biology Physics*, 99(2):E731–E732, 2017.

[166] Christopher Daniel Johnstone and Magdalena Bazalova-Carter. MicroCT imaging dose to mouse organs using a validated Monte Carlo model of the small animal radiation research platform (SARRP). *Physics in Medicine & Biology*, 63(11):115012, 6 2018.

[167] S. Agostinelli, J. Allison, K. Amako, J. Apostolakis, H. Araujo, P. Arce, M. Asai, D. Axen, S. Banerjee, G. Barrand, F. Behner, L. Bellagamba, J. Boudreau, L. Broglia, A. Brunengo, H. Burkhardt, S. Chauvie, J. Chuma, R. Chytracek, G. Cooperman, G. Cosmo, P. Degtyarenko, A. Dell'Acqua, G. Depaola, D. Dietrich, R. Enami, A. Feliciello, C. Ferguson, H. Fesefeldt, G. Folger, F. Foppiano, A. Forti, S. Garelli, S. Giani, R. Giannitrapani, D. Gibin, J. J. Gomez Cadenas, I. Gonzalez, G. Gracia Abril, G. Greeniaus, W. Greiner, V. Grichine, A. Grossheim, S. Guatelli, P. Gumplinger, R. Hamatsu, K. Hashimoto, H. Hasui, A. Heikkinen, A. Howard, V. Ivanchenko, A. Johnson, F. W. Jones, J. Kallenbach, N. Kanaya, M. Kawabata, Y. Kawabata, M. Kawaguti, S. Kelner, P. Kent, A. Kimura, T. Kodama, R. Kokoulin, M. Kossov, H. Kurashige, E. Lamanna, T. Lampen, V. Lara, V. Lefebure, F. Lei, M. Liendl, W. Lockman, F. Longo, S. Magni, M. Maire, E. Medernach, K. Minamimoto, P. Mora de Freitas, Y. Morita, K. Murakami, M. Nagamatu, R. Nartallo, P. Nieminen, T. Nishimura,

K. Ohtsubo, M. Okamura, S. O'Neale, Y. Oohata, K. Paech, J. Perl, A. Pfeiffer, M. G. Pia, F. Ranjard, A. Rybin, S. Sadilov, E. di Salvo, G. Santin, T. Sasaki, N. Savvas, Y. Sawada, S. Scherer, S. Sei, V. Sirotenko, D. Smith, N. Starkov, H. Stoecker, J. Sulkimo, M. Takahata, S. Tanaka, E. Tcherniaev, E. Safai Tehrani, M. Tropeano, P. Truscott, H. Uno, L. Urban, P. Urban, M. Verderi, A. Walkden, W. Wander, H. Weber, J. P. Wellisch, T. Wenaus, D. C. Williams, D. Wright, T. Yamada, H. Yoshida, and D. Zschiesche. GEANT4 - A simulation toolkit. *Nuclear Instruments and Methods in Physics Research, Section A: Accelerators, Spectrometers, Detectors and Associated Equipment*, 506(3):250–303, 2003.

[168] Y. Prezado, G. Fois, G. Le Duc, and A. Bravin. Gadolinium dose enhancement studies in microbeam radiation therapy. *Medical Physics*, 36(8):3568–3574, 2009.

[169] C. Lindsay, J. Kumlin, A. Jirasek, R. Lee, D. M. Martinez, P. Schaffer, and C. Hoehr. 3D printed plastics for beam modulation in proton therapy. *Physics in Medicine and Biology*, 60(11):N231–N240, 2015.

[170] C. Lindsay, J. Kumlin, D. M. Martinez, A. Jirasek, and C. Hoehr. Design and application of 3D-printed stepless beam modulators in proton therapy. *Physics in Medicine and Biology*, 61(11):N276–N290, 2016.

[171] Brian W. Miller, Jared W. Moore, Harrison H. Barrett, Teresa Fryé, Steven Adler, Joe Sery, and Lars R. Furenlid. 3D printing in X-ray and gamma-ray imaging: A novel method for fabricating high-density imaging apertures. *Nuclear Instruments and Methods in Physics Research, Section A: Accelerators, Spectrometers, Detectors and Associated Equipment*, 659(1):262–268, 2011.

[172] Joseph Newton, Mark Oldham, Andrew Thomas, Yifan Li, John Adamovics, David G. Kirsch, and Shiva Das. Commissioning a small-field biological irradiator using point, 2D, and 3D dosimetry techniques. *Medical Physics*, 38(12):6754–6762, 2011.

[173] Guerda Massillon-JL, Diego Cueva-Prócel, Porfirio Díaz-Aguirre, Miguel Rodríguez-Ponce, and Flor Herrera-Martínez. Dosimetry for Small Fields in Stereotactic Radiosurgery Using Gafchromic MD-V2-55 Film, TLD-100 and Alanine Dosimeters. *PLoS ONE*, 8(5), 2013.

[174] L. Wack, W. Ngwa, E. Tryggestad, P. Tsiamas, R. Berbeco, S. K. Ng, J. Hesser, and P. Zygmanski. High throughput film dosimetry in homogeneous and heterogeneous media for a small animal irradiator. *Physica Medica*, 30(1):36–46, 2014.

[175] Stella Avtzi, Athanasios Zacharopoulos, Stylianos Psycharakis, and Giannis Zacharakis. Fabrication and characterization of a 3-D non-homogeneous tissue-like mouse phantom for optical imaging. *Proc. SPIE*, 9032(November 2013):903206, 2013.

[176] Phuong Diep, Sanjana Pannem, Jordan Sweer, Justine Lo, Michael Snyder, Gabriella Stueber, Yanyu Zhao, Syeda Tabassum, Raeef Istfan, Junjie Wu, Shyamsunder Erramilli, and Darren Roblyer. Three-dimensional printed optical phantoms with customized absorption and scattering properties. *Biomedical Optics Express*, 6(11):4212, 2015.

[177] Brian Z. Bentz, Anmol V. Chavan, Dergan Lin, Esther H. R. Tsai, and Kevin J. Webb. Fabrication and application of heterogeneous printed mouse phantoms for whole animal optical imaging. *Applied Optics*, 55(2):280, 2016.

[178] Julian R Perks, Steven Lucero, Arta M Monjazeb, and Jian Jian Li. Anthropomorphic Phantoms for Confirmation of Linear Accelerator-Based Small Animal Irradiation. *Cureus*, 7(3):e254, 3 2015.

[179] D. Welch, A. D. Harken, G. Randers-Pehrson, and D. J. Brenner. Construction of mouse phantoms from segmented CT scan data for radiation dosimetry studies. *Physics in Medicine and Biology*, 60(9):3589–3598, 2015.

[180] David Welch, Leah Turner, Michael Speiser, Gerhard Randers-Pehrson, and David J. Brenner. Scattered Dose Calculations and Measurements in a Life-Like Mouse Phantom. *Radiation Research*, 187(4):433–442, 2017.

[181] Cheng Chia Wu, Kunal R. Chaudhary, Yong Hum Na, David Welch, Paul J. Black, Adam M. Sonabend, Peter Canoll, Yvonne M. Saenger, Tony J.C. Wang, Cheng Shie Wuu, Tom K. Hei, and Simon K. Cheng. Quality Assessment of Stereotactic Radiosurgery of a Melanoma Brain Metastases Model Using a Mouselike Phantom and the Small Animal Radiation Research Platform. *International Journal of Radiation Oncology Biology Physics*, 99(1):191–201, 2017.

[182] Steven T. Bache, Titania Juang, Matthew D. Belley, Bridget F. Koontz, John Adamovics, Terry T. Yoshizumi, David G. Kirsch, and Mark Oldham. Investigating the accuracy of microstereotactic-body-radiotherapy utilizing anatomically accurate 3D printed rodent-morphic dosimeters. *Medical Physics*, 42(2):846–855, 1 2015.

[183] Haozhao Zhang, Kun Hou, Joe Chen, Brandon A Dyer, Jyh-Cheng Chen, Xiaojing Liu, Fuquan Zhang, Yi Rong, and Jianfeng Qiu. Fabrication of an anthropomorphic heterogeneous mouse phantom for multimodality medical imaging. *Physics in Medicine & Biology*, 63(19):195011, 9 2018.

[184] B Walters, I Kawrakow, and D W O Rogers. *DOSXYZnrc Users Manual Report No. PIRS-794, rev. B.* Ionizing Radiation Standards at the National Research Council of Canada, Ottawa: NRC, 2017.

[185] M. L. Taylor, R. L. Smith, F. Dossing, and R. D. Franich. Robust calculation of effective atomic numbers: The Auto- ¡i¿ Z ¡sub¿eff¡/sub¿ ¡/i¿ software. *Medical Physics*, 39(4):1769–1778, 3 2012.

[186] Tsuicheng D. Chiu, Tatsuya J. Arai, James Campbell III, Steve B. Jiang, Ralph P. Mason, and Strahinja Stojadinovic. MR-CBCT image-guided system for radiotherapy of orthotopic rat prostate tumors. *PLOS ONE*, 13(5):e0198065, 5 2018.

[187] Christopher Daniel Johnstone, François Therriault-Proulx, Luc Beaulieu, and Magdalena Bazalova-Carter. Characterization of a plastic scintillating detector for the Small Animal Radiation Research Platform (SARRP). *Medical Physics*, 46(1):394–404, 12 2019.

[188] Mária Martišíková, Benjamin Ackermann, and Oliver Jäkel. Analysis of uncertainties in Gafchromic® EBT film dosimetry of photon beams. *Physics in Medicine and Biology*, 53(24):7013–7027, 2008.

[189] Jalil ur Rehman, Zahra, Nisar Ahmad, Muhammad Khalid, H.M. Noor ul Huda Khan Asghar, Zaheer Abbas Gilani, Irfan Ullah, Gulfam Nasar, Malik Muhammad Akhtar, and Muhammad Nauman Usmani. Intensity modulated radiation therapy: A review of current practice and future outlooks. *Journal of Radiation Research and Applied Sciences*, 11(4):361–367, 10 2018.

[190] Laura A Dawson and David A Jaffray. Advances in Image-Guided Radiation Therapy. *Journal of Clinical Oncology*, 25(8):938–946, 3 2007.

[191] Simon S Lo, Achilles J Fakiris, Eric L Chang, Nina A Mayr, Jian Z Wang, Lech Papiez, Bin S Teh, Ronald C McGarry, Higinia R Cardenes, and Robert D Timmerman. Stereotactic body radiation therapy: a novel treatment modality. *Nature Reviews Clinical Oncology*, 7:44–54, 12 2010.

[192] Marco Durante and Jay S. Loeffler. Charged particles in radiation oncology. *Nature Reviews Clinical Oncology*, 7(1):37–43, 1 2010.

[193] Shirley Hornsey and D K Bewley. Hypoxia in Mouse Intestine Induced by Electron Irradiation at High Dose-rates. *International Journal of Radiation Biology and Related Studies in Physics, Chemistry and Medicine*, 19(5):479–483, 1 1971.

[194] Edward Epp, Herbert Weiss, Bozidar Djordjevic, and Ann Santomasso. The Radiosensitivity of Cultured Mammalian Cells Exposed to Single High Intensity Pulses of Electrons in Various Concentrations of Oxygen. *Radiation Research*, 52(2):324–332, 1972.

[195] S B Field and D K Bewley. Effects of Dose-rate on the Radiation Response of Rat Skin. *International Journal of Radiation Biology and Related Studies in Physics, Chemistry and Medicine*, 26(3):259–267, 1 1974.

[196] Vincent Favaudon, Laura Caplier, Virginie Monceau, Frédéric Pouzoulet, Mano Sayarath, Charles Fouillade, Marie-France Poupon, Isabel Brito, Philippe Hupé, Jean Bourhis, Janet Hall, Jean-Jacques Fontaine, and Marie-Catherine Vozenin. Ultrahigh dose-rate FLASH irradiation increases the differential response between normal and tumor tissue in mice. *Science Translational Medicine*, 6(245):245ra93 LP – 245ra93, 7 2014.

[197] Marine Potez, Audrey Bouchet, Jeannine Wagner, Mattia Donzelli, Elke Bräuer-Krisch, John W. Hopewell, Jean Laissue, and Valentin Djonov. Effects of Synchrotron X-Ray Microbeam Irradiation on Normal Mouse Ear Pinnae. *International Journal of Radiation Oncology Biology Physics*, 101(3):680–689, 2018.

[198] Swati Girdhani, Eric Abel, Alexander Katsis, Andrew Rodriquez, Angel Kuvillanueva, Isabel L Jackson, John Eley, Renate Parry, Varian Medical Systems, Palo Alto, Varian Medical, Varian Medical, and Varian Medical. FLASH: A novel paradigm changing tumor irradiation platform that enhances therapeutic ratio by reducing normal tissue toxicity and activating immune pathways. In *AACR*, pages 2–3, 2019.

[199] I. Kawrakow, D. W. O. Rogers, and B. R. B. Walters. Large efficiency improvements in BEAMnrc using directional bremsstrahlung splitting. *Medical Physics*, 31(10):2883–2898, 10 2004.

[200] F Verhaegen, A E Nahum, S Van de Putte, and Y Namito. Monte Carlo modelling of radiotherapy kV x-ray units. *Physics in Medicine and Biology*, 44(7):1767–1789, 7 1999.

[201] Robin Hill, Brendan Healy, Lois Holloway, Zdenka Kuncic, David Thwaites, and Clive Baldock. Advances in kilovoltage x-ray beam dosimetry. *Physics in Medicine and Biology*, 59(6):R183–R231, 3 2014.

[202] Peter G. F. Watson and Jan Seuntjens. Technical Note: Effect of explicit ¡i¿M¡/i¿ and ¡i¿N¡/i¿ -shell atomic transitions on a low-energy x-ray source. *Medical Physics*, 43(4):1760–1763, 3 2016.

[203] S C Klevenhagen. The build-up of backscatter in the energy range 1 mm Al to 8 mm Al HVT (radiotherapy beams). *Physics in Medicine and Biology*, 27(8):1035–1043, 8 1982.

[204] Billy W. Loo, Emil Schuler, Frederick M. Lartey, Marjan Rafat, Gregory J. King, Stefania Trovati, Albert C. Koong, and Peter G. Maxim. (P003) Delivery of Ultra-Rapid Flash Radiation

Therapy and Demonstration of Normal Tissue Sparing After Abdominal Irradiation of Mice. *International Journal of Radiation Oncology*Biology*Physics*, 98(2):E16, 2017.

[205] Arash Darafsheh, Yao Hao, Townsend Zwart, Miles Wagner, Daniel Catanzano, Jeffrey F. Williamson, Nels Knutson, Baozhou Sun, Sasa Mutic, and Tianyu Zhao. Feasibility of proton FLASH irradiation using a synchrocyclotron for preclinical studies. *Medical Physics*, 2020.

[206] Michele M. Kim, Ioannis I. Verginadis, Denisa Goia, Allison Haertter, Khayrullo Shoniyozov, Wei Zou, Amit Maity, Theresa M. Busch, James M. Metz, Keith A. Cengel, Lei Dong, Costas Koumenis, and Eric S. Diffenderfer. Comparison of flash proton entrance and the spread-out bragg peak dose regions in the sparing of mouse intestinal crypts and in a pancreatic tumor model. *Cancers*, 13(16), 2021.

[207] Feng Gao, Yiwei Yang, Hongyu Zhu, Jian Xin Wang, Dexin Xiao, Zheng Zhou, Tangzhi Dai, Yu Zhang, Gang Feng, Jie Li, Binwei Lin, Gang Xie, Qi Ke, Kui Zhou, Peng Li, Xuming Sheng, Hanbin Wang, Longgang Yan, Chenglong Lao, Ming Li, Yanhua Lu, Menxue Chen, Jianheng Zhao, Song Feng, Xiaobo Du, and Dai Wu. First demonstration of the FLASH effect with ultrahigh dose-rate high energy X-rays. *bioRxiv*, pages 1–14, 2020.

[208] Patricia van Marlen, Max Dahele, Michael Folkerts, Eric Abel, Berend J. Slotman, and Wilko F.A.R. Verbakel. Bringing FLASH to the Clinic: Treatment Planning Considerations for Ultrahigh Dose-Rate Proton Beams. *International Journal of Radiation Oncology Biology Physics*, 106(3):621–629, 2020.

[209] Nolan Esplen and Luca Egoriti. Developing a spatially-fractionated FLASH-RT x-ray platform. In *WIMP2020*, Winter Institute of Medical Physics, 2020. Breckenridge, CO, USA.

[210] R. B. Miller. *Electronic Irradiation of Foods: An Introduction to the Technology.* New York, NY: Springer, 2005.

[211] L Egoriti, M Cervantes, T Day Goodacre, and A Gottberg. Material development towards a solid 100 kW electron-gamma converter for TRIUMF-ARIEL. *Nuclear Instruments and Methods in Physics Research Section B: Beam Interactions with Materials and Atoms*, 463:232–236, 2020.

[212] Olivier Shelbaya, Tiffany Angus, Rick Baartman, Paul M. Jung, Oliver Kester, Spencer Kiy, Thomas Planche, and Stephanie D. Rädel. Autofocusing drift tube linac envelopes. *Physical Review Accelerators and Beams*, 24(12):124602, 2021.

[213] R LaForce, R F Berning, and L F Coffin Jr. High-Temperature, Low-Cycle Fatigue Behavior of Tantalum (CR-1930). Technical Report September 1971, GE: Ohio, Washington: NASA, 1971.

[214] Dan Wilcox. Simulating Performance of Tantalum-Clad Tungsten Targets. In *IWSMT13*, number November, 2016.

[215] J. H. Bechtold. Tensile properties of annealed tantalum at low temperatures. *Acta Metallurgica*, 3:249–254, 1955.

[216] J R Davis. *Tantalum and Tantalum Alloys*. Materials Park, OH, ASM International, 2001.

[217] Zhiliang Pan. *Comparative study of the effect of impurities on the ductility of tantalum and tungsten based on atomistic and first principles calculations*. PhD thesis, The University of North Carolina at Charlotte, 2012.

[218] ICRU. Tissue substitutes in radiation dosimetry and measurement (ICRU Report 44). Technical report, ICRU, Bethesda, MD: ICRU, 1989.

[219] Elise Badun, Frédéric Tessier, Reid Townson, Ernesto Mainegra-Hing, Margaret-Anne Storey, and Magdalena Bazalova-Carter. Introducing the Voxel Interactive Contour Tool for Online Radiation Intensity Analytics (VICTORIA). pages 1–5, 2021.

[220] ASM International Handbook Committee. *Properties and Selection: Nonferrous Alloys and Special-Purpose Materials*, volume 2. Materials Park, OH, ASM International, 1991.

[221] E. D. Marquardt, J. P. Le, and Ray Radebaugh. Cryogenic Material Properties Database. In *11th International Cryocooler Conference*, pages 681–687. Boulder, CO: NIST, 2002.

[222] F. F. Schmidt and H. R. Ogden. The Engineering Properties of Tantalum and Tantalum Alloys (DMIC Report 189). Technical report, Bettelle Memorial Institute, Columbus, OH: DMIC, 1963.

[223] C. Y. Ho, R. W. Powell, and P. E. Liley. Thermal Conductivity of the Elements, 1974.

[224] Kurt C Schulz and G. T. Yahr. Preliminary Fracture Analysis of the Core Pressure Boundary Tube for the Advanced Neutron Source Research Reactor (ORNL/M-4619). Technical Report August, ORNL, Oak Ridge, TN: ORNL, 1995.

[225] G. T. Yahr. *Fatigue Design Curves for 6061-T6 Aluminum*. Oak Ridge, TN: ORNL, 1993.

[226] Jean Bourhis, Wendy Jeanneret Sozzi, Patrik Gonçalves Jorge, Olivier Gaide, Claude Bailat, Fréderic Duclos, David Patin, Mahmut Ozsahin, François Bochud, Jean François Germond, Raphaël Moeckli, and Marie Catherine Vozenin. Treatment of a first patient with FLASH-radiotherapy. *Radiotherapy and Oncology*, 139:18–22, 2019.

[227] Niklas Ophoven, Eric Mauerhofer, Jingjing Li, Ulrich Rücker, Paul Zakalek, Johannes Baggemann, Thomas Gutberlet, Thomas Brückel, and Christoph Langer. Monte Carlo simulation of proton- and neutron-induced radiation damage in a tantalum target irradiated by 70 MeV protons. *Applied Physics A: Materials Science and Processing*, 127(8):1–14, 2021.

[228] M. Papakyriacou, H. Mayer, C. Pypen, H. Plenk, and S. Stanzl-Tschegg. Influence of loading frequency on high cycle fatique properties of b.c.c and h.c.p. metals. *Materials Science and Engineering A*, 308(1-2):143–152, 2001.

[229] M. Papakyriacou, H. Mayer, H. Plenk, and S. Stanzl-Tschegg. Cyclic plastic deformation of tantalum and niobium at very high numbers of cycles. *Materials Science and Engineering A*, 325(1-2):520–524, 2002.

[230] Chris Nelson. Material Properties of Tantalum Including High Cycle Fatigue. In *Proceedings of the 14th International Workshop on Spallation Materials Technology*, volume 28 of *JPS Conference Proceedings*. Journal of the Physical Society of Japan, 2 2020.

[231] P J Rudd, D Prior, and S Austin-Smith. Neutron contamination of 10 MV X-rays: its relevance to treatment room door and maze design. *The British Journal of Radiology*, 80(954):469–475, 6 2007.

[232] Alireza Naseri and Asghar Mesbahi. A review on photoneutrons characteristics in radiation therapy with high-energy photon beams. *Reports of Practical Oncology and Radiotherapy*, 15(5):138–144, 2010.

[233] Peter Schardt, Josef Deuringer, Jörg Freudenberger, Erich Hell, Wolfgang Knüpfer, Detlef Mattern, and Markus Schild. New x-ray tube performance in computed tomography by introducing the rotating envelope tube technology. *Medical Physics*, 31(9):2699–2706, 2004.

[234] K. Kokurewicz, E. Brunetti, G. H. Welsh, S. M. Wiggins, M. Boyd, A. Sorensen, A. J. Chalmers, G. Schettino, A. Subiel, C. DesRosiers, and D. A. Jaroszynski. Focused very high-energy electron beams as a novel radiotherapy modality for producing high-dose volumetric elements. *Scientific Reports*, 9(1), 12 2019.

[235] L. Whitmore, R. I. Mackay, M. van Herk, J. K. Jones, and R. M. Jones. Focused VHEE (very high energy electron) beams and dose delivery for radiotherapy applications. *Scientific Reports*, 11(1), 12 2021.

[236] Muhammad Ramish Ashraf, Mahbubur Rahman, Rongxiao Zhang, Benjamin B. Williams, David J. Gladstone, Brian W. Pogue, and Petr Bruza. Dosimetry for FLASH Radiotherapy: A Review of Tools and the Role of Radioluminescence and Cherenkov Emission. *Frontiers in Physics*, 8(August):1–20, 2020.

[237] Francesco Romano, Claude Bailat, Patrik Gonçalves Jorge, Michael Lloyd Franz Lerch, and Arash Darafsheh. Ultra-high dose rate dosimetry: Challenges and opportunities for FLASH radiation therapy. *Medical Physics*, 49(7):4912–4932, 7 2022.

[238] Jolyon Hendry. Taking Care with FLASH Radiation Therapy. *International Journal of Radiation Oncology*Biology*Physics*, i:1–4, 2020.

[239] Guangming Zhou. Mechanisms underlying FLASH radiotherapy, a novel way to enlarge the differential responses to ionizing radiation between normal and tumor tissues. *Radiation Medicine and Protection*, 1(1):35–40, 2020.

[240] Thomas Planche, Katherine Pachal, and Richard Milner. ARIEL Accelerator Overview. *Journal of Physics: Conference Series*, 2391(1):012003, 12 2022.

[241] Azam Niroomand-Rad, Sou Tung Chiu-Tsao, Michael P. Grams, David F. Lewis, Christopher G. Soares, Leo J. Van Battum, Indra J. Das, Samuel Trichter, Michael W. Kissick, Guerda Massillon-JL, Paola E. Alvarez, and Maria F. Chan. Report of AAPM Task Group 235 Radiochromic Film Dosimetry: An Update to TG-55. *Medical Physics*, 47(12):5986–6025, 12 2020.

[242] Antony L. Palmer, Alexis Dimitriadis, Andrew Nisbet, and Catharine H. Clark. Evaluation of Gafchromic EBT-XD film, with comparison to EBT3 film, and application in high dose radiotherapy verification. *Physics in Medicine and Biology*, 60(22):8741–8752, 2015.

[243] Spencer M. Robinson, Nolan Esplen, Derek Wells, and Magdalena Bazalova-Carter. Monte Carlo simulations of EBT3 film dose deposition for percentage depth dose (PDD) curve evaluation. *Journal of Applied Clinical Medical Physics*, 21(12):314–324, 12 2020.

[244] Elsa Y. León-Marroquín, José M. Lárraga-Gutiérrez, J. Alfredo Herrera-González, Miguel A. Camacho-López, José E. Villarreal Barajas, and Olivia A. García-Garduño. Investigation of EBT3 radiochromic film's response to humidity. *Journal of Applied Clinical Medical Physics*, 19(3):283–290, 5 2018.

[245] Slobodan Devic. Radiochromic film dosimetry: Past, present, and future. *Physica Medica*, 27(3):122–134, 2011.

[246] Davide Cusumano, Maria Luisa Fumagalli, Francesco Ghielmetti, Linda Rossi, Giuliano Grossi, Raffaella Lanzarotti, Laura Fariselli, and Elena De Martin. Sum signal dosimetry: A new approach for high dose quality assurance with Gafchromic EBT3. *Journal of Applied Clinical Medical Physics*, 18(2):181–190, 2017.

[247] Caroline E. Blevins, Natalie A. Celeste, and James O. Marx. Effects of Oxygen Supplementation on Injectable and Inhalant Anesthesia in C57BL/6 Mice. *Journal of the American Association for Laboratory Animal Science*, 60(3):289–297, 5 2021.

[248] Pierre Montay-Gruel, Munjal M. Acharya, Kristoffer Petersson, Leila Alikhani, Chakradhar Yakkala, Barrett D. Allen, Jonathan Ollivier, Benoit Petit, Patrik Gonçalves Jorge, Amber R. Syage, Thuan A. Nguyen, Al Anoud D. Baddour, Celine Lu, Paramvir Singh, Raphael Moeckli, François Bochud, Jean François Germond, Pascal Froidevaux, Claude Bailat, Jean Bourhis, Marie Catherine Vozenin, and Charles L. Limoli. Long-term neurocognitive benefits of FLASH radiotherapy driven by reduced reactive oxygen species. *Proceedings of the National Academy of Sciences of the United States of America*, 166(22):10943–10951, 2019.

[249] Alexander Hart, Daniel Cecchi, Cloe Giguère, Frédérique Larose, François Therriault-Proulx, Nolan Esplen, Luc Beaulieu, and Magdalena Bazalova-Carter. Lead-doped scintillator dosimeters for detection of ultrahigh dose-rate x-rays. *Physics in Medicine and Biology*, 67(10), 5 2022.

[250] S R Manohara, S M Hanagodimath, and L Gerward. Studies on effective atomic number, electron density and kerma for some fatty acids and carbohydrates. *Physics in Medicine and Biology*, 53(20):N377–N386, 10 2008.

[251] S.R. Manohara, S.M. Hanagodimath, K.S. Thind, and L. Gerward. On the effective atomic number and electron density: A comprehensive set of formulas for all types of materials and energies above 1keV. *Nuclear Instruments and Methods in Physics Research Section B: Beam Interactions with Materials and Atoms*, 266(18):3906–3912, 9 2008.

[252] VishwanathP Singh and NM Badiger. Effective atomic numbers of some tissue substitutes by different methods: A comparative study. *Journal of Medical Physics*, 39(1):24, 2014.

[253] Tetsu Fujii and Hideaki Imura. Natural-convection heat transfer from a plate with arbitrary inclination. *International Journal of Heat and Mass Transfer*, 15(4):755–767, 4 1972.

[254] Stuart W. Churchill and Humbert H.S. Chu. Correlating equations for laminar and turbulent free convection from a horizontal cylinder. *International Journal of Heat and Mass Transfer*, 18(9):1049–1053, 9 1975.

[255] Amir Akbari, Erfan Mohammadian, Seyed Ali Alavi Fazel, Mehdi Shanbedi, Mahtab Bahreini, Milad Heidari, Parham Babakhani Dehkordi, and Siti Nurliyana Che Mohamed Hussein. Natural Convection from the Outside Surface of an Inclined Cylinder in Pure Liquids at Low Flux. *ACS Omega*, 4(4):7038–7046, 4 2019.

[256] M G Fouad and Norbert V Ibl. Natural convection mass transfer at vertical electrodes under turbulent flow conditions. *Electrochimica Acta*, 3:233–243, 1960.

[257] Xinxin Wang, Jiankang Huang, Yong Huang, Ding Fan, and Yanning Guo. Investigation of heat transfer and fluid flow in activating TIG welding by numerical modeling. *Applied Thermal Engineering*, 113:27–35, 2017.

[258] Hongbin Dai, Xiuqiang Shen, and Haoran Wang. The influence of TIG-Arc physical characteristics on the penetration and weld width under different Ar and He supply conditions. *Results in Physics*, 9:1120–1126, 6 2018.

[259] Suresh V. Garimella and Vincent P. Schroeder. Local Heat Transfer Distributions in Confined Multiple Air Jet Impingement. *Journal of Electronic Packaging*, 123(3):165–172, 9 2001.

[260] I. Bitharas, N. A. McPherson, W. McGhie, D. Roy, and A. J. Moore. Visualisation and optimisation of shielding gas coverage during gas metal arc welding. *Journal of Materials Processing Technology*, 255:451–462, 5 2018.

[261] S.H.P. Chen and S.C. Saxena. Thermal conductivity of argon in the temperature range 350 to 2500 K. *Molecular Physics*, 29(2):455–466, 2 1975.

[262] ASM International Handbook Committee. *Corrosion: Fundamentals, Testing, and Protection*, volume 13. Materials Park, OH, ASM International, Materials Park, OH, 2003.

[263] Yena Kwon, Byeong-Seon An, Ji-Yun Moon, Jae-Hyun Lee, Hyunjae Yoo, Dongmok Whang, and Cheol-Woong Yang. Control of oxidation behavior in high vacuum transmission electron microscopy. *Materials Characterization*, 172:110870, 2 2021.

[264] M Parkman, R Pape, R McRae, D. Brayton, and L. Reed. Solubility and diffusion of oxygen in tantalum (NASA-CR-1276). Technical report, Varian Associates, Washington, DC: NASA, 1969.

[265] Jeffery B. DeLisio, Xizheng Wang, Tao Wu, Garth C. Egan, Rohit J. Jacob, and Michael R. Zachariah. Investigating the oxidation mechanism of tantalum nanoparticles at high heating rates. *Journal of Applied Physics*, 122(24), 12 2017.

[266] Nestor Perez. High-Temperature Oxidation. In *Electrochemistry and Corrosion Science*, pages 389–425. Springer International Publishing, Cham, 2016.

[267] Daniel Pero-Sanz Elorz José Antonio
}and Fernández González and Verdeja Luis Felipe. Structural Materials: Metals. In *Structural Materials: Properties and Selection*, pages 19–76. Springer International Publishing, Cham, 2019.

[268] R. Nakamura, T. Toda, S. Tsukui, M. Tane, M. Ishimaru, T. Suzuki, and H. Nakajima. Diffusion of oxygen in amorphous Al2O3, Ta 2O5, and Nb2O5. *Journal of Applied Physics*, 116(3), 7 2014.

[269] N.L. Peterson. Diffusion in refractory metals (WADD-TR-60-793. Technical report, Advanced Metals Research Corporation, Ohio: WADD, 1961.

[270] Boris S. Bokstein, Mikhail I. Mendelev, and David J. Srolovitz. *Thermodynamics and Kinetics in Materials Science*. Oxford University Press, 6 2005.

[271] E.A. Moshey. A compilation of outgassing data on vacuum materials. Technical report, Princeton University Plasma Physics Laboratory, Princeton, NJ: PPPL, 1982.

[272] Muneo FURUSE, Kazue TAKAHASHI, and Yuuichi ISHIKAWA. Outgassing Characteristics of Tantalum. *SHINKU*, 29(5):259–261, 1986.

[273] American Iron and Steel Institute. High-temperature characteristics of stainless steels. Technical report, NiDI, Washington, D.C., 2020.

[274] T.H. Kuehn and R.J. Goldstein. Correlating equations for natural convection heat transfer between horizontal circular cylinders. *International Journal of Heat and Mass Transfer*, 19(10):1127–1134, 10 1976.

[275] G D Raithby and K G T Hollands. A General Method of Obtaining Approximate Solutions to Laminar and Turbulent Free Convection Problems. In Thomas F Irvine and James P Hartnett, editors, *Advances in Heat Transfer*, volume 11 of *Advances in Heat Transfer*, pages 265–315. Elsevier, Amsterdam, NL, 1975.

[276] Wael Al-Kouz, Aiman Alshare, Ammar Alkhalidi, and Suhil Kiwan. Two dimensional analysis of low pressure flows in the annulus region between two concentric cylinders. *SpringerPlus*, 5(1), 12 2016.

[277] Hongyu Zhu, Dehuan Xie, Yiwei Yang, Shaomin Huang, Xingwang Gao, Yinglin Peng, Bin Wang, Jianxin Wang, Dexin Xiao, Dai Wu, Changzhi Li, Chenghua Li, Chao Nan Qian, and Xiaowu Deng. Radioprotective effect of X-ray abdominal FLASH irradiation: Adaptation to oxidative damage and inflammatory response may be benefiting factors. *Medical Physics*, 49(7):4812–4822, 2022.

Appendix A

Appendix

A.1 SFRT irradiations on the SARRP

In follow-up to the initial multi-slit collimator (MSC) prototype derived from the optimization work in Chapter 3, alternative strategies for delivering novel spatially micro-fractionated using 2D micro-beam array (GRID) collimators were investigated and compared against the in-house divergent-slit MSC design (see Figure 3.12).

Two 3D-printed tungsten GRID collimators, of varying size and divergence, were procured to facilitate cross-modality comparison. The smaller, 1.6cm×1.6cm×1.0cm (microGRID) collimator boasted 400 µm square apertures and 287.5-µm thick septa; by comparison, the larger, 5.0cm×5.0cm×1.0cm (miniGRID) Wolfmet® 3D collimator (Wolfmet, Manchester, UK) had 1200-µm wide hexagonal apertures and 300-µm thick septa.

The effectiveness of each collimation scheme was again evaluated using EBT3® Gafchromic films. Key performance metrics, which included the peak and valley dose-rates as well as the PVDR, were evaluated at various depths. Typically, a PVDR >10 is desirable such that valley doses do no exceed 10% of the peak entrance dose.

Four treatment configurations were evaluated, each leveraging the SARRP 220 kVp therapy beam operating at maximum tube current (13 mA, large focal spot). MSC treatments comprised a single-beam irradiation of an anatomically correct 3D-printed mouse phantom (see Chapter 4) and 360°arc treatment of a $5.8 \times 5.8 \times 6\,\text{cm}^3$ phantom (Figure A.1a) with doses scored using films oriented parallel to the incident beam direction. GRID irradiations utilized the same beam parameters as for the MSC treatment, however the collimators were instead placed directly on top of the square phantom, at source-to-collimator distances (SCD) best suited to match their in-built divergence.

The highly divergent ($\text{SCD}_{ideal} = 10.5\,\text{cm}$), microGRID collimator was used along with the SARRP ($10 \times 10\,\text{mm}^2$) treatment nozzle and positioned at the minimum achievable SCD, 30 cm (Figure 11b). By contrast, the less divergent ($\text{SCD}_{ideal} \approx 3\,\text{m}$) miniGRID collimator was irradiated with an open field at the maximum possible SCD, 80 cm (Figure A.1c). For each GRID irradiation, films were placed at various depths (i.e. d=0, 0.3, 0.9, 1.8, 2.7 cm) between the $(5.8 \times 5.8 \times 0.3)\,\text{cm}^3$

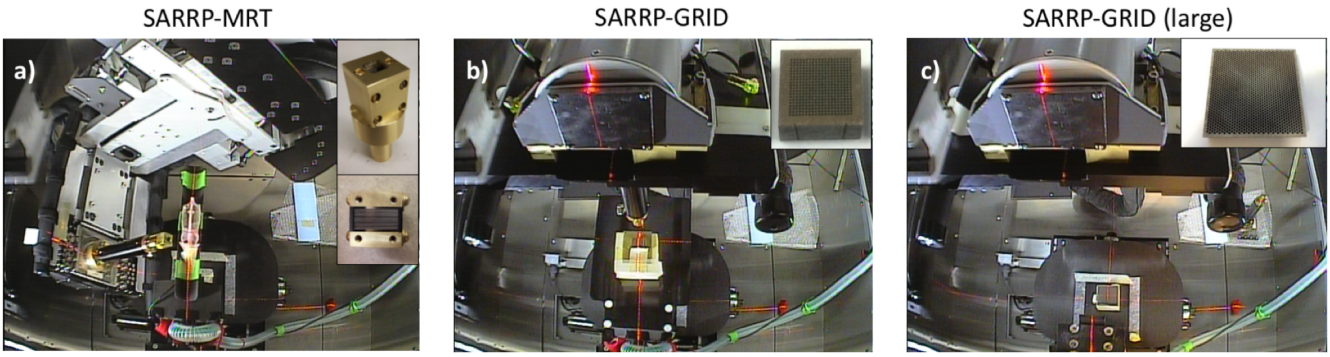

Figure A.1: Experimental setups for MRT (a), short-SSD ($1 \times 1\,\mathrm{cm}^2$) collimated GRID (b), and large-SSD open-field GRID (c) irradiations within the SARRP cabinet. Image insets depict the collimators employed in each case. The MRT collimator prototype was designed and manufactured in-house, while the GRID collimators were 3D printed by third parties. The MRT collimator was designed to replace the stock treatment nozzles within the SARRP tertiary collimator and thus enabled co-planar and arc MRT deliveries in our anatomically correct 3D-printed mouse phantom. By contrast, static (surface) collimation was used for GRID irradiations of a square ($6\,\mathrm{cm}^3$) phantom, comprised of 20x 3-mm thick solid-water slabs. A realistic, heterogeneous 3D-printed mouse phantom was employed for the single-beam and arc-MRT (a) irradiations.

slabs which comprised the square phantom. In all cases, suitable irradiation times were estimated from output and depth-dose data so that doses remained within the film's optimal sensitivity range of 0.2–10 Gy. Film (2D) dose distribution data and derived dose profiles (Figure A.2) help to illustrate the relative effectiveness of each collimation scheme. Depth dose data and derived PVDR values (Figure A.3) suggested that using the microGRID collimator, in conjunction with the $10 \times 10\,\mathrm{mm}^2$ treatment nozzle, offered the most desirable dose distribution characteristics. This is evidenced through the low valley doses and exceptionally high PVDR values achieved (58.9 on surface) while still providing the benefit of comparatively high dose rates afforded by the shorter SSD (Figure A.3g-i). Furthermore, the depth dose data reveal a unique linear PVDR trend, clearly driven by the peak dose behavior, which could potentially improve sparing within superficial structures.

The SARRP-mounted MSC produced a quasi-parallel array of 9×200-µm wide microbeams, as expected, with an approximate field size of $4\,\mathrm{mm} \times 8\,\mathrm{mm}$ (Figure A.2a). This contrasts with the expected $8\,\mathrm{mm} \times 8\,\mathrm{mm}$ array of 16 uniform beamlets which points to a difference between the effected and intended slit divergence of the MSC. Nevertheless, there is significant utility derived from using a gantry-mounted collimator to deliver non-static irradiations. The single-beam MRT irradiation of the mouse phantom (Figure A.3a-c) boasted the second-highest surface PVDR (12.9), albeit with a stronger depth dependence that may have resulted from increased phantom scatter and beam broadening at larger SSD. The arc-MRT delivery, by contrast, (Figure A.3d-f) yielded the lowest PVDR results (4.7 on surface), but featured a unique symmetry as well as transient increase in PVDR about the treatment isocenter.

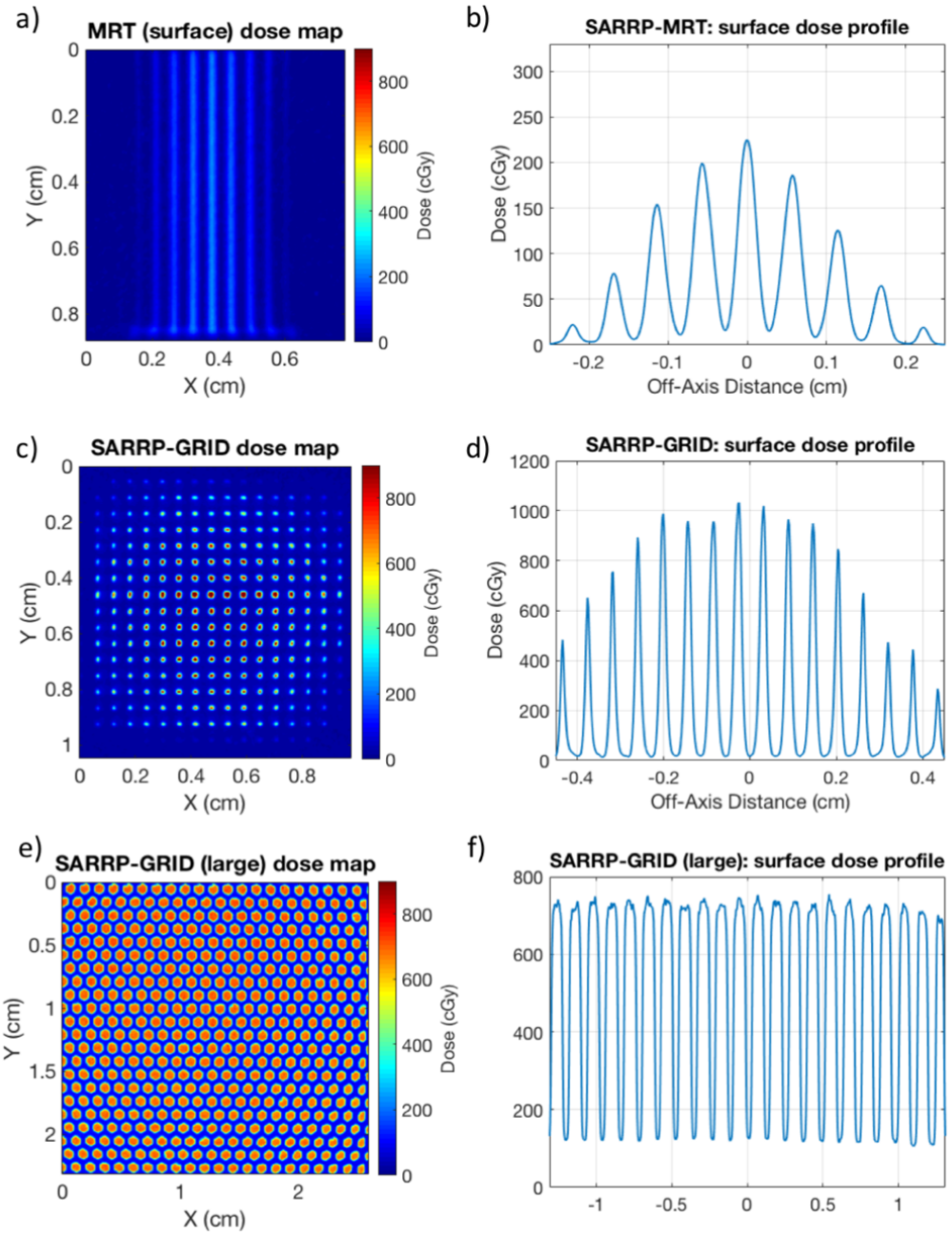

Figure A.2: Surface film dose distributions (a,c,e) and CAX lateral profiles (b,d,f) for each collimator variety. MRT data (a,b) correspond to a stand-alone 1-min irradiation delivered with the SARRP 220 kVp therapy beam. Dose was measured at the surface of the square phantom with an SSD of ∼31 cm so as to be consistent with the setup for the presented GRID treatments (c–f). The source settings remained the same for all irradiations, but the beam-on time for the small- (c,d) and large-field (e,f) GRID irradiations were noticeably longer at 290 s and 660 s, respectively.

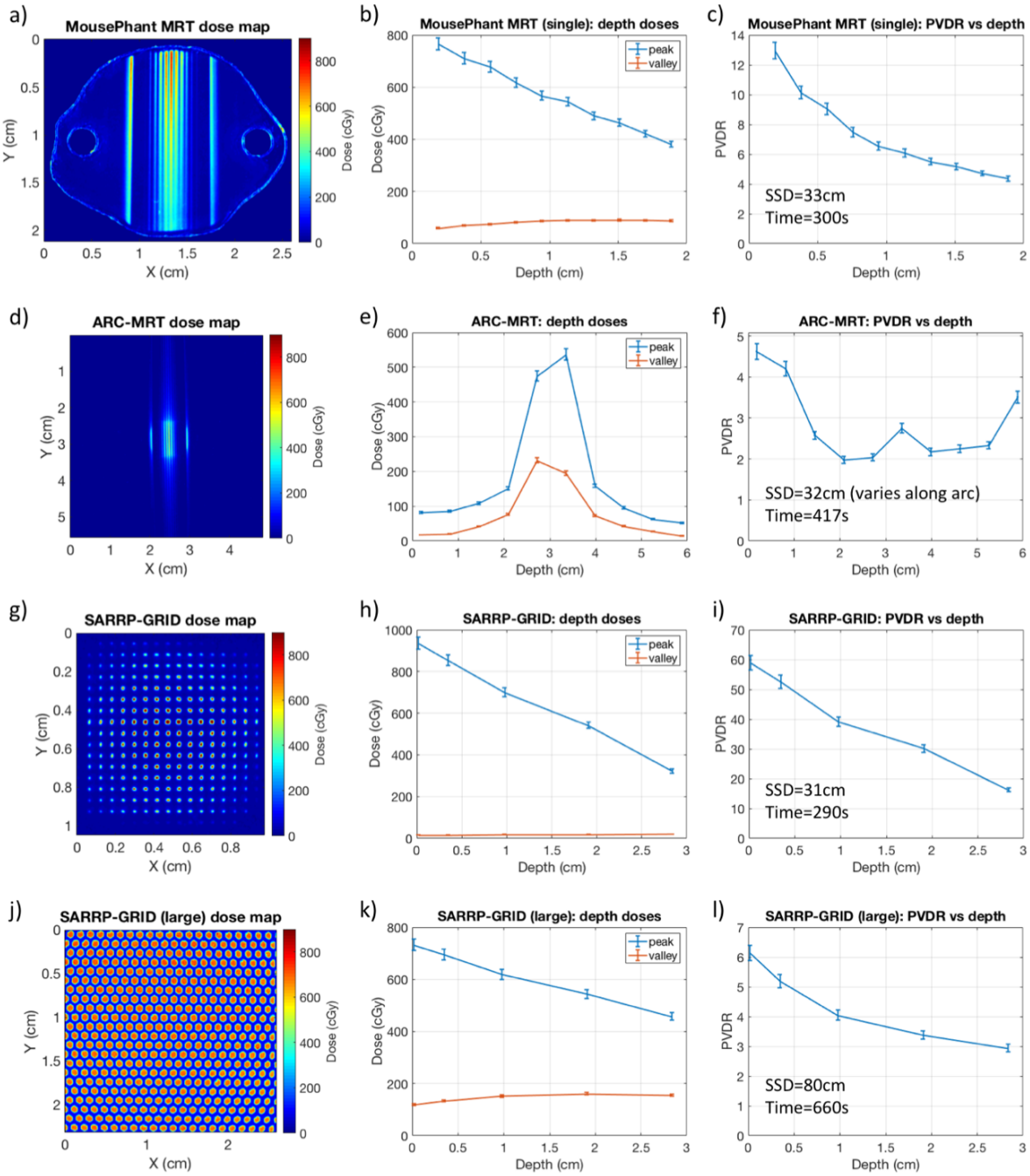

Figure A.3: Dose maps (left column), depth dose (middle column) and PVDR (right column) data for all spatial fractionation schemes utilized on the SARRP. The peak-to-valley dose ratio (PVDR) is calculated as the ratio of the mean peak to valley doses for the central microbeam. Each irradiation leveraged a different experimental setup and treatment time in order to ensure peak and valley doses remained within the film's optimal sensitive range (0.2–10Gy). Valley doses were minimized and PVDR maximized in the case of the small-field GRID setup (g–i), which further boasted the unique behavior of a linear PVDR trend, having been driven by the peak dose decrease. It should be noted that the valley doses are expected to scale almost linearly with peak dose and thus different prescribed doses should not significantly affect the PVDR trends presented here.

Use of the large, low-divergence, miniGRID collimator yielded superior uniformity across the sampled dose region (Figure A.2e,f). On the other hand, the increased ratio of aperture width to septal width and the significant beam divergence at large SSD promoted a sizeable increase in valley dose and consequent reduction in PVDR (6.2 on surface) (Figure A.3j-i).

Based on the results of this comparative collimation study, the best overall SFRT (i.e. PVDR and dose-rate) performance was observed when using the 3D-printed microGRID collimator, though this required a static collimation setup, in contrast with the gantry-mounted MSC which benefits from flexible multi-beam and novel arc-MRT deliveries. As microbeam and GRID therapies have now successfully been implemented on the SARRP system, using various delivery strategies and collimator designs - which are summarized in Table A.1 - it has become apparent that 3D metal printing is a tantalizingly viable option for micro-fractionated collimator design and may prove to be a feasible option for any future work in SFRT. Additive manufacturing, and 3D metal printing in particular, have significantly improved within the last few years and the technology is thus being considered for future design iterations as well as for SFRT collimator design on the ARIEL FLASH-SFRT system.

Table A.1: Summary of SFRT collimator physical and performance metrics of interest.

Collimator	Slit width (µm)	Septal width (µm)	PVDR	$\dot{D}_{iso}$ (cGy/s)
MSC	200	300	12.9	2.27
microGRID	400	287.5	58.9	2.53
miniGRID	1200	300	6.2	5.65

A.2 3D phantom material composition details and Z_{eff} calculation

For the 3D-printed mouse phantom design covered in Chapter 4, Table 4.2 summarized the mass densities and effective atomic numbers (Z_{eff}) for the various simulated materials. Energy-dependent Z_{eff} values were determined using the Auto-Z_{eff} software and the methods of Taylor *et al.* [185] were applied to calculate a spectrum-weighted average $(Z_{eff})_{\text{sw}}$ along with the value at the spectral mean energy ($\approx 80\,\text{keV}$) for the SARRP's 220-kVp beam $(Z_{eff})_{\text{m}}$. A lower-than-expected Z_{eff} value for PMMA, and the consequent similarity to soft tissue and, interestingly, organic fatty acids [250], is observed because the SARRP beam's mean energy ($\bar{E}$) lies near the 'Compton plateau' of the calculated $Z_{eff}(E)$ curve (i.e. where the Z-dependence becomes small).

Figure A.4 showcases the above-stated energy dependence of Z_{eff}, calculated using the Auto-Zeff software [185]. The location of both $(Z_{eff})_m$ (i.e. value at the mean energy) and the spectral-weighted average, $(Z_{eff})_{sw}$, have been identified. With reference to the figure, it is readily apparent that these two values of Z_{eff} lie close to one another, near the bottom of the steepest portion of the curve. As such, it may be inferred that the lower-than-expected Z_{eff} value for PMMA (and soft tissue by the same argument) is, in our case, a product of the large energy dependence of Z_{eff} at low energy (diminishing as Compton interactions predominate) and the energy fluence spectrum of our source. Evidently, with even a slight decrease in beam energy the value of Z_{eff} would ascend the curve and we would quickly reestablish the traditional (power-law derived) trend whereby soft-tissue maintains a higher Z_{eff} relative to PMMA. It should be noted that the methods employed yields different results when compared with the power-law (i.e. Mayneord) formalism [185]. However, the method presented in this work produces results that are in good agreement with other direct calculation methods, such as those utilized by Manohara *et al.* [250, 251] and derivative works.

Results were also compared against another commonly employed polymer and potential tissue-analogue, polyethylene terephthalate (PET - $C_{10}H_8O_4$) [252]. It is interesting to note that the Z_{eff} values for PMMA are remarkably close to the intersection point with the soft-tissue curve. By contrast, the use of PET appears appropriate only within the limited diagnostic ($< 50\,\text{keV}$) energy range; above this range, the Z_{eff} calculated by the power-law method [185] appears similar to PMMA and soft-tissue despite a divergence in tissue-equivalence between these material types. Note, however, that similar Z_{eff} values in this analysis points to the similar attenuation properties, but not necessarily dose deposition within, these phantom materials.

For each MC simulation performed in the study of Chapter 4 (see section 4.8), the chemical composition of the 3D-printed PMMA-like photo-polymer body and bone material (i.e. hydrocarbon) was proprietary and thus not fully known. Nevertheless, the agreement between measurement and MC results served to indicate the suitability of a simplified (mass-density based) material definition.

To further support the methodology and phantom dosimetry, the results of the mouse simulations were compared against those which utilized a more accurate composition (and Z_{eff}) that was derived from MSDS documents (Table A.2). Specifically, two cases were considered for which the two primary

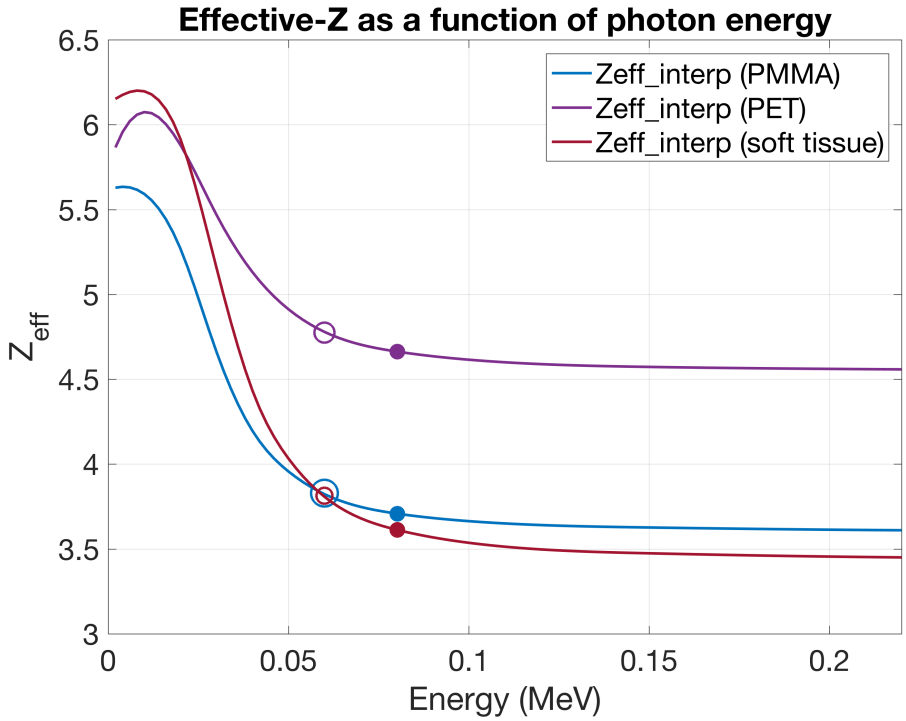

Figure A.4: Effective atomic number (Z) dependence on photon energy. Values are calculated using Auto-Zeff software and spline interpolation is used to determine Z_{eff} at the spectral mean energy (filled circles). The methods of Taylor *et al.* [185] were employed to calculate a spectral-weighted average for Z_{eff} (open circles).

constituents - those boasting the largest relative mass fractions in the overall chemical formulae - were simulated at their maximum and minimum concentrations. This, in turn, provided a means to estimate of the range of dose calculation errors due to simplifying the material definition in TOPAS. At a glance, the data showcase the relative predominance of hydrocarbons, which we assumed *a priori*, and help to explain the relative insensitivity of the MC dose calculation to the precise mass fraction decomposition.

Table A.2: Summary of chemical composition data for 3D-printed, PMMA-like, body material (Veroclear® RGD810) used in the bulk construction of the mouse phantom. Included are CAS registration numbers, the shorthand names, where provided, and % composition by weight. The constrained range corresponds to the minimum and maximum range for % composition derived from the MSDS composition data.

CAS number	**Formula**	**MSDS name**	**% composition limits** [by weight]	**Constrained range (min/max)**
5117-12-04	$C_7H_{11}NO_2$	Acrylic monomer	<30% (15-30%)	15/30%
5888-33-5	$C_{13}H_{20}O_2$	Isobornyl acrylate	<25% (15-30%)	15/25%
62395-94-2	$C_{26}H_{33}ClO_7$	Acrylic oligomer	<15% (10-15%)	10/15%
42594-17-2	$C_{18}H_{24}O_4$	Acrylic monomer	<10% (5-10%)	5/10%
75980-60-8	$C_{22}H_{21}O_2P$	Photo-initiator	<2% (1-5%)	1/2%
52408-84-1	$C_{21}H_{32}O_9$	Acrylic acid ester	<0.3% (0.1-1%)	0.1/0.3%

Using the MIN and MAX composition configurations of the phantom, it was possible to calculate the energy-dependent Z_{eff} using Auto-Zeff. The data are presented in Figure A.5, which additionally highlights the value of Z_{eff} at the mean energy of the SARRP treatment beam (i.e. $\bar{E} \approx 80\,\text{keV}$ - filled circles) and at the spectral-weighted mean value (open circles).

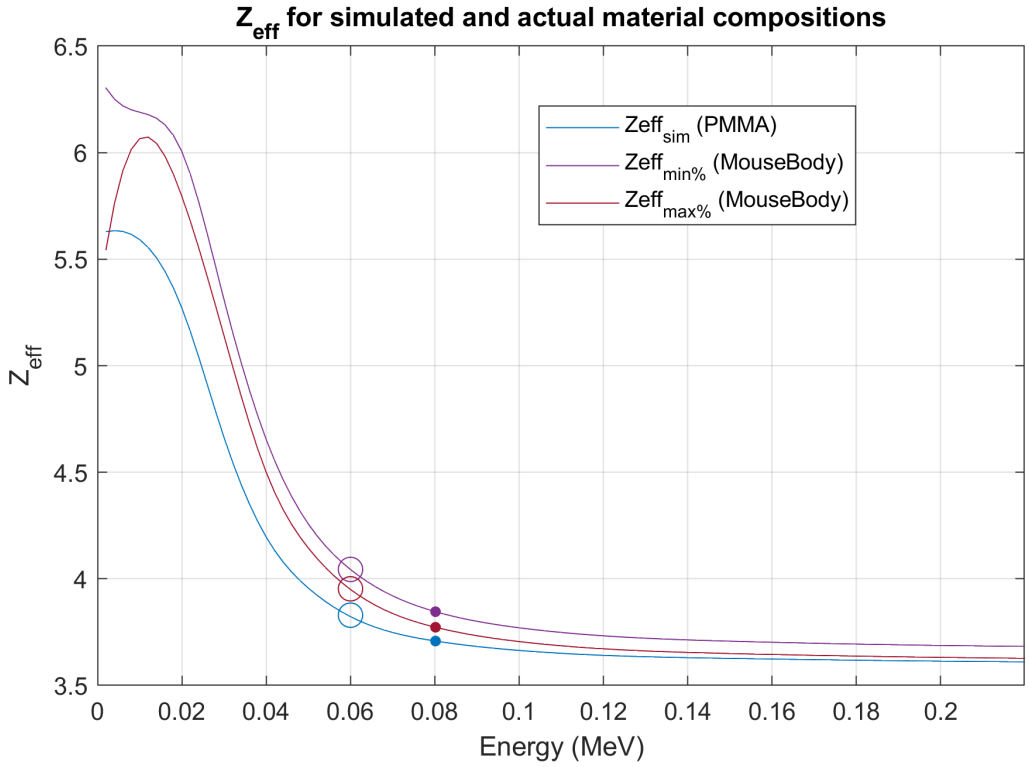

Figure A.5: Calculated Z_{eff} values for the simulated (PMMA) mouse-body material and the actual compositions derived from the Veroclear® MSDS documents. Presented are two variations of the real 'mouse body' material reflecting compositions for which the two primary constituents (see Table A.2) are at their maximum (max% - red line) and minimum concentrations (min% - purple line). Z_{eff} values for each material type are highlighted for the SARRP 220 kVp beam mean energy (filled circles) as are the spectrum-weighted averages (open circles).

From this figure, the spectrum-weighted Z_{eff} value for PMMA is found to be ≈5.3% and 3.1% lower than that of the MIN and MAX 'MouseBody' materials, respectively. The Z_{eff} values at the beam's mean energy are less variable, however, with only a 3.6% and 1.7% difference, respectively, between the MIN and MAX compositions with the PMMA result. Given that the material is likely to have constituent mass fractions, and thus Z_{eff} values, which are intermediate between the extremes presented, it seems reasonable to expect that the dose differences should remain $< 5\%$ as intended for the phantom design.

A.3 ARIEL UHDR target prototype offline tests and modeling

An offline (without beam) test of the prototype converter design for FIRST (Chapters 5.6–6) was conducted in order to test the resistance of the target to thermal shock and thermal cycling under more extreme conditions than are expected during operation. Moreover, it provided a test of model parameter assumptions and their degree of conservatism in the target design simulations (Section 5.6). In an attempt to re-create the power deposition and, more importantly, rapid heating conditions that the target would face during electron bombardment on the ARIEL e-linac, an in-atmosphere test using a tungsten-inert-gas (TIG) welding apparatus was devised (Figure A.6).

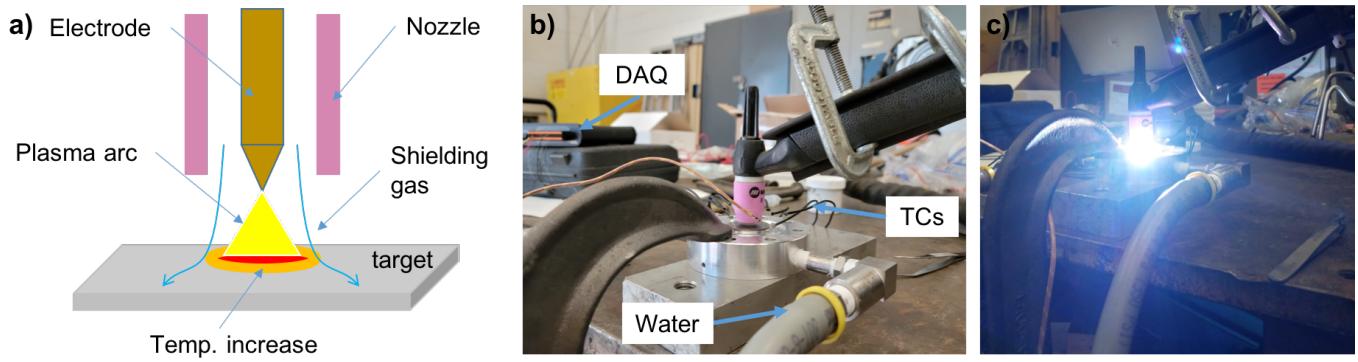

Figure A.6: Schematic illustration of the TIG torch setup (a). Photo of the experimental setup for the water-cooled prototype offline target test (b). Four thermocouples (TCs) were installed around the perimeter to measure temperature evolution for TIG heating times between 1–10 s. Temperature data was measured on the connected data acquisition module (DAQ)

During TIG welding, a plasma arc provides power input while argon (Ar) shielding gas protects the heat affected zone from rapid oxidation in the oxygen-rich environment. To asses the validity of our model assumptions a modest TIG power was first used (200 W) while investigating longer (10 s) heating periods, approaching steady-state conditions. In this way, both transient and steady-state FEA solutions could be compared against measured data. In practice, the temperature was measured using a real-time WebDAQ 316 data logger (Measurement Computing, Norton, MA) and four K-type thermocouples (TC). A digital trigger was used to ensure real-time collection started consistently at a pre-defined temperature threshold. The TCs were placed at four locations around the perimeter of the target and on either side of the Ta-Al (plug) interface. Small $\approx$ 3-mm deep port holes were drilled into either the explosion-bonded plug or the Al flange at approximately the following (r, θ) coordinates for each numbered TC: TC7(Ta)$(1.25, 0)$, TC3(Al)$(1.55, 0)$, TC12(Ta)$(1.25, 90)$, TC10(Al)$(1.55, 90)$. To improve thermal contact, a silver-filled conductive paste (Kurt J. Lesker, Jefferson Hills, PA) was used to fill the hole and provide a conductive bond between each TC and its respective measurement port.

With this setup, it was possible to test the quality of the shrink fit contact and whether our conservative estimate for thermal conductance (see Section 5.7.2) was appropriate. The setup was

therefore modeled in ANSYS using a combination of convective (natural, in-air) boundary conditions appropriate to the region of interest - for brevity the details briefly summarized in section A.3.1 below. The location of the thermocouple probes in the ANSYS mesh model, accurately depicting those of the real setup, are shown in Figure A.7. Temperatures could be sampled at hole depths of $\approx 3\,\text{mm}$ as measured along each path for comparison against the measured TC data.

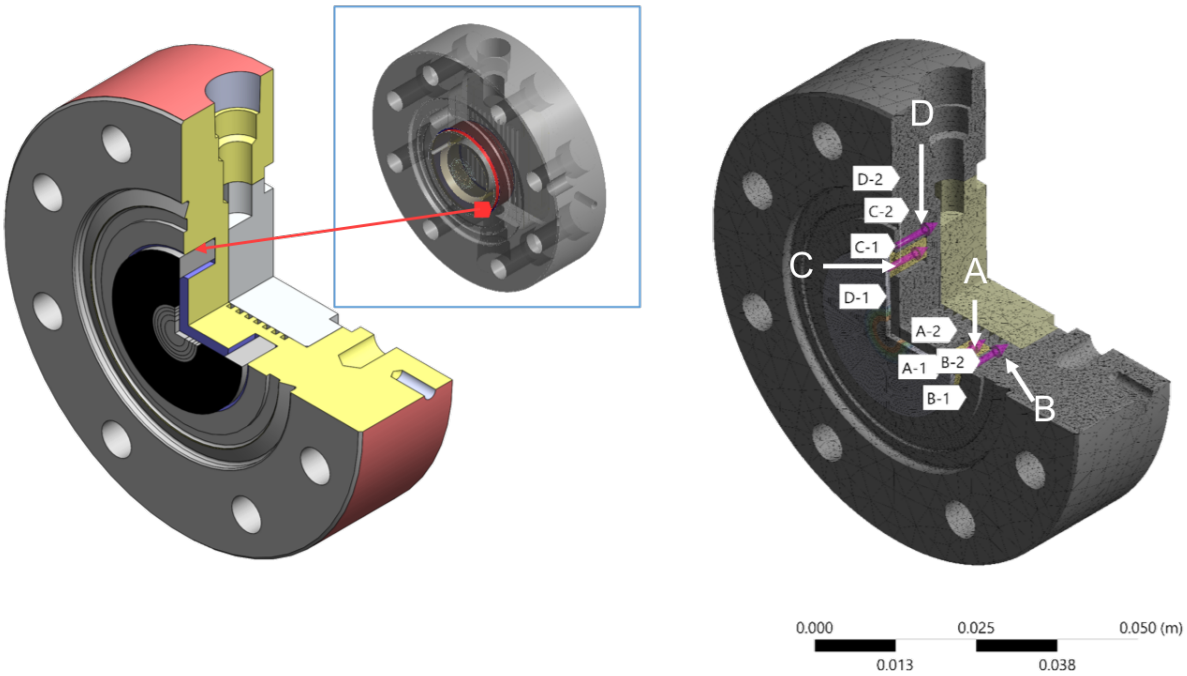

Figure A.7: Cross-section CAD model (left) of the TIG simulation geometry. The various convection domains include the central axis (CAX) Ta target region (grey), the outer target (black), the flange front-face (grey), and the outer cylindrical surface (red). The probe paths corresponding to the TC holes in the test flange are also shown (right) where paths A,B,C, and D correspond to TC#7,3,12, and 10, respectively. The inset shows the shrink-fit thermal contact interface in the FEA model, which was set as either perfect (bonded) or assigned the same thermal conductance ($h_c = 2360\,\text{W}\,\text{m}^{-2}\,^{\circ}\text{C}^{-1}$) that was previously derived for the ARIEL target design (Section 5.7.2.)

A subset of the measured TIG temperature transient data is plotted in Figure A.8a. Overlaid in the figure are steady-state limits, corresponding to the range of depths probed in the ideal (bonded) simulation at the location of the TCs, from the surface to the nominal TC probe depth of 3 mm. While 200 W shots of varying length are included, the averaged heating curves in Figure A.8a,b are derived only from the 10-s long shot data. Transient simulation results, for the ideal and non-ideal thermal contact at the shrink-fit interface, are compared against the averaged experimental data in Figure A.8b; the 3D temperature distributions for these transient simulations, sampled at 10 s, are presented in Figure A.9.

Evidently, the peak Ta temperatures at 10 s ($T_{Ta}(t = 10)$) were not substantially different between the contact scenarios; the temperatures at the probe points, on the other hand, do change dramatically. This observation thus provided a means to assess whether selecting a conservative contact

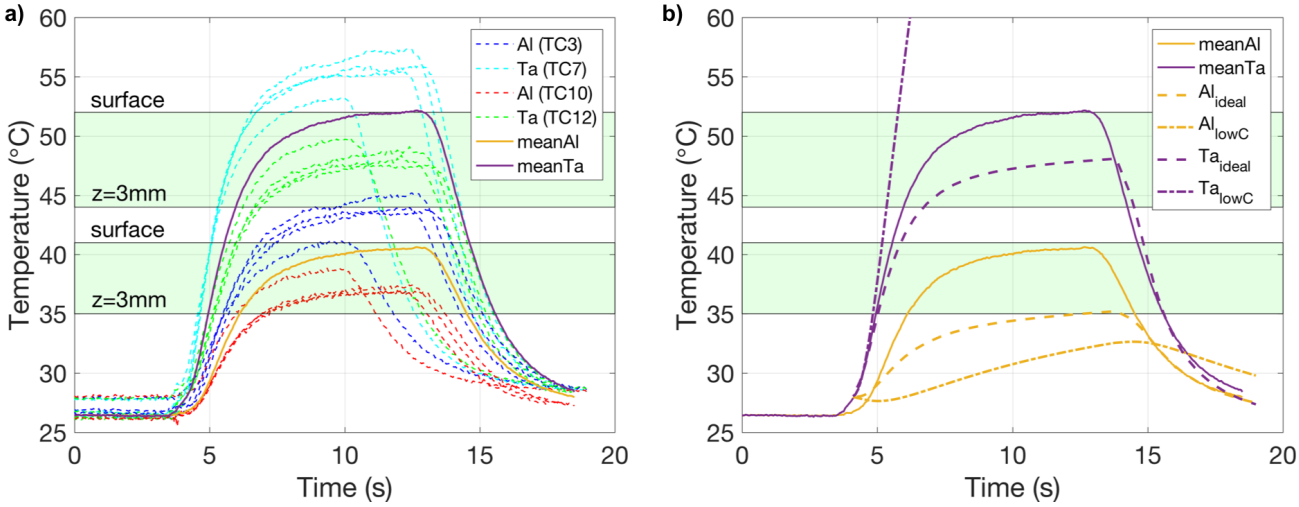

Figure A.8: Summary of 200 W TIG transient temperature data for all TCs (dotted lines), averaged data (solid lines) for the 10 s data set, and simulated steady-state result domain (shaded region) are plotted in a). The simulated transient thermal results for both ideal bonded and non-ideal (low conductance) are presented in b) alongside the mean measured data and steady-state simulation results for comparison.

conductance (h_c) was appropriate to the target design simulations. Specifically, by referring to the data in Figure A.8b, it is apparent that the simulation results for both the Ta and Al probe locations grossly overestimated the actual temperature evolution when a conductance of 2360 $\mathrm{W\,m^{-2}\,^{\circ}C}$ was applied at the shrink fitted (plug-flange) interface. By contrast, the ideal bonded case afforded much better agreement with measurements and would therefore imply that the thermal contact quality of the shrink-fit design is better than expected, likely due to the stringent manufacturing and surface finish tolerances demanded of the design. To further support this assertion, the non-ideal (low conductance) simulation was re-run without the 2× safety-factor for the water-cooling convective heat-transfer coefficient, keeping all other variables constant. In this case, the non-ideal TC probe temperatures were reduced by $< 10\%$ which was insufficient to reconcile the differences with the measured data. Taken together, these observations appeared to support the conclusion that the low h_c scenario affords a highly conservative estimate for heat conduction to the water-cooled flange in the simulations of Chapter 5. Nevertheless, Figure A.9 also demonstrates that the central, peak Ta temperatures were not nearly as affected, possibly due to the target heating being heat-capacity rather than conductivity limited on short time-scales. Since the peak operating temperatures and resulting thermal strains drive the reliability of the target flange and its expected life, the application of conservatively calculated h_c for the shrink-fit interface provided an effective means of introducing yet an additional operational factor of safety.

To test the consequences of an extreme thermal shock scenario, five 1-s long shots at 1 kW power on the TIG torch were delivered. The TCs were unable to adequately measure the temperature spike as they the test resulted in immediate oversaturation, although the target integrity was clearly maintained. Based on ANSYS FEA simulations, the peak temperatures for this test ($> 3000\,^{\circ}$C)

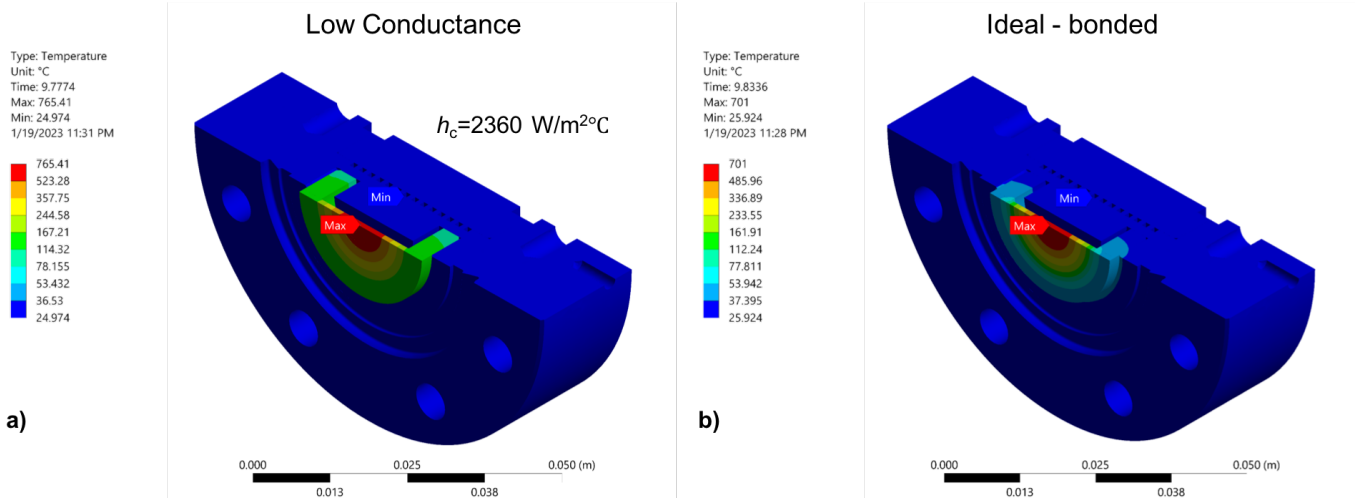

Figure A.9: ANSYS temperature distribution at $t \approx 10\,\mathrm{s}$ for the prototype flange and 200 W TIG heat source, with cooling by natural convection only. The results are provided for both the ideal shrink-fit (bonded contact) and non-ideal contact scenario, in which a thermal conductance of $2360\,\mathrm{W\,m^{-2}\,°C}$ was applied at the plug-flange interface.

may have exceeded briefly the melting point of Ta (3020°C). While the target did not show signs of structural failure and 200–500 W tests continued afterwards, a buildup of oxide layer became noticeable afterwards (see discussion below). Fortunately, while this corrosion failure mode is not expected to occur in the vacuum of the ARIEL beamline, the experiment nonetheless prompted the oxidation study covered in Appendix section A.4.

Based on mechanical simulations (not shown) using the above thermal results as input, the maximum stresses and strains were calculated in ANSYS. In order replicated the peak temperatures and times-scales (i.e. $t < 1\,\mathrm{s}$) used during 1 kW e-beam irradiation in FLASH mode, rather than surface power density, a (500 W) TIG setting was used. Unfortunately, because stresses and strains could not be measured *in situ* for the offline experiment in our setup, instead the fatigue life was to be tested and was first calculated as per the method in 5.7.2. The estimated design life for the 500 W TIG tests, was of the order 700 cycles.

The offline target tests were conducted for over 100 cycles across all power ratings $> 200\,\mathrm{W}$, but had to be terminated early due to substantial surface oxidation and scaling under the heat and argon (Ar) shielding gas flow (at $\approx$ 10–12 $\mathrm{L\,min^{-1}}$ (lpm)). This was determined to be caused by obstructions within the shielding gas nozzle, possible caused by evaporated oxidation products (i.e. oxides) ($T > 1500$°C at the surface), possibly instigated by the 1 kW thermal shock tests. Nevertheless, the experiment demonstrated that the target could remain structurally sound with no macroscopic thermal-strain related defects or structural failures. Most importantly, the tests approximated severe off-normal operating conditions for over 100 thermal cycles, providing peak Ta temperatures larger than what are routinely expected during FLASH-mode (single-pulse) beam delivery, and for longer periods of time (1-10 s).

A.3.1 Convective cooling under TIG heating and low-velocity jet impingement modelling

Convective heat transfer coefficients (h) for the various surfaces of the TIG test flange were calculated using a number of correlations derived from the literature and are briefly summarized in this section and the convection domains were previously highlighted in Figure A.7.

Firstly, the upward-facing (front) face of the target flange was modelled as though it was a horizontal plate [253] free in-air. The Nusselt number (Nu) value in this case may be found using Equation A.1 for Rayleigh numbers (Ra) between 10^4 and 10^7, where $Ra = GrPr$ is a product of the Grashof (Gr) and Prandtl (Pr) numbers:

$$Nu = 0.54Ra^{1/4} = 0.54\left(\frac{c_p}{\mu k}\left(g\beta\rho^3(T - T_{ref}\delta^3\right)\right)^{1/4} \tag{A.1}$$

where g is the acceleration due to gravity ($9.81\,\mathrm{m\,s^{-2}}$), β is the linear expansion coefficient, $T_f = (T - T_{ref})/2$ is the film temperature, T_{ref} is the reference temperature ($20\,^\circ\mathrm{C}$), μ is the dynamic viscosity, δ is a characteristic length, c_p is the specific heat capacity, k the thermal conductivity, and $\rho = \rho(T = T_{ref})(T_{ref} + 273)/(T_f + 273)$, according to the ideal gas law. In the current treatment, the properties are defined for air at standard temperature and pressure (STP).

For the bottom flange surface, an effective conductivity was applied to the interface with the grounding block, based on a very conservative thermal conductance estimate ($h_{cond} = 5\,\mathrm{W\,m^{-2}\,K}$. Radiative heat transfer, based on Stefan-Boltzmann thermal (blackbody) emission, was not explicitly included, but is captured in the input heat flux for the TIG source, discussed below. All thermo-mechaniical properties for Al and Ta were derived from the literature defined in Section 5.7.2.

In contrast to Equation A.1, convection around the outer cylindrical surface of the flange was modelled based on the following correlation (Eq. A.2) for $10^{-5} <= Ra_D <= 10^{12}$ [113, 254, 255]. This produced a lower Nu value as compared with a conservative correlation (Eq. A.3) for vertical cylinders by Fouad and Ibl (1960) [256] which accounted for the sensitivity to inclination [255].

$$Nu = \left(0.60 + \frac{0.387Ra_D^{1/6}}{(1 + (0.559k/c_p\mu)^{9/16})^{8/27}}\right)^2 \quad [254]$$
$$\text{where } Ra_D = \frac{g\beta\rho^2 c_p(T - T_{ref})D^3}{k\mu} \tag{A.2}$$

$$Nu = (0.31GrPr)^{0.28} \quad [255, 256] \tag{A.3}$$

The characteristic length appearing in the above equations, and sub-scripted to Ra, is either the cylinder diameter (D) or, in the case of the horizontal 'plate', the ratio of the surface area to the perimeter (A/P). Furthermore, each of these formulae yield Nu, from which the convective heat

transfer coefficient h can be calculated using the following definition:

$$h = Nuk/\delta \tag{A.4}$$

where δ is the characteristic length scale, which is either the cylinder diameter (D) or, in the case of a horizontal 'plate', the ratio of the surface area to the perimeter (A/P).

The parameters input into the various models described above and the calculated h values are included in Table A.3. The calculated h values corresponding to the regions delineated in Figure A.7 were 5.16 $\mathrm{W\,m^{-2}\,K^{-1}}$ for the flange front face (TIG facing), 5.48 $\mathrm{W\,m^{-2}\,K^{-1}}$ for the rear flange face, and 5.2 $\mathrm{W\,m^{-2}\,K^{-1}}$ for the outer cylindrical face.

Table A.3: Input parameters for natural convective cooling in air for input into horizontal plate and cylinder correlations. From left to right, the data is grouped in terms of flow, geometric, and thermal parameters for stagnant air between the annular flow region of the offline test flange.

Pr	0.6938	D	0.08 m	$T_{i,air}$	28 °C
Ra	varies	$(D - D_{Ta})^b$	0.052 m	k_{air}	0.0261 $\mathrm{W\,m^{-1}\,K}$
T_{ref}	20 °C	P	0.5751 m	β	0.0034 $\mathrm{K^{-1}}$
T_f	35 °C	A^a	0.004227 m^2	c_p	1007 $\mathrm{J\,kg^{-1}}$
ρ	varies[a] $\mathrm{g\,m^{-3}}$			μ	0.0000185 $\mathrm{kg\,m^{-1}\,s^{-1}}$

[a] Depends on temperature under ideal gas law assumption: $\rho = 1.201(T_{ref} + 273)/(T_f + 273)$

[b] Ta target diameter or area is subtracted

For heating and cooling of the Ta surface under the plasma arc and surrounding shielding gas flow, the situation became quite a complicated hydrodynamic and coupled heat transfer problem. Fortunately, investigations of surface heating and the gas flow parameters for TIG welding had previously been studied in depth by Wang *et al.* (2017) [257]. Consequently, the experimental setup was modelled as close as possible to the conditions set by those authors so that the published bell-shaped power (heat input) distribution for the weld surface (i.e. q; units: $\mathrm{W\,m^{-2}}$), which had desirable Gaussian-like symmetry [257, 258], could be applied to the Ta target model in ANSYS. This was accomplished by means of regional heat flux boundary conditions (BCs) using annular segmentation in the center of the target CAD model.

Like [257], the TIG torch in the offline test used a 3.2-mm diameter tungsten rod (electrode) with an Ar flow rate of 20-25 cfh (cubic foot hours), equivalent to $\approx 10 - 12\,lpm$. The nozzle exit diameter in the experiment was $\approx$ 11.1 mm which corresponds to a hydraulic diameter (d), equal to the difference between the nozzle and electrode diameter, of $d \approx 7.9\,mm$. The orifice (or electrode) to heater (target) distance (H) was set to 3 mm. For these conditions, it was assumed that the surface power distribution of [257] for a TIG current of 150 A, which imparted 1131 W (86.3% thermal efficiency) (P_{heat}/P_{TIG}), may be scaled linearly with current to account for different TIG power inputs.

While the model of Wang *et al.* (2017) [257] informed the input and initial conditions, further

assumptions and modifications to target convective cooling were made. Importantly, cooling in the region beyond the heat affected zone of the TIG plasma arc was presumed to be driven by forced convection due to Ar shielding gas impingement. The details of the model are introduced here based on published solutions for heat transfer from the heater region, which in this case is simply the target region heated by the TIG torch. Specifically, a correlation for thermal transfer by a single Argon 'jet' impingement at orthogonal orientation was employed based on Equation 3 of Garimella and Schroeder (2001) [259](note: this did not account for the area that the electrode occupies or interaction with the arc plasma, but this should be implicit to the heat-flux BC derived from the results in [257]).

Since the correlation is only valid for ($1000 <= Re <= 5000$), a key consideration was whether the Ar flow velocity (u) results in laminar ($Re < 1000$) or turbulent flow ($Re > 5000$). The Re (Reynolds number) is proportional to ρ and μ, which depend on the temperature of the Ar gas, and u. The relevant values of u for convective cooling within the target heating region (weld pool) were expected to be on the order of 1-10 m/s [260]; this might be expected from volumetric flow arguments assuming 12 lpm Ar flow through an $d = 7.9$ mm nozzle, whereby $u \approx 4.1\, m/s$. Since Ar is not very conductive, with $Pr \approx 30$, it might be assumed that far-field flow (away from the plasma arc) is not heated. However, the results of [260] indicate that temperature may be substantially higher than ambient, even at radial distances (r) regions outside the diameter (D_e) of the 'heater' region (i.e. $r > D_e$). If an assumption that the density (ρ) remains constant ($\rho \approx 1.6 - 1.7$) and velocity of order 10^{-1} m/s [257,260], then for the dynamic viscosity ($\mu = 2.23 \times 10^{-5}$ Pa s), $Re = \rho u d/\mu > 5000$. By assuming that the flow is sufficiently rapid and turbulent for the single-jet impingement term, Nu was calculated for $H = 3$ mm, $d = 7.9$ mm, $Re = 4000$, and $Pr = 30$. Using the correlation results with Equation A.4, and values for Ar at STP, the calculated value for h was 682 W m^{-2} K^{-1}, although the value may be higher by accounting for how k_{Ar} increases with temperature [261].

To stay conservative and consistent with the plotted data of Garimella *et al.* [259] - referencing the data for $H/d = 0.5$, $Re = 5000$ - an h of 400 W m^{-2} K^{-1} was assumed for Ar (single jet) cooling. For the target region beyond the 'heater' region (i.e. $10\,\text{mm} < r < 28\,\text{mm}$ or $1.26 < r/d < 3.5$), h was instead assigned a more conservative value of 100 W m^{-2} K^{-1}, extrapolated for a setup with $H/d \approx 0.4$ though the authors found negligible sensitivity to H/d this Re value. It should be noted that while the selected model may not provide an exact representation of the TIG flow parameters, for the purposes of this experiment it was sufficient to calculate target heating based on conservative cooling parameters while probing the system's sensitivity to h_c for the interface between the target plug and Al flange (see Figure A.7). As with the simulations of Section 5.7.2, the water-cooling channels provided the dominant convective cooling mechanism, accounting for 86 to 90% of the total heat transfer, based on $h_{H_2O} = 32000$ or 16 000 W m^{-2} K^{-1}, respectively. The corresponding heat transfer through Ta convective surface cooling was 9 and 12% ($\approx$ 1% through natural convection), making forced convection a small but non-negligible contributor to the overall heat balance.

A.4 ARIEL vacuum simulation and UHDR target oxidation model

A.4.1 Oxidation chemistry and physico-kinetics for a tantalum target

In the course of the work presented in Chapter 5.6, a supplementary study on oxidation kinetics was conducted to assess the reliability and potential longevity of the tantalum (Ta) thin-target design under the anticipated ultra-high vacuum (UHV) conditions and high-temperature operation.

In the presence of oxygen, tantalum (Ta) is liable to oxidize resulting in the formation of an oxide scale. The production of the scale corrodes the metallic surface in exchange for a thin passivation layer that can protect the base metal from further oxidation or chemical attack [262]. However, in the context of the thin (1 mm) ARIEL converter target, scale formation can affect the photon-conversion efficiency, as well as thermal and mechanical stability (i.e. strength and fatigue life). In particular, for the high-temperature operation under vacuum there is a question of whether the oxidation reaction proceeds, based on thermodynamic arguments, and if so, how much oxide scale growth occurs become pertinent questions.

Due to the UHV pressures ($\approx 10^{-9}$ mbar) within the beamline, oxidation without beam at ambient room temperature (i.e. $T_{Ta} \approx 300\,\mathrm{K}$) is not expected to proceed at a perceptible rate ($< 1\,\mathrm{nm/yr}$) based on steady-state calculations, further explained below. Under high-temperature operating conditions, however, such as during cyclic e-beam irradiation (and thus rapid heating), metal-gas interfaces may experience oxide scale growth despite the low oxygen concentrations under UHV [263]. This can result from higher oxidation rates governed by the increased oxygen diffusivity within the Ta (and formed oxide). On the other hand, at higher temperature the equilibrium partial pressure for spontaneous oxidation and stable scale formation at the metal interface also increases. Thus, a first step was to estimate what the O_2 partial pressure for spontaneous oxidation at high-T would be and if it poses a risk considering the UHV conditions within the ARIEL beamline.

At high temperature, the stable oxide is Ta_2O_5 [264, 265] and the basic formation equation based on a pure Ta target substrate exposed to gaseous oxygen is:

$$2\,\mathrm{Ta} + \frac{5}{2}\,\mathrm{O_2} \longrightarrow \mathrm{Ta_2O_5} \tag{A.5}$$

$$\frac{4}{5}\,\mathrm{Ta} + \mathrm{O_2} \longrightarrow \frac{2}{5}\,\mathrm{Ta_2O_5} \tag{A.6}$$

The Gibbs free energy of (oxide) formation ΔG^o determines whether a reaction may proceed and is dependant upon the gas (O_2) partial pressure in the environment [266]. The thermodynamics of oxide reactions which dictate the form of ΔG^o as a function of pressure and temperature are described by Ellingham diagrams [266, 267]. The mathmatical form of these diagrams is a straight line equation with the following form [266]:

$$\Delta G^o = \Delta H^o - T\Delta S^o = -RTln(K) \tag{A.7}$$

where ΔH^o and ΔS^o are the standard enthalpy and entropy changes at temperature (T), R is the gas constant ($8.314\,\mathrm{J\,K^{-1}\,mol}$), and K is the reaction equilibrium constant. Note that K for a metal-oxide reaction is the ratio of the concentration to the power of the stoichiometric coefficient (see A.6), which for tantalum pentoxide (Ta_2O_5) is:

$$K = \left(\frac{[Ta_2O_5]^{2/5}}{[Ta]^{4/5}[O_2]} \right) = \frac{1}{[O_2]} = 1/P_{O_2}$$

$$\text{with A.7: } P_{O_2} = \exp\left(\frac{\Delta G^o}{8.314\,T} \right)$$

where [X] is the activity of species X (equal to 1 by definition for pure solids or liquids) and P_o is the partial pressure of O_2 required for spontaneous oxidation of Ta. By the ideal gas law, $[O_2]$ (molar concentration) can be set equal to P_{O_2}/P_o where P_o = 1atm (since n_{STP}=1 mol) and gives the resulting $[O_2] = P_{O_2}$, consistent with the activity in the above equation.

The form of the Ta_2O_5 Ellingham line equation was derived from the data in [267], taken (arbitrarily) for 273 and 1273 K. The resulting line equation is $\Delta G^o = -191.3 + (0.034)T$ and is plotted in A.10.

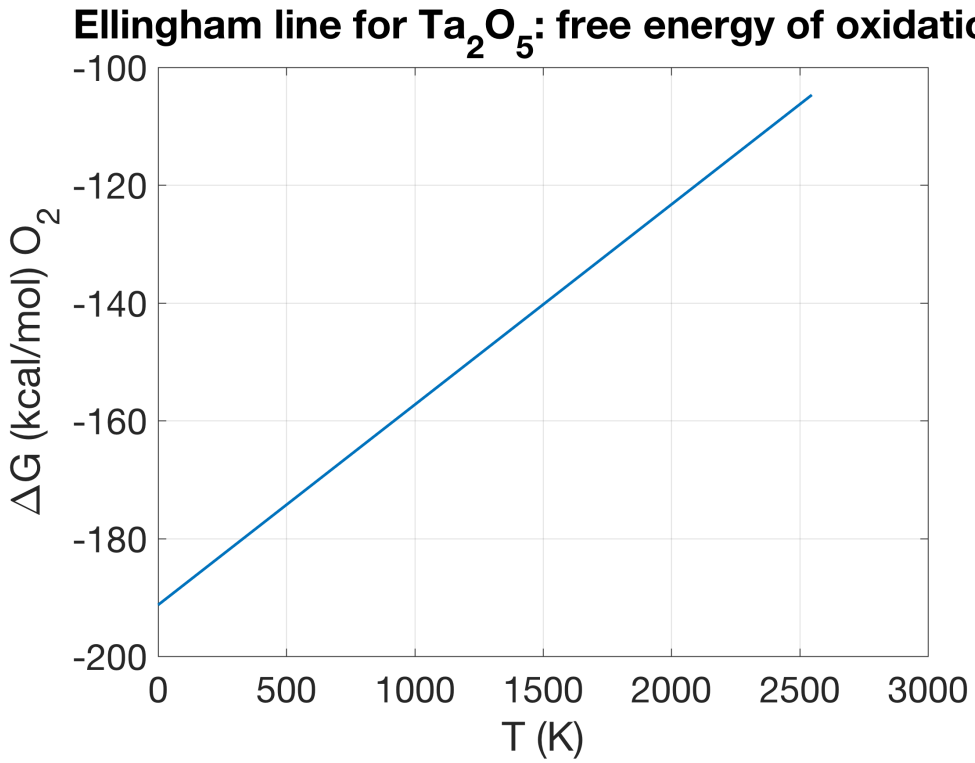

Figure A.10: Ellingham line based on a linear fit to data derived from [267].

The corresponding oxidation threshold partial pressures ($P_{O_2,thresh}$) were plotted as a function of temperature (T) in Figure A.11a.

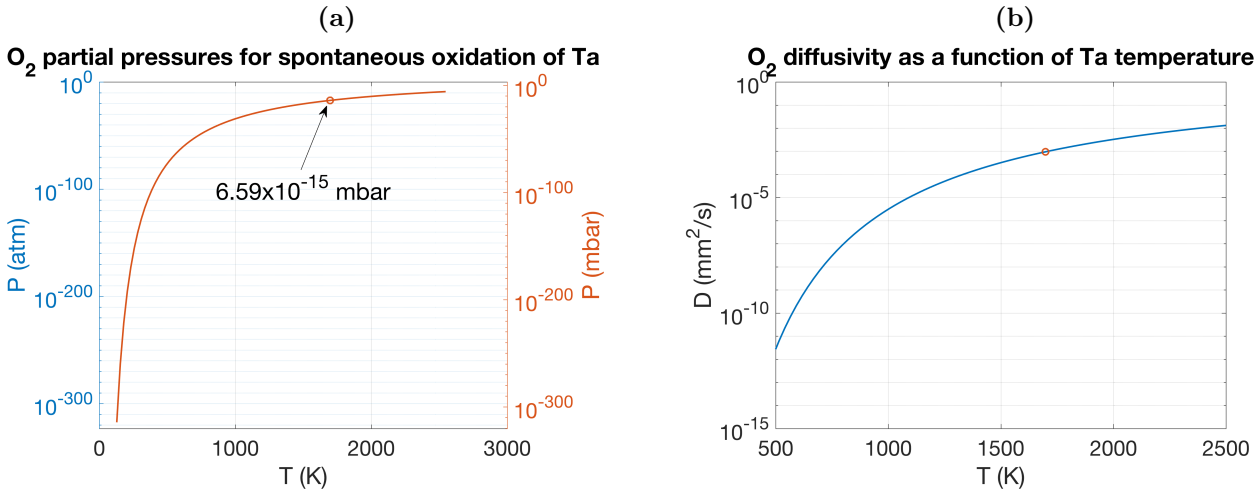

Figure A.11: Threshold O_2 partial pressure as a function of temperature (a). The value for the highest temperature expected for 10 MV FLASH irradiation based on FEA simulation results (Figure 5.16) is shown. The O_2 diffusivity (D), which drives oxide growth, is plotted as a function of temperature (b).

Based on this data, the oxidation reaction may proceed considering $P_{O_2} \simeq 2.07 \times 10^{-13}$atm $\geq P_{O_2,thresh}$ at the higher transient temperatures encountered during FLASH-mode irradiation (Section 5.6). In this case the assumption is made that the relative abundance for oxygen is maintained in the UHDR beamline (i.e. $P_{O2} = 0.21 P_{vac}$). However, the oxidation rate strongly depends upon the diffusion coefficient (D; mm s^{-1}) which is itself a function of temperature and follows an Arrhenius-type relationship of the following form [266]:

$$D = D_o \exp\left(-\frac{Q}{RT}\right) \tag{A.8}$$

where Q is the activation energy (in eV) and D_o is a pre-exponential factor. For the oxide model used herein, D_o was derived from the data of [265], where $D = 5.2 \times 10^{-14}$ m^2 s^{-1} at T=773 K, based on rapid-heating Ta nanoparticle experiments, which included crystalline state oxide (γ-Ta_2O_5) formation, as opposed to the data for amorphous oxides (a-Ta_2O_5) from [268]. Together with Eq. A.8, this yielded $D_o = 3.46$ mm^2 s^{-1}. Interestingly, the observation of a lower D_o value for γ-Ta_2O_5 as compared to a-Ta_2O_5 is consistent with what has been observed in alumina [268]. Note that use of a higher D_o affords a much larger diffusivity and thus oxide formation rate. The value for Q was taken to be 1.2 eV from [268] and was consistent with an upper-end estimate based on the data of [269] for Ta, which reported Q=1.15–1.19 eV. Given the short time-scales for heating, O_2 is assumed to be the diffusing species (i.e. toward the Ta-Ta_2O_5 interface) for which the solubility in Ta is sufficiently high for all T [264]. The form of $D(t)$ is shown in Figure A.11b.

Assuming diffusion-limited kinetics for our time-scale of interest, solutions for the oxide scale thickness (x) with time (t) follow from Fick's first and second laws of diffusion [270]. From [266], the molar flux (J; mol cm^{-1} s) can be defined in two ways:

$$J = -D\frac{dC}{dx} = -C\frac{dx}{dt} \tag{A.9}$$

where C is the (molar) concentration of the diffusing O_2 and assumed to be time-independent. Additionally, the sample is presumed to be initially degassed with no initial oxide layer. Upon solving for dx/dt and integrating, the solution becomes $x = \sqrt{Kt}$, where K is a rate constant which can be approximated as $2D$. Therefore, the final parabolic form for oxide thickness growth is [266]:

$$x(t) = \sqrt{2Dt} \tag{A.10}$$

$$x(t) = \sqrt{2\int_0^t D(t)\,dt\,t} \tag{A.11}$$

In contrast with the form of known solutions to Fick's second law, the simplified parabolic model of Eq. A.10 is consistent with high-T oxidation of Ta on short time-scales (order of ms), for which there is an expected change from linear (kinetically limited) to parabolic (diffusion-limited) behavior. This is seen, for example, in small high-heating rate, high-T oxidation in Ta nanoparticles with a Deal-Grove model demonstrated by DeLisio *et al.* (2017) [265]. The simple relation of Eq. A.10 is appropriate for steady-state oxide growth assuming spatially-constant diffusivity (i.e. $dD/dt = dD/dx = 0$). However, because D depends strongly upon temperature, the equation is modified (Eq A.11) to allow for a time-dependent diffusivity $D((T(t))$ as for the case of a temperature transient $T(t)$ that exists during irradiation. A plot of $x(t)$ using the time-dependent $D(t)$ and solving Eq. A.11 by numerical integration is included in Figure A.12. The time-dependence of $D(t)$ from Eq. A.8 was derived from the temperature transient of the 10 MeV, 1 mA electron beam with $2\sigma = 5$ mm (Figure 5.16).

While C is assumed to be constant, in reality the dC/dx (i.e. concentration gradient) within the target's thin-slab geometry is expected to change with time as the oxide layer (and diffusion length) grows substantially in relation to the total Ta target thickness. The time-dependence in C (and thus $dC(t)/dx$) is addressed by solving Fick's second law directly [270]. For example, assuming that the ambient source of oxygen has a constant P_{O_2}, such that $C(x = 0, t) = C_{O_2} = const.$, and that the target represents a semi-infinite slab, the solution takes the following form:

$$C(x,t) = C_{O_2}\,\mathrm{erfc}\left(\frac{x}{2\sqrt{D(t)t}}\right) \approx C_o\left[1 - 2\left(\frac{x}{2\sqrt{\int_0^t D(t)\,dt}}\right)\right] \tag{A.12}$$

where the second equation is the Taylor series expansion of $\mathrm{erfc}(x) = 1 - \mathrm{erf}(x)$, and $\mathrm{erf}(x)$ is the error function. Rearranging Eq. A.9, as before, and substituting the derivative d/dx of $C(x,t)$ from Eq. A.12 then yields:

$$\frac{dx}{dt} = -D_o\frac{\exp\left(-\frac{Q}{k_bT(t)}\right)}{2\sqrt{\int_0^t D(t)\,dt} - x} \tag{A.13}$$

where k_b is the Boltzmann constant ($8.617 \times 10^{-5}\,\mathrm{eV\,K^{-1}}$). By separating the variables, integrating,

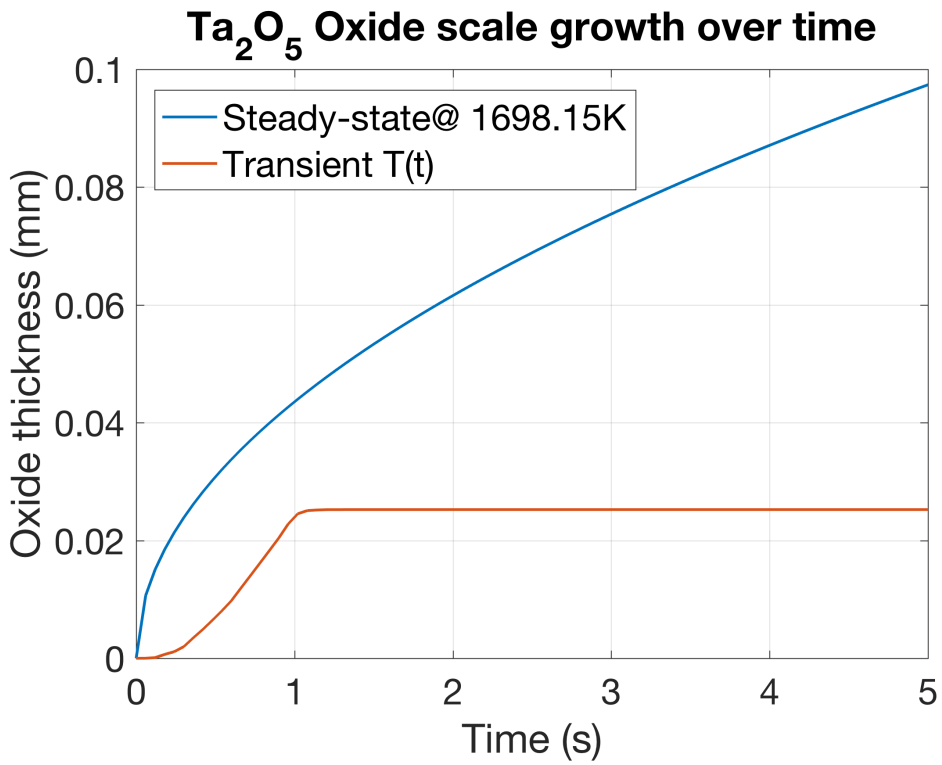

Figure A.12: Oxide growth functions for two models as a function of time for transient high-temperature heat load imparted by electron beam heating of the tantalum target. $T(t)$ data are from Figure 5.16 for a 10 MeV,1 mA ($2\sigma = 5$ mm) beam in FLASH mode. Also included is the steady-state growth assuming long term operation at the peak temperature for the same beam under CW CONV irradiation.

and solving for x, we arrive back at the familiar form with a different constant , or more precisely $x = (1+\sqrt{3})\sqrt{\int_0^t D(t)\,dt}$.

This latter solution supports the time-dependent parabolic model albeit with a different constant (see Eq. A.11). A a more accurate model considering the finite thickness of the target Ta and non-zero initial O_2 dissolution would involve substituting solutions for $C(x,t)$ based on a so-called thin-slab geometry. However, such a model would necessarily be complicated by the difference in pressure between the beamline and vacuum pocket (see Section A.4.2) while providing a more conservative estimate of scale growth. Consequently, the inclusion of the thin-slab solution is omitted here and the semi-infinite slab model was adopted as a worse-case scenario for risk assessment.

Substantial accumulation of the tantalum oxide film would not only degrade the superficial conversion layer, but also poses a minor risk of oxide delamination or erosion (i.e. from flaking or evaporation), re-crystallization potentially leading to crack formation and increased oxidation, or surface melting. For example, the vapor pressure of Ta_2O_5 at the peak calculated operating temperature (1425°C) approaches the UHV vacuum pressure, of the order 10×10^{-9} mbar. Fortunately, these risks are mitigated largely through beam-power, and thus temperature, limits for the target ($\max(T_{Ta}) = 1425$°C; Ch.5.6). Furthermore, the above calculations demonstrate that the expected

scale thickness (diffusion length), under conservative assumptions for a full 1 s irradiation at 10 MeV, should remain $< 3\%$ of the total thickness and only in localized regions which experience the greatest heating rate (and electron current density). Ideally, the new oxide layer would passivate the metal, but because of re-heating through subsequent irradiations, the low crystallization temperature ($\approx$ 500–700 °C [265, 268]) and the melting temperature (1872°C [268]) being near to the peak operating temperature presents a few unknowns. Notably, the melting point could be exceeded during off-normal operation, such as if an electron peak-current spike were to occur; on one hand, localized melting could help to seal microscopic cracks formed in the oxide layer, but cyclic re-crystallization could then result in new crack formation and oxide growth [265].

In general, the protectiveness of the oxide scale can be characterized by the Pilling-Bedworth (PB) ratio, defined as the ratio of of volume of the formed oxide (V_o) and metal substrate (V_m):

$$\mathrm{PB} = \frac{V_o}{V_m} = \left[\frac{[zA_w/\rho]_o}{[zA_w/\rho]_m}\right] \tag{A.14}$$

where ρ is the mass density ($\rho_{Ta} = 16.65\,\mathrm{g\,cm^{-3}}$;$\rho_{\mathrm{Ta_2O_5}} = 8.2\,\mathrm{g\,cm^{-3}}$), A is the atomic or molecular weight ($A_{Ta} = 180.95\,\mathrm{g\,mol^{-1}}$;$A_{\mathrm{Ta_2O_5}} = 441.9\,\mathrm{g\,mol^{-1}}$) and z_i are the coefficients in the balanced oxidation equation (A.6). If $\mathrm{PB} \in [1, 2]$ then the oxide scale is considered protective, adherent and stable. Moreover, for $\mathrm{PB} > 1$ the oxide is presumed to cover the metal surface and thus restrict oxidation since only solid-state diffusion of reactants through the oxide layer itself should be possible [267]. For Ta_2O_5, $\mathrm{PB} = 2.48$ and the oxide is considered theoretically non-protective, although there are numerous exceptions to the PB ratio; for example, the Ta scales are considered stable at STP affording Ta its characteristically low reactivity [262]. A high PB ratio nevertheless appears consistent with the extant potential for crack formation or scaling of the Ta_2O_5 layer under large compression stresses [262, 267], as has been observed, for example, in crystallized Ta_2O_5 under high heating rates [265], alike to those expected from e-beam heating of the target. Limiting total beam-on time for 1 kW operation therefore becomes the best mitigation against risk of oxidative erosion at the target surface.

A.4.2 Vacuum simulations of the UHV beamline and pocket pressure calculation

In this brief section, a summary of the beamline vacuum simulation is provided with application to the relative oxidation risk at the two interfaces of the thin-window target design for the Ta target converter discussed in the preceding section.

Molflow+ (see Section 2.4.1.1) was used to simulate the outgassing and equilibrium gas pressure within the EMBD beamline section of the ARIEL e-lianc that contains the new target converter and nearby ion guage (see Figure A.13a). The model was simplified by using basic geometries made available within the MC software, based on beamline dimensions (i.e. lengths, diameters) reproduced from the beamline CAD model. A vacuum pumping speed of $200\,\mathrm{L\,s^{-1}}$ at the location of the ion pump

was included while all other surfaces (facets) were assigned outgassing rates based on data taken from the literature. In particular, for steel (SS304), aluminum (6061-T6) and ceramic (alumina) surfaces, these rates were set to 1.31×10^{-11}, 3.32×10^{-8} and 1.33×10^{-8} mbar L s^{-1} cm^{-2} [271]. Due to the temperature sensitivity of the outgassing (q) rates in material, governed by changes in oxygen diffusivity and solubility, a Ta target temperature of 773 K (500 °C), assuming steady-state operation, was used and the corresponding value of q was based on data from [272]. Specifically, under the assumption that substantial target heating time was accumulated over many thermal cycles, such as during beam commissioning, a lower-end estimate for q based on the 1850°C curve was selected where $q \approx 5 \times 10^{-4}$ Pa m^3 s^{-1} m^{-2}.

In all, a total of 1×10^9 hits were recorded and the pressure results were scored at various locations of interest and along the central axis of all modeled pipe sections (Figure A.13b).

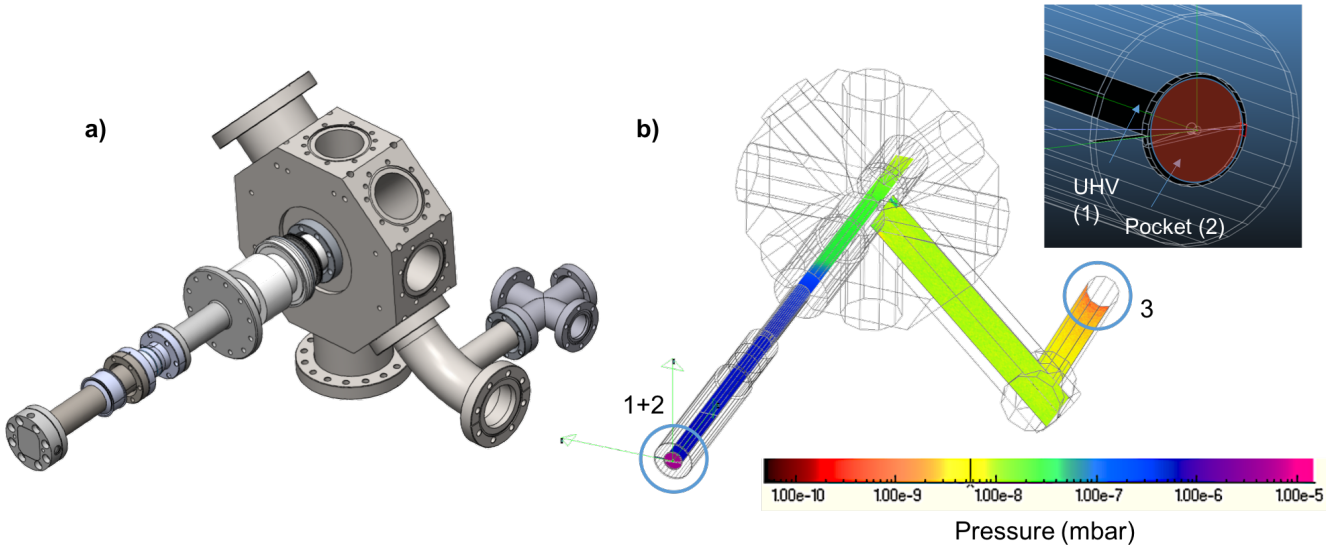

Figure A.13: CAD model for a section of the ARIEL beamline (a) and pressure data are plotted along the beamline central axis and in the upstream diagnostic box (b). Pressures were recorded at the target for both the UHV-facing Ta surface (1) and inside the vacuum pocket (2, see inset), as well as at the location of the iong guage (3)

The facets of interest corresponded to the ion gauge, and at the target, as labeled in the previous figure. The corresponding pressure values and are summarized in Table A.4.

Table A.4: Simulation results for absolute pressure due to outgassing at selected locations in the EMBD section of the UHV ARIEL beamline.

Location	Pressure (mbar)
Ta pocket (1)	6.9×10^{-6}
UHV Ta (2)	4.3×10^{-7}
ion guage (3)	1.3×10^{-9}

At the location of the target, the pressure at the surface on the UHV (beamline-facing) and

vacuum-pocket (flange-facing) interfaces was of particular interest. Due to the small size of the port connecting these two cavities, there is a very low conductance, and therefore rate of gas flow, between the pocket and beamline proper. This resulted in a persistent pressure differential across the target which amounted to a time-averaged pressure ratio of ≈ 16. This bares relevance to the potential for increased oxygen partial pressure, namely on the pocket-side, which might induce or accelerate high-temperature oxidation risk.

While the exact pressure in the beamline was of lesser importance for this investigation, it is interesting to note that the steady-state (constant flow) pressure at the location of the ion (vacuum) gauge of the diagnostic box (label 3 in Figure A.13), was $\approx 2 \times 10^{-9}$ mbar, which is within a factor of 4 of the measured value.

A.5 ARIEL electron collimator design and trip thresholds

The purpose of the electron collimator (COL), which was installed and electrically isolated upstream of the target (Figure A.14), was to ensure that no accidental beam misalignment, or kick, would allow for direct beam impingement on sensitive components that might impose risk to the beamline integrity. This was accomplished by constraining the steel beam-pipe aperture of the COL such that the delivered electron beam was unable to intercept any region of the target (or other beamline components) which were not actively water-cooled (collimator excluded). This amounted to a simple geometric projection of the worst-case off-center beam scenario ($\approx \pm 5mm$)[1]. Based on this maximal allowed beam misalignment (i.e. at the location of the last steerer before the target), the maximum allowable COL inner diameter (ID) was 2 cm. This ID ensured that the edge of a beam with RMS (σ) width of 2.5 mm (i.e. $2\sigma = 5\,mm$ as usual) strikes only the water-cooled Ta target or Al flange, and not the adjacent steel beam pipe immediately upstream.

Upon intercepting the beam and registering a current greater than a pre-determined threshold, the beam would be tripped to prevent any potential damage to the downstream components, or the collimator itself should the beam be left on the collimator too long. Due to space restrictions for the collimator section (through existing concentric lead shielding) and the need for a rapid feedback system, natural convection cooling was deemed sufficient for this application since very little power would be integrated on the COL, and thus a low amount of total energy/heat absorbed to go into heating the material (SS 304). A future design would nevertheless benefit from a water-cooled design to afford an increased trip threshold, and therefore less sensitive beam centering requirements during beam setup and parameter tuning, which is currently laborious to ensure highly centered beam owing to the presence of a substantial beam halo.

An overarching requirement was that temperature of the COL remains low enough temperatures to avoid plastic deformation in the steel, which might otherwise compromise the vacuum seal or

[1] Based on operator experience and machine protection system limits

promote increased creep and fatigue failure risks in the long term. To a first-order approximation, this was assessed by asserting that $< 0.2\%$ expansion would be allowed based on the linear expansion coefficient for 304 stainless steel (SS) [273]. The corresponding temperature (T) was $T \approx 150\,^{\circ}\mathrm{C}$ and the corresponding heat deposition required to elicit this was estimated to be 5 W - which ultimately defined the peak current trip limit of 500 nA (or 50 nC integrated over 100 ms).

To assess the thermal and mechanical effects of 5 W of beam power on COL, FEA simulations were run in ANSYS (Section 2.4.2) where all the incident power is converted to heat rather than conversion or re-radiation to include an implicit safety factor in the design strategy. An exploratory parametric study (not shown) indicated that a worse-case scenario for beam interception involved the power being deposited at the end (downstream) flange, likely to occur only in the case of severe misalignment at the beam steerer with incorrect magnet settings (see Figure A.14a). Alternative scenarios included striking the edge of the collimator aperture entrance and at various positions along the length of the collimator bore. The 5 W was applied uniformly to a $5 \times 5\mathrm{mm}^2$ region at the edge of the bore interior to approximate interaction of the comparatively flat electron distribution within the beam (Gaussian) tail (i.e. $>> 2\sigma$) or broader halo region.

The collimator is a steel tube enclosed within a plastic sheath (i.e. concentric cylinders) that is open to the ambient environment of FIRST. Since the collimator is not actively (water) cooled, cooling of the outer cylindrical surfaces for the end flanges (Figure A.14b) occurs only by natural convection, which was modeled using the same theory briefly outlined in A.3 for the offline target heating tests (Equation A.2 [113, 254]). However, for an annular region between the collimator and the surrounding sheath (see Figure A.14b), the correlations (Equations 23a,b,25,26) of Kuehn and Goldstein (1976) [274] are considered. As for other boundary layer models, the Nusselt number (Nu) has been correlated with thermophysical and geometric properties, which are then used to calculate an effective h using the equation $Nu = hD_i/k_{eff}$. For brevity, the detailed calculations are not described here and instead the heat transfer coefficient as a function of temperature ($h(t)$) for the model is presented in Figure A.15.

The calculated values of h are in good agreement with estimates using an effective conductivity (k_{eff}) defined in the relations (Equation 35) of Raithby and Hollands (1975) [275], which is applicable where $Ra > 100$, as in the present case (for $Ra < 100$, $k \rightarrow k_{eff}$). The expression of an inner cylinder Nusselt number (Nu_i), and thus h, can then be used such as in $k_{eff}/k = \bar{Nu}_i \ln(D_o/D_i)/2$, as defined in [276]. As compared to the temperature-averaged result from Figure A.15 ($\approx 5\,\mathrm{W\,m^{-2}\,K}$, the results derived from k_{eff} based on the method of [275], was $4.9\,\mathrm{W\,m^{-2}\,K}$. The input parameters necessary for both correlations are provided in Table A.5.

To reasonably apply the calculated h to the simulation, an implicit assumption of laminar, moderate Rayleigh (Ra) number ($10^2 < Ra < 10^7$) ambient air flow (i.e. $T_o = 20\,^{\circ}\mathrm{C}$, $P = 1\,\mathrm{bar}$, Prandtl (Pr) number ($Pr \approx 0.7$)), and where the air is assumed stagnant (only true at short times). It is important to note that, initially, as steel T is low, the Rayleigh number will be low, and so the

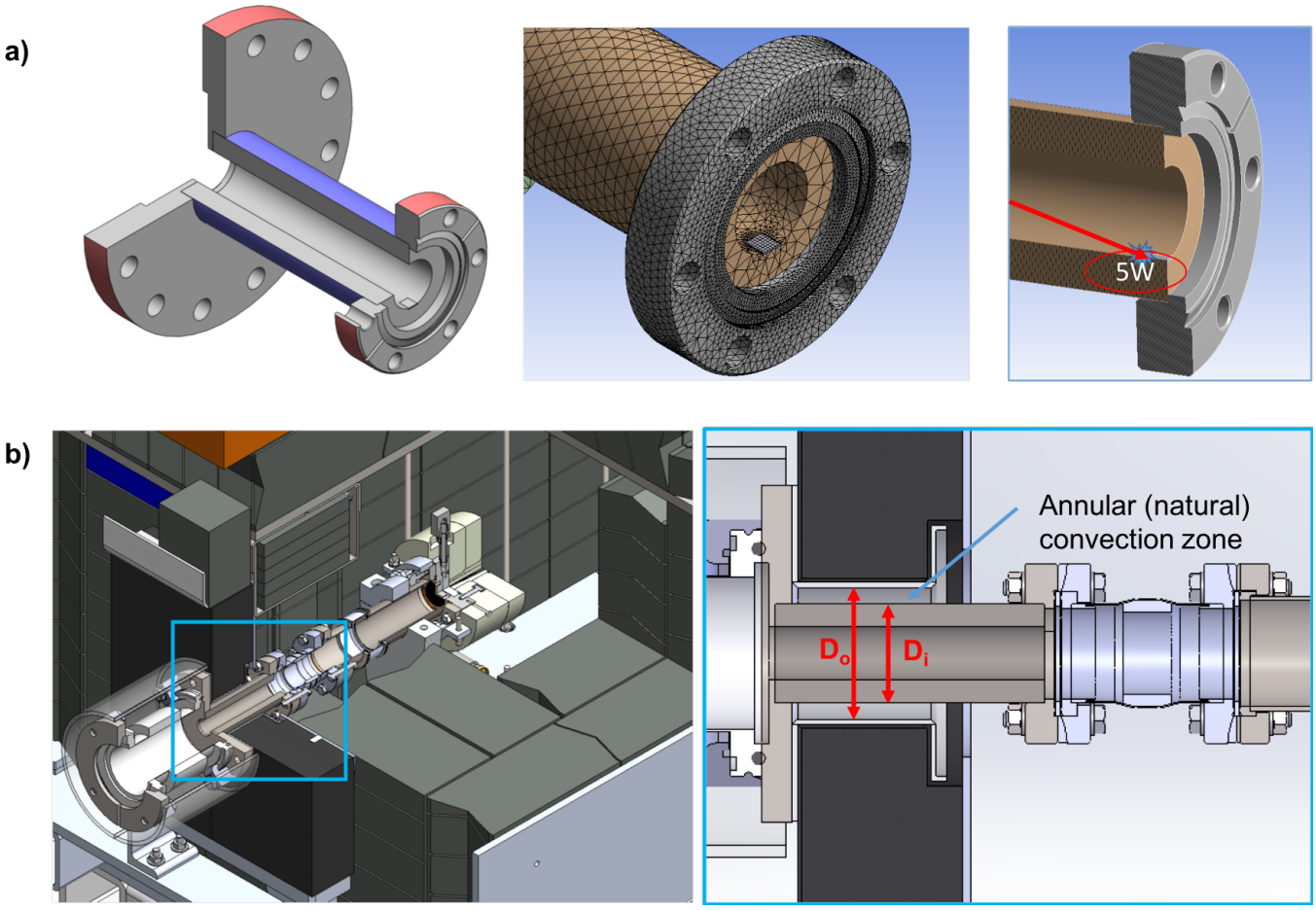

Figure A.14: The COL CAD geometry cross-ection as well as mesh geometries are shown in a). The red and blue colored regions of the model (left panel), correspond to the horizontal (free in air) cylinder and concentric (annular) cylindrical regions, respectively. In b) a depiction of the annular convection region between the inner and outer cylindrical surfaces, denoted by diameters D_i and D_o, respectively, is placed in the context of the irradiation platform.

Table A.5: input parameters for natural convective cooling in air for input into concentric cylinder and horizontal cylinder correlations. From left to right, the data is grouped in terms of flow, geometric, and thermal parameters for stagnant air between the annular flow region of COL.

Pr	0.713774
Ra	varies[a]
T_{ref}	20 °C
T_f	varies[b] °C
ρ_{ref}	1.201 g m^{-3}
ρ	varies[c] g m^{-3}

D_o	0.051 m
D_i	0.0381 m
b^d	0.00645 m
l^d	0.05334 m

k_{air}	0.0261 W m^{-1} K
β	0.0034 K^{-1}
T_o	20 °C
T_i	any °C
c_p	1007 J kg^{-1}
μ	0.0000185 kg m^{-1} s^{-1}

[a] see Figure A.15
[b] $T_f = (T_o - T_i)/2$
[c] Depends on temperature under ideal gas law assumption: $\rho = \rho_{ref}(T_{ref} + 273)/(T_f + 273)$
[d] $b = (D_o - D_i)/2; l =$ length of annular region

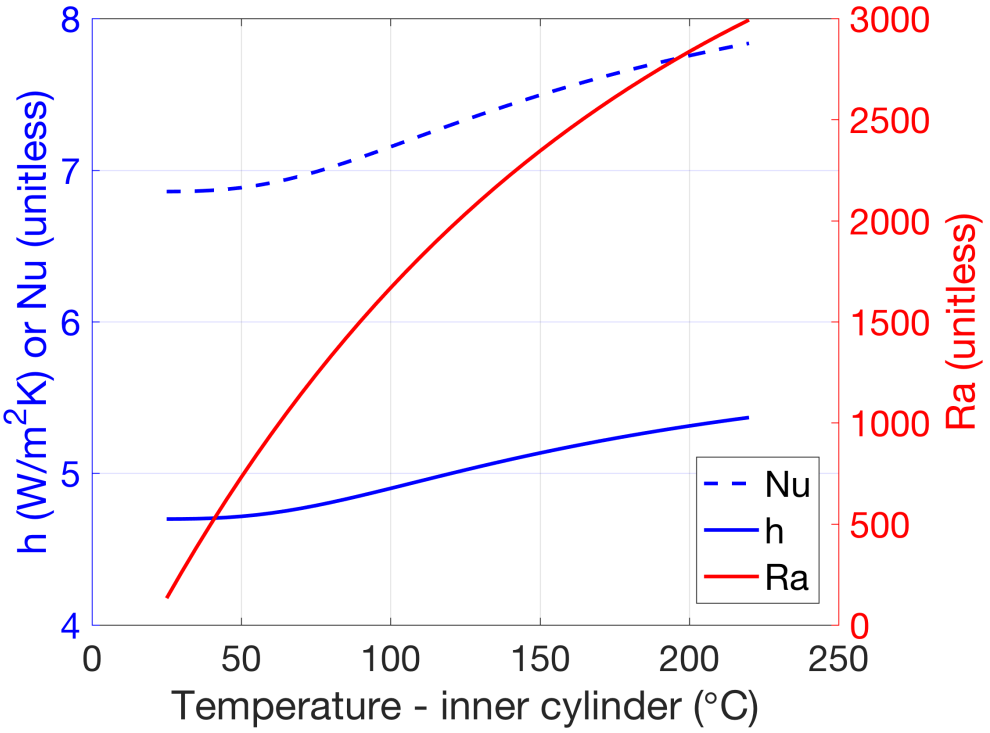

Figure A.15: Convective heat transfer coefficient as a function of temperature ($h(t)$) between two concentric cylinders based on the Kuehn and Goldstein (1976) correlations [274]. Also plotted are the Rayleigh number (Ra) and the Nusselt number (Nu).

heat transfer is conduction dominant; as T_i increases, convection becomes increasingly important as advection contributes more to the overall heat transport. Since only the stead-state temperatures were considered in the current model, however, a single average value for h which accounts for both conductive and convective mechanisms, such that $h_{conv} = f(Nu_{cond}, Nu_{conv}$.

The calculated h for natural convection at each cylindrical face of the end flanges (Figure A.14a) were $5\,\mathrm{W\,m^{-2}\,K^{-1}}$, while for the annular region, assuming a more conservative value for $T_f = 35\,^{\circ}\mathrm{C}$, h was calculated to be $4.7\,\mathrm{W\,m^{-2}\,^{\circ}C}$.

The results of the COL simulations employing the above parameters and the model for h are shown in Figure A.16. Evidently the peak operating temperatures are maintained around the upper $150\,^{\circ}\mathrm{C}$ limit even in steady-state, assuming a 5 W heat source with power density $1\,\mathrm{W\,mm^{-2}}$. Moreover, mechanical modeling based on the high-T mechanical properties of 304 SS [273] showed that the total strain is everywhere within the elastic regime and so a large number of trip events are expected to be tolerated under the defined current limits discussed above. Note that the vacuum pressure BCs were derived from results of the work in Appendix A.4 and the COL is free to expand axially, owing to the presence of bellows, and radially without translation laterally or under gravity.

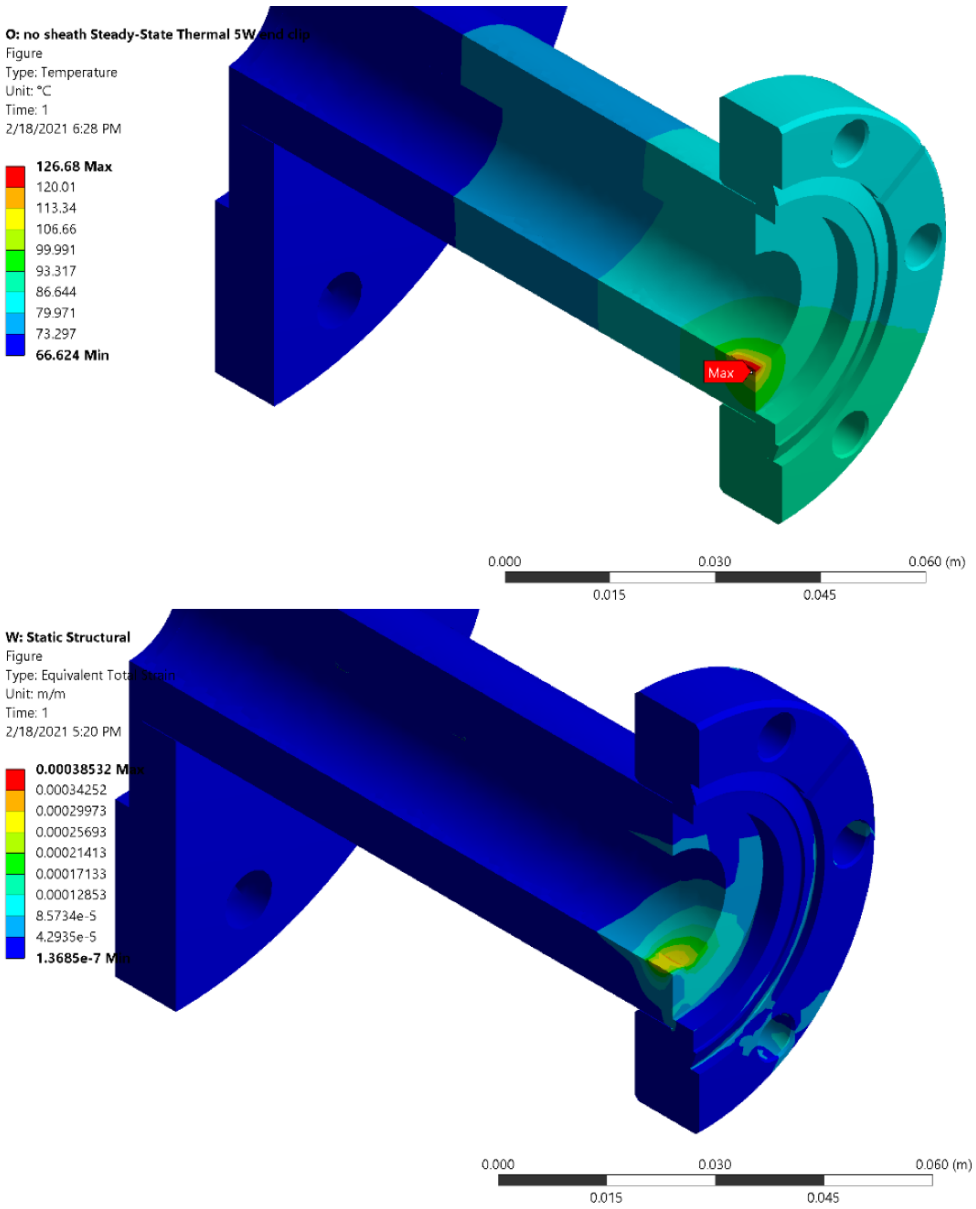

Figure A.16: ANSYS temperature (top) and total strain (bottom) distributions for 5 W worst-case (end-clip) scenario.

A.6 Supplementary stress-strain data for the ARIEL target design

The following figures are an extension of the stress-strain results from ANSYS FEA simulations conducted for the UHDR x-ray target design for the FIRST platform presented in Section 5.6. These results were included as supplementary data provided for the published article summarizing this work [53][2].

As an additional, albeit brief, exploration, a TOPAS simulation of energy deposition within the Ta target itself for the FLASH treatment beam (1 kW power) was conducted to produce a depth-power

[2]steady-state simulation figures derived from the work of Luca Egoriti in [53]

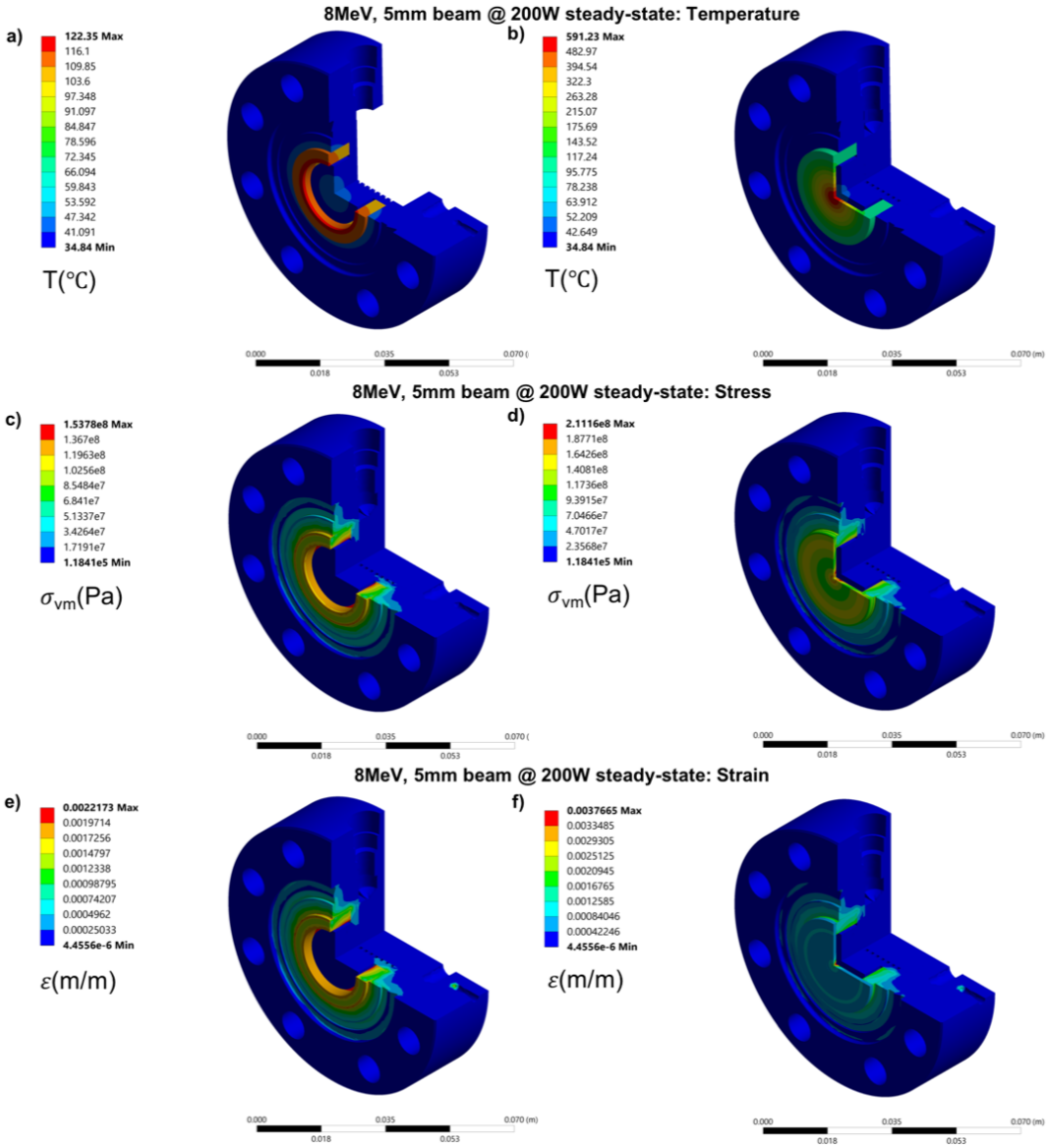

Figure A.17: Summary of steady-state ANSYS® FEA simulation results for the 8 MeV CW beam with a 5 mm beam size and 200 W average power. The temperature (a,b), von Mises stress (b,e) and total strain (c,f) distributions are shown in aluminum-only (a-c) and full target (d-f) views.

distribution (Figure A.19). The simulation was run for the same beam size ($2\sigma = 5$ mm) and power (1 kW) for both 8 and 10 MeV beam energy and the data were averaged over the entire surface area at each sampled depth. While the results comprise the integrated power deposition, they omit spatial dependencies and localized regions of increased power density that may arise due to differences in stopping and scattering powers for electrons at these different energies. Nevertheless, an important observation could be made that the 10 MeV beam affords a broader power distribution for a similar integrated power (i.e. $\int_o^z (dP_{8MeV}/dz - dP_{10MeV}/dz)\, dz \approx 12$ W) and helps to explain the reduced heating rate at higher energy. Notably, the 8 MeV beam features more localized power deposition at a shallower depth which would explain higher peak temperatures in Ta at that beam energy. The

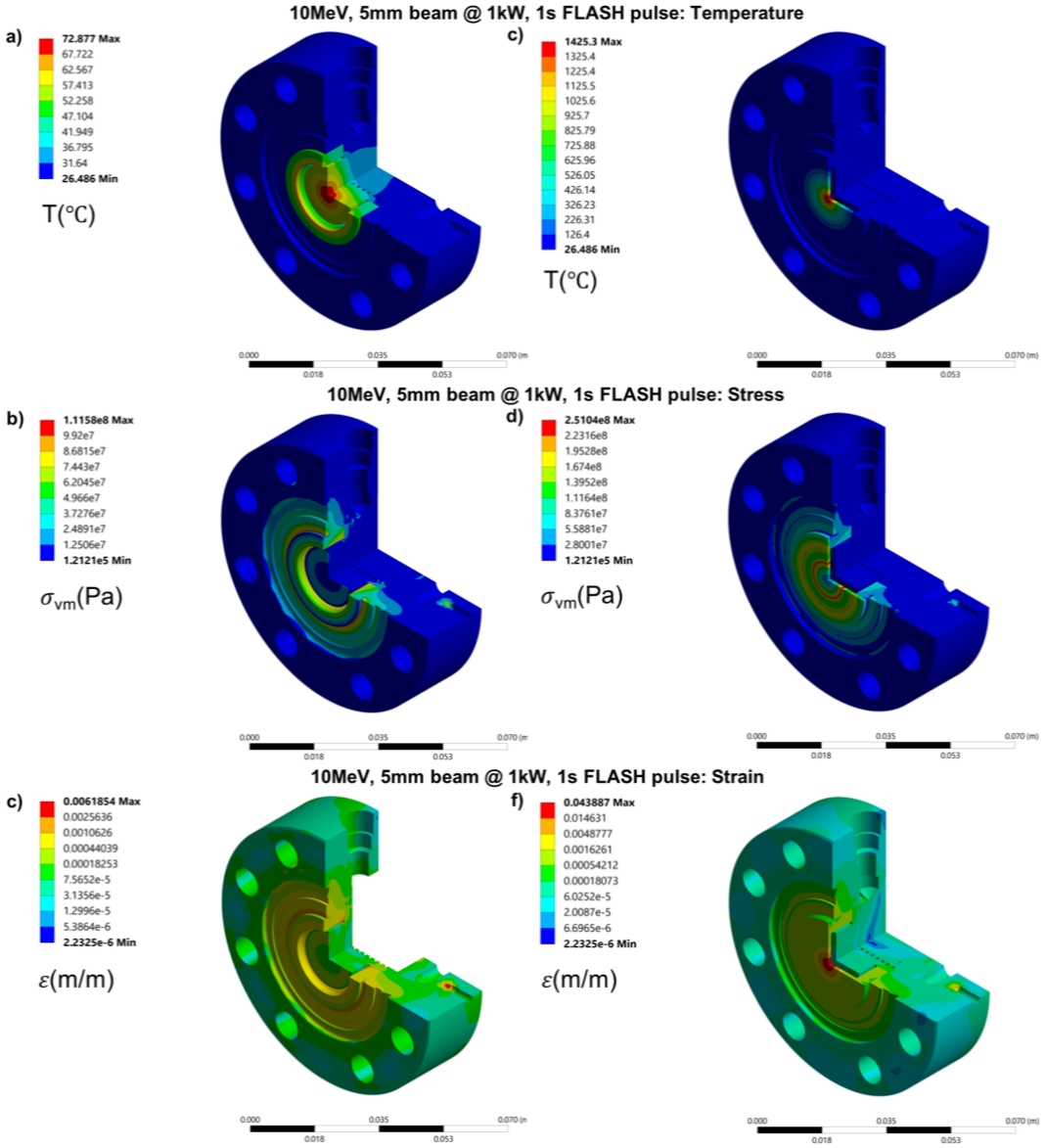

Figure A.18: Summary of transient ANSYS® FEA simulation results for the 10 MeV FLASH (pulsed) beam with a 5 mm beam size and 1 kW average power operating for 1 s. The temperature (a,b), von Mises stress (b,e) and total strain (c,f) distributions are shown in aluminum-only (a-c) and full target (d-f) views. All data are generated at the end of a 1 s electron beam pulse.

fact that the power deposition peak arises at nearly the geometric center of the Ta target layer also provides a benefit of reducing superficial heating and potential defect formation paired with lower thermal strain.

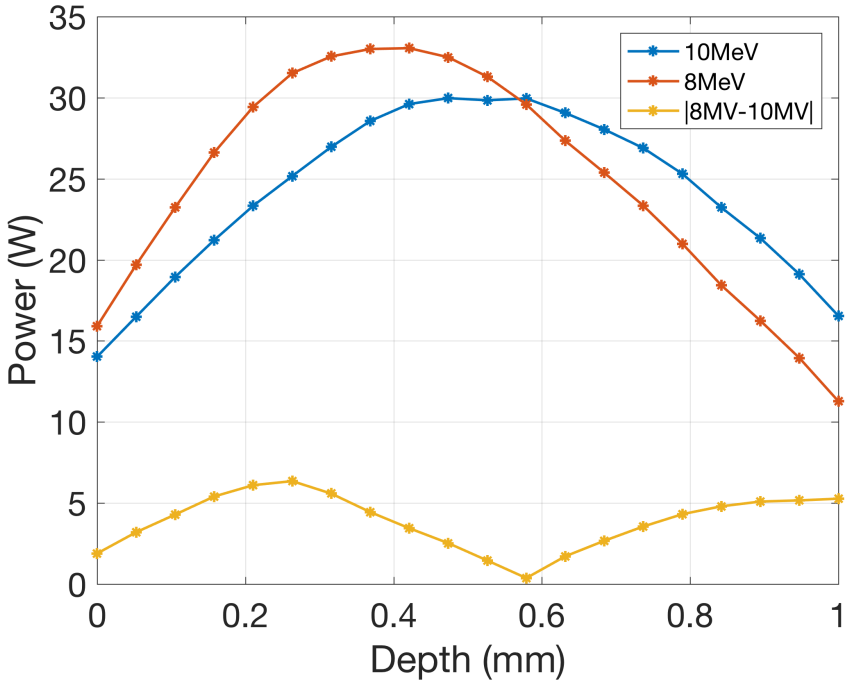

Figure A.19: Surface area average power distribution as a function of depth within the Ta target for both the 8 and 10 MeV FLASH beams at 1 kW beam power. The absolute different of between the 8 and 10 is also shown.

A.7 *Drosophila* larvae irradiations at ARIEL: PDD verification for FLASH and CONV

In a exploratory application of 10 MV UHDR x-rays for accessible biological models for improved experimental scalability, *drosophila melanogaster* larvae were irradiated at the new FIRST UHDR x-ray irradiation platform located on the ARIEL beamline at TRIUMF.

Four groups (2 dose cohorts) each with $N \simeq 20$ larvae were exposed to UHDR or conventional CONV-RT 10 MV x-rays. The larvae were immobilized in custom-made (5.8×5.8) acrylic phantom slabs with 3-mm deep larvae cavities placed at 5 and 13-mm depth in solid-water. Localization fiducials to ensure beam centering and restrain the larvae within the field dimensions ($\approx 1 \times 1\,\text{cm}^2$). EBT3 Gafchromic films were placed in-between the phantom slabs at the surface (groups A and B only) and at depths of 3, 8, 11 and 16 cm (all groups).[3]. Intermediate data points at 5 and 13 mm, corresponding to the depth of the simultaneously irradiated *drosophila* larvae, were calculated by interpolation of the bounding film doses.

Doses of approximately 10 (groups C,D) and 14 Gy (groups A,B) were delivered to a depth of 1-cm in solid water using both FLASH (A,C) and CONV (B,D) beam modes, per the methods described in sections 6.2.4.1 and 6.2.4.2. Specifically, the FLASH irradiations were first delivered by scaling ACCT current, and thus dose-rate, measurements; immediately following FLASH delivery, the

[3]Holder design, experimental setup and irradiations were conducted in collaboration with Alex Hart and Dr. Magdalena Bazalova-Carter

ACCT-to-EMDB conversion factor (TF; see Section 6.2.4) was applied to determine the appropriate total charge required on the EMBD/target to achieve the same dose delivered to the paired FLASH cohort. The calculated charges amounted to 17.14 and 14.00 µC for the high and low dose treatments, respectively[4]. The motion stage allowed for accurate positioning of each phantom within a single lockup by translating (up to 10 cm) between phantoms placed on top of and within the mouse holder and additionally separated by 1.5 cm of tantalum shielding. In all, four irradiations were conducted; the parameters (i.e. actual delivery current and charge) and film dosimetry results are summarized in Tables A.6 and A.7 for the high and low dose prescriptions, respectively.

Table A.6: Summary of high dose group (A,B) FLASH and CONV drosophila irradiations

FLASH						
Name	Depth (mm)	Dose (Gy)	Time (s)	Dose rate (Gy/s)	EMBD charge (µC)	ACCT current (µA)
A0	0	25.45	0.165	154.24		
A1	3	18.98	0.165	115.03		
AF1	5	16.805	0.165	101.85		
A2	8	14.63	0.165	88.67	—	62.5
A3	11	13.63	0.165	82.61		
AF2	13	12.26	0.165	74.30		
A4	16	10.89	0.165	66.00		
CONV						
B0	0	25.70	266	9.66E-02		
B1	3	18.60	266	6.99E-02		
BCW1	5	16.38	266	6.16E-02		
B2	8	14.16	266	5.32E-02	17.22	—
B3	11	13.57	266	5.10E-02		
BCW2	13	12.38	266	4.65E-02		
B4	16	11.19	266	4.21E-02		

*AF and BCW designate the location of the fly cohorts for FLASH and CONV groups, respectively

Unexpected movement between setup and retrieval meant that the final number of larvae and those within the field at the time of irradiation was uncertain[5]. Nevertheless, the irradiations served to produce depth-dose film data for consecutive FLASH and CONV irradiations conducted under identical setup conditions, which was not possible for the dosimetry methods and small-animal studies outlined in Chapter 6. Depth dose curves derived from the tabulated data are shown in Figure A.20 below. Evidently, the constancy of the PDD between paired (dose) groups imply that the beam spectra is practically unchanged between the FLASH and CONV delivery - something which, at the time of writing, has not been possible while using other UHDR photon sources [44, 131, 277].

[4]These charges were derived on the conversion factor for the first beam tune. See Chapter 6.
[5]The follow-up study is beyond the scope of this dissertation

Table A.7: Summary of low dose group (C,D) FLASH and CONV *drosophila* irradiations

Name	Depth (mm)	Dose (Gy)	Time (s)	Dose rate (Gy/s)	EMBD charge (µC)	ACCT current (µA)
FLASH						
C1	3	14.07	0.131	107.40	—	64.30
CF1	5	12.33	0.131	94.08		
C2	8	10.58	0.131	80.76		
C3	11	10.33	0.131	78.85		
CF2	13	9.40	0.131	71.72		
C4	16	8.46	0.131	64.58		
CONV						
D1	3	14.42	268	5.38E-02	14.10	—
DCW1	5	12.60	268	4.70E-02		
D2	8	10.77	268	4.02E-02		
D3	11	10.25	268	3.82E-02		
DCW2	13	9.41	268	3.51E-02		
D4	16	8.56	268	3.19E-02		

*CF and DCW designate the location of the fly cohorts for FLASH and CONV groups, respectively

Moreover, the procedure demonstrated the effectiveness for using pre-calculated TF conversion factors to translate measured/delivered ACCT current values into an equivalent EMBD (integrated) charge for equivalent FLASH and CONV dose delivery. The plateau regions in the depth-dose curve are due to the voids, and thus lack of attenuation, in the fly-compartment of the acrylic phantom slabs.

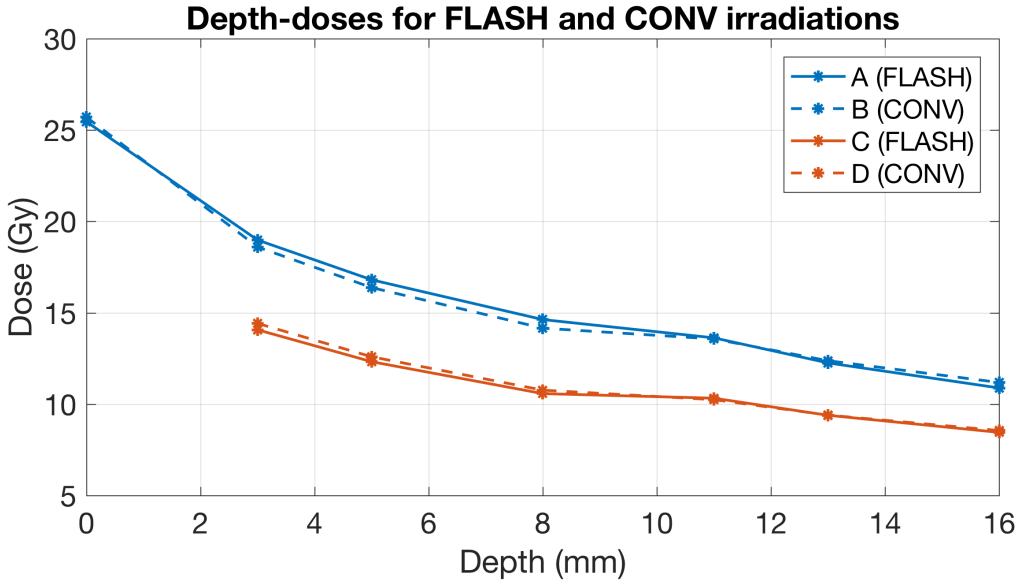

Figure A.20: Summary of drosophila depth-doses data for paired FLASH and CONV irradiations at two dose levels. Groups (A,B) and (C,D) were delivered such that each paired CONV irradiation (dotted lines) immediately followed the FLASH single-pulse delivery (solid lines) within a single lockup. N ≃20 per group.